

# Journal of the National Science Foundation of Sri Lanka





NATIONAL  
SCIENCE  
FOUNDATION

## JOURNAL OF THE NATIONAL SCIENCE FOUNDATION OF SRI LANKA

### Editorial Board

Ajit Abeysekera (Editor in Chief)  
J.K.D.S. Jayanetti  
L.P. Jayatissa  
P. Prasad M. Jayaweera  
Jagath Manatunge  
S.S.N. Perera  
Rohini de A. Seneviratne  
Saman Seneweera  
S.A.H.A. Suraweera  
P. Wijekoon  
M.J.S. Wijeyaratne

### Language Editor

R.D. Guneratne  
M.C.M. Iqbal

### Editorial Office

Nadeeja Wickramarachchi (Principal Scientific Officer)  
Upuli Rathnayake (Scientific Officer)  
Supun de Silva (Information Officer)

Designing & Typesetting  
Kanchana Sewwandi

### Contact details

Editorial Office, National Science Foundation,  
47/5, Maitland Place, Colombo 07, Sri Lanka.

E-mail : [jnsf@nsf.gov.lk](mailto:jnsf@nsf.gov.lk)  
Phone : +94-11- 2696771  
JNSF online submission portal :  
<https://jnsfsl.sljol.info/about/submissions>  
JNSF home page :  
<http://www.nsf.gov.lk/index.php/nsfscience-magazine>

**Publication** : Published quarterly (March, June, September and December) by the National Science Foundation of Sri Lanka.

**Manuscripts** : Research Articles, Research Communications, Reviews and Correspondences in all fields of Science and Technology can be submitted for consideration for publication. A guide to the preparation of manuscripts is provided in each issue. The guidelines may also be obtained by visiting the NSF website or JNSF online submission portal.

**Disclaimer** : No responsibility is assumed by the National Science Foundation of Sri Lanka for statements and opinions expressed by contributors to this Journal.

**Publication** : A publication fee of US\$ 250 will be levied for each manuscript in two stages except, when the corresponding author is affiliated with a Sri Lankan institution.

- A processing fee of US\$ 20 will be levied for each manuscript at the peer-review stage.
- The remaining US\$ 230 will be charged for accepted articles at the time of publication.

**Copyright** : © National Science Foundation of Sri Lanka

Articles in the Journal of the National Science Foundation of Sri Lanka are Open Access articles published under the Creative Commons CC-BY-ND License (<http://creativecommons.org/licenses/by/4.0/>). This license permits the use, distribution and reproduction, commercial and non-commercial, provided that the original work is properly cited and has not been changed anyway.

**Indexing** : The JNSF is indexed in Science Citation Index Expanded, Journal Citation Reports/ Science Edition, BIOSIS Previews, Zoological Record, Biological Abstracts, Chemical Abstracts, Scopus, DOAJ, TEEAL, Ulrich's, AGRICOLA and EBSCOhost, CAB Abstracts, SafetyLit, Journal TOCs, EBSCO Applied Science & Technology Source Ultimate

**JOURNAL OF THE  
NATIONAL SCIENCE FOUNDATION  
OF SRI LANKA**

Volume 52 Number 4 December 2024

---

## CONTENTS

---

### EDITORIAL

- 417 **Big molecules that do not go away**  
*Ajit Abeysekera*
- 

### RESEARCH ARTICLES

- 419 **Decadal trends in antimicrobial susceptibility of *Escherichia coli* and *Salmonella* spp. in chicken from small-scale farm shops in Kandy district, Sri Lanka**  
*DS Thilakarathne, BYI Gamage, KSA Kottawatta, KGR Abayawansa, WSN Gunawardana and RS Kalupahana*
- 435 **Symmetric encryption using snake graphs and supermagic covering**  
*PGRS Ranasinghe, RMVV Bandara and AMSLK Athapaththu*
- 441 **Maximum likelihood estimation for the two-parameter Maxwell distribution**  
*P Kasap and AO Faouri*
- 459 **Estimating plant dominance using field-measured structural parameters and remotely sensed data; A case study from Rekawa mangrove forest, southern coast of Sri Lanka**  
*SMTM Samarakoon, SK Madarasinghe, NDS D Thilakarathne, AMNN Bandularathne, HD Wijayathilaka, and KAS Kodikara*
- 469 **Simplification of large-scale solid element model for seismic structural response analysis of buildings**  
*HMSC Rathnasiri, JASC Jayasinghe and AJ Dammika*
- 481 **Athlete body power and strength estimation using skeleton point cloud**  
*H Rangala, S Samaraweera, KD Sandaruwan, TA Weerasinghe and DC Ranasinghe*
- 493 **Establishment and evaluation of real-time PCR based SELEX platform for the identification of protein binding aptamers: A pilot study in Sri Lanka**  
*AI Abeykoon, KMN Kumarasinghe, NV Chandrasekharan and PMTB Wickramasinghe*
- 501 **Enhanced privacy-preserving federated convivial learning for internet of medical things (IoMT) through block-chain-enabled trust Q-learning**  
*Sudharson K, G Babu, R Santhiya and CS Anita*
- 515 **Optimizing the alkaline concentration for coir fibre treatment and estimation of lifetime**  
*LG Chamath, LKT Srimal, GA Sewvandi, R Gallage and J Epaarachchi*

**527 Unveiling the depths of underwater image enhancement with spatial blended CNN: Diving into clarity**

*R Ahila Priyadharshi, S Arivazhagan and K Ramajeyam*

---

**I List of Referees**

**V Author Index**

**XI Subject Index**

---

**Guidelines for Contributors**



**Cover:** a, b, c, Underwater Images from UIEB, UFO-120 and EUVP datasets  
a1, b1, c1, Enhanced Underwater Images using Spatial Approach  
See *J.Natn.Sci.Foundation Sri Lanka* 2024 **52**(4): 527 - 540

## EDITORIAL

# Big molecules that do not go away

Life forms on earth depend vitally upon biopolymers, big molecules consisting of smaller molecules which are linked together, as exemplified by the nucleic acids, proteins and cellulose. In general, biopolymers have both structural and functional roles in living organisms. The lifestyle of humans in modern societies is equally dependent on a different type of big molecule, man-made synthetic polymers (plastics) formed by linking together smaller molecules usually obtained from petrochemicals.

Plastics are ubiquitous, and are encountered in daily life in almost every activity one can think of. One of the properties of plastics that make them so useful is their durability, in contrast to biopolymers which degrade in the natural environment. Ironically, it is also responsible for making plastics one of the biggest environmental problems facing the world today. A major concern is microplastics, resulting from macroscopic degradation

of plastic products, which now pollute the oceans and air, and have been shown to enter into biological systems. In microplastics the basic molecular structure of the polymeric materials is intact. These big molecules are not susceptible to break down by microorganisms; they just don't go away!

Tackling the worldwide problem of pollution by plastics require a multi-pronged approach including better waste management, recycling, developing biodegradable plastics, avoiding single usage products and reducing production. The recent failure of the United Nations Plastic Pollution Treaty, mainly due to a group of petrochemicals producing countries not agreeing to placing limits on the production of plastics, reflects at a deeper level the conceptual conflict between unlimited growth and sustainability. It is apparent that the idea that unlimited growth on a planet with limited resources is not sustainable, is not yet universally accepted.

**Ajit Abeysekera**



## RESEARCH ARTICLE

### Food Microbiology

# Decadal trends in antimicrobial susceptibility of *Escherichia coli* and *Salmonella* spp. in chicken from small-scale farm shops in Kandy district, Sri Lanka

DS Thilakarathne<sup>1\*</sup>, BYI Gamage<sup>2</sup>, KSA Kottawatta<sup>2</sup>, KGR Abayawansa<sup>2</sup>, WSN Gunawardana<sup>3</sup> and RS Kalupahana<sup>2</sup>

<sup>1</sup> Department of Veterinary Pathobiology, Faculty of Veterinary Medicine and Animal Science, University of Peradeniya, Sri Lanka.

<sup>2</sup> Department of Public Health and Pharmacology, Faculty of Veterinary Medicine and Animal Science, University of Peradeniya, Sri Lanka.

<sup>3</sup> Department of Farm Animal Production and Health, Gatambe, Peradeniya, Sri Lanka.

Submitted: 02 November 2023; Revised: 22 October 2024; Accepted: 25 October 2024

**Abstract:** *E. coli* and *Salmonella* spp. are two important foodborne pathogens that rapidly develop antimicrobial resistance (AMR) and frequently contaminate animal products, particularly chicken meat. In Sri Lankan small scale poultry operations, substandard hygienic practices are common. The current study reports and compares two consecutive studies conducted in 2010-2011 and 2020-2021, which investigated AMR *E. coli* and *Salmonella* spp. contamination in chicken meat sold at small-scale farm shops in the Kandy district, Sri Lanka. The first study included 72 chicken meat samples collected from 10 out of the 20 divisional secretariat divisions (DSDs), while the second study included 37 meat samples from the same DSDs, collected 10 years later. *Salmonella* spp. and *E. coli* were isolated and identified, and AMR profiles were obtained using disc diffusion assay and CLSI guidelines. The first study reported 100% *E. coli* contamination in chicken meat, but a decade later, the percentage had significantly decreased to 70.3%. In both studies, *E. coli* isolates demonstrated resistance to more antimicrobials than *Salmonella* isolates, and the proportion of multidrug-resistant (MDR) *E. coli* isolates (defined as resistance to five or more antimicrobials) was higher than that of the *Salmonella* spp. isolates. Significantly lower MDR *E. coli* isolates were detected in the recent study. However, tetracycline resistance among *E. coli* isolates was higher compared to the previous study. Despite these improvements, the contamination level of chicken meat in small-scale retail shops remains concerning. Therefore, it is crucial to promote prudent antimicrobial use and ensure proper food processing practices at all levels of production in Sri Lanka.

**Keywords:** Antimicrobials, chicken, *E. coli*, meat, resistance *Salmonella* spp.

## INTRODUCTION

Food safety is a growing public health concern worldwide, owing to the rising numbers of foodborne illness (FI) cases and the demand to meet food standards to ensure consumer safety (Gizaw, 2019). Foodborne illnesses cause significant morbidity and mortality, posing a noteworthy influence in terms of the cost of medical care, resulting in a substantial loss of productive hours for the nation (Newman *et al.*, 2015a; 2015b). Even in the United States, where the food supply is considered one of the safest in the world, 48 million cases of FI occur each year (Huffaker & Hartmann, 2021). However, these numbers are considered an underestimation, because milder cases are often undiagnosed and thus unreported (Todd, 2014). The scenario with FI is even worse in developing countries, because no proper surveillance system is in place and thus reported cases might only be the tip of the iceberg (Grace, 2015). Among FI caused by known agents, bacteria continue to be a major cause of foodborne diseases worldwide (Bintsis, 2017). As a result, qualitative or quantitative assessments of bacteria have been a priority in meeting food safety standards.

\* Corresponding author (dsamanthikat@gmail.com;  <https://orcid.org/0000-0002-8790-033X>)



This article is published under the Creative Commons CC-BY-ND License (<http://creativecommons.org/licenses/by-nd/4.0/>). This license permits use, distribution and reproduction, commercial and non-commercial, provided that the original work is properly cited and is not changed in anyway.

*Escherichia coli* (*E. coli*) and *Salmonella* spp. are major foodborne pathogens that have been prioritized in all food safety standards (Abebe *et al.*, 2020). According to the Center for Disease Control and Prevention (CDC), pathogenic *E. coli* is one of the top five pathogens responsible for domestically acquired FI resulting in hospitalization, while *Salmonella* spp. (non-typhoidal) is among the top five pathogens resulting both hospitalization and death (CDC, 2011). Both these pathogens share some common features such as the source of infection, pathogenicity, and development of resistance against antimicrobials. *E. coli* and *Salmonella* spp. are found colonized in intestinal tracts of a variety of wild and domestic animals, especially farm animals. Therefore, contaminated food of animal origin has been identified as the main source of infection (Heredia & García, 2018). Upon infection, these pathogens often cause mild to moderate self-limiting enteritis unless it is complicated or progresses into an invasive condition which may be fatal (Croxen *et al.*, 2013; Marchello *et al.*, 2022). Moreover, due to the intensive use of antimicrobials in farming, these pathogens demonstrate an increased rate of acquired resistance against commonly used antimicrobial agents (Frye & Jackson, 2013). Additionally, these pathogens carry multidrug resistant determinants that can be disseminated via horizontal and vertical transfer (Card *et al.*, 2017; Li *et al.*, 2021). Further, contaminated poultry meat has identified to be an important source of transmitting these pathogens (Heredia & García, 2018).

Chicken meat is the most consumed meat variety in Sri Lanka and the per capita consumption has significantly increased during the past few decades (Alahakoon *et al.*, 2016). The popularity of chicken meat is primarily due to the absence of cultural or religious obstacles, availability in retail markets and relatively low cost. Previous studies conducted in Sri Lanka have demonstrated substantial contamination of chicken eggs and meat with *E. coli* and *Salmonella* spp. (Kalupahana *et al.*, 2017; Kulasooriya *et al.*, 2019).

Different scales of poultry operations function within Sri Lanka and their management practices are diverse. Even though large-scale companies release quality-certified branded chicken meat to the market, a considerable fraction of meat consumers prefer purchasing fresh chicken meat from small-scale retail shops. Generally, the chicken sold in these small-scale farm shops is processed in facilities not designed as processing plants, where slaughtering and evisceration are done manually and mostly on-site. Like in many other developing countries, hygienic practices in these small

scale retail meat shops are often below the standards and function with minimum resources. Therefore, the potential of meat getting contaminated with foodborne pathogens is relatively high. Meat contamination with bacteria found in animal guts and the presence of AMR strains can be used to assess operational hygiene at both the production and processing levels. It was hypothesized that substandard processing practices in small scale farm shops would increase contamination of chicken meat with foodborne *E. coli* and *Salmonella* spp.. Additionally, these bacteria might exhibit resistance to antimicrobials commonly used in veterinary practice. Therefore, two investigations were done 10 years apart to reveal the level of *E. coli* and *Salmonella* spp. contamination in chicken meat sold at small scale shops in the Kandy district, Sri Lanka and the antimicrobial susceptibility of these contaminants.

---

## MATERIALS AND METHODS

### Study area and sampling design

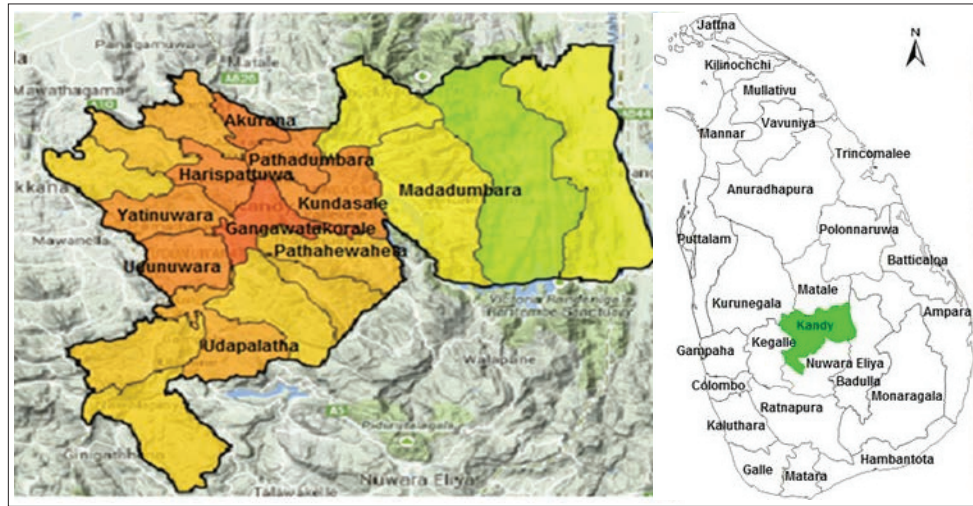
The two investigations were done in 2010-2011 and 2020-2021 in Kandy district, one of the most densely populated districts of Sri Lanka. The Kandy district consists of 20 divisional secretariat divisions (DSDs). To address the variation in population density among DSDs (the number of meat retail shops varies accordingly) and to increase the precision of the study, the DSDs of Kandy district were considered as strata.

Only the small scale 'farm shops' were sampled to avoid selection bias, and to maintain uniformity among sampling sites. In Sri Lanka, a 'farm shop' is typically a small scale retail shop where fresh or frozen and thawed poultry carcasses are sold by keeping them in display units at 10-15°C. Most of these shops sell only poultry products such as whole carcasses, cuts, poultry visceral organs, eggs, and the value-added products such as sausages, meatballs, etc. However, some farm shops may also sell food products from other animals (dried fish, canned fish, etc.) and food products of non-animal origin. These farm shops are often found in the centre of a town and, besides, they can be found scattered in certain streets in larger towns.

As reliable data on the number of farm shops in each DSD was unavailable, the sample size was calculated based on an estimated 150 farm shops in the study area. Assumptions included a 90% prevalence of *E. coli* contamination in chicken meat, a 95% confidence interval, and a 5% margin of error. This resulted in a required sample size of 73 farm shops for investigation.

It was assumed that population densities proportional to the farm shops available in each DSD. The top five DSDs based on the population were selected purposefully and the remaining five were picked randomly using Minitab software. In the 2010-2011 investigation, chicken meat samples were collected from 72 small-scale farm

shops across 10 DSDs (Figure 1). In the 2020-2021 investigation, efforts were made to collect samples from the same geographical locations. However, only 37 farm shops could be sampled due to permanent shop closures, COVID-19 restrictions, and financial limitations.



(The colours used in the map do not indicate any scale or a variable)

**Figure 1:** Divisional Secretariat Divisions (DSDs) of Kandy district of Sri Lanka sampled during two studies

**Sample collection**

In Sri Lanka, traditionally, the central market/main stall complex is located adjacent to the central bus stand. Therefore, sampling was performed in the main

population centre of each DSD starting from the farm shop proximal to the central bus stand and continued along the main street until the required sample size was fulfilled. The number of farm shops sampled in the main centre of each DSD is shown in Table 1.

**Table 1:** Number of farm shops sampled from the main population centre of the selected DSDs during each investigation

Selected divisional secretariat divisions	Main population centre	Number of farm shops sampled	
		2010-2011 investigation	2020-2021 investigation
Gangawatakorale	Kandy	20	5
Udapalatha	Gampola	13	5
Akurana	Akurana	9	5
Harispattuwa	Katugastota	9	5
Pasbagakorale	Nawalapitiya	6	5
Yatinuwara	Pilimathalawa	3	3
Udunuwara	Geliya	3	*
Pathahewaheta	Thalathuoya	3	3
Madadumbara	Theldeniya	3	3
Kundasale	Kundasale	3	3
Total		72	37

\* No sampling was done

At each farm shop, a chicken leg was purchased as the sample assuming that it is the part which has the highest possibility of contamination during carcasses handling and manual evisceration. The collected samples were transported to the Food Microbiology Laboratory of the Department of Veterinary Public Health and Pharmacology, University of Peradeniya and stored at 4°C until the isolation and identification of foodborne bacteria were done.

### Isolation, identification, and confirmation of *E. coli* and *Salmonella*

The qualitative identification protocols described by SLS 516: part 3: 1982 were followed, with certain modifications for isolation and identification of *E. coli*. If summarized, 25 g of meat were weighed, blended and homogenized with 225 mL of buffered peptone water (BPW) (Oxoid, CM0509). The homogenate was incubated for 18 - 24 h at 36 °C ± 1°C in a screw-capped bottle. A loop full (10 µg) of this enriched homogenate was taken and streaked on a MacConkey (MAC) agar (Oxoid, CM0007) plate and incubated at 36°C ± 1°C for 18-24 h. A presumptive *E. coli* colony (red, non-mucoid colonies) was picked and cultured on an Eosin-methylene blue (EMB) agar (Oxoid, CM0069) plate, incubating for 36°C ± 1°C for 18 - 24 h. A typical *E. coli* colony (purple colour colonies with a green metallic sheen) from an EMB plate was sub-cultured on nutrient agar (Oxoid, CM0003), incubating at 37°C for 18 - 24 h. Confirmation was done by subjecting the isolates to Grams staining and a panel of biochemical tests (Catalase test, Triple Sugar Iron reaction, Urease test, Citrate test, motility test, and Kovacs' Indole test).

For isolation and identification of *Salmonella*, methods described in ISO 6579 were followed. In brief, from the sample, 25 g of meat were weighed and blended using stomacher for 2 minutes to homogenize with 225 ml of BPW (Oxoid, CM0509). The homogenate was incubated 16 – 20 hours at 36 °C ± 1°C in a screw-capped bottle. From this pre-enrichment 0.1 mL was mixed with 10 mL of Rappaport-Vassiliadis (RV) broth (Oxoid, CM0669) and incubated at 41.5°C ± 0.5°C for 18 - 24 h. A loop full (10 µg) of this selective enrichment was taken and streaked on a Xylose Lysine Deoxycholate (XLD) agar (Oxoid, CM0469) plate, which was then incubated at 36°C ± 1°C for 18 - 24 h. The plate was observed for the presence of typical *Salmonella* spp. colonies (red colonies with black centers) and such colonies were sub-cultured on nutrient agar (Oxoid, CM0003) at 37°C for 18 - 24 h. Confirmation of recovered *Salmonella* spp. was done by Grams staining, biochemical testing (Catalase

test, Triple Sugar Iron reaction, Urease test, Citrate test, and motility test) and performing an agglutination test with polyvalent *Salmonella* antiserum.

### Antimicrobial susceptibility testing

*E. coli* and *Salmonella* spp. isolates were subjected to disk diffusion assay to identify their antimicrobial susceptibility profiles. Guidelines and clinical breakpoints given by the Clinical Laboratory Standard Institute, 2008, were used to conduct the disk diffusion assay and to interpret the results. However, in situations where the particular antimicrobial was not listed in the publication, breakpoints of the closest antimicrobial within the same group were used for interpretation. In each investigation the panel of antimicrobials was selected based on availability as well as considering whether the antimicrobials are repetitively used in poultry medicine and in humans. *E. coli* ATCC 25922 was used as the quality control strain.

The antimicrobial panel of both studies included ampicillin (10 µg), ciprofloxacin (5 µg), chloramphenicol (30 µg), gentamicin (10 µg), streptomycin (10 µg), and tetracycline (30 µg). However, amoxicillin (10 µg), cephalothin (30 µg), enrofloxacin (5 µg), and neomycin (10 µg) were only available for the 2010-2011 investigation, whereas amikacin (30 µg), amoxicillin-clavulanic acid (30 µg), cefotaxime (30 µg), ceftazidime (30 µg), nalidixic acid (30 µg) and trimethoprim-sulphonamide (25 µg) were only available for the 2020-2021 investigation. Multidrug resistance was defined as resistance to five or more antimicrobials from different classes tested in the study.

### Data management

Microsoft Excel spreadsheets were used to manage data and GraphPad was used to generate figures. Two sample proportion analyses were conducted on Minitab statistical software where  $p \leq 0.05$  was considered significant.

## RESULTS AND DISCUSSION

### Contamination of meat with *Salmonella* spp. and *E. coli*

The study conducted in 2010-2011 detected *E. coli* in all (100%) meat samples tested and *Salmonella* spp. in 34/72 (47.2%) of the meat samples tested (Figure 2a and 2b). However, in 2020-2021 investigation, *E. coli* contamination was 70.3% (26/37) and *Salmonella* spp. contamination was 59.45% (22/37) (Figure 2c and 2d).

Statistical comparison between the proportions revealed that the *E. coli* contamination observed in the 2020-2021 investigation is significantly lower ( $p = 0.00$ ) than that

of the 2010-2011 study, and the difference observed for *Salmonella* spp. contamination is not statistically significant.

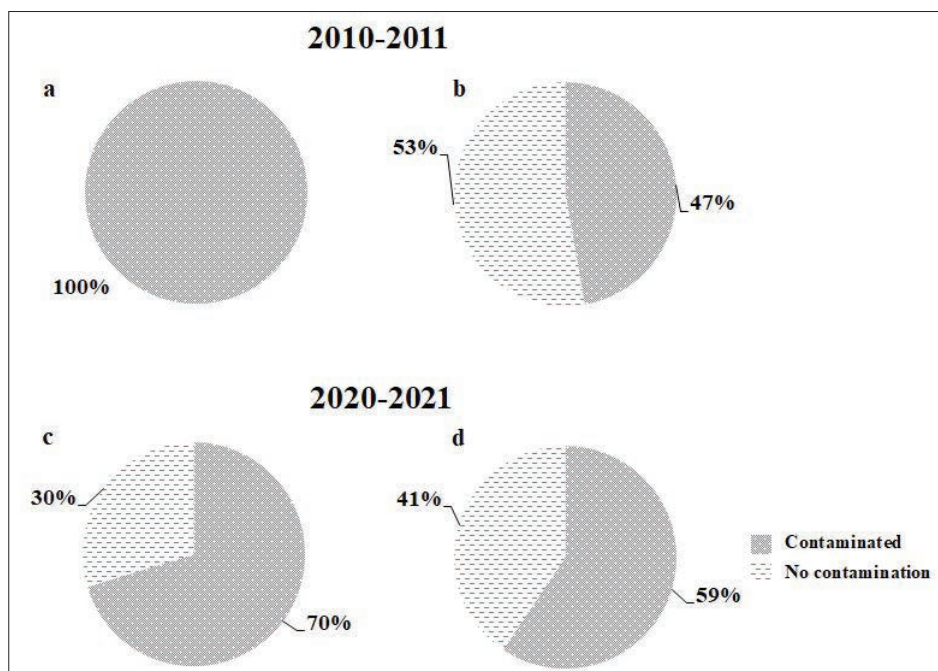


**Figure 2:** a) *E. coli* contamination in chicken meat detected in 2010 - 2011, b) *Salmonella* spp. contamination in chicken meat detected in 2010 - 2011, c) *E. coli* contamination in chicken meat detected in 2020 - 2021, and d) *Salmonella* spp. contamination in chicken meat detected in 2020 - 2021.

**Table 2:** *E. coli* and *Salmonella* contamination in meat by DSD

Selected Divisional Secretariat Divisions	Main town	2010-2011				2020-2021			
		<i>E. coli</i> contamination		<i>Salmonella</i> contamination		<i>E. coli</i> contamination		<i>Salmonella</i> contamination	
		Proportion	Percentage	Proportion	Percentage	Proportion	Percentage	Proportion	Percentage
Gangawatakorale	Kandy	20/20	100.0	7/20	35.0	3/5	60.0	3/5	60.0
Udapalatha	Gampola	13/13	100.0	8/13	61.5	3/5	60.0	2/5	40.0
Akurana	Akurana	9/9	100.0	4/9	44.4	3/5	60.0	2/5	40.0
Harispattuwa	Katugastota	9/9	100.0	3/9	33.3	4/5	80.0	3/5	60.0
Pasbagakorale	Nawalapitiya	6/6	100.0	5/6	83.3	4/5	80.0	2/5	40.0
Yatinuwara	Pilimathalawa	3/3	100.0	0/3	0.0	3/3	100.0	2/3	66.6
Udunuwara	Geliyoa	3/3	100.0	3/3	100.0				
Pathahewaheta	Thalathuoya	3/3	100.0	0/3	0.0	3/3	100.0	2/3	66.6
Madadumbara	Theldeniya	3/3	100.0	2/3	66.7	1/3	33.3	3/3	100.0
Kundasale	Kundasale	3/3	100.0	2/3	66.7	2/3	66.6	3/3	100.0

Table 2 shows the contamination of meat samples by DSD in each investigation. Despite the fact that the data were collected a decade apart, meat sold in all of the farm shops investigated is tainted with *E. coli* and *Salmonella* spp.

**Antimicrobial susceptibility profiles of the isolates**

*E. coli* isolates of the investigation conducted in 2010-2011 showed a markedly higher level of resistance against the panel of antimicrobials tested than those of *Salmonella* spp. isolated from the same investigation. *E. coli* isolates reported the highest percentage of resistance (97.2%) against neomycin and the least percentage of

resistance (8.3%) resistance against chloramphenicol (Figure 3). The percentages of *E. coli* isolates exhibited resistance against ampicillin, amoxicillin, cephalothin, streptomycin, and tetracycline (30 µg) are 90.3%, 83.3%, 80.5%, 77.8%, and 61.1% respectively.

*E. coli* isolated during the 2010-2011 investigation also demonstrated higher levels of resistance to the panel of antimicrobials tested than *Salmonella* spp. isolated during the same period. The highest percentage of resistance (69.2%) was observed in *E. coli* against ampicillin and tetracycline. Furthermore, 61.5% of the *E. coli* isolates tested were resistance to the trimethoprim-sulphonamide combination.

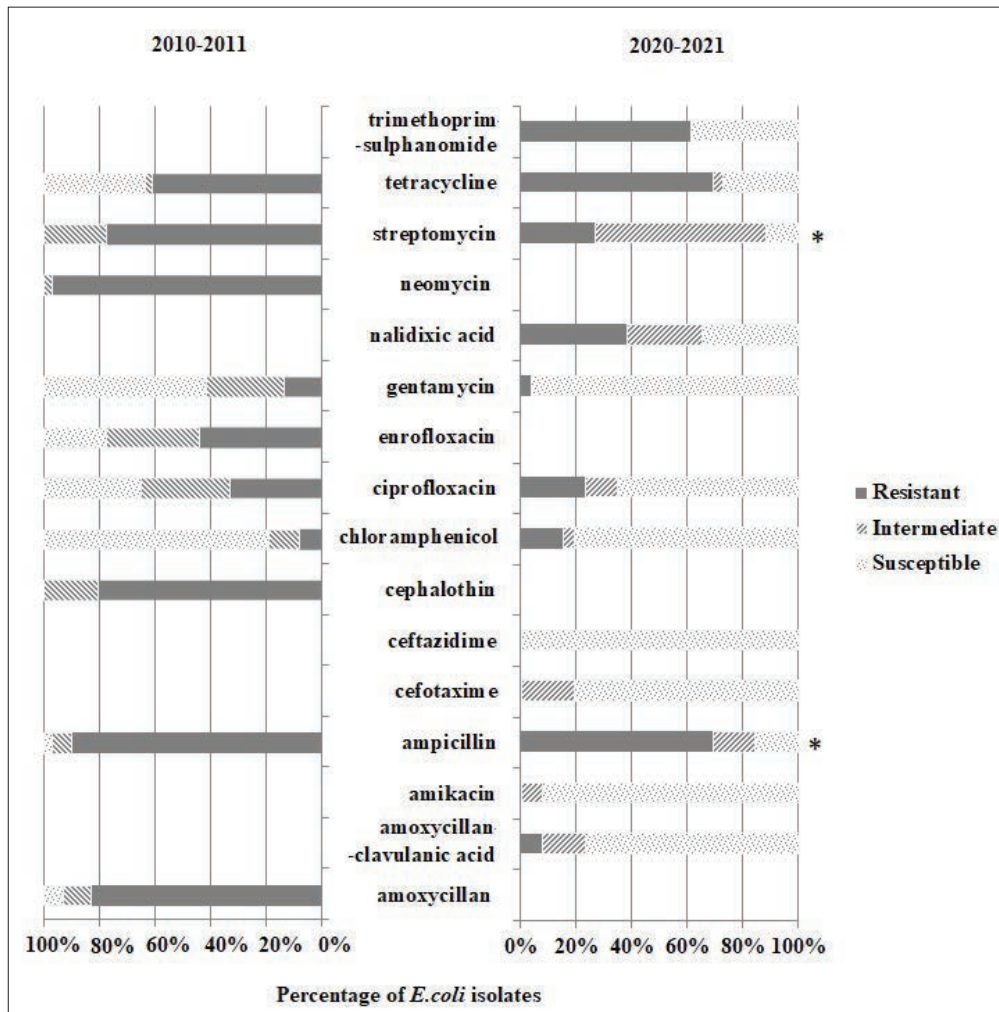


**Figure 3:** Antimicrobial resistance observed in chicken meat contaminant *E. coli* from the 2010-2011 study and the 2020-2021 study.

When resistance to antimicrobials common to both investigations was considered, *E. coli* isolates from the 2020-2021 study exhibited a significantly lower proportion of resistance to ampicillin ( $p = 0.01$ ) and streptomycin ( $p = 0.00$ ) than *E. coli* isolates from the previous study.

More than 40% of the *Salmonella* spp. isolates from the 2010-2011 study were resistant to neomycin (55.8%), streptomycin (35.3%), ampicillin (41.2%), and amoxicillin (41.2%) (Figure 4). Furthermore, only a small percentage of *Salmonella* spp. isolates from the same study were resistant to tetracycline (20.6%),

enrofloxacin (20.6%), cephalothin (11.8%), gentamycin (8.8%), chloramphenicol (5.9%), and ciprofloxacin (2.9 %).

In the 2020-2021 investigation, 54.5% of the *Salmonella* spp. isolates tested positive for tetracycline resistance, while 40.9% and 27.2% tested positive for ampicillin and nalidixic acid resistance, respectively. Antimicrobials such as amikacin, amoxicillin-clavulanic acid, cefotaxime, ceftazidime, chloramphenicol, gentamycin, and trimethoprim-sulphonamide were effective against more than 90% of the *Salmonella* spp. isolated during this study.

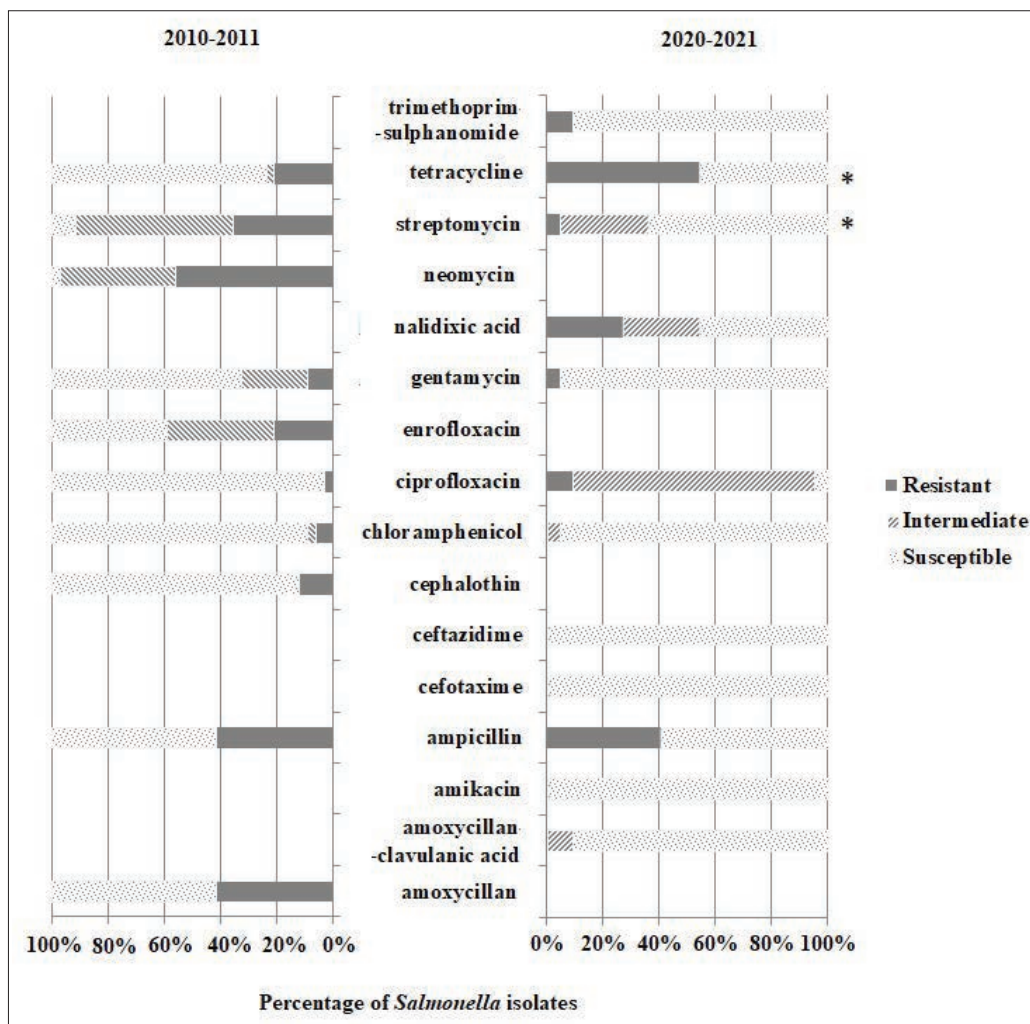


**Figure 4:** Antimicrobial resistance observed in chicken meat contaminant *Salmonella* spp. isolates from the 2010-2011 study and the 2020-2021 study.

**Table 3:** Percentage of *E. coli* and *Salmonella* spp. isolates showing antimicrobial resistance by divisional secretariat divisions in study 2010-2011

Divisional Secretariat Division	Percentage (%)																			
	AMP <i>E. coli</i>	AMP <i>Salm.</i>	AML <i>E. coli</i>	AML <i>Salm.</i>	CEP <i>E. coli</i>	CEP <i>Salm.</i>	NEO <i>E. coli</i>	NEO <i>Salm.</i>	GEN <i>E. coli</i>	GEN <i>Salm.</i>	STR <i>E. coli</i>	STR <i>Salm.</i>	TET <i>E. coli</i>	TET <i>Salm.</i>	ENR <i>E. coli</i>	ENR <i>Salm.</i>	CIP <i>E. coli</i>	CIP <i>Salm.</i>	CHL <i>E. coli</i>	CHL <i>Salm.</i>
Gangawatakorale	100	42.8	85	42.8	85	28.6	95	57.1	5	14.3	55	57.1	50	0	35	0	25	0	15	0
Udapalatha	92.3	25	92.3	25	84.6	0	92.3	50	0	12.5	92.3	50	61.5	25	30.8	25	30.8	0	7.7	0
Akurana	88.9	75	88.9	75	77.8	50	100	75	55.5	25	77.8	25	44.4	25	66.7	50	55.5	25	44.4	0
Harispathuwa	100	0	88.9	0	77.8	0	100	33.3	11.1	0	88.9	0	88.9	0	88.8	0	55.5	0	11.1	0
Pasbagakorale	100	20	100	20	100	0	100	6	16.7	0	83.3	40	83.3	20	50	20	50	0	0	40
Pathahewaheta	100	0	100	0	100	0	100	0	66.7	0	100	0	100	0	0	0	0	0	0	0
Madadumbara	33.3	100	33.3	100	66.7	0	100	0	0	0	100	0	33.3	100	33.3	0	33.3	0	0	0
Kundasale	66.7	50	66.7	50	66.7	0	100	50	0	0	100	0	66.7	0	0	50	0	0	0	0
Yatinuwara	100	0	100	0	100	0	100	0	0	0	100	0	66.7	0	33.3	0	33.3	0	0	0
Udunuwara	33.3	66.7	33.3	66.7	33.3	0	100	100	0	0	33.3	0	33.3	33.3	0	33.3	0	0	0	0

**Table 4:** Percentage of *E. coli* and *Salmonella* spp. showing antimicrobial resistance by divisional secretariat divisions in study 2020-2021

Divisional Secretariat Division	Percentage (%)													
	AMP	GEN	STR	TET	CIP	CHL	AMC	AK	CTX	CAZ	NA	SXT		
Gangawatakorale	33.3	100	0	66.7	0	33.3	0	0	0	0	0	33.3	33.3	33.3
Udapalatha	66.7	50	0	33.3	0	100	50	0	0	0	0	33.3	0	66.7
Akurana	100	100	0	50	66.7	100	33.3	50	0	0	0	66.7	100	100
Harispathuwa	100	0	0	0	75	100	0	25	0	25	0	0	0	25
Pasbagakorale	25	0	0	0	50	0	0	0	0	0	0	50	0	50
Pathahewaheta	66.7	0	0	66.7	0	100	100	66.7	0	33.3	0	66.7	0	100
Madadumbara	100	66.7	100	0	100	33.3	100	0	100	0	0	100	66.7	100
Kundasale	100	0	0	0	50	100	0	0	0	50	0	0	0	50
Yatinuwara	66.7	50	0	33.3	0	33.3	50	33.3	0	0	0	33.3	50	66.7
Udunuwara														

The proportion of *Salmonella* spp. isolates recovered with tetracycline resistance during the 2020-2021 study is significantly higher ( $p = 0.01$ ) than in the previous study. Furthermore, the proportion of *Salmonella* spp. isolated in the 2020-2021 study with streptomycin resistance was significantly lower ( $p = 0.01$ ) than in the previous study.

Geographic areas with the highest number of resistant isolates were identified based on the assumption that these farm shops receive birds for slaughter or carcasses for sale from the same DSD. Tables 3 and 4 show the percentage of *E. coli* and *Salmonella* spp. isolates that showed resistance to the selected panel of antimicrobials by DSDs in the 2010-2011 study and the 2020-2021 study, respectively.

In the 2010-2011 study, more than 50% of the *E. coli* isolates from the Akurana, Harispattuwa, and Pasbagekorale DSDs were resistant to 8/10 of the antimicrobials tested. Furthermore, over 50% of the *E. coli* isolates from Pathahewaheta and Kundasale were

resistant to 7/10 antimicrobials tested, while more than 50% of the *E. coli* isolates from the Gangawatakorale, Udapalatha, and Yatinuwara DSDs were resistant to 6/10 antimicrobials in the panel. *Salmonella* spp. isolates from the same study were mostly susceptible to the majority of antimicrobials tested. However more than half of the *Salmonella* spp. isolates from Akurana DSDs were reported to be resistant to 5/10 antimicrobials used in the study.

During the 2020-2021 investigation, more than half of the *E. coli* isolated from the Madadumbara and Pathahewaheta DSDs were resistant to 8/12 and 6/12 antimicrobials tested, respectively. Furthermore, more than half of the *Salmonella* spp. isolated from the Akurana DSD were resistant to 6/12 of the antimicrobials tested.

**Multidrug resistance (MDR)**

Fifty-six *E. coli* isolates (77.8%) from the 2010-2011 investigation met the MDR criteria (see Figure 5).

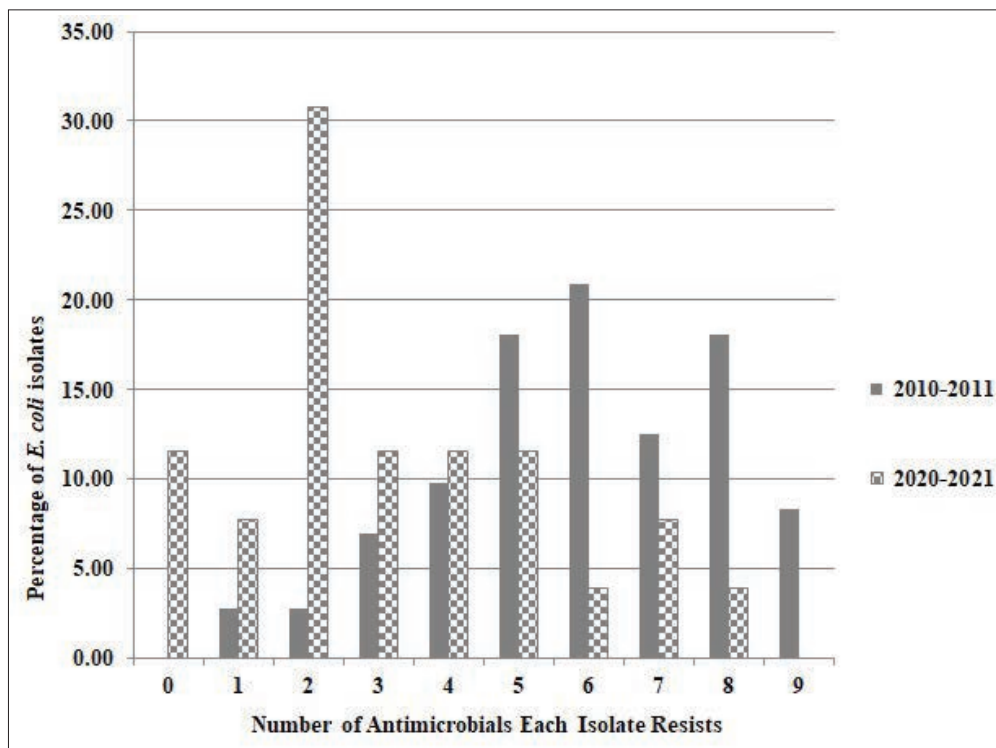


**Figure 5:** Numbers of chicken meat contaminant *E. coli* with multiple drug resistance in the 2010-2011 study and the 2020-2021 study.

In particular, 13 isolates (18%) were resistant to five antimicrobials, while 15 (20.8%) were resistant to all six antimicrobials tested in this study. Resistance to seven and eight antimicrobials was found in nine (12.5%) and 13 (18%) *E. coli* isolates, respectively. Furthermore, six *E. coli* isolates (8.3%) were resistant to 9/10 antimicrobials in the panel. Only five (14.7%) of the *Salmonella* spp. isolates studied in 2010 - 2011 had MDR profiles. *Salmonella* spp. isolates were twice as susceptible to all antimicrobials tested (10 isolates, 29.4%).

Only seven *E. coli* isolates (26.9%) from the 2020-2021 investigation were identified as MDR isolates (Figure 5). One (3.8%) was resistant to 8/12 antimicrobials tested, while two (7.7%) were resistant to 7/12 antimicrobials in the panel. Another *E. coli* isolate (3.8%) was resistant to 6/12 antimicrobials tested, while the remainder (11.5%) was resistant to 5/12 antimicrobials tested. Only one *Salmonella* spp. isolate (4.5%) from Akurana DSD showed MRD during the same investigation, and this isolate was resistant to 5/12 antimicrobials tested in the study.

When the two studies are compared, there is a significant reduction ( $p = 0.00$ ) in the proportions of MDR *E. coli* isolates in the 2020-2021 study compared to the previous one. Even though the proportion of MDR *Salmonella* spp. detected in the 2020-2021 study was lower than in the previous study, the difference was not statistically significant.

Food-borne illnesses in Sri Lanka have historically received less research attention compared to other infectious diseases (Sandipani *et al.*, 2020). There is either no or very limited epidemiological data on animal-origin foodborne pathogens and their antimicrobial resistance profiles. In such a context, this study reveals the potential risk of acquiring AMR *E. coli* and *Salmonella* spp. through consumption of contaminated chicken meat sold at small scale farm shops, as well as trends in AMR profiles following a decade.

The number of farm shops operating in each population centre in Kandy district was greater than we anticipated; however, the operational hygiene of all farm shops is substandard as the following unsanitary practices were observed: the same person issuing all available animal products with bare hands, repetitive freezing and thawing of meat, the lack of a functional cooler, fly access to meat, and visually unclean meat. All of these unsanitary practices have been shown to promote food-

borne bacteria contamination, multiplication, and spread. For instance, Todd *et al.* (2009) clearly demonstrated how workers contributed to the spread of *E. coli* and *Salmonella* spp. through unsanitary meat handling. According to Mohammed *et al.* (2021), repeated freezing and thawing increases microbial counts in chicken meat (Mohammed *et al.*, 2021). Casanova *et al.* (2021) demonstrated the importance of maintaining a cold chain for poultry meat in order to reduce the multiplication of foodborne bacteria. According to Barreiro *et al.* (2013), flies can transmit foodborne pathogens along with their associated toxin or resistance, and bacteria in the *enterobacteriaceae* group are the most common pathogen transmitted by flies.

Substandard slaughtering and handling hygiene in meat retail shops has been reported in many developing countries, including India (Balakrishnan *et al.*, 2018; Vaidya *et al.*, 2016), Pakistan (Mallhi *et al.*, 2019; Zakki *et al.*, 2017), Bangladesh (Uddin *et al.*, 2019) and Nepal (Bantawa *et al.*, 2018; Khanal & Poudel, 2017). One major reason for this poor operational hygiene is the willingness of consumers with low to medium incomes to buy these meats despite their sanitary status. These customers appear to prefer low-cost fresh meat over expensive branded frozen meat. As a result, retailers believe that it is unnecessary to invest in additional labour and money to upgrade their outlets because it has no effect on demand. Other possible explanations include lack of resources, lack of awareness on foodborne pathogens, and false sense of security about the cooking method etc. Therefore, identifying these issues and enacting the necessary regulations to ensure food safety is critical at this time (Kurugala, 2022)

According to the current study, *E. coli* contamination of chicken meat sold in these stores has decreased significantly over the past 10 years. However, because the sample size in the second investigation is smaller than in the first, it should be interpreted with caution. According to recent research, *E. coli* contamination of chicken meat was 4.8% in Nepal (Shrestha *et al.*, 2017), 43.5% in Pakistan (Zainab *et al.*, 2022), 85% in Bangladesh (Islam *et al.*, 2018), and 91% in India (Hussain *et al.*, 2017). *E. coli* is a marker of faecal contamination (Ekici & Dümen, 2019), and therefore cross contamination during evisceration or handling, or due to fly sitting, may have contributed to the high *E. coli* contamination. *E. coli* detection in meat is of little value, and most food standards recommend enumeration of *E. coli* to ensure that the numbers are within acceptable limits. However, contamination of chicken meat with AMR/MDR *E. coli*

or *E. coli* pathotypes (diarrheogenic *E. coli*, ExPEC or APEC that becomes ExPEC later in life) has always been a serious concern (Díaz-Jiménez et al., 2021; Rahman et al., 2020; Seo & Lee, 2018).

In both studies reported here, *E. coli* isolates had a higher level of AMR than *Salmonella* spp. isolates. Tetracycline resistance has increased significantly over the years, and in both studies, more than 60% of the isolates were ampicillin resistant. Differences in the antimicrobial panel used in the two studies made a fair comparison difficult, however the observed trends are consistent with a previous study conducted in Sri Lanka (Kulasooriya et al., 2019). Even studies from other South Asian regions report markedly high resistance in *E. coli* for tetracycline (Hussain et al., 2017; Islam et al., 2018; Zainab et al., 2022) and ampicillin (Islam et al., 2018; Shrestha et al., 2017). The first study disclosed 77.8 % MDR *E. coli* isolates as contaminants, while the second study revealed it as 26.9%. This significant reduction in MDR could be attributed to the difference of the antimicrobial disks used in each study. If the same antimicrobial panel was tested in each of these studies, the results could have been different. Despite the fact that the criterion for defining MDR has been different in this study, 100% MDR *E. coli* have been found in recent investigations in Bangladesh (Parvin et al., 2020) and Pakistan (Zainab et al., 2022). Further, the most recent percentages of MDR *E. coli* in contaminated chicken meat in India and Nepal have been 80% and 68%, respectively (Hussain et al., 2017; Shrestha et al., 2017). This highlights the potential risk of acquiring MDR *E. coli* from chicken meat. Therefore, urgent action is required, particularly in developing countries, to reduce contamination and acquisition of foodborne MDR *E. coli* via chicken meat.

The first study found 47.2% *Salmonella* spp. contamination in chicken meat, while the second study found a statistically insignificant increase (59.45%) in the *Salmonella* spp. contamination. Both studies showed higher *Salmonella* spp. contamination than values previously reported in Sri Lanka (8.9% and 11.6%) Jayaweera et al. (2020). According to Jayaweera et al. (2021), the majority of these contaminated chicken meats harbour a number of virulence related pathogenicity islands. Given that the prevalence of *Salmonella* spp. in broiler birds in Sri Lanka is 9% (Kottawatta et al., 2014), spilled gut content may not be the only source of contamination. According to Alwis et al. (2014), meat contact surfaces and utensils in Sri Lankan retail shops are highly contaminated with *Salmonella* spp..

Because unsanitary conditions promote *Salmonella* spp. colonization and biofilm formation (Merino et al., 2019), not only careless evisceration but also operational hygiene appear to have a significant impact on *Salmonella* contamination of meat. *Salmonella* contamination in chicken meat has been reported to be 70%, 40%, 33%, and 26.2% in Bangladesh (Islam et al., 2018), India (Sharma et al., 2019), Pakistan (Samad et al., 2018), and Nepal (Shrestha et al., 2017), respectively.

*Salmonella* spp. isolates recovered from both studies were susceptible to the majority of antimicrobials tested, which is consistent with Jayaweera et al., (2020). However, 58% of the *Salmonella* spp. in the first study were resistant to neomycin, while 54% of the *Salmonella* spp. in the second study were resistant to tetracycline. According to recent regional reports, tetracycline resistance among *Salmonella* spp. isolates recovered from chicken meat is 85.7% in Bangladesh and 100% in India (Islam et al., 2018; Sharma et al., 2019). *Salmonella* spp. isolates with MDR profiles were 14.7% in 2010-2011 and 4.5% in 2020-2021 studies, respectively. These MDR *Salmonella* spp. percentages are lower than the MDR *Salmonella* spp. percentages isolated from chicken meat in Nepal (85.2%) and India (100%) (Sharma et al., 2019; Shrestha et al., 2017). Nonetheless, it should be noted that the criteria used to define MDR differ among studies.

The AMR *E. coli* and *Salmonella* spp. isolates from these two studies did not show any prominent spatial clustering. The spatial variation in AMR profiles is attributed to the level of antimicrobials used within a region, the number of farms located in each region, the degree of environmental contamination with resistant bacteria, the extent of husbandry/other practices favouring resistance dissemination and socio-economic factors, etc. (Galvin et al., 2013).

The findings of this study underscore the significant risk of harvest and post-harvest cross-contamination of chicken meat sold at small-scale farm shops in Kandy district, as well as the persistent risk of consumers being exposed to AMR *E. coli* and *Salmonella* spp.. This situation highlights the urgent need for interventions to limit the emergence and spread of MDR bacteria in animal-origin food products in Sri Lanka. Establishing a national surveillance system to monitor antimicrobial usage in food animals and detect emerging antimicrobial resistance in bacteria from these animals is crucial. Additionally, promoting antimicrobial stewardship among veterinarians is essential.

It is also important to mandate the registration of meat retail shops with relevant authorities to ensure traceability in the event of a FI outbreak. Implementing a regular quality monitoring and grading system for meat retail shops is necessary. Moreover, awareness programmes targeting both retailers and consumers should be conducted to reduce cross-contamination and the spread of AMR foodborne pathogens.

## CONCLUSION

Chicken meat sold in small-scale shops in Kandy district is frequently contaminated with *E. coli* and *Salmonella* spp.. Although *E. coli* contamination has decreased over the past decade, *Salmonella* spp. colonization in meat has increased. Antimicrobial resistance and multidrug resistance are prevalent among *E. coli* isolates contaminating chicken meat, with a higher frequency compared to *Salmonella* spp.. Resistance to tetracycline is commonly observed in both *E. coli* and *Salmonella* spp. found in chicken meat. These findings highlight the urgent need to implement measures to reduce bacterial contamination in chicken meat and to address the rise of antimicrobial resistance in farming environments.

## REFERENCES

- Abebe, E., Gugsu, G., & Ahmed, M. (2020). Review on major food-borne zoonotic bacterial pathogens. *Journal of Tropical Medicine*, 2020(1), 4674235. <https://doi.org/10.1155/2020/4674235>
- Alahakoon, A. U., Jo, C., & Jayasena, D. D. (2016). An overview of meat industry in Sri Lanka: A comprehensive review. *Korean Journal for Food Science of Animal Resources*, 36(2), 137–144. <https://doi.org/10.5851/kosfa.2016.36.2.137>
- Alwis, U. S., Mudannayake, D. C., Jayasena, D. D., & Ubeyarathna, K. J. (2014). Evaluation of Salmonella cross contamination at retail chicken meat outlets in Kandy, Sri Lanka. *Korean Journal of Agricultural Science*, 41(1), 35–40. <http://dx.doi.org/10.7744/cnujas.2014.41.1.035>
- Balakrishnan, S., Sangeetha, A., & Dhanalakshmi, M. (2018). Prevalence of *Salmonella* in chicken meat and its slaughtering place from local markets in Orathanadu, Thanjavur district, Tamil Nadu. *Journal of Entomology and Zoology studies*, 6(2), 2468–2471. [https://www.entomoljournal.com/2018/6\(2\)pdf](https://www.entomoljournal.com/2018/6(2)pdf)
- Bantawa, K., Rai, K., Subba Limbu, D., & Khanal, H. (2018). Food-borne bacterial pathogens in marketed raw meat of Dharan, eastern Nepal. *BMC Research Notes*, 11, 618, 1–5. <https://doi.org/10.1186/s13104-018-3722-x>
- Barreiro, C., Albano, H., Silva, J., & Teixeira, P. (2013). Role of flies as vectors of foodborne pathogens in rural areas. *International Scholarly Research Notices*, 2013(1), 718780. <http://dx.doi.org/10.1155/2013/718780>
- Bintsis, T. (2017). Foodborne pathogens. *AIMS Microbiology*, 3(3), 529–563. <https://doi.org/10.3934/microbiol.2017.3.529>
- Card, R. M., Cawthraw, S. A., Nunez-Garcia, J., Ellis, R. J., Kay, G., Pallen, M. J., Woodward, M. J., & Anjum, M. F. (2017). An in vitro chicken gut model demonstrates transfer of a multidrug resistance plasmid from *Salmonella* to commensal *Escherichia coli*. *MBio*, 8(4), 10–1128. <https://doi.org/10.1128/mBio.00777-17>
- Casanova, C. F., Souza, M. A. D., Fisher, B., Colet, R., Marchesi, C. M., Zeni, J., Cansian, R. L., Backes, G. T., & Steffens, C. (2021). Bacterial growth in chicken breast fillet submitted to temperature abuse conditions. *Food Science and Technology*, 42, e47920. <https://doi.org/10.1590/fst.47920>
- CDC (2011). Estimates of foodborne illness in the United States. *Center for Disease Control and Prevention (CDC)*. <https://www.cdc.gov/foodborneburden/estimates-overview.html>
- Croxen, M. A., Law, R. J., Scholz, R., Keeney, K. M., Wlodarska, M., & Finlay, B. B. (2013). Recent advances in understanding enteric pathogenic *Escherichia coli*. *Clinical Microbiology Reviews*, 26(4), 822–880. <https://doi.org/10.1128/CMR.00022-13>
- Diaz-Jimenez, D., García-Meniño, I., Herrera, A., Leston, L., & Mora, A. (2021). Microbiological risk assessment of Turkey and chicken meat for consumer: Significant differences regarding multidrug resistance, mcr or presence of hybrid aEPEC/ExPEC pathotypes of *E. coli*. *Food Control*, 123(8), 107713. <http://dx.doi.org/10.1016/j.foodcont.2020.107713>
- Ekici, G., & Dümen, E. (2019). *Escherichia coli* and food safety. In *The universe of Escherichia coli*. IntechOpen. <https://doi.org/10.5772/intechopen.82375>
- Frye, J. G., & Jackson, C. R. (2013). Genetic mechanisms of antimicrobial resistance identified in *Salmonella enterica*, *Escherichia coli*, and *Enterococcus* spp. isolated from US food animals. *Frontiers in Microbiology*, 4, 135. <https://doi.org/10.3389/fmicb.2013.00135>
- Galvin, S., Bergin, N., Hennessy, R., Hanahoe, B., Murphy, A. W., Cormican, M., & Vellinga, A. (2013). Exploratory spatial mapping of the occurrence of antimicrobial resistance in *E. coli* in the community. *Antibiotics*, 2(3), 328–338. <https://doi.org/10.3390/antibiotics2030328>
- Gizaw, Z. (2019). Public health risks related to food safety issues in the food market: a systematic literature review. *Environmental Health and Preventive Medicine*, 24, 68, 1–21. <https://doi.org/10.1186/s12199-019-0825-5>
- Grace, D. (2015). Food safety in low and middle income countries. *International Journal of Environmental Research and Public Health*, 12(9), 10490–10507. <https://doi.org/10.3390/ijerph120910490>
- Heredia, N., & García, S. (2018). Animals as sources of foodborne pathogens: A review. *Animal Nutrition*, 4(3), 250–255. <https://doi.org/10.1016/j.aninu.2018.04.006>
- Huffaker, R., & Hartmann, M. (2021). Reconstructing dynamics of foodborne disease outbreaks in the US cattle market from monitoring data. *Plos One*, 16(1), e0245867. <https://doi.org/10.1371/journal.pone.0245867>

- doi.org/10.1371/journal.pone.0245867
- Hussain, A., Shaik, S., Ranjan, A., Nandanwar, N., Tiwari, S. K., Majid, M., Baddam, R., Qureshi, I. A., Semmler, T., Wieler, L. H., Islam, M. A., Chakravorty, D., & Ahmed, N. (2017). Risk of transmission of antimicrobial resistant *Escherichia coli* from commercial broiler and free-range retail chicken in India. *Frontiers in Microbiology*, 8, 2120. <https://doi.org/10.3389/fmicb.2017.02120>
- Islam, M. K., Kabir, S. L., Haque, A. Z., Sarker, Y. A., & Sikder, M. H. (2018). Molecular detection and characterization of *Escherichia coli*, *Salmonella* spp. and *Campylobacter* spp. isolated from broiler meat in Jamalpur, Tangail, Netrokona and Kishoreganj districts of Bangladesh. *African Journal of Microbiology Research*, 12(32), 761-770. <http://doi.org/10.5897/AJMR2018.8945>
- Jayaweera, T. S. P., Ruwandeepika, H. A. D., Deekshit, V. K., Vidanarachchi, J. K., Kodithuwakku, S. P., Karunasagar, I., & Cyril, H. W. (2020). Isolation and Identification of *Salmonella* spp. from Broiler Chicken Meat in Sri Lanka and their Antibiotic Resistance. *Journal of Agricultural Sciences (Sri Lanka)*, 15(3), 395-410. <http://doi.org/10.4038/jas.v15i3.9031>
- Jayaweera, T. S. P., Ruwandeepika, H. A. D., Deekshit, V. K., Vidanarachchi, J. K., Kodithuwakku, S. P., Karunasagar, I., & Cyril, H. W. (2021). Prevalence of *Salmonella* pathogenicity island (SPI1, SPI2, SPI3 and SPI5) genes in *Salmonella* species isolated from fresh Broiler Chicken Meat in Sri Lanka. *Journal of Agricultural Sciences (Sri Lanka)*, 16(2), 333-351. <http://doi.org/10.4038/jas.v16i2.9339>
- Kalupahana, R. S., Rajapaksa, D. I. G., Fernando, P. S., Thilakarathne, D. S., & Abeynayake, P. (2017). Occurrence and characterization of nontyphoidal *Salmonella* in retail table eggs in Kandy district of Sri Lanka. *Food Control*, 72(Part B), 244-248. <https://doi.org/10.1016/j.foodcont.2016.04.024>
- Khanal, G., & Poudel, S. (2017). Factors associated with meat safety knowledge and practices among butchers of Ratnanagar municipality, Chitwan, Nepal: a cross-sectional study. *Asia Pacific Journal of Public Health*, 29(8), 683-691. <https://doi.org/10.1177/1010539517743850>
- Kottawatta, K. S. A., Bandara, J. M. K. V., Thilakarathne, D. S., Rajapaksha, D. I. G., Abeynayake, P., & Kalupahana, R. S. (2014). Occurrence of motile salmonella in broiler flocks and antimicrobial susceptibility patterns of isolates. *Proceedings of the Peradeniya Univ. International Research Sessions, Sri Lanka*, 18, 187. <http://dlib.pdn.ac.lk/handle/1/4728>
- Kulasooriya, G. D. B. N., Amarasiri, M. K. U. T., Abeykoon, A. M. H., & Kalupahana, R. S. (2019). *Salmonella*, *Campylobacter* and *Escherichia coli* in raw chicken meat, chicken products and cooked chicken in retail markets in Kandy, Sri Lanka. *Sri Lanka Veterinary Journal*, 66(1), 19-26. <http://doi.org/10.4038/slvj.v66i1.33>
- Kurugala, G. C. S. (2022). Consumers' consciousness on quality of meat, while purchasing from meat outlets in Kaduwela Municipal Council area: Conciencia de los consumidores sobre la calidad de la carne cuando compran en los puntos de venta de carne en el área del Consejo Municipal de Kaduwela. *South Florida Journal of Environmental and Animal Science*, 2(2), 152-161. <https://doi.org/10.53499/sfjeasv2n2-012>
- Li, Z., Shi, L., Wang, B., Wei, X., Zhang, J., Guo, T., Kong, J., Wang, M., & Xu, H. (2021). In vitro assessment of antimicrobial resistance dissemination dynamics during multidrug-resistant-bacterium invasion events by using a continuous-culture device. *Applied and Environmental Microbiology*, 87(6), e02659-20. <https://doi.org/10.1128/AEM.02659-20>
- Mallhi, I. Y., Sohaib, M., Khan, A. U., Nawaz, M., & Abdullah. (2019). Evaluating food safety knowledge, practices, and microbial profile of meat in abattoirs and butchery shops in Lahore, Pakistan. *Journal of Food Safety*, 39(2), e12612. <https://doi.org/10.1111/jfs.12612>
- Marchello, C. S., Birkhold, M., Crump, J. A., Martin, L. B., Anshar, M. O., Breggi, G., Canals, R., Fiorino, F., Gordon, M. A., Kim, J. H., Hamaluba, M., Hanumunthadu, B., Jacobs, J., Kariuki, S., Malvolti, S., Mantel, C., Marks, F., Medagliani, D., Mogasale, V., ... & Tack, B. (2022). Complications and mortality of non-typhoidal salmonella invasive disease: a global systematic review and meta-analysis. *The Lancet Infectious Diseases*, 22(5), 692-705. [https://doi.org/10.1016/S1473-3099\(21\)00615-0](https://doi.org/10.1016/S1473-3099(21)00615-0)
- Merino, L., Procura, F., Trejo, F. M., Bueno, D. J., & Golowczyk, M. A. (2019). Biofilm formation by *Salmonella* sp. in the poultry industry: Detection, control and eradication strategies. *Food Research International*, 119, 530-540. <https://doi.org/10.1016/j.foodres.2017.11.024>
- Mohammed, H. H. H., He, L., Nawaz, A., Jin, G., Huang, X., Ma, M., Abdegadir, W. S., Elgasim, E. A., & Khalifa, I. (2021). Effect of frozen and refrozen storage of beef and chicken meats on inoculated microorganisms and meat quality. *Meat Science*, 175, 108453. <https://doi.org/10.1016/j.meatsci.2021.108453>
- Newman, K. L., Leon, J. S., Rebolledo, P. A., & Scallan, E. (2015a). The impact of socioeconomic status on foodborne illness in high-income countries: A systematic review. *Epidemiology and Infection*, 143(12), 2473-2485. <https://doi.org/10.1017/S0950268814003847>
- Newman, K. L., Leon, J. S., & Newman, L. S. (2015b). Estimating occupational illness, injury, and mortality in food production in the United States: A farm-to-table analysis. *Journal of Occupational and Environmental Medicine*, 57(7), 718-725. <https://doi.org/10.1097/JOM.0000000000000476>
- Parvin, M. S., Talukder, S., Ali, M. Y., Chowdhury, E. H., Rahman, M. T., & Islam, M. T. (2020). Antimicrobial resistance pattern of *Escherichia coli* isolated from frozen chicken meat in Bangladesh. *Pathogens*, 9(6), 420. <http://dx.doi.org/10.3390/pathogens9060420>
- Rahman, M. M., Husna, A., Elshabrawy, H. A., Alam, J., Runa, N. Y., Badruzzaman, A. T. M., Banu, N. A., Mamun M. A., Paul, B., Das, S., Rahman, M. M., Mahbub-E-Elahi, A. T. M., Khairalla, A. S. & Ashour, H. M. (2020). Isolation

- and molecular characterization of multidrug-resistant *Escherichia coli* from chicken meat. *Scientific Reports*, 10(1), 21999. <https://doi.org/10.1038/s41598-020-78367-2>
- Samad, A., Abbas, F., Tanveer, Z., Ahmad, Z., Ahmad, I., Patching, S. G., Nawaz, N., Asmat, T. M., Raziq, A., Asadullah, Sheikh, I. S., Naeem, M., Pokryshko, O., & Mustafa, Z. M. (2018). Prevalence of *Salmonella* spp. in chicken meat from Quetta retail outlets and typing through multiplex PCR. *Romanian Biotechnological Letters*, 24(2), 271-9. <http://dx.doi.org/10.25083/rbl/24.2/271.279>
- Sandipani, H. A. D. C. L., Dharmarathna, E. K. G. P. U., Wimaladharma, S. T. C. I. & Abeyrathne, E. D. N. S. (2020). A food risk assessment model based on HACCP for small scale restaurants. *Journal of Agriculture and Value Addition*, 3(2): 41-55. [https://www.uwu.ac.lk\(2021\)java-3\(2\)41-55.pdf](https://www.uwu.ac.lk(2021)java-3(2)41-55.pdf)
- Seo, K. W., & Lee, Y. J. (2018). Prevalence and characterization of  $\beta$ -lactamases genes and class 1 integrons in multidrug-resistant *Escherichia coli* isolates from chicken meat in Korea. *Microbial Drug Resistance*, 24(10), 1599-1606. <https://doi.org/10.1089/mdr.2018.0019>
- Sharma, J., Kumar, D., Hussain, S., Pathak, A., Shukla, M., Kumar, V. P., Anisha, P. N., Rautela, R., Upadhyay, A. K., & Singh, S. P. (2019). Prevalence, antimicrobial resistance and virulence genes characterization of nontyphoidal *Salmonella* isolated from retail chicken meat shops in Northern India. *Food Control*, 102, 104-111. <https://doi.org/10.1016/j.foodcont.2019.01.021>
- Shrestha, A., Bajracharya, A. M., Subedi, H., Turha, R. S., Kafle, S., Sharma, S., Neupane, S., & Chaudhary, D. K. (2017). Multi-drug resistance and extended spectrum beta lactamase producing Gram negative bacteria from chicken meat in Bharatpur Metropolitan, Nepal. *BMC Research Notes*, 10, 1-5. <https://doi.org/10.1186/s13104-017-2917-x>
- Todd E. C. D. (2014). Foodborne diseases: Overview of biological hazards and foodborne diseases. *Encyclopedia of Food Safety*, 221-242. <https://doi.org/10.1016/B978-0-12-378612-8.00071-8>
- Todd, E. C. D., Greig, J. D., Bartleson, C. A., & Michaels, B. S. (2009). Outbreaks where food workers have been implicated in the spread of foodborne disease. Part 6. Transmission and survival of pathogens in the food processing and preparation environment. *Journal of Food Protection*, 72(1), 202-219. <https://doi.org/10.4315/0362-028x-72.1.202>
- Uddin, J., Hossain, K., Hossain, S., Saha, K., Jubyda, F. T., Haque, R., Billah, B., Talukder, A. A., Parvez, A. K., & Dey, S. K. (2019). Bacteriological assessments of foodborne pathogens in poultry meat at different super shops in Dhaka, Bangladesh. *Italian Journal of Food Safety*, 8(1), 6720. <https://doi.org/10.4081/ijfs.2019.6720>
- Vaidya, D. N., Ghugare, P. S., & Kutty, M. (2016). Prevalence of pathogens in raw chicken sold at retail poultry shops in Pune city, India. *Journal of Global Biosciences*, 5(4), 3970-3975.
- Zainab, L., Ibrar, K., Sadiq, A., Hamid, A. K., Ullah, M., & Noor, R. (2022). Extended spectrum beta lactamases-producing *Escherichia coli* in retail chicken meat from Khyber Pakhtunkhwa, Pakistan. *Saudi Journal of Biological Sciences*, 29(6), 103280. <https://doi.org/10.1016/j.sjbs.2022.103280>
- Zakki, S. A., Qureshi, R., Hussain, A., Ghias, W., Sharif, M., & Ansari, F. (2017). Microbial quality evaluation and prevalence of bacteria and fungus in different varieties of chicken meat in Lahore. *Journal of Pharmaceutical Sciences*, 5(1), 30-37. <https://www.researchgate.net/publication/316512251>



## RESEARCH ARTICLE

# Cryptography

## Symmetric encryption using snake graphs and supermagic covering

PGRS Ranasinghe\*, RMVV Bandara and AMSLK Athapaththu

*Department of Mathematics, Faculty of Science, University of Peradeniya, Peradeniya, Sri Lanka.*

Submitted: 18 May 2024; Revised: 17 September 2024; Accepted: 26 September 2024

**Abstract:** Cryptography involves the exploration of methods for safeguarding sensitive information. In this pursuit, graph-theoretic approaches play a significant role. Graph labeling, a key aspect of this, assigns labels or values to vertices and edges within a graph, serving as a means to encode information. It is instrumental in designing cryptographic protocols centered around graph-based structures. The sheer variety of labeling methods makes it challenging to discern the specific technique employed and distinguish between the graphs used for encryption. Notably, in 2020, Giridaran utilized super magic labeling as an encryption technique. Building upon this foundation, our present cryptographic scheme leverages graphs with snake vertex labeling to symmetrically encrypt plaintext. This encryption process harnesses the inherent randomness within super magic covering wheel graphs of odd order, in tandem with an advanced shift cipher. In this scheme, both the sender and receiver possess a secret key pair  $(k, l)$ , carefully selected for the task at hand. The encryption process employs an odd number  $k$ , representing the sides of a cyclic graph (polygon), while  $l$  is chosen to preserve the symmetries of consecutive snake graphs. The use of graph labeling proves to be an effective tool in the creation of flexible, efficient, and secure cryptographic protocols. Our protocol, tailored for encryption, ensures a high level of security by capitalizing on the intrinsic structure and the stochastic nature of graph labeling. Through the careful selection of the labeling scheme, we have devised a protocol that remains resilient against a range of potential attacks, including impersonation and replay attacks.

**Keywords:** Shift cipher, snake vertex labeling, supermagic covering, wheel graph.

## INTRODUCTION

Today, information security stands as a paramount concern, encompassing a spectrum of tools and methodologies designed to safeguard sensitive data. Cryptography, the field dedicated to the development of techniques for ensuring information security, plays a pivotal role in this endeavor. Among the mathematical tools used in implementing cryptographic schemes, graph theoretical concepts are prominent.

To state a couple of related results in literature, in 2014, Al Etaiwi (2014) presented an encryption algorithm using spanning trees and in 2020, Giridaran (2020) used super magic labeling in encryption which is the base for the present study.

In the present cryptographic scheme, we use graphs with snake vertex labeling to encrypt a plaintext symmetrically (symmetric encryption means using one key to encrypt and decrypt the message) using the randomness of the distribution of super magic covering of wheel graphs of odd order. The sender and the receiver hold the secret key pair  $(k, l)$  which has been chosen appropriately;  $k$  is the number of sides of a cyclic graph (polygon) and  $l$  is chosen to preserve the symmetries of numbers labeled on vertices of consecutive snake graphs.

\* Corresponding author ([rajithamath@sci.pdn.ac.lk](mailto:rajithamath@sci.pdn.ac.lk); <https://orcid.org/0009-0008-4973-8299>)



This article is published under the Creative Commons CC-BY-ND License (<http://creativecommons.org/licenses/by-nd/4.0/>). This license permits use, distribution and reproduction, commercial and non-commercial, provided that the original work is properly cited and is not changed in anyway.

**METHODOLOGY**

First, we shall provide some graph theoretic terminologies in relation to our cryptographic scheme.

**Definition 1.** A snake graph  $C_{k,q}^m$  is the fusion of  $m$  number of  $k$ -cycles,  $C_k$ , such that, for  $2 \leq i \leq m$ , a shared vertex called the vertebrae, denoted  $v_i$ , results from the fusion where a minimal path of length  $q$  joins  $v_{i-1}$  and  $v_i$ .

The points of fusion, denoted  $v_i$ , are the internal vertebrae of the snake,  $2 \leq i \leq m$ . Additionally, the vertebra  $v_1$  is a vertex in the first cycle that has a path of  $q$  edges between it and  $v_2$ , while the vertebra  $v_{m+1}$  is a vertex in the  $m^{th}$  cycle that has a path of  $q$  edges between it and  $v_m$ .

A minimal path of length  $qm$  from  $v_1$  to  $v_{m+1}$  is called the spine. The vertices along the spine which are not shared between two cycles are referred to as  $s_i^i$ , where  $i$  refers to the cycle to which the spine vertex belongs and  $l$  refers to the distance between  $s_i^i$  and  $v_i$ . For all snakes,  $1 \leq i \leq m$  and  $1 \leq l \leq q - 1$ .

The path of  $(k - q)m$  edges from  $v_1$  to  $v_{m+1}$  that does not contain any vertices on the spine is called the belly of the snake graph. The vertices along the belly not shared between two cycles are referred to as  $b_j^i$ , where  $i$  refers to the cycle to which the belly vertex belongs and  $j$  specifies the distance between  $b_j^i$  and  $v_i$ . For all snakes,  $1 \leq i \leq m$  and  $1 \leq j \leq k - q - 1$ .

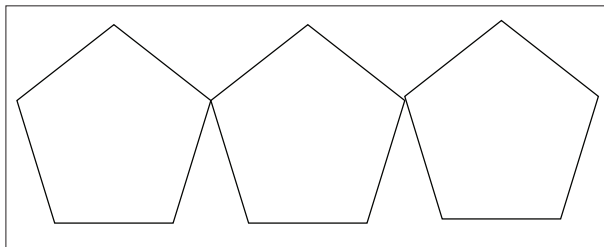


**Figure 1:** A snake graph with 3 cyclic graphs of 5 vertices

**Definition 2.** The assignment of integers to the vertices, edges, or both based on some condition is known as graph labeling.

**Definition 3.** A cyclic snake labeling is defined by the following bijective mapping

$f(x):V(C_{k,q}^m) \rightarrow \{1,2, \dots, m\}$ . For any vertex  $x$  in  $C_{k,q}^m$  such that  $1 \leq i \leq m + 1, 1 \leq j \leq k - q - 1$ , and  $1 \leq l \leq q - 1$ ,

$$f(x) = \begin{cases} ik - i - k + 2 & \text{if } x = v_i, \\ ik - i + 1 - q + l & \text{if } x = s_l^i, \\ ik - i - k + j + 2 & \text{if } x = b_j^i. \end{cases}$$

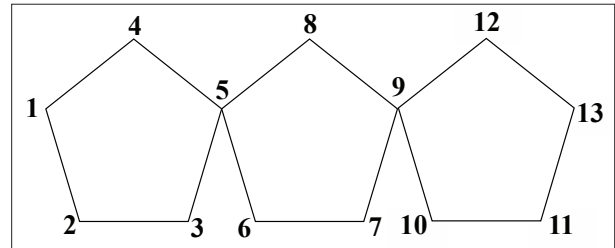


**Figure 2:** Cyclic snake labeling of a snake graph.

**Definition 4.** A wheel graph  $w_n$  of order  $n$  is a graph that contains a cycle of order  $n - 1$  and for which every graph vertex in the cycle is connected to one other graph vertex.

**Definition 5.** The process of assigning labels to the edges of  $G$  such that the sum over the edges incident with any vertex is the same, independent of the choice of vertex is known as magic labeling.

In magic labeling, if the labels assigned are the first  $q$  positive integers, where  $q$  is the number of edges in the graph, then such a labelling is called supermagic labeling.

**Definition 6.** Let  $G = (V, E)$  be a finite simple graph. An edge-covering of  $G$  is a family of subgraphs  $H_1, \dots, H_k$  such that each edge of  $E$  belongs to at least one of the subgraphs  $H_i, 1 \leq i \leq k$ . Then it is said that  $G$  admits an  $(H_1, \dots, H_k)$  (edge) covering. If every  $H_i$  is isomorphic to a given graph  $H$ , then  $G$  admits an  $H$ -covering.

Suppose that  $G = (V, E)$  admits an  $H$ -covering. A bijective function  $f:V \cup E \rightarrow \{1,2, \dots, |V| + |E|\}$ , is an  $H$ -magic labeling of  $G$  whenever, for every subgraph  $H' = (V', E')$  of  $G$  isomorphic to  $H, F(H') = \sum_{v \in V'} f(v) + \sum_{e \in E'} f(e)$  is constant. In this case, we say that the graph  $G$  is  $H$ -magic. If  $F(V) = \{1,2, \dots, |V|\}$ , then  $G$  is said to be  $H$ -supermagic. The constant value that every copy of  $H$  takes under the labeling  $f$  is denoted by  $m(f)$  in the magic case and by  $s(f)$  in the super magic case [2].

In the present cryptographic scheme, we use graphs with snake vertex labeling to encrypt a plaintext symmetrically using the randomness of the distribution of super magic labeling of wheel graphs of odd order. Both the sender and the receiver hold the secret key  $k$ , where  $k$  is the number of sides of a cyclic graph (polygon) and  $l$  is chosen to preserve the symmetries of consecutive snake graphs.

**RESULTS AND DISCUSSION**

Encryption and decryption algorithms are stated below along with an example.

**Encryption algorithm with an illustration**

For example, suppose we want to encrypt the plaintext  $M = \text{mathematics}$ , with  $r = 11$  number of characters.

*Step 1.* The secret key pair  $(k, l)$  is chosen appropriately. We choose positive integers  $p = 3, s = 2 (< k = 5)$  such that  $pk - (p - 1) = r + s = 13$ , thus, we get  $k = (r + s + p - 1)/p = (11 + 2 + 3 - 1)/3 = 5$ . We can construct a snake graph with  $p = 3$  cyclic graphs of  $k = 5$  vertices.

*Step 2.* We convert each character of  $M$  into 3-digit ASCII representations and  $s$  is the number of dummy characters that are attached to the original message (such as spaces). Thus, we get  $r + s = 11 + 2 = 13$ , 3-digit ASCII representations.

*Step 3.* We assign each ASCII representation to each vertex according to the snake graph labeling. ASCII representations of each letter in 'mathematics' are [109,097,116,104,101,109,097,116,105,099,115].

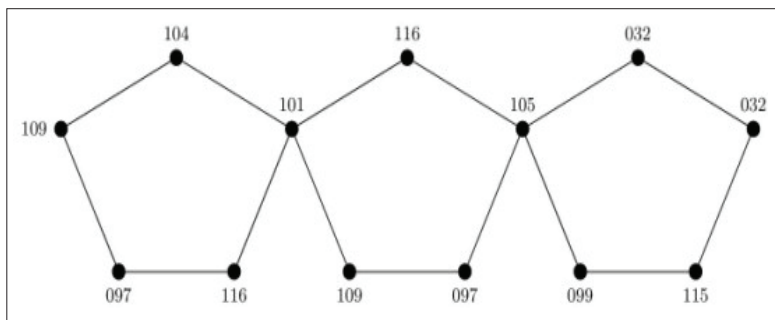


Figure 3: Snake graph with vertices labeled using ASCII representations

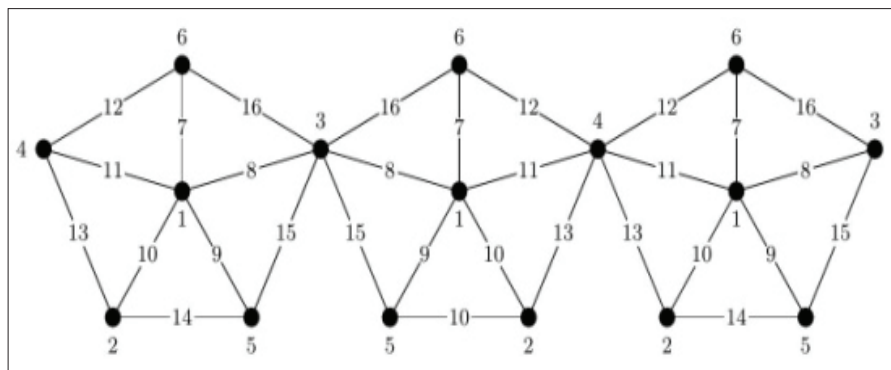


Figure 4: Wheel snake graph labeled using supermagic labeling

*Step 4.* We construct a similar cyclic graph, modify it into a wheel graph, and label it with  $C_3$ -supermagic labeling. In this step we assign the value  $l = 3$  to the connecting vertex of the first cycle of the snake graph and the next cycle is constructed as the mirror graph of the previous one.

*Step 5.* We consider the two snake graphs in steps 3 and 4. Each assigned ASCII value is multiplied by the corresponding vertex label value and the value assigned to an edge between consecutive vertices is added to that.

The final value (mod 128) is replaced with the original vertex in the graph of step 3.

For example, consider the first letter ‘m’ of the plaintext. ASCII representation of ‘m’ is 109, the corresponding vertex label value is 4 and the edge label value of the edge between the vertex and the consecutive vertex is 13. Therefore, we have to multiply 109 by 4 and add 13 under modulo 128.  $(109 \times 4) + 13 = 449 \equiv 65 \pmod{128}$ . So, we get 065 as the new vertex label value.

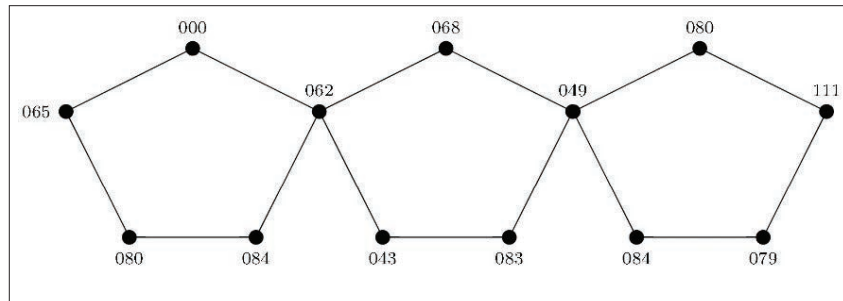


**Figure 5:** Snake graph labeled with newly assigned vertex labels

*Step 6.* We obtain the characters represented by ASCII values as the encrypted message [A, P, T, NUL, >, +, S, D, I, T, O, P, o].

**Decryption algorithm with an illustration**

Now, suppose we want to decrypt the encrypted message, using the shared secret key pair  $(k, l)$ ;  $k = 5$  is the odd number of sides of a cyclic graph, and  $l = 3$  is the number we consider for symmetries of snake cycle graphs.

*Step 1.* First, we count the number of characters in the encrypted message, and it is the value of  $r + s = 13$ . Since we know the value for  $k = 5$ , we use the equation  $pk - (p - 1) = r + s$  to calculate  $p$  (number of cycles in the snake graph).  $(p \times 5) - (p - 1) = 13 \Rightarrow p = 3$ .

*Step 2.* Next, we can construct a snake graph with  $p = 3$  cyclic graphs of  $k = 5$  vertices and assign ASCII representations of each character in the encrypted message consecutively. Let those values be  $m_i$ .

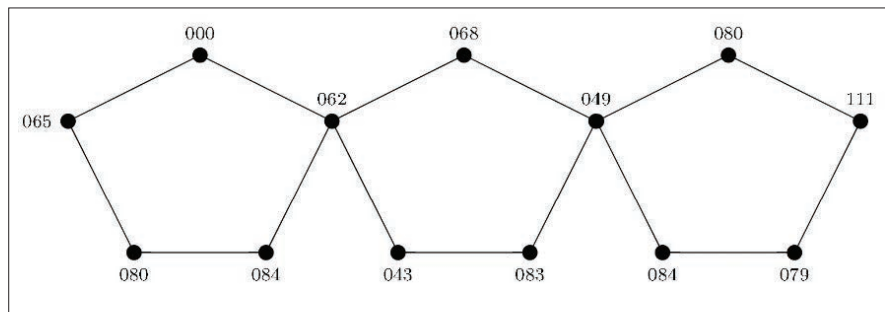


**Figure 6:** Snake graph labeled using the encrypted message

Step 3. We construct a similar cyclic graph into a wheel graph and label it with supermagic covering. In this step we assign the value  $l = 3$  to the connecting vertex of

the first cycle of the snake graph and the next cycle is constructed as the mirror graph of the previous one.

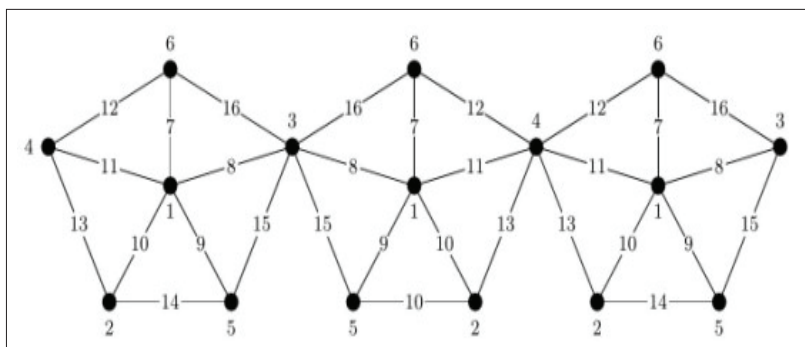


Figure 7: Wheel snake graph with supermagic labeling

Step 4. We consider the two snake graphs in steps 2 and 3. We denote each ASCII value in the encrypted snake graph as  $d_i$  in the snake cyclic graph of step 2 and the snake wheel graph of step 3, the edge value between two consecutive vertices is  $e_i$  and the previous vertex value be  $l_i$ . To decrypt the encrypted message, we find solutions  $(m_i)$  for the system of congruences;  $l_i m_i + e_i \equiv d_i \pmod{128}$ . Here the largest solution for  $m_i \pmod{128}$  is the ASCII value corresponding to each character of the original message.

For example, consider the letter ‘A’ of the encrypted message. Here,  $l_i = 4, e_i = 13$  and  $d_i = 65$ . Solving  $4m_i + 13 = 65 \pmod{128}$  we get  $m_i \equiv 13, 45, 77,$  and  $109 \pmod{128}$ . Since  $109$  is the largest value, it is the ASCII value corresponding to the first character of the original message.

Step 5. Finally, using the ASCII table we can obtain characters represented by ASCII values  $(m_i)$  as the original message  $M = \text{‘mathematics’}$ .

### CONCLUSION

The wheel  $w_k$  for  $k \geq 5$  odd, is  $C_3$ -supermagic [2]. Hence for every odd number  $k$ , we can choose the appropriate key pair  $(k, l)$ . The uniqueness of the labeling of the snake wheel graph is preserved by defining a total labeling  $f$  of  $W_n$  as follows. Set  $f(v) = 1, f(v_n, v_1) = 2n + 2$  and for  $1 \leq i < n, f(v_i, v_{i+1}) = 3n + 2 - i$ , where  $v$  is the center vertex of a wheel.

Error handling is essential in cryptographic protocols to ensure reliability and security. Our scheme implements input validation to prevent processing errors, robust key management for secure key generation and renewal, and error detection codes to verify data integrity during transmission. Additionally, the system is designed for graceful degradation, providing informative error messages while safeguarding sensitive information.

The key parameters in our cryptographic scheme are chosen with careful consideration to enhance security and performance. An odd number of sides in cyclic graphs promotes randomness in labeling, complicating pattern recognition for attackers. Snake graphs are utilized for their complex interconnections, while super magic labeling ensures uniformity and randomness. The shift cipher approach offers efficiency and an added layer of security through modular arithmetic.

Given the wide array of graph labeling methods found in literature, the utilization of graphs in cryptography is considered secure, primarily due to the challenge of identifying the specific labeling technique and distinguishing between encrypted graphs. In our study, we harnessed the randomness of the supermagic covering and a sophisticated shift cipher approach for the encryption and decryption of confidential messages. As a future direction, we aim to explore the application of diverse graph-theoretic techniques to further enhance the security of our cryptographic scheme. Some potential extensions include investigating other graph labeling methods and incorporating additional graph structures.

---

**REFERENCES**

- Etaiwi, W. (2014). Encryption algorithm using graph theory. *Journal of Scientific Research and Reports*, 3(19), 2519-2527. <https://doi.org/10.9734/jsrr/2014/11804>
- Giridaran, M. (2020). Application of super magic labeling in cryptography. *International Journal of Innovative Research in Science, Engineering and Technology*, 9(6): 4816-4822. <https://doi.org/10.15680/IJIRSET.2020.0906003>
- Lladó, A., & Moragas, J. (2007). Cycle-magic graphs. *Discrete Mathematics*, 307(23), 2925-2933. <https://doi.org/10.1016/j.disc.2007.03.007>

## RESEARCH ARTICLE

### Statistics

# Maximum likelihood estimation for the two-parameter Maxwell distribution

P Kasap\* and AO Faouri

Department of Statistics, Faculty of Science, Ondokuz Mayıs University, Atakum, Samsun, Turkey.

Submitted: 08 August 2024; Revised: 13 November 2024; Accepted: 26 November 2024

**Abstract:** The Maxwell distribution is popular in physics, chemistry and statistical dynamics. Since the estimators obtained using the maximum likelihood method have the desired properties of being efficient, consistent, and asymptotically normal under regularity conditions, this method is a widely used method to estimate the parameters of a probability distribution. Although parameter estimates can be obtained using this method, the derivatives of the log-likelihood equations, known as ML estimation equations, with respect to the parameters do not always have clear solutions. Therefore, numerical methods are used to solve these equations. Various traditional numerical methods for this purpose are well-documented in the literature. Additionally, highly powered algorithms with no required mathematical assumption that improve the computational efficiency like heuristic algorithms can be used to solve these equations. In this article, the maximum likelihood method is applied to estimate the location and scale parameters of the two parameter Maxwell distribution. High-performance heuristic algorithms, such as particle swarm optimization and genetic algorithms, are used and compared with traditional numerical techniques, including Nelder-Mead and Quasi-Newton methods. To show the performance of these techniques, an extensive Monte Carlo simulation study was conducted to compare the efficiencies of maximum likelihood estimators of model parameters concerning bias, mean square error, and deficiency criteria. Simulation results showed that genetic algorithm and particle swarm optimization estimators are more efficient than the other traditional algorithms for estimating the location and scale parameters for the two-parameter Maxwell distribution.

**Keywords:** Iterative methods, heuristic and traditional algorithms, maximum likelihood, Monte Carlo simulation, two-parameter Maxwell distribution.

## INTRODUCTION

The Maxwell distribution is widely used in many scientific fields, including physics, chemistry, and statistical mechanics. This distribution is an appropriate alternative for modelling lifetime data such as flood levels, wind speeds, or failure rates in various application areas like engineering, environment, finance, insurance, and medical science (Pasha *et al.* 2006; Krishna & Malik, 2012; Hernandez, 2017; Prativiera *et al.*, 2020; Omar *et al.* 2021;). James Maxwell proposed the Maxwell distribution (Maxwell, 1860; Maxwell, 1867). It was first used for modelling lifetime data in 1989 (Tyagi & Bhattacharya, 1989a; Tyagi & Bhattacharya, 1989b). They used Bayes estimation method to estimate the scale parameter for the Maxwell distribution.

The Maxwell distribution is considered as a special case of the generalized Rayleigh distribution (Pham-Gia, 1994). In 1998, the Gamma distribution was transformed into the Maxwell distribution, and its scale parameter was estimated by classical and Bayesian methods (Chaturvedi & Rani, 1998). It is also considered a special case of the generalized Weibull distribution (Al-Mutairi & Agarwal, 1999). The parameter of the Maxwell distribution is estimated by the Bayesian method using the modified linear exponential loss function (MLINEX) (Podder & Roy, 2003). The maximum likelihood (ML) estimator, Bayesian estimator, and empirical Bayesian estimator of the Maxwell distribution derived and compared in

\* Corresponding author (pelin.kasap@omu.edu.tr;  <https://orcid.org/0000-0002-1106-710X>)



This article is published under the Creative Commons CC-BY-ND License (<http://creativecommons.org/licenses/by-nd/4.0/>). This license permits use, distribution and reproduction, commercial and non-commercial, provided that the original work is properly cited and is not changed in anyway.

terms of efficiency using Monte Carlo simulation study (Bekker & Roux, 2005). The reliability properties of the Maxwell-Boltzmann distribution under type II censored data were estimated by using the Bayesian and maximum likelihood methods, and the efficiencies of the estimates generated by these estimation methods were compared by performing a Monte Carlo simulation study (Krishna & Malik, 2009). The relationship between ML, moments (MOM) estimators, and the variance of Maxwell distribution is reviewed with theoretical steps. Also, for quadratic loss functions, the minmax (minimax) estimator of the Maxwell distribution is determined using the Lehmann theorem, and the estimators are compared. (Dey and Maiti, 2010). ML estimator and variance-covariance matrix are found for the Maxwell distribution under type I censoring data (Kasmi *et al.*, 2011). In 2013, Al-Baldawi also made another comparison between some Bayesian estimators using uninformative priors under two different loss functions and ML estimators for the scale parameter of the Maxwell distribution (Al-Baldawi, 2013). Rasheed and Khalifa (2016) used the Bayesian estimation method with a quadratic loss function to estimate the scale parameter of the Maxwell distribution. Many different data sets collected from the literature in 2016 were analyzed using the Maxwell distribution (Hossain & Huerta, 2016). Li used Minmax, Bayes, and ML methods to estimate the scale parameter of the Maxwell-Boltzmann distribution (Li, 2016).

In practice, distributions with only one parameter are limited and hard to fit, so it is better for data analysis to expand the family of distributions by adding an extra parameter using various techniques to give more flexibility (Dey *et al.*, 2016).

The extension of the Maxwell distribution by adding the location parameter provides a new, extended and more flexible type of distribution known as the two-parameter Maxwell distribution. Dey *et al.* (2016) extended this distribution and estimated the location and scale parameters using both classical and Bayesian methods. A new method based on algebraic approximation is used to correct the bias of ML estimator bias for the location and scale parameters of the Maxwell distribution (Maghami & Bahrami, 2020). Arslan *et al.* (2021) obtained the location and scale parameters of the Maxwell distribution using the modified maximum likelihood (MML) method along with other statistical methods for both complete and censored samples, they then compared the performance of the MML estimators with the ML, LS and MOM estimators through a Monte Carlo simulation study.

Chowdhury (2022) constructed statistical confidence intervals for the two-parameter Maxwell distribution with ML, MOM and MML methods and the study shows that statistical confidence intervals based on ML estimators offer little improvement over other interval estimators when sample sizes are small.

Among these estimation methods, the ML method is widely used in many studies due to its well-known asymptotic properties such as asymptotic unbiasedness, consistency, efficiency, etc. It is known that ML is an estimation process based on maximizing the likelihood function for the concerned parameters. However, in some cases, the maximum likelihood equations do not have explicit solutions due to their nonlinear functions. In such cases, iterative algorithms can be utilized to the results.

The key objective of this study is to demonstrate the two-parameter Maxwell distribution's relevance in numerous scientific domains and to estimate the location and scale parameters of this distribution. The main problem addressed in this work is the absence of an explicit solution to the likelihood equations for this distribution. To address this, iterative numerical methods, using both heuristic and traditional algorithms, are applied to obtain maximum likelihood estimators.

As it is also seen in the literature, ML estimators can be obtained numerically by using the Newton-Raphson (NR) algorithm to solve the equation systems formed by the partial derivatives of the likelihood function. The main limitation of this algorithm is its reliance on gradient-based search methods (Martinez, 2000). To address this issue, well-known heuristic algorithms such as Genetic Algorithms (GA) and Particle Swarm Optimization (PSO) are often employed. Additionally, other efficient traditional algorithms, including Nelder-Mead (NM) and Quasi-Newton (QN), are also used. Even though the traditional numerical techniques are widely used, they often face challenges such as convergence issues, low computational efficiency, and high costs when applied to non-linear equations. (Chen *et al.*, 2023). Iterative methods, while an alternative, can also encounter several issues: (i) failure to converge, (ii) slow convergence, and (iii) convergence to an incorrect root (Barnett, 1966; Puthenpura and Sinha, 1986; Vaughan, 1992). In order to show the high performance of heuristic algorithm estimators, an extensive Monte Carlo simulation study was carried out to compare the ML estimators of GA and PSO with the other ML estimators for NM and QN.

The parameters of various statistical distributions and models, including Weibull, skewed normal, Nakagami, EMLOG, and others, were estimated using the maximum likelihood (ML) method, implemented with genetic algorithms (GA) and/or particle swarm optimization (PSO). (Yalçınkaya *et al.*, 2018; Karakoca & Pekgör, 2019; Faouri & Kasap, 2023; Kasap & Faouri, 2024). To the best of our knowledge, this study is considered the first to obtain the ML estimators for the location and scale parameters of the two-parameter Maxwell distribution by using the heuristic algorithms. The rest of the article is organized as follows: In the section Materials and Methods section, the two-parameter Maxwell distribution and its properties are presented. Parameter estimation methodology via heuristic and the other traditional numerical techniques is introduced. In the results and discussion, the Monte Carlo simulation study is presented. Two real-life dataset are implemented as an application of this distribution. In the final section, the conclusion of this work is presented.

## MATERIALS AND METHODS

### Two-parameter Maxwell distribution

Maxwell distribution can be used to describe the distribution of gas molecules with respect to their speed distributions and relate them to the temperature (Atkins and De Paula, 2011). The probability density function (pdf) of the Maxwell distribution is given by:

$$f(v) = 4\pi \left(\frac{m}{2\pi kT}\right)^{3/2} v^2 e^{-\left(\frac{m}{2kT}v^2\right)}, v > 0 \quad \dots(1)$$

Where,

$T$  : The temperature of the gas in kelvin

$K$  : The constant value in J/K is  $1.380649 \times 10^{-23}$ , in J/K, which is considered as the proportionality factor that establishes a relationship between the average relative thermal energy of a gas's particles and its thermodynamic temperature.

$m$  : The molecule's weight in kg/mol

$v$  : The speed of molecule

The Maxwell distribution of speeds and its variation with temperature are given in Figure 1.

When the re-parameterization  $\sigma = \sqrt{\frac{2kT}{m}}$  is applied and location parameter  $\mu$  is added to equation (1),

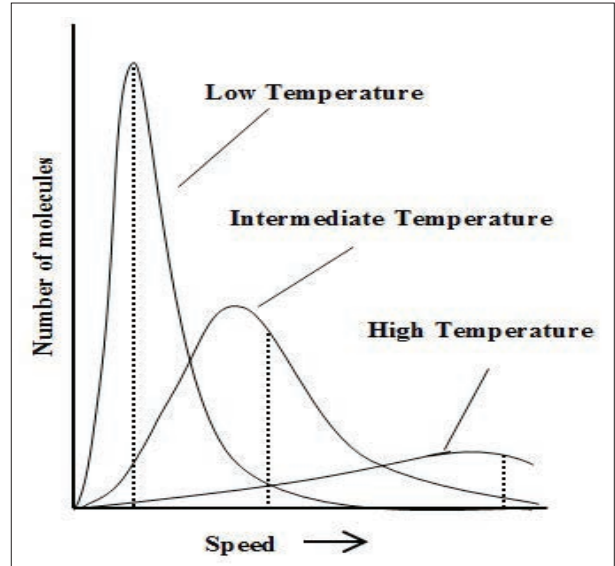


Figure 1: Maxwell distribution of speeds and its variation with temperature.

the resulting distribution is called the two-parameter Maxwell distribution.

Let  $X$  be a random variable that follows a two-parameter Maxwell distribution with parameters  $\mu$  and  $\sigma$  then the probability density function (pdf) is:

$$f(x; \mu, \sigma) = \frac{4}{\sigma \Gamma(1/2)} \left(\frac{x-\mu}{\sigma}\right)^2 e^{-\left(\frac{x-\mu}{\sigma}\right)^2}, \mu \leq x < \infty, \sigma \geq 0 \quad \dots(2)$$

where,

$\mu$ : location parameter and  $\sigma$ : scale parameters

The corresponding cumulative distribution function (cdf) of this distribution is:

$$F(x; \mu, \sigma) = \frac{4}{\Gamma(3/2)} \Gamma\left[\left(\frac{x-\mu}{\sigma}\right)^2, 3/2\right] \quad \dots(3)$$

The mean and variance of the random variable  $X$  are given by:

$$E(X) = \mu + \frac{2\sigma}{\sqrt{\pi}} \quad \dots(4)$$

$$Var(X) = \frac{\sigma^2(3\pi-8)}{2\pi} \quad \dots(5)$$

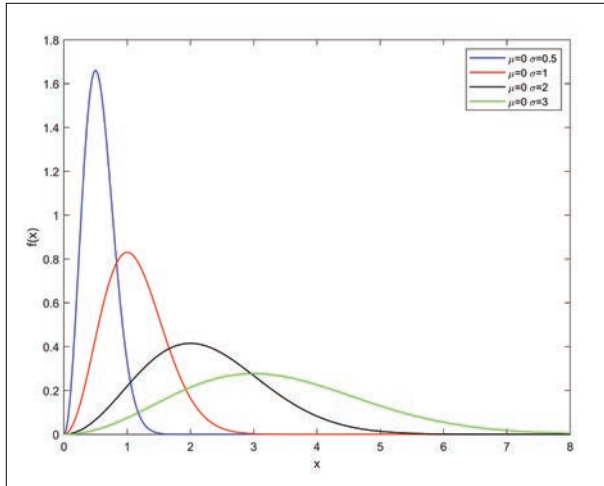


**Figure 2:** Two-parameter Maxwell distribution for certain values of  $\sigma$   $\mu = 0$ .

**Maximum likelihood estimation**

The maximum likelihood estimates are the values that maximize the likelihood function (Miura, 2011). The log-likelihood function (*LL*) for estimating the unknown parameters  $\mu$  and  $\sigma$  for the  $\mu$  two-parameter Maxwell distribution is given  $\mu$  the follows:

$$LL = n \ln \left( \frac{4}{\sigma \Gamma(1/2)} \right) + 2 \sum_{i=1}^n \left( \frac{x_i - \mu}{\sigma} \right) - \sum_{i=1}^n \left( \frac{x_i - \mu}{\sigma} \right)^2 \quad \dots(6)$$

The normal equations for estimating the location parameter  $\mu$  and the scale parameter  $\sigma$  are shown as below:

$$\frac{\partial LL}{\partial \mu} = \frac{-2}{\sigma} \sum_{i=1}^n \left( \frac{1}{x_i - \mu} \right) + \frac{2}{\sigma} \sum_{i=1}^n \left( \frac{x_i - \mu}{\sigma} \right) = 0 \quad \dots(7)$$

and

$$\frac{\partial LL}{\partial \sigma} = \frac{n}{\sigma} - \frac{2}{\sigma} \sum_{i=1}^n (x_i - \mu) + \frac{2}{\sigma} \sum_{i=1}^n \left( \frac{x_i - \mu}{\sigma} \right)^2 = 0 \quad \dots(8)$$

respectively

These normal equations are taken from the partial derivative of the *LL* function for the parameter of interest. Then these equations are equated to zero to find the solutions which represent the resulting ML estimate values of  $\mu$  and  $\sigma$ . As shown in the normal equations (7) and (8), the functions are nonlinear, and an explicit solution for the likelihood equations cannot be determined. Therefore, we need iterative techniques to find the solutions and to obtain ML estimators of  $\mu$  and  $\sigma$ .

Iterative techniques PSO, GA, NM, and QN are briefly introduced in the following subsections.

**Particles swarm optimization (PSO)**

PSO is a population-based heuristic optimization technique developed from swarm intelligence and derived from the manual behaviour of bird flocks. It was proposed for the first time in 1995 (Kennedy & Eberhart, 1995). It is also known as an evolutionary self-adaptive search technique. Practically, it is preferred to be used for continuous optimization problems (Kachitvichyanukul, 2012). In this method, each solution is called a particle, and for any set of solutions, is called a population. It can be used in many fields because of its easy implementation, high precision, and fast convergence. The main advantage of PSO is that it can avoid the solution from being trapped in local optima and help to reach the global optimum or very close to it by searching at different points and different regions of the search space (Salehizadeh *et al.*, 2009). Each solution (particle) consists of a set of parameters and represents a point in multi-dimensional space. The basic idea of the PSO method can be summarized as a process of continuously moving a swarm of particles in a specific search space concerning certain formulas until finally reaching the optimal solution (Júnior *et al.*, 2020). PSO flowchart is shown in figure 3. For the PSO algorithm steps, see Júnior *et al.*, 2020; Ren *et al.*, 2014; Ab Talib and Mat Darus, 2017.

**Genetic algorithm (GA)**

GA is the first heuristic random optimization search technique that is inspired by biological evolution operating under natural selection (Whitley, 1994). Like PSO, it is an evolutionary self-adaptive method and it's useful in finding approximately the best solution in optimization problems, especially in discrete optimization (Kachitvichyanukul, 2012). It was first presented by John Holland in the early 1960s (Holland, 1975) and was greatly improved by his student Golberg later on (Golberg, 1989). In GA, each candidate solution represents a chromosome and each set of solutions (chromosomes) represents a population. The *LL* function represents the fitness value for each chromosome in the population, and in every iteration, the fitness value is calculated and evaluated. During the iteration, a certain modification process is applied according to the mechanism of biological evolution to reach the optimal solution at the end. GA flow chart is shown in figure 4; for more details of GA algorithm steps, see (Yalçinkaya *et al.*, 2018).

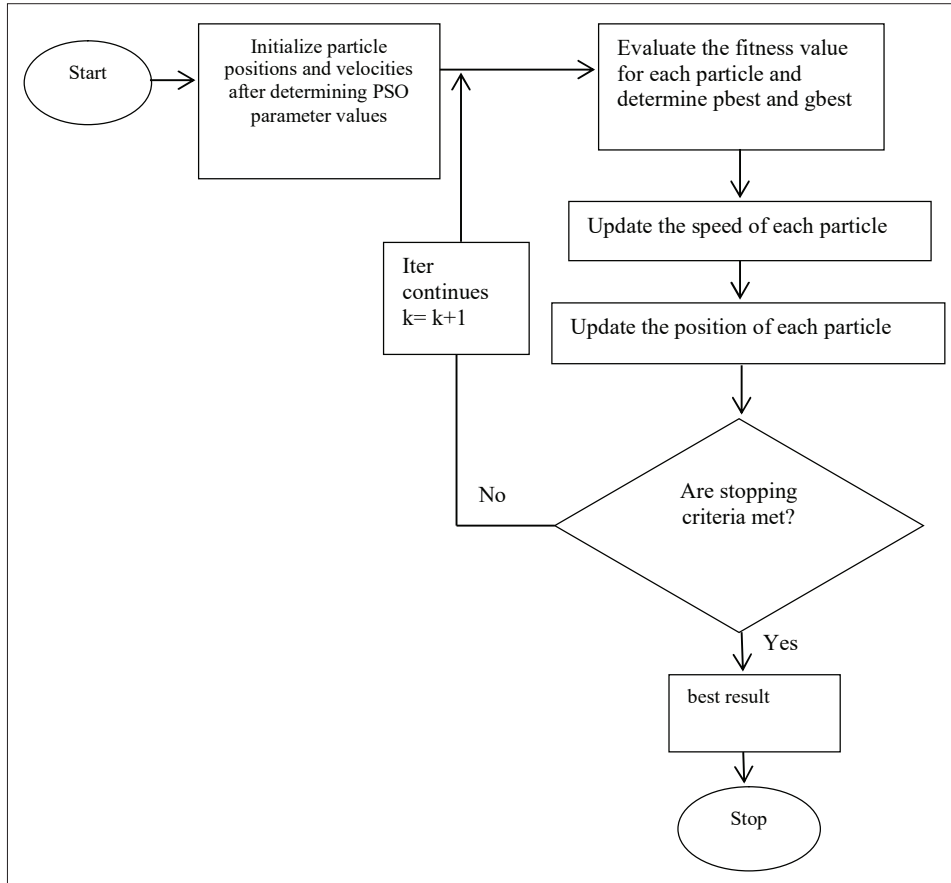


Figure 3: Flow chart of the PSO.

**Nelder mead (NM)**

The NM simplex algorithm is a popular deterministic direct search method, commonly used in n-dimensional space for finding a local minimum of the objective function in optimization problems. It was devised by John Nelder and Roger Mead in 1965 (Júnior *et al.*, 2020). This simplex method denotes a convex hull geometric figure for n-dimensional problems with n+1 vertices, so for two-dimensional problems, the simplex is a triangle with three vertices. The pattern search method of this algorithm is based on ordering the vertices according to their fitness values, with the highest value considered as the worst and replaced with the newly generated vertex, forming a new simplex. This search process is repeated, making a sequence of generated simplexes with different shapes and sizes pass through the main four operations until finally reaching the optimal minimum (or maximum). In this study, the function that needs to be minimized is:

$$f(\theta) = -LL(\theta), \text{ where } \theta = (\mu, \sigma) \in R \times R^+$$

In the implementation of the NM algorithm method, the main four operations are reflection, expansion, contraction, and shrink. Their coefficients are taken as  $\alpha = 1$ ,  $\gamma = 2$ ,  $\rho = 1/2$  and  $\beta = 1/2$  respectively, in the literature. For the NM algorithm steps (Nelder & Mead, 1965; Kucukdeniz & Esnaf, 2018; Gao & Han, 2012).

**Quasi-Newton (QN)**

The QN algorithm is the most commonly used numerical technique for finding solutions to nonlinear unconstrained objective functions by using quadratic approximation. This method is based on the regular Newton-Raphson (NR) method. However, in some situations, NR is difficult to apply because in every iteration, a partial derivative must be computed and a linear system must be solved, which demands extra time and costs (Martinez, 2000).

This fact motivated the development of quasi-Newton by Davidon in 1959 (Davidon, 1991). The QN is the same as NR concerning twice differentiability of the objective function; the initial starting point should be close to the true root; and it uses the same search direction. The only difference is that for QN, the gradient of the objective

function is used to estimate the inverse Hessian matrix in many different approximation algorithms. More details on that can be found in the literature (Broyden, 1967; Shanno, 1970; Fletcher & Powell, 1963). For the QN algorithm steps, see (Karakoca & Pekgör, 2019).

#### ***Advantages of the GA and PSO algorithm in comparison***

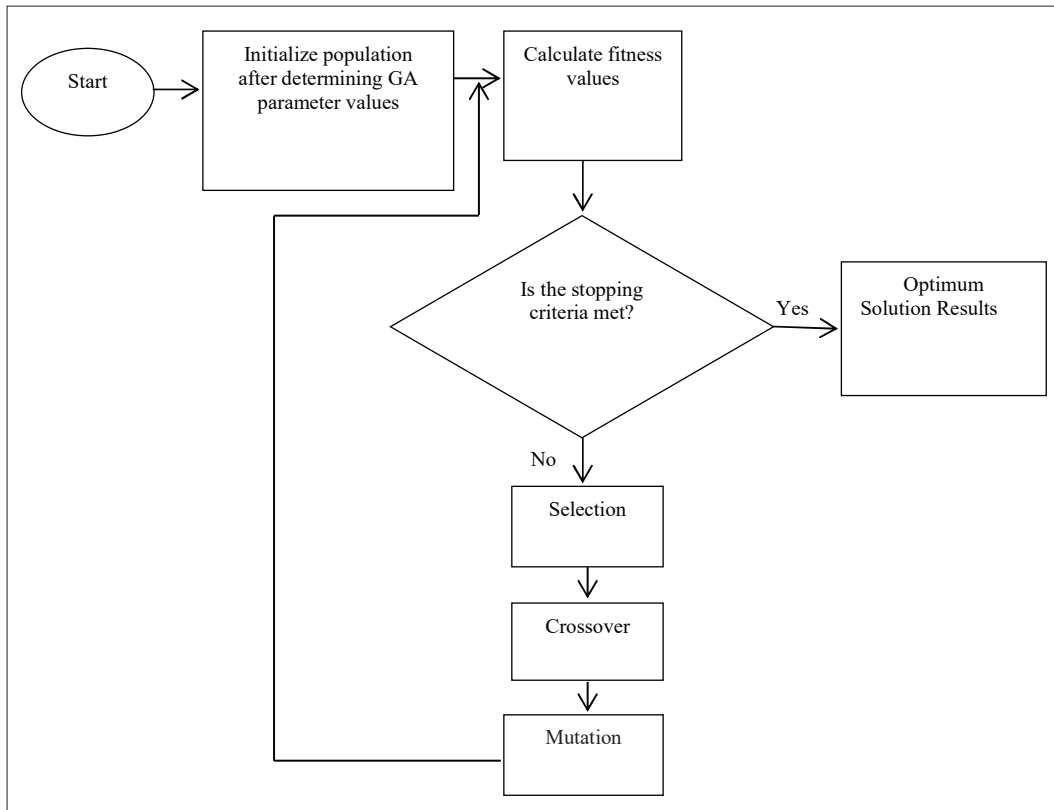


**Figure 4:** Flow chart of the GA.

#### ***with other algorithms used in this study.***

- GA and PSO are considered as the simplest heuristic algorithm for programming purposes, and it can be easily used for any distribution by implementing the log-likelihood as a fitness function of the model in the programme.
- The efficiency of GA and PSO as a heuristic-based algorithms are better than other traditional algorithms used in this study, according to the simulation results.
- Having a starting point as an initial value that must be close to the optimum solution is critical for traditional iterative algorithms such as NM and QN to

successfully converge at the end. However, in GA and PSO, the initial value problem does not exist because they do not depend on it for convergence. Instead, operation of GA and PSO starts with a set of solutions called the population, and it only needs a search space that is considered as an interval containing the global optimum. It is known that defining an interval that includes the solution root is much better than defining a single starting guess value. However, according to the simulation results for this study model, if the starting point for traditional methods is selected very carefully to be very close to the solution, it may need less time to reach the solution, but even if that is the case, the efficiency of the GA and PSO method is

- better.
- The GA and PSO methods eliminate the need for mathematical assumptions based on differentiability, as in the Newton method, and instead relies solely on the evaluation of the objective function, demonstrating the method’s simplicity.
- The flexibility of the GA and PSO methods allows it to be applied to optimization problems with linear or nonlinear functions, and it can be identified in the discrete, continuous, or mixed search space.

## RESULTS AND DISCUSSION

### Monte Carlo (MC) simulations study

In this section, an extensive Monte Carlo (MC) simulation study is conducted in which the efficiency of the PSO and GA estimators is compared with the NM, and QN estimators. All computations are conducted by using the following functions: “particleswarm”, “ga”, “fminsearch”, and “fminunc” for programming PSO, GA, NM, and QN respectively in MATLAB 2021a software. The values of the initial conditions for PSO and other methods used in this study are considered to be the default for the fixed parameters; that is, the inertia weight = max {0.1, 1.1}, and the accelerating coefficients  $c1 = c2 = 1.49$ . The maximum iteration number until convergence happens is taken to be 400, which is equivalent to the number of estimated parameters (two parameters in this study) multiplied by 200, and the convergence is achieved according to the stopping rule:  $|\theta^{k+1} - \theta^k| < \epsilon$ .

Each Monte Carlo (MC) simulation run is executed 2000 times. The location parameter  $\mu$  and scale  $\sigma$  are considered to be ( $\mu = 0, 1, 2$ ) and ( $\sigma = 1, 2$ ) respectively. The sample size is taken as small ( $n = 10, 20, 30$ ), moderate ( $n = 50$ ) and large ( $n = 100, 250, 500$ ). The search space (SS) is selected for both  $\mu$  and  $\sigma$  parameters to be [0,5]. NM estimates were obtained by taking the starting point values [0.01, 0.01] for all sample sizes, and the same starting point can be used for QN for small and moderate sample sizes only. However, for large sample sizes, this point is not advised, so the point [0.1,0.01] was chosen for the QN method to guarantee convergence. The resulting estimates for location  $\mu$  and scale  $\sigma$  parameters in the simulations are denoted by  $\hat{\mu}$  and  $\hat{\sigma}$ , respectively. The main criteria used to compare between estimators are Mean, Bias, Mean Square Error (MSE), and Deficiency (Def). Also, the necessary iteration number (Iter) and the required time (Time) in seconds to reach the solution for every sample have been generated in the simulations for all methods. The sum of total estimated values over the total number of MC simulation runs (average) is called

the mean; mathematically it can be expressed as:

$$Mean(\hat{\theta}) = \frac{\sum_i^n \hat{\theta}_i}{n} \quad \dots(9)$$

where  $n$  is the number of MC simulation runs. The difference between the expected value of the estimator and the true value of the parameter is called Bias. Mathematically, it can be expressed as:

$$Bias(\hat{\theta}) = E(\hat{\theta}) - \theta \quad \dots(10)$$

MSE is one of the main criteria to compare biased estimators according to their efficiencies. Any estimator with the smallest value of MSE is considered the most efficient and the best choice between other estimators, mathematically it can be expressed as:

$$MSE(\hat{\theta}) = Var(\hat{\theta}) + (Bias(\hat{\theta}))^2 \quad \dots(11)$$

The variance and Standard Error (SE) of an estimator are calculated and expressed mathematically as the following equalities:

$$Var(\hat{\theta}) = \frac{1}{n-1} \sum_{i=1}^n (\hat{\theta}_i - Mean \hat{\theta})^2 \quad \dots(12)$$

and

$$SE(\hat{\theta}) = \sqrt{Var(\hat{\theta})} \quad \dots(13)$$

respectively,

Deficiency is an essential major of the joint efficiency of the estimators  $\mu$  and  $\sigma$ , which is defined as the sum of the MSE of the parameter estimators. It can be formulated mathematically as:

$$Def(\hat{\mu}, \hat{\sigma}) = MSE(\hat{\mu}) + MSE(\hat{\sigma}) \quad \dots(14)$$

Iteration is the process of repeating a step continually until convergence occurs. For every method used in this study, the total number of iterations required for the estimation process for each sample was summed up and then divided over the total number of MC simulation runs to calculate the average number of iterations. It has the following mathematical expression:

$$\overline{Iter}(\hat{\theta}) = \frac{\sum_i^n Iter(\hat{\theta})_i}{n} \quad (15)$$

To calculate the average amount of time needed to estimate the parameters, the total time (measured in seconds) needed for each simulation run is added up and then divided by the total number of simulation runs.

$$\overline{Time}(\hat{\theta}) = \frac{\sum_i^n Time(\hat{\theta})_i}{n} \quad \dots(16)$$

The resulting simulated values of Mean, Bias, MSE, and Def for  $\hat{\mu}$  and  $\hat{\sigma}$  are shown in Tables (1-5) in appendix and the best results are highlighted in bold in these tables. The simulation results show that the heuristic algorithms have better results among the other traditional algorithms. It should be noted that before analyzing the simulation results, it was verified that all of the randomly generated samples have real roots (exitflag = 1).

For bias criteria, the results are as follows:

- When  $\mu = 0, \sigma = 1$ , the smallest value of bias belongs to QN for  $\hat{\mu}$  and  $\hat{\sigma}$  estimators for all sample sizes, and the largest values belong to GA for the small and moderate sample sizes, but for the large sample size, it belongs to NM, as shown in Table 1 in appendix.
- When  $\mu = 1, \sigma = 1$  the smallest value of bias belongs to GA for  $\hat{\mu}$  and  $\hat{\sigma}$  estimators for all sample sizes as shown in Table 2 in appendix.
- When  $\mu = 1, \sigma = 2$ , the smallest values of bias belong to PSO for  $\hat{\mu}$  and  $\hat{\sigma}$  estimators for all sample sizes (except when  $n = 10, 20$ , the smallest bias values belong to NM and GA, respectively), as shown in Table 3 in appendix.
- When  $\mu = 2, \sigma = 1$ , the smallest values of bias belong to GA for  $\hat{\mu}$  and  $\hat{\sigma}$  estimators (except when  $n = 20$ , the smallest bias values belong to PSO) for all sample sizes as shown in Table 4 in appendix.
- When  $\mu = 2, \sigma = 2$ , the smallest values of bias belong to GA for the  $\hat{\mu}$  estimator, and the smallest values of bias belong to PSO for the  $\hat{\sigma}$  estimator (except when  $n = 20$ , the smallest bias values belong to PSO) as shown in Table 5 in appendix.

The worst bias with the largest values in all cases (except when  $\mu = 0, \sigma = 1$ ) belongs to QN for all sample sizes, as shown in Tables 2 - 5 in appendix.

Concerning MSE and Def values for the location estimator  $\hat{\mu}$  and scale estimator  $\hat{\sigma}$ , the results are as follows

- When  $\mu = 0, \sigma = 1$  we see that PSO estimators have the best values for all sample sizes. The NM estimator has the worst values among all other estimators, especially at large sample sizes. Also, it's clear that when sample size increases, the MSE values of GA improve to be slightly better than QN and so close to the PSO values as shown in Table 1 in appendix.

According to the Def criteria, the PSO shows that it has the best performance with the smallest values in comparison with the other estimators for all cases. The results of QN are so close to PSO in the small and moderate sample sizes, but in large sample sizes ( $n=250, 500$ ), GA outperforms QN to be the second method with the smallest Def values after PSO.

- When  $\mu = 1, \sigma = 1$  we see that the GA then PSO estimators have the best values for all sample sizes and the NM and QN estimators have the largest values respectively as shown in Table 2 in appendix.
- When  $\mu = 1, \sigma = 2, \mu = 2, \sigma = 1$  and  $\mu = 2, \sigma = 2$  we see that the GA then PSO estimators have the best values for all sample sizes and the NM and QN estimators have the largest values respectively as shown in Tables 3-5. However when  $\mu = 2, \sigma = 2$  it's noticed that in moderate and large sample sizes the MSE as well as the Def values of GA is enhanced with better values than the other algorithms used.
- When  $\mu = 2, \sigma = 2$  we see that the GA then PSO estimators have the best values for all sample sizes and the NM and QN estimators have the largest values respectively. According to the Def criteria, the GA shows that it has the best performance with the smallest values in comparison with the other estimators for all cases (except when  $\mu = 0, \sigma = 1$ ) as shown in Tables 2-5. Also we can notice that when  $\mu = 2, \sigma = 2$  in moderate and large sample sizes the MSE as well as the Def values of GA is enhanced with noticeably better values than the other algorithms used as illustrated in figures 5-7.

All that can lead us to say that heuristic algorithms represented by GA and PSO are better than traditional algorithms such as NM and QN for estimating the location  $\hat{\mu}$  and scale  $\hat{\sigma}$  parameters for the two-parameter Maxwell distribution.

Based on the average number of iterations, QN requires the fewest iterations, followed by PSO, GA, and NM, respectively. In terms of the average time needed to reach a solution, NM and QN are faster than PSO and GA. However, it is important to note that both the number of iterations and the time required to reach a solution depend heavily on the choice of the initial point. If a poor initial point is selected, both the iteration count and the solution time may increase significantly. The main issue is that traditional algorithms such as NM and QN may be forced to stop because convergence has not occurred. For these reasons, even though traditional methods are faster in some situations, methods based on

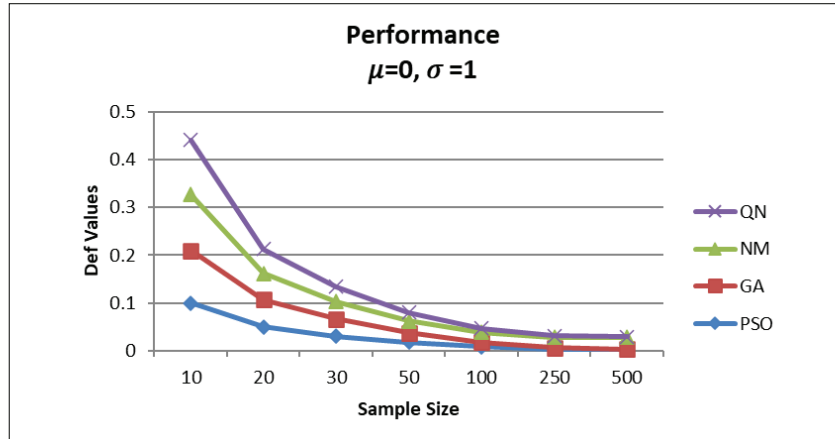


Figure 5: Performance of GA, PSO, NM, and QN according to the Def values when  $\mu=0, \sigma=1$

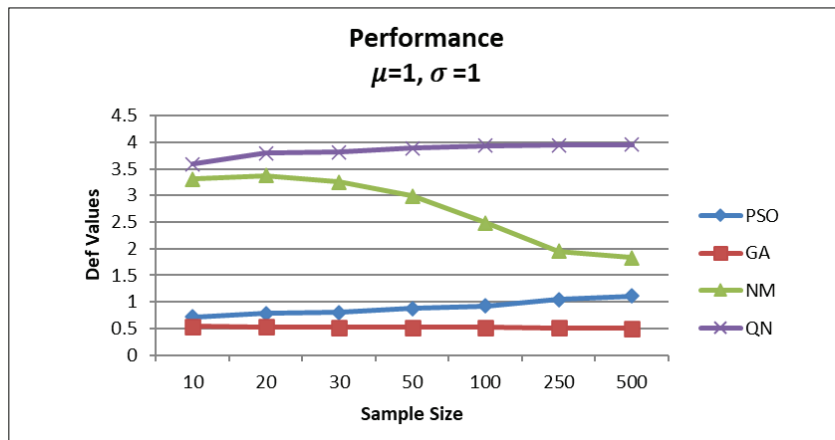


Figure 6: Performance of GA, PSO, NM, and QN according to the Def values when  $\mu=1, \sigma=1$

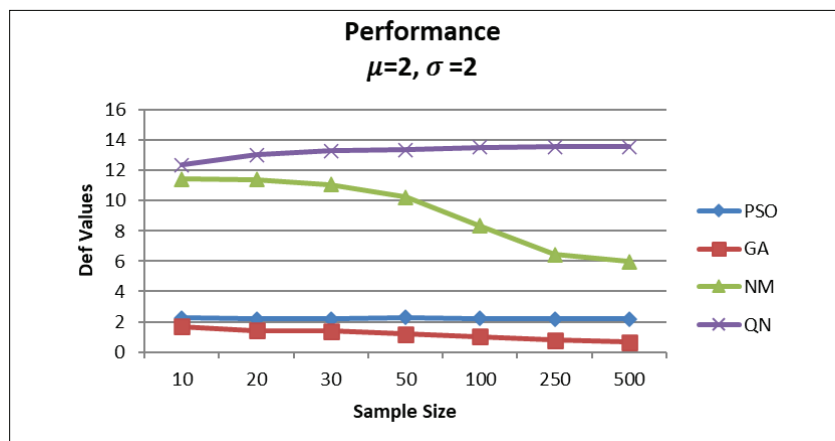


Figure 7: Performance of GA, PSO, NM, and QN according to the Def values when  $\mu=2, \sigma=2$

heuristic algorithms are preferred.

In this study, we can classify the four estimation methods into two groups: heuristic algorithm methods (including PSO and GA) and traditional methods (including NM and QN). When comparing PSO and GA as heuristic-based algorithms used in this study, the GA algorithm shows fewer deficiency values for different values of  $\mu$  and  $\sigma$ . Additionally, both algorithms require approximately the same time to complete all iterations needed to estimate the model parameters. Simultaneously, when only traditional methods are compared, NM is preferred over the QN algorithm with respect to the deficiency values for different values of  $\mu$  and  $\sigma$ , while QN is preferred over the NM due to its slightly lower required iteration number and time, even though they almost require the same calculation time. When we compare the two groups, it is clear that heuristic algorithms have the best performance according to Def values regardless of the number of iteration and calculation time, because these criteria are highly dependent on the starting point value for traditional methods. At the same time, in large sample sizes, the GA method outperforms the QN method (when  $\mu = 0$ ,  $\sigma = 1$ ), implying that heuristic algorithms outperform traditional algorithms when large sample sizes are used. Finally, based on the simulation results, it can be said that heuristic algorithms including GA and PSO are more efficient than the other traditional algorithms used in the study for estimating the parameters of the two-parameter Maxwell distribution.

## Applications

For applications 1 and 2 the two-parameter Maxwell distribution is used in this section to model two real data sets. The unknown parameters are estimated via the maximum likelihood method for each dataset and evaluated using the PSO, GA, NM, and QN algorithms. The modelling performance for fitted Maxwell distribution is compared and evaluated between all methods used in this study by using well-known selection criteria including log-likelihood (LL), Akaike Information Criterion (AIC), and corrected AIC (AICc), see (Anderson *et al.*, 1998). The method that best fits these criteria is considered to have the lowest values.

### Application 1: Aircraft windshield service time data

This dataset, is widely used in many engineering and statistical sectors which is used for method implementation (Tahir *et al.*, 2015; Balogun *et al.*, 2021). It includes 63 observations about aircraft windshields' service times (1000 hours is the measurement unit used). *Observations*

*on the aircraft windshield service time dataset:*

0.046, 1.436, 2.592, 0.140, 1.492, 2.600, 0.150, 1.580, 2.670, 0.248, 1.719, 2.717, 0.280, 1.794, 2.819, 0.313, 1.915, 2.820, 0.389, 1.920, 2.878, 0.487, 1.963, 2.950, 0.622, 1.978, 3.003, 0.900, 2.053, 3.102, 0.952, 2.065, 3.304, 0.996, 2.117, 3.483, 1.003, 2.137, 3.500, 1.010, 2.141, 3.622, 1.085, 2.163, 3.665, 1.092, 2.183, 3.695, 1.152, 2.240, 4.015, 1.183, 2.341, 4.628, 1.244, 2.435, 4.806, 1.249, 2.464, 4.881, 1.262, 2.543, 5.140.

Table 6 in appendix shows the descriptive statistics for this dataset that contain the values of sample size (n), Minimum (Min), First Quartile (1<sup>st</sup> Qu.), Mean, Mode, Median, Third Quartile (3<sup>rd</sup> Qu.), Maximum (Max), Variance ( $S^2$ ), skewness ( $\gamma_1$ ), and kurtosis ( $\gamma_2$ ) coefficients, respectively.

The parameter estimates corresponding to the selection criteria are given in table 7 in appendix. The results show that the PSO and GA methods have the best performance fitting for the two-parameter Maxwell distributions, in comparison with other traditional methods like NM and QN.

### Application 2: Vinyl chloride data

This dataset is concerned with environmental investigation issues and includes 34 observations. The dataset is provided below and the descriptive statistics for this dataset are given in table 8 in the appendix. More details about this dataset can be found in (Bhaumik *et al.*, 2009; Shukla, 2019). *Observations of the vinyl chloride dataset:*

5.1, 1.2, 1.3, 0.6, 0.5, 2.4, 0.5, 1.1, 8, 0.8, 0.4, 0.6, 0.9, 0.4, 2, 0.5, 5.3, 3.2, 2.7, 2.9, 2.5, 2.3, 1, 0.2, 0.1, 0.1, 1.8, 0.9, 2, 4, 6.8, 1.2, 0.4, 0.2

Table 9 in appendix shows the parameter estimate results for the various selection criteria. The second application yields the same result as the first, namely that the PSO and GA methods outperform other traditional methods like NM and QN in fitting the two-parameter Maxwell distributions, demonstrating that heuristic algorithms outperform classical and traditional methods. However, when we compare NM and QN, we see that QN performs better in the first application while NM performs better in the second application, which leads us to the conclusion that we cannot rely on a single traditional method for estimating the parameters. Hence, we can claim that GA and PSO are the best methods for estimating the parameters of the two-parameters Maxwell distribution.

## CONCLUSION

In this study, the ML method is used to estimate the location and scale parameters of the two-parameter Maxwell distribution. In many cases, it is hard to have a solution for the parameters of interest for complicated nonlinear maximum likelihood equations. For these complicated nonlinear maximum likelihood equations, we need an efficient numerical technique to reach the best estimate values. This is the originality of this study. By conducting an intensive MC simulation study, the PSO, GA, NM, and QN algorithms are selected, and the performance of these algorithm estimators is compared with each other according to bias, MSE, Def, the number of required iterations (*Iter*), and calculation time criteria. Concerning these criteria, the results show that the heuristic algorithms used in this study, which are PSO and GA, respectively have the best performance values with robust efficient solutions regardless of the number of iterations and calculation time due to the fact that the performance criteria of traditional methods' are heavily reliant on the starting point value. However, heuristic algorithm-based methods such as GA and PSO are more efficient than traditional search optimization methods and yield the best results across all sample sizes, so these algorithms are more recommended for the study model.

## REFERENCES

- Ab Talib, M. H., & Mat Darus, I. Z. (2017). Intelligent fuzzy logic with firefly algorithm and particle swarm optimization for semi-active suspension system using magneto-rheological damper. *Journal of Vibration and Control*, 23(3), 501-514. <https://doi.org/10.1177/1077546315580693>
- Anderson, D. R., Burnham, K. P., & White, G. C. (1998). Comparison of Akaike information criterion and consistent Akaike information criterion for model selection and statistical inference from capture-recapture studies. *Journal of Applied Statistics*, 25(2), 263-282. <https://doi.org/10.1080/02664769823250>
- Arslan, T., Acitas, S., & Senoglu, B. (2021). Parameter estimation for the two-parameter Maxwell distribution under complete and censored samples. *REVSTAT-Statistical Journal*, 19(2), 237-253. <https://doi.org/10.57805/revstat.v19i2.341>
- Atkins, P., & De Paula, J. (2011). *Physical chemistry for the life sciences*. Oxford University Press, USA.
- Balogun, O. S., Arshad, M. Z., Iqbal, M. Z., & Ghamkhar, M. (2021). A new modified Lehmann type-II G class of distributions: exponential distribution with theory, simulation, and applications to engineering sector. *F1000Research*, 10(483), 483. <https://doi.org/10.12688/f1000research.52494.1>
- Barnett, V. D. (1966). Evaluation of the maximum-likelihood estimator where the likelihood equation has multiple roots. *Biometrika*, 53(1/2), 151-165. <https://doi.org/10.2307/2334061>
- Bekker, A. J. J. J., & Roux, J. J. J. (2005). Reliability characteristics of the Maxwell distribution: A Bayes estimation study. *Communications in Statistics-Theory and Methods*, 34(11), 2169-2178. <https://doi.org/10.1080/STA-200066424>
- Bhaumik, D. K., Kapur, K., & Gibbons, R. D. (2009). Testing parameters of a gamma distribution for small samples. *Technometrics*, 51(3), 326-334. <https://doi.org/10.1198/tech.2009.07038>
- Broyden, C. G. (1967). Quasi-Newton methods and their application to function minimisation. *Mathematics of Computation*, 21(99), 368-381. <https://doi.org/10.2307/2003239>
- Chen, X., Zhang, K., Ji, Z., Shen, X., Liu, P., Zhang, L., & Yao, J. (2023). Progress and challenges of integrated machine learning and traditional numerical algorithms: taking reservoir numerical simulation as an example. *Mathematics*, 11(21), 4418.
- Davidon, W. C. (1991). Variable metric method for minimization. *SIAM Journal on Optimization*, 1(1), 1-17. <https://doi.org/10.1137/0801001>
- Dey, S., & Maiti, S. S. (2010). Bayesian estimation of the parameter of Maxwell distribution under different loss functions. *Journal of Statistical Theory and Practice*, 4(2), 279-287. <https://doi.org/10.1080/15598608.2010.10411986>
- Dey, S., Dey, T., Ali, S., & Mulekar, M. S. (2016). Two-parameter Maxwell distribution: Properties and different methods of estimation. *Journal of Statistical Theory and Practice*, 10(2), 291-310. <https://doi.org/10.1080/15598608.2015.1135090>
- Faouri, A. O., & Kasap, P. (2023). Maximum likelihood estimation for the nakagami distribution using particle swarm optimization algorithm with applications. *Necmettin Erbakan Üniversitesi Fen ve Mühendislik Bilimleri Dergisi*, 5(2), 209-218.
- Fletcher, R., & Powell, M. J. (1963). A rapidly convergent descent method for minimization. *The computer journal*, 6(2), 163-168. <https://doi.org/10.1093/comjnl/6.2.163>
- Gao, F., & Han, L. (2012). Implementing the Nelder-Mead simplex algorithm with adaptive parameters. *Computational Optimization and Applications*, 51(1), 259-277. <http://dx.doi.org/10.1007/s10589-010-9329-3>
- Golberg, D. E. (1989). Genetic algorithms in search, optimization, and machine learning. *Addison wesley*, 1989(102), 36.
- Holland John, H. (1975). *Adaptation in natural and artificial systems*. Ann Arbor: University of Michigan Press.
- Hernandez, H. (2017). Standard Maxwell-Boltzmann distribution: definition and properties. *ForsChem Research Reports*, 2, 2017-2. <https://doi.org/10.13140/RG.2.2.29888.74244>
- Júnior, S. F. A. X., Xavier, É. F. M., da Silva Jale, J., de Oliveira, T. A., & Sabino, A. L. C. (2020). An application of Particle Swarm Optimization (PSO) algorithm with daily precipitation data in Campina Grande, Paraíba, Brazil. *Research, Society and Development*, 9(8), e444985841-e444985841 <https://doi.org/10.33448/rsd->

- v9i8.5841
- Kachitvichyanukul, V. (2012). Comparison of three evolutionary algorithms: GA, PSO, and DE. *Industrial Engineering and Management Systems*, 11(3), 215-223. <https://doi.org/10.7232/iems.2012.11.3.215>
- Karakoca, A., & Pekkör, A. (2019). Maximum likelihood estimation of the parameters of progressively type-2 censored samples from weibull distribution using genetic algorithm. *Academic Platform-Journal of Engineering and Science*, 7(2), 189-199. <https://doi.org/10.21541/apjes.452564>
- Kasap, P., & Faouri, A. O. (2024). Comparison of the meta-heuristic algorithms for maximum likelihood estimation of the exponentially modified logistic distribution. *Symmetry*, 16(3), 259.
- Kennedy, J., & Eberhart, R. (1995, November). Particle swarm optimization. In *Proceedings of ICNN'95-international conference on neural networks* (Vol. 4, pp. 1942-1948). IEEE. <https://doi.org/10.1109/ICNN.1995.488968>
- Krishna, H., & Malik, M. (2012). Reliability estimation in Maxwell distribution with progressively type-II censored data. *Journal of Statistical Computation and Simulation*, 82(4), 623-641. <http://dx.doi.org/10.1080/00949655.2010.550291>
- Kucukdeniz, T., & Esnaf, S. (2018). Hybrid revised weighted fuzzy c-means clustering with Nelder-Mead simplex algorithm for generalized multisource Weber problem. *Journal of Enterprise Information Management*, 31(6), 908-924.
- Maghami, M. M., & Bahrami, M. (2020). Improved maximum likelihood estimation of parameters in the Maxwell distribution. *Journal of Statistical Modelling: Theory and Applications*, 1(2), 99-113.
- Martinez, J. M. (2000). Practical quasi-Newton methods for solving nonlinear systems. *Journal of computational and Applied Mathematics*, 124(1-2), 97-121. [https://doi.org/10.1016/S0377-0427\(00\)00434-9](https://doi.org/10.1016/S0377-0427(00)00434-9)
- Maxwell, J. C. (1860). V. Illustrations of the dynamical theory of gases.—Part I. On the motions and collisions of perfectly elastic spheres. *The London, Edinburgh, and Dublin Philosophical Magazine and Journal of Science*, 19(124), 19-32. <https://doi.org/10.1080/14786446008642818>
- Maxwell, J. C. (1867). IV. On the dynamical theory of gases. *Philosophical transactions of the Royal Society of London*, (157), 49-88. <https://doi.org/10.1098/rstl.1867.0004>
- Miura, K. (2011). An introduction to maximum likelihood estimation and information geometry. *Interdisciplinary*
- Nelder, J. A., & Mead, R. (1965). A simplex method for function minimization. *The computer journal*, 7(4), 308-313. <https://doi.org/10.1093/comjnl/7.4.308>
- Omar, M. H., Arafat, S. Y., Hossain, M. P., & Riaz, M. (2021). Inverse Maxwell Distribution and Statistical Process Control: An Efficient Approach for Monitoring Positively Skewed Process. *Symmetry*, 13(2), 189. <https://doi.org/10.3390/sym13020189>
- Pasha, G. R., Aslam, M., & Javed, M. (2006). Deviation of the Variances of Classical Estimators and Negative Integer Moment Estimator from Minimum Variance Bound with Reference to Maxwell Distribution. *Pakistan Journal of Statistics and Operation Research*, 145-150. <https://doi.org/10.18187/pjsor.v2i2.98>
- Prataviera, F., Ortega, E. M., & Cordeiro, G. M. (2020). A new bimodal Maxwell regression model with engineering applications. *Applied Mathematics & Information Sciences*, 14, 817-31. <http://dx.doi.org/10.18576/amis/140509>
- Puthenpura, S., & Sinha, N. K. (1986). Modified maximum likelihood method for the robust estimation of system parameters from very noisy data. *Automatica*, 22(2), 231-235. [https://doi.org/10.1016/0005-1098\(86\)90085-3](https://doi.org/10.1016/0005-1098(86)90085-3)
- Ren, C., An, N., Wang, J., Li, L., Hu, B., & Shang, D. (2014). Optimal parameters selection for BP neural network based on particle swarm optimization: A case study of wind speed forecasting. *Knowledge-based systems*, 56, 226-239. <https://doi.org/10.1016/j.knosys.2013.11.015>
- Salehizadeh, S. M. A., Yadmellat, P., & Menhaj, M. B. (2009, March). Local optima avoidable particle swarm optimization. In *2009 IEEE Swarm Intelligence Symposium* (pp. 16-21). IEEE. <https://doi.org/10.1109/SIS.2009.4937839>
- Shanno, D. F. (1970). Conditioning of quasi-Newton methods for function minimization. *Mathematics of computation*, 24(111), 647-656. <https://doi.org/10.1090/S0025-5718-1970-0274029-X>
- Shukla, K. K. (2019). A comparative study of one parameter lifetime distributions. *Biometrics & Biostatistics International Journal*, 8(4), 111-123. <https://doi.org/10.15406/bbij.2019.08.00280>
- Tahir, M. H., Cordeiro, G. M., Mansoor, M., & ZUBAIR, M. (2015). The Weibull-Lomax distribution: properties and applications. *Hacettepe Journal of Mathematics and Statistics*, 44(2), 455-474. <https://doi.org/10.15672/HJMS.2014147465>
- Tyagi, R. K., & Bhattacharya, S. K. (1989a). Bayes estimation of the Maxwell's velocity distribution function. *Statistica*, 29(4), 563-567.
- Tyagi, R. K., & Bhattacharya, S. K. (1989b). A note on the MVU estimation of reliability for the Maxwell failure distribution. *Estadística*, 41(137), 73-79.
- Vaughan, D. C. (1992). On the Tiku-Suresh method of estimation. *Communications in Statistics-theory and Methods*, 21(2), 451-469. <https://doi.org/10.1080/03610929208830788>
- Whitley, D. (1994). A genetic algorithm tutorial. *Statistics and computing*, 4(2), 65-85. <https://doi.org/10.1007/BF00175354>
- Yalçınkaya, A., Şenoğlu, B., & Yolcu, U. (2018). Maximum likelihood estimation for the parameters of skew normal distribution using genetic algorithm. *Swarm and Evolutionary Computation*, 38, 127-138. <https://doi.org/10.1016/j.swevo.2017.07.007>

APPENDIX

**Table 1:** Simulated Mean, Bias, Variance, MSE, and Def values when  $\mu=0, \sigma=1$ .

	$\mu=0, \sigma=1$	Mean	Bias	Variance	MSE	Mean	Bias	Variance	MSE	Def	$\overline{Iter}$	$\overline{Time}$
10	PSO	0.1564	0.1564	<b>0.0301</b>	<b>0.0546</b>	0.8711	-0.1289	<b>0.0287</b>	<b>0.0453</b>	<b>0.0999</b>	48	0.1644
	NM	0.1229	0.1229	0.0493	0.0644	0.8955	-0.1045	0.0425	0.0534	0.1178	64	0.0058
	QN	<b>0.1048</b>	<b>0.1048</b>	0.0509	0.0619	<b>0.9084</b>	<b>-0.0916</b>	0.0438	0.0522	0.1141	<b>5</b>	<b>0.0053</b>
20	PSO	0.1027	0.1027	<b>0.0155</b>	<b>0.0260</b>	0.9154	-0.0846	<b>0.0164</b>	<b>0.0236</b>	<b>0.0496</b>	48	0.1644
	GA	0.1130	0.1130	0.0184	0.0312	0.9078	-0.0922	0.0173	0.0258	0.0570	77	0.2124
	NM	0.0804	0.0804	0.0237	0.0302	0.9321	-0.0679	0.0206	0.0252	0.0554	64	0.0058
30	PSO	0.0800	0.0800	<b>0.0096</b>	<b>0.0160</b>	0.9394	-0.0606	<b>0.0105</b>	<b>0.0142</b>	<b>0.0302</b>	47	0.1797
	GA	0.0885	0.0885	0.0119	0.0197	0.9333	-0.0667	0.0115	0.0159	0.0357	76	0.2217
	NM	0.0687	0.0687	0.0151	0.0198	0.9480	-0.0520	0.0138	0.0165	0.0363	63	0.0058
50	PSO	0.0572	0.0572	<b>0.0057</b>	<b>0.0090</b>	0.9533	-0.0467	<b>0.0060</b>	<b>0.0082</b>	<b>0.0172</b>	46	0.3535
	GA	0.0632	0.0632	0.0069	0.0109	0.9489	-0.0511	0.0067	0.0093	0.0202	76	0.4302
	NM	0.0595	0.0595	0.0103	0.0138	0.9517	-0.0483	0.0085	0.0108	0.0247	62	0.0121
100	PSO	0.0372	0.0372	<b>0.0028</b>	<b>0.0042</b>	0.9715	-0.0285	<b>0.0032</b>	<b>0.0040</b>	<b>0.0082</b>	47	0.2236
	GA	0.0415	0.0415	0.0034	0.0051	0.9683	-0.0317	0.0036	0.0046	0.0097	76	0.2606
	NM	0.0695	0.0695	0.0072	0.0120	0.9477	-0.0523	0.0055	0.0082	0.0203	61	0.0076
250	PSO	0.0213	0.0213	<b>0.0009</b>	<b>0.0014</b>	0.9831	-0.0169	<b>0.0011</b>	<b>0.0014</b>	<b>0.0027</b>	46	0.2905
	GA	0.0234	0.0234	0.0011	0.0016	0.9815	-0.0185	0.0013	0.0016	0.0033	75	0.3153
	NM	0.0920	0.0920	0.0049	0.0134	0.9307	-0.0693	0.0033	0.0081	0.0215	59	0.0098
500	PSO	0.0141	0.0141	<b>0.0004</b>	<b>0.0006</b>	0.9893	-0.0107	<b>0.0006</b>	<b>0.0007</b>	<b>0.0013</b>	45	0.3739
	GA	0.0151	0.0151	0.0005	0.0007	0.9886	-0.0114	0.0006	0.0007	0.0015	74	0.3734
	NM	0.1059	0.1059	0.0044	0.0156	0.9211	-0.0789	0.0027	0.0089	0.0245	57	0.0148
	QN	<b>0.0039</b>	<b>0.0039</b>	0.0009	0.0009	<b>0.9969</b>	<b>-0.0031</b>	0.0008	0.0008	0.0017	4	<b>0.0071</b>

**Table 2:** Simulated Mean, Bias, Variance, MSE, and Def values when  $\mu=1, \sigma=1$ .

$n$	Algoritma	$\hat{\mu}$				$\hat{\sigma}$				Def	$\overline{Iter}$	$\overline{Time}$
		Mean	Bias	Variance	MSE	Mean	Bias	Variance	MSE			
10	PSO	0.4500	-0.5500	0.2898	0.5923	1.1968	0.1968	0.0854	0.1242	0.7165	43.3835	0.2431
	GA	<b>0.6094</b>	<b>-0.3906</b>	0.3007	<b>0.4533</b>	<b>1.1014</b>	<b>0.1014</b>	0.0792	<b>0.0894</b>	<b>0.5427</b>	77.2170	0.2891
	NM	-0.5045	-1.5045	0.2256	2.4892	1.8483	0.8483	0.1043	0.8239	3.3131	64.3280	0.0057
	QN	-0.5808	-1.5808	0.1926	2.6916	1.9026	0.9026	<b>0.0850</b>	0.8998	3.5914	4.3280	0.0049
20	PSO	0.3875	-0.6125	0.2657	0.6409	1.2507	0.2507	0.0792	0.1421	0.7830	42.8830	0.2514
	GA	<b>0.6024</b>	<b>-0.3976</b>	0.2843	<b>0.4424</b>	<b>1.1237</b>	<b>0.1237</b>	0.0765	<b>0.0918</b>	<b>0.5342</b>	76.3650	0.3005
	NM	-0.5507	-1.5507	0.1074	2.5121	1.8947	0.8947	0.0592	0.8598	3.3719	63.3000	0.0060
	QN	-0.6612	-1.6612	0.0596	2.8191	1.9746	0.9746	0.0282	0.9781	3.7972	4.1475	0.0050
30	PSO	0.3779	-0.6221	0.2664	0.6534	1.2609	0.2609	0.0811	0.1492	0.8026	42.6250	0.2670
	GA	<b>0.6226</b>	<b>-0.3774</b>	0.2872	<b>0.4296</b>	<b>1.1168</b>	<b>0.1168</b>	0.0801	<b>0.0937</b>	<b>0.5233</b>	77.2630	0.3260
	NM	-0.5242	-1.5242	0.1002	2.4234	1.8788	0.8788	0.0564	0.8287	3.2521	62.1020	0.0061
	QN	-0.6712	-1.6712	0.0368	2.8297	1.9857	0.9857	0.0173	0.9889	3.8185	4.3190	0.0053
50	PSO	0.3169	-0.6831	0.2440	0.7106	1.3019	0.3019	0.0737	0.1649	0.8755	41.8845	0.2575
	GA	<b>0.6312</b>	<b>-0.3688</b>	0.2880	<b>0.4240</b>	<b>1.1182</b>	<b>0.1182</b>	0.0819	<b>0.0959</b>	<b>0.5199</b>	76.6295	0.3225
	NM	-0.4551	-1.4551	0.1161	2.2332	1.8298	0.8298	0.0673	0.7558	2.9890	59.2225	0.0068
	QN	-0.6908	-1.6908	0.0208	2.8795	2.0015	1.0015	0.0101	1.0131	3.8926	6.3730	0.0057
100	PSO	0.2844	-0.7156	0.2344	0.7465	1.3264	0.3264	0.0736	0.1801	0.9266	41.6075	0.2813
	GA	<b>0.6477</b>	<b>-0.3523</b>	0.2927	<b>0.4169</b>	<b>1.1144</b>	<b>0.1144</b>	0.0889	<b>0.1020</b>	<b>0.5188</b>	77.7595	0.3571
	NM	-0.3236	-1.3236	0.1245	1.8763	1.7356	0.7356	0.0712	0.6122	2.4886	53.9095	0.0096
	QN	-0.7010	-1.7010	0.0106	2.9038	2.0114	1.0114	0.0049	1.0278	3.9316	4.9035	0.0062
250	PSO	0.1828	-0.8172	0.1703	0.8382	1.3906	0.3906	0.0561	0.2087	1.0469	40.4855	0.3234
	GA	<b>0.6684</b>	<b>-0.3316</b>	0.2987	<b>0.4086</b>	<b>1.1082</b>	<b>0.1082</b>	0.0962	<b>0.1079</b>	<b>0.5165</b>	78.1880	0.4149
	NM	-0.1810	-1.1810	0.1013	1.4962	1.6320	0.6320	0.0557	0.4552	1.9513	48.7935	0.0118
	QN	-0.7060	-1.7060	0.0039	2.9142	2.0167	1.0167	0.0018	1.0355	3.9497	4.9205	0.0065
500	PSO	0.1259	-0.8741	0.1239	0.8879	1.4256	0.4256	0.0419	0.2230	1.1109	39.7900	0.3949
	GA	<b>0.6793</b>	<b>-0.3207</b>	0.2936	<b>0.3964</b>	<b>1.1025</b>	<b>0.1025</b>	0.0956	<b>0.1062</b>	<b>0.5026</b>	78.7870	0.5216
	NM	-0.1494	-1.1494	0.0900	1.4111	1.6094	0.6094	0.0492	0.4205	1.8316	47.2120	0.0151
	QN	-0.7077	-1.7077	0.0020	2.9183	2.0188	1.0188	0.0010	1.0390	3.9573	5.4170	0.0069

**Table 3:** Simulated Mean, Bias, Variance, MSE, and Def values when  $\mu=1, \sigma=2$ .

n	Algoritma	$\hat{\mu}$				$\hat{\sigma}$				Def	$\overline{Iter}$	$\overline{Time}$
		Mean	Bias	Variance	MSE	Mean	Bias	Variance	MSE			
10	PSO	<b>1.3783</b>	<b>0.3783</b>	0.2818	0.4249	1.5433	-0.4567	0.1424	0.3510	0.7759	48.1750	0.2485
	GA	1.4286	0.4286	0.1916	<b>0.3753</b>	1.5089	-0.4911	0.1019	<b>0.3431</b>	<b>0.7184</b>	69.7605	0.2671
	NM	0.3223	-0.6777	1.0498	1.5092	<b>2.2860</b>	<b>0.2860</b>	0.5129	0.5947	2.1038	68.4380	0.0060
	QN	0.2524	<b>-0.7476</b>	1.0595	1.6184	2.3367	0.3367	0.5200	0.6334	2.2518	5.4490	0.0058
20	PSO	<b>1.3193</b>	<b>0.3193</b>	0.1612	0.2631	1.5975	-0.4025	0.0813	<b>0.2433</b>	0.5064	47.7480	0.2906
	GA	1.3799	0.3799	0.0873	<b>0.2317</b>	<b>1.5542</b>	<b>-0.4458</b>	0.0452	0.2440	<b>0.4757</b>	69.1095	0.3026
	NM	0.0136	-0.9864	0.5655	1.5385	2.5386	0.5386	0.2964	0.5865	2.1250	65.4665	0.0061
	QN	-0.0872	-1.0872	0.5567	1.7387	2.6143	0.6143	0.2894	0.6668	2.4055	5.0940	0.0053
30	PSO	<b>1.3017</b>	<b>0.3017</b>	0.1312	0.2223	<b>1.6081</b>	<b>-0.3919</b>	0.0704	0.2240	0.4462	47.4780	0.3168
	GA	1.3582	0.3582	0.0612	<b>0.1895</b>	1.5671	-0.4329	0.0345	<b>0.2219</b>	<b>0.4114</b>	69.3300	0.3255
	NM	-0.1420	-1.1420	0.2893	1.5935	2.6577	0.6577	0.1545	0.5870	2.1805	63.2035	0.0058
	QN	-0.2555	-1.2555	0.2629	1.8392	2.7437	0.7437	0.1364	0.6894	2.5286	5.1630	0.0053
50	PSO	<b>1.2734</b>	<b>0.2734</b>	0.1119	0.1866	<b>1.6297</b>	<b>-0.3703</b>	0.0621	0.1993	0.3859	47.7395	0.3423
	GA	1.3320	0.3320	0.0353	<b>0.1455</b>	1.5870	-0.4130	0.0205	<b>0.1910</b>	<b>0.3365</b>	69.1030	0.3428
	NM	-0.2055	-1.2055	0.1187	1.5720	2.7102	0.7102	0.0655	0.5699	2.1419	61.6825	0.0066
	QN	-0.3449	-1.3449	0.0989	1.9077	2.8165	0.8165	0.0515	0.7182	2.6258	5.2395	0.0055
100	PSO	<b>1.2695</b>	<b>0.2695</b>	0.0703	0.1430	<b>1.6279</b>	<b>-0.3721</b>	0.0389	0.1773	0.3203	47.4200	0.3721
	GA	1.3121	0.3121	0.0188	<b>0.1162</b>	1.5969	-0.4031	0.0113	<b>0.1738</b>	<b>0.2899</b>	68.8375	0.3629
	NM	-0.1998	-1.1998	0.0550	1.4944	2.7033	0.7033	0.0331	0.5277	2.0222	58.7150	0.0079
	QN	-0.3829	-1.3829	0.0299	1.9424	2.8435	0.8435	0.0148	0.7263	2.6687	5.8740	0.0060
250	PSO	<b>1.2516</b>	<b>0.2516</b>	0.0548	0.1181	<b>1.6406</b>	<b>-0.3594</b>	0.0295	0.1587	0.2768	47.6015	0.4519
	GA	1.2876	0.2876	0.0089	<b>0.0916</b>	1.6143	-0.3857	0.0052	<b>0.1540</b>	<b>0.2456</b>	69.1105	0.4229
	NM	-0.0970	-1.0970	0.0340	1.2373	2.6269	0.6269	0.0215	0.4146	1.6519	53.0555	0.0112
	QN	-0.3864	-1.3864	0.0106	1.9328	2.8491	0.8491	0.0058	0.7267	2.6595	5.8620	0.0064
500	PSO	<b>1.2404</b>	<b>0.2404</b>	0.0511	0.1089	<b>1.6481</b>	<b>-0.3519</b>	0.0275	0.1513	0.2602	47.3030	0.8843
	GA	1.2773	0.2773	0.0050	<b>0.0819</b>	1.6212	-0.3788	0.0028	<b>0.1463</b>	<b>0.2282</b>	69.2405	0.7616
	NM	-0.0343	-1.0343	0.0201	1.0898	2.5785	0.5785	0.0125	0.3472	1.4370	49.3285	0.0210
	QN	-0.3907	-1.3907	0.0057	1.9398	2.8516	0.8516	0.0033	0.7286	2.6685	5.9590	0.0075

**Table 4:** Simulated Mean, Bias, Variance, MSE, and Def values when  $\mu=2, \sigma=1$ .

n	Algorithm	$\hat{\mu}$				$\hat{\sigma}$				Def	$\overline{Iter}$	$\overline{Time}$
		Mean	Bias	Variance	MSE	Mean	Bias	Variance	MSE			
10	PSO	0.1709	-1.8291	0.2147	3.5604	1.7970	0.7970	0.1078	0.7430	4.3035	41.4535	0.2603
	GA	<b>0.2539</b>	<b>-1.7461</b>	0.3019	<b>3.3508</b>	<b>1.7421</b>	<b>0.7421</b>	0.1172	<b>0.6679</b>	<b>4.0187</b>	79.9150	0.3025
	NM	-0.5220	-2.5220	0.1917	6.5520	2.2890	1.2890	0.1270	1.7886	8.3406	65.9750	0.0060
	QN	-0.5396	-2.5396	0.1839	6.6335	2.3015	1.3015	0.1242	1.8180	8.4515	5.5580	0.0053
20	PSO	0.0516	-1.9484	0.0412	3.8374	<b>1.8842</b>	<b>0.8842</b>	0.0429	0.8246	4.6620	40.4100	0.1811
	GA	<b>0.1124</b>	<b>-1.8876</b>	0.1035	<b>3.6666</b>	1.8446	0.8446	0.0558	<b>0.7692</b>	<b>4.4357</b>	82.2830	0.2526
	NM	-0.6053	-2.6053	0.0817	6.8690	2.3591	1.3591	0.0600	1.9072	8.7762	66.7145	0.0062
	QN	-0.6337	-2.6337	0.0685	7.0048	2.3797	1.3797	0.0525	1.9561	8.9608	4.7425	0.0058
30	PSO	0.0274	-1.9726	0.0171	3.9082	1.9142	0.9142	0.0271	0.8629	4.7711	40.2390	0.1829
	GA	<b>0.0675</b>	<b>-1.9325</b>	0.0432	<b>3.7776</b>	<b>1.8874</b>	<b>0.8874</b>	0.0345	<b>0.8221</b>	<b>4.5997</b>	83.0015	0.2547
	NM	-0.6148	-2.6148	0.0664	6.9035	2.3810	1.3810	0.0463	1.9535	8.8570	67.1320	0.0061
	QN	-0.6591	-2.6591	0.0439	7.1147	2.4131	1.4131	0.0339	2.0307	9.1455	4.6910	0.0053
50	PSO	0.0126	-1.9874	0.0088	3.9586	1.9228	0.9228	0.0167	0.8682	4.8268	40.2900	0.2006
	GA	<b>0.0324</b>	<b>-1.9676</b>	0.0172	<b>3.8888</b>	<b>1.9089</b>	<b>0.9089</b>	0.0189	<b>0.8450</b>	<b>4.7338</b>	85.5275	0.2769
	NM	-0.6277	-2.6277	0.0550	6.9598	2.3891	1.3891	0.0358	1.9653	8.9250	66.2955	0.0071
	QN	-0.6815	-2.6815	0.0248	7.2150	2.4281	1.4281	0.0194	2.0590	9.2740	4.7130	0.0059
100	PSO	0.0036	-1.9964	0.0003	3.9861	1.9304	0.9304	0.0076	0.8732	4.8594	40.1990	0.2143
	GA	<b>0.0167</b>	<b>-1.9833</b>	0.0044	<b>3.9378</b>	<b>1.9212</b>	<b>0.9212</b>	0.0087	<b>0.8573</b>	<b>4.7951</b>	86.6155	0.3022
	NM	-0.5835	-2.5835	0.0727	6.7474	2.3591	1.3591	0.0423	1.8894	8.6367	64.9055	0.0075
	QN	-0.6894	-2.6894	0.0130	7.2459	2.4363	1.4363	0.0098	2.0726	9.3186	6.2960	0.0063
250	PSO	0.0023	-1.9977	0.0023	3.9930	1.9343	0.9343	0.0036	0.8766	4.8696	40.1365	0.2761
	GA	<b>0.0037</b>	<b>-1.9963</b>	0.0009	<b>3.9862</b>	<b>1.9332</b>	<b>0.9332</b>	0.0034	<b>0.8742</b>	<b>4.8604</b>	88.9490	0.3809
	NM	-0.4700	-2.4700	0.1113	6.2123	2.2792	1.2792	0.0609	1.6974	7.9096	61.1335	0.0096
	QN	-0.6978	-2.6978	0.0048	7.2827	2.4455	1.4455	0.0040	2.0933	9.3761	6.1940	0.0066
500	PSO	0.0016	-1.9984	0.0018	3.9955	1.9334	0.9334	0.0021	0.8734	4.8688	40.1100	0.3472
	GA	<b>0.0020</b>	<b>-1.9980</b>	0.0021	<b>3.9942</b>	<b>1.9332</b>	<b>0.9332</b>	0.0020	<b>0.8729</b>	<b>4.8671</b>	90.6585	0.4587
	NM	-0.3702	-2.3702	0.1265	5.7445	2.2050	1.2050	0.0685	1.5206	7.2651	57.5255	0.0131
	QN	-0.7000	-2.7000	0.0025	7.2927	2.4458	1.4458	0.0021	2.0925	9.3852	6.1360	0.0072

**Table 5:** Simulated Mean, Bias, Variance, MSE, and Def values when  $\mu=2, \sigma=2$ .

<i>n</i>	Algorithm	$\hat{\mu}$				$\hat{\sigma}$				Def	$\overline{Iter}$	$\overline{Time}$
		Mean	Bias	Variance	MSE	Mean	Bias	Variance	MSE			
10	PSO	1.1104	-0.8896	1.1697	1.9611	<b>1.9193</b>	<b>-0.0807</b>	0.2730	0.2795	2.2406	43.0340	0.2512
	GA	<b>1.4029</b>	<b>-0.5971</b>	1.0497	<b>1.4063</b>	1.7596	-0.2404	0.2120	<b>0.2699</b>	<b>1.6761</b>	73.5635	0.2893
	NM	-0.9880	-2.9880	0.5801	9.5086	3.2982	1.2982	0.2516	1.9368	11.4454	68.2965	0.0061
	QN	-1.1206	-3.1206	0.4806	10.2190	3.3928	1.3928	0.1904	2.1302	12.3492	5.3160	0.0050
20	PSO	1.1329	-0.8671	1.1462	1.8980	<b>1.9464</b>	<b>-0.0536</b>	0.2733	0.2762	2.1742	42.6110	0.2623
	GA	<b>1.5250</b>	<b>-0.4750</b>	0.9274	<b>1.1530</b>	1.7326	-0.2674	0.1925	<b>0.2641</b>	<b>1.4171</b>	72.4415	0.3032
	NM	-1.0106	-3.0106	0.3514	9.4148	3.3391	1.3391	0.1806	1.9739	11.3888	66.4270	0.0065
	QN	-1.2463	-3.2463	0.1494	10.6878	3.5092	1.5092	0.0565	2.3343	13.0221	6.6040	0.0055
30	PSO	1.1288	-0.8712	1.1566	1.9156	<b>1.9620</b>	<b>-0.0380</b>	0.2804	0.2818	2.1974	42.4375	0.2665
	GA	<b>1.5645</b>	<b>-0.4355</b>	0.9138	<b>1.1035</b>	1.7286	-0.2714	0.2022	<b>0.2758</b>	<b>1.3793</b>	71.7285	0.3079
	NM	-0.9650	-2.9650	0.3626	9.1539	3.3104	1.3104	0.2008	1.9179	11.0718	65.2705	0.0068
	QN	-1.2858	-3.2858	0.0883	10.8849	3.5425	1.5425	0.0339	2.4133	13.2982	5.2700	0.0053
50	PSO	1.0947	-0.9053	1.1844	2.0039	<b>1.9896</b>	<b>-0.0104</b>	0.2978	0.2979	2.3018	42.4375	0.2800
	GA	<b>1.7020</b>	<b>-0.2980</b>	0.7911	<b>0.8799</b>	1.6668	-0.3332	0.1821	<b>0.2931</b>	<b>1.1730</b>	71.3795	0.3242
	NM	-0.8444	-2.8444	0.4063	8.4966	3.2248	1.2248	0.2250	1.7251	10.2217	62.8565	0.0078
	QN	-1.2953	-3.2953	0.0572	10.9159	3.5524	1.5524	0.0198	2.4297	13.3455	5.1490	0.0067
100	PSO	1.1525	-0.8475	1.1959	1.9141	<b>1.9742</b>	<b>-0.0258</b>	0.3152	0.3158	2.2299	42.3335	0.3019
	GA	<b>1.8120</b>	<b>-0.1880</b>	0.6786	<b>0.7139</b>	1.6246	-0.3754	0.1682	<b>0.3092</b>	<b>1.0231</b>	70.9385	0.3466
	NM	-0.5677	-2.5677	0.4418	7.0349	3.0277	1.0277	0.2424	1.2986	8.3335	57.0310	0.0087
	QN	-1.3174	-3.3174	0.0260	11.0313	3.5743	1.5743	0.0105	2.4891	13.5204	5.3150	0.0057
250	PSO	1.1798	-0.8202	1.1820	1.8548	<b>1.9645</b>	<b>-0.0355</b>	0.3259	0.3271	2.1819	42.6730	0.3734
	GA	<b>1.9462</b>	<b>-0.0538</b>	0.4637	<b>0.4666</b>	1.5559	-0.4441	0.1218	<b>0.3190</b>	<b>0.7856</b>	69.8560	0.4079
	NM	-0.2944	-2.2944	0.3233	5.5878	2.8282	0.8282	0.1779	0.8638	6.4516	52.2095	0.0125
	QN	-1.3237	-3.3237	0.0110	11.0576	3.5789	1.5789	0.0051	2.4981	13.5558	5.6160	0.0063
500	PSO	1.1791	-0.8209	1.1786	1.8524	<b>1.9669</b>	<b>-0.0331</b>	0.3318	0.3329	2.1853	42.0765	0.4807
	GA	<b>2.0160</b>	<b>0.0160</b>	0.3264	<b>0.3266</b>	1.5192	-0.4808	0.0904	<b>0.3216</b>	<b>0.6482</b>	69.2880	0.5222
	NM	-0.2240	-2.2240	0.2717	5.2178	2.7751	0.7751	0.1449	0.7457	5.9634	50.8045	0.0160
	QN	-1.3241	-3.3241	0.0087	11.0587	3.5776	1.5776	0.0095	2.4983	13.5569	5.7860	0.0067

**Table 6:** The descriptive statistics for aircraft windshield service time data.

<i>n</i>	<i>Min</i>	1 <sup>st</sup> Qu.	Mean	Mode	Median	3 <sup>rd</sup> Qu.	<i>Max</i>	S <sup>2</sup>	$\gamma_1$	$\gamma_2$
63	0.0460	1.1070	2.0853	0.0460	2.0650	2.8197	5.1400	1.5506	0.4396	2.7326

**Table 7:** The parameter estimates, LL, AIC, AICc, values for aircraft windshield service time data.

Method	$\hat{\mu}$	$\hat{\sigma}$	-LL	AIC	AIC <sub>c</sub>
PSO	0	1.9789	<b>115.4526</b>	<b>234.9052</b>	<b>235.1052</b>
GA	0	1.9789	<b>115.4535</b>	<b>234.9070</b>	<b>235.1070</b>
NM	0.3638	1.7301	125.3900	254.7800	254.9800
QN	0.0413	2.0310	122.7079	249.4158	249.6158

**Table 8:** The descriptive statistics for the vinyl chloride data.

<i>n</i>	<i>Min</i>	1 <sup>st</sup> Qu.	Mean	Mode	Median	3 <sup>rd</sup> Qu.	<i>Max</i>	S <sup>2</sup>	$\gamma_1$	$\gamma_2$
34	0.1000	0.5000	1.8794	0.4000	1.1500	2.500	8.000	3.8126	1.6037	5.0054

**Table 9:** The parameter estimates, LL, AIC, AICc, values for the vinyl chloride data.

Method	$\hat{\mu}$	$\hat{\sigma}$	-LL	AIC	AIC <sub>c</sub>
PSO	0	2.1959	<b>97.3287</b>	<b>198.6574</b>	<b>199.0445</b>
GA	0	2.1959	<b>97.3290</b>	<b>198.6580</b>	<b>199.0451</b>
NM	0.2638	2.0511	113.6900	271.3800	271.7671
QN	0.0679	1.0473	197.6675	399.3350	399.7221

## RESEARCH ARTICLE

### Remote Sensing

# Estimating plant dominance using field-measured structural parameters and remotely sensed data; A case study from Rekawa mangrove forest, southern coast of Sri Lanka

SMTM Samarakoon\*, SK Madarasinghe, NDS Thilakarathne, AMNN Bandularathne, HD Wijayathilaka, and KAS Kodikara

*Department of Botany, Faculty of Science, University of Ruhuna, Matara, Sri Lanka.*

Submitted: 03 May 2024; Revised: 24 September 2024; Accepted: 25 October 2024

**Abstract:** The conventional method of determining plant dominance using the basal area is challenging for inaccessible ecosystems. Thus, the present study aimed to develop a new method to determine plant dominance in such inaccessible ecosystems using a remote sensing (RS) method. The target ecosystem of the study was the Rekawa mangrove forest. In this study, plant dominance was determined using both conventional and RS-based methods for two selected vegetation types in the Rekawa mangrove forest, *i.e.*, monospecific and mixed vegetation stands. Google Earth (GE) satellite images and drone images were used to digitize the crown area using on-screen digitization technique in ArcMap v.10.3. Finally, plant dominance values, determined through the three methods (conventional method, using GE satellite images, and using drone images) were compared in terms of their percentage deviation calculated with reference to the conventional method. This study reveals that there is a weak positive correlation ( $P < 0.05$ ,  $r = 0.132$ ) between basal area and individual tree crown area in a mangrove forest. Moreover, for both mangrove vegetation types, the drone imagery method has shown the least average percentage deviation in determination of plant dominance, compared to that of the GE satellite imagery method. For instance, the drone imagery method could be used with 100% and 86.02% average accuracies respectively for monospecific and mixed mangrove vegetation, whereas the GE satellite imagery method could be used with 97.85% and 42.15% average accuracies, respectively for monospecific and mixed mangrove vegetation. Therefore, this RS-based method could be used as an alternative method to the conventional basal area-based method of determining plant dominance in dense mangrove forests.

**Keywords:** Crown area, drone imagery, Google Earth satellite imagery, plant dominance, Rekawa mangrove forest, remote sensing.

## INTRODUCTION

Plant dominance refers to the relative importance of a plant species in terms of the degree of influence it exerts on other plants and animals of the community (Pau & Dee, 2016). It delineates stronger links to ecological research, as it reflects the context of an ecological community. According to Pau & Dee (2016), tracking dominance facilitates early warning signs of ecosystem changes due to climate change impacts or any other impact on the ecosystem. Conventionally, plant dominance is determined by a field-based method using plant basal area. Here, the circumference at the tree base is measured by conducting a field survey. Field work becomes challenging in an inaccessible ecosystem such as a dense forest, mangrove forest, or swamp, due to certain limitations such as inundation, boggy substrate, thick cover, intensive labour and time-consuming procedures. Particularly, the harsh environment in mangrove ecosystems makes the field measurements more challenging (Wanga *et al.*, 2019), especially in the middle and water edges of mangrove forests. Hence it is necessary to develop a new method that can readily be used in determination of plant dominance in such inaccessible

\* Corresponding author ([madusamarakoon29@gmail.com](mailto:madusamarakoon29@gmail.com);  <https://orcid.org/0009-0004-2655-8990>)



This article is published under the Creative Commons CC-BY-ND License (<http://creativecommons.org/licenses/by-nd/4.0/>). This license permits use, distribution and reproduction, commercial and non-commercial, provided that the original work is properly cited and is not changed in anyway.

areas. Remote sensing (RS) methods are being widely used nowadays by the ecologists and field researchers for finding new ways to approach their research (Kerr & Ostrovsky, 2003). Therefore, the aim of this study is to develop a new method to determine plant dominance in such inaccessible ecosystems using a more feasible RS method. In this case, an RS-based approach could be a good solution to overcome the above-mentioned limitations faced in accessing and taking measurements in the mangrove ecosystems.

Even though, plenty of studies have addressed different types of biodiversity measures (Purvis & Hector, 2000; Hillebrand *et al.*, 2008) using RS, RS-based studies focused on plant dominance still remains as a gap (Pau & Dee, 2016). Therefore, this study attempts to fill the knowledge gap on the determination of plant dominance, using RS-based methods with the use of a mangrove forest as a model ecosystem, where accessibility is challenging.

According to previous studies, much of the literature related to biodiversity has focused on species richness but literature on plant dominance is lacking (Purvis & Hector, 2000; Hillebrand *et al.*, 2008). According to the literature, many RS studies have been conducted to detect

species richness (Warren *et al.*, 2014; Pau & Dee, 2016) and species distributions (Pau *et al.*, 2013; He *et al.*, 2015). Moreover, different RS approaches have been practiced by researchers, including satellite and aerial RS (Nagendra, 2001; Turner *et al.*, 2003; Gillespie *et al.*, 2008) in order to track the biodiversity and ecosystem functions. Although there is limited scientific attention on RS studies focused on plant dominance, Pau & Dee (2016) have shown that there are some studies that address shifts in dominant vegetation (Schroeder *et al.*, 2010) and species invasions (Schroeder *et al.*, 2010).

When mangrove ecosystems are taken into consideration, RS techniques have been applied in different studies in order to study various aspects including measuring their spatial extent (Long & Skewes, 1996; Conchedda *et al.*, 2008; Nandy & Kushwaha, 2011; Purnamasayangsukasih *et al.*, 2016) and vegetation dynamics (Madarasinghe *et al.*, 2020a; 2020b). However, no literature is available on using RS methods to estimate the plant dominance in mangrove ecosystems and therefore this study will offer a novel approach for scientists and researchers in the field of Ecology when conducting research in such inaccessible mangrove ecosystems.

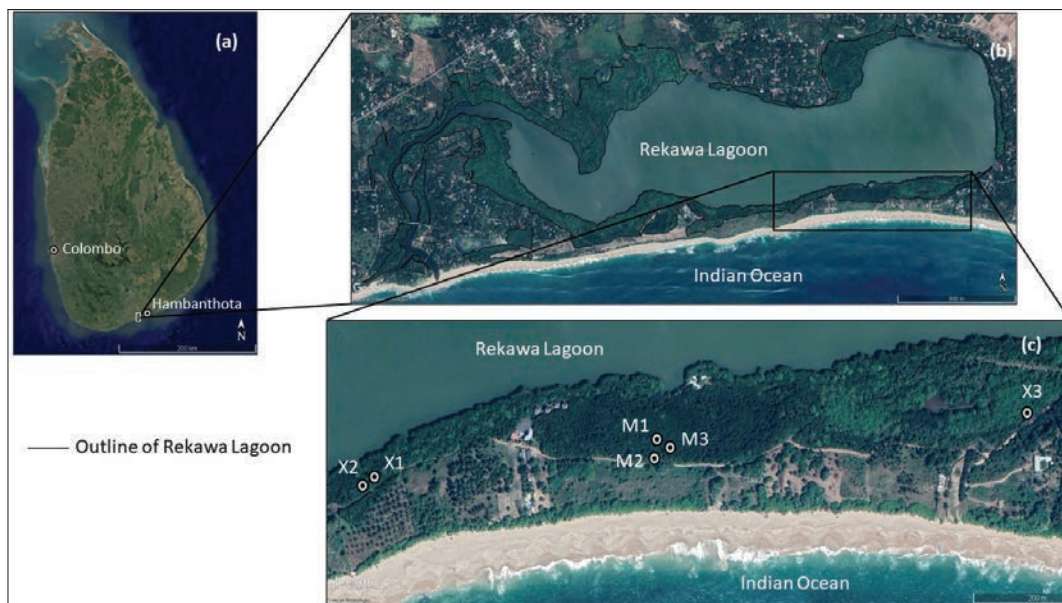


**Figure 1:** (a) Map of Sri Lanka showing the location of the study area indicated by a white square; (b) Map of Rekawa lagoon showing the study area indicated by a black square; (c) Google Earth (GE) satellite image (Maxar Technologies on 22.01.2022) of the study area showing mono-specific vegetation plots (M1: Mono-specific vegetation plot No.1, M2: Mono-specific vegetation plot No.2, M3: Mono-specific vegetation plot No.3) and mixed mangrove vegetation plots (X1: Mixed vegetation plot No.1, X2: Mixed vegetation plot No.2, X3: Mixed vegetation plot No.3)

**MATERIALS AND METHODS**

**Study site**

Since mangrove forests are among the most productive ecosystems with high biodiversity and significant degree of inaccessibility, a mangrove forest was selected as the target ecosystem in this study. The Rekawa mangrove forest, which is considered as one of the most untouched mangrove forests in southern Sri Lanka, consists of high mangrove biodiversity

including 11 true mangrove species and 14 mangrove associates (Jayatissa *et al*, 2002). This mangrove diversity has led to the establishment of both mixed vegetation stands and monospecific vegetation stands in the same mangrove forest. Therefore, the Rekawa mangrove forest associated with the Rekawa lagoon (coordinates 6° 2' 59.784" N and 80°50' 30.2244" E; De Silva & Amarasinghe, 2021), in the Tangalle District Secretariat Division in the Hambantota District in the southern coast of Sri Lanka, was taken as a model site in the present study.

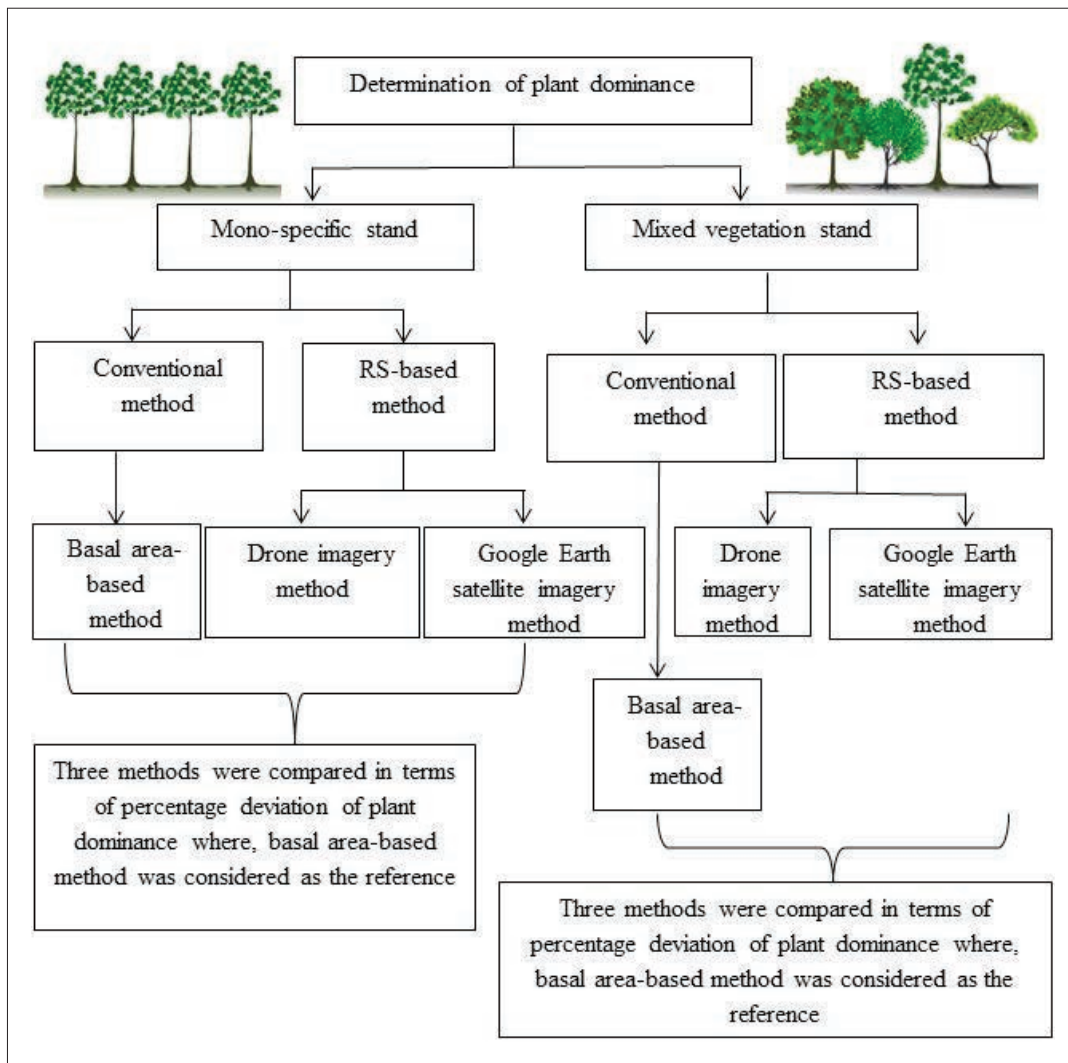


**Figure 2:** Flow chart showing the summary of methods followed in the study.

## Data collection

### Field data collection

According to previous research studies and ground observations two sampling sites were selected representing the two mangrove vegetation types available in Rekawa lagoon, *i.e.*, monospecific mangrove vegetation and mixed mangrove vegetation. Here, Mangrove patches having more than three different species were considered as mixed-species sites and sites which have only one species or mainly one species with few trees of another mangrove species were considered as monospecific/monodominant site.

Then, three quadrats, where each quadrat was 20 m × 20 m in size, were plotted for each type of mangrove vegetation, following the stratified random sampling method using a grid map of Rekawa lagoon and a random number table. Ground truthing was carried out during the field survey. In order to increase the accuracy of GPS coordinates, each corner of all six plots was manually related to a tree or landmark(s) which are clearly identifiable in both drone images and GE satellite images. Circumference at the tree base, diameter at breast height (DBH), tree height, and individual tree crown area in each plot were then measured. Tree height was estimated by ocular method while DBH was measured using a diameter tape. According to Fadrique *et al.* (2021), only the mangrove plants with DBH ≥ 10 cm were taken in to account in this case. Circumference at the tree base was measured to calculate the basal area which is used when calculating plant dominance. Photograph(s) covering the whole individual tree crown area of each plant was captured by using a smartphone (Redmi Note 11) with the aid of a reference scale and the reference scale was held at 1.3 m height from ground level with the help of a tripod. Then, individual tree crown areas were measured using ImageJ v.2006 software. Here, polygons were sketched according to the crown shape and area measurement tool was used to calculate the individual crown area. The exact individual crown area of each species in each plot was extrapolated by using the above crown area measurements (calculated via ImageJ v.2006) and tree height.

### Remote sensing - based data collection

Four drone images (obtained from DJI Mavic Air 2 on 08.09.2022) and three GE satellite images (Maxar Technologies on 22.01.2022), which delineate the studied plots were used in this study (see Figure 1). Drone images of each plot were captured at an altitude of 50 m. The GE

satellite image for mono specific plots, *i.e.*, M1, M2 and M3 (see Figure 1) were downloaded at an eye altitude of 146 m, whereas mixed vegetation plots, *i.e.*, X1 and X2 at 203 m and X3 (see Figure 1) at a 161 m eye altitude. The aforementioned images were downloaded at the best eye altitude that shows crown attributes for identification of different species of the particular plot. All these drone images and GE satellite images were geo-referenced on ArcMap v.10.3 using ground control points obtained from GPS (eTrex Garmin 10). Thereafter, the crown area of each species was digitized and the generated map of each plot was validated with ground truthing. Then the crown area values of each species in each plot were measured. Similarly, species-wise crown area measurements were estimated for both drone images and GE satellite images of each plot. As the location of each plant in the plot was validated with ground truthing, the error/accuracy values are given due to the errors in mapping the crowns.

## Determination of plant dominance

### Conventional method

The basal area for each tree (DBH ≥ 10 cm) was calculated using circumference at tree base data obtained from field surveys. Then the correlation between the basal area and the individual tree crown area (obtained by analyzing the photograph(s) on ImageJ v.2006 software) of mangrove species was checked and a regression equation was formulated. The original equation of plant dominance is given in Equation 1, while the formulated regression equation is given in Equation 2.

$$\text{Plant dominance} = \frac{\text{Basal area of the species}}{\text{Total basal area of all species}} \quad \dots(1)$$

$$\text{Individual tree crown area} = 5.67(\text{Basal area}) + 1303.5 \quad \dots(2)$$

Plant dominance was calculated for all the mangrove species of each plot by following the three methods; conventional method (using basal area- Equation 1), drone imagery method and GE satellite imagery method.

### Remote sensing-based methods

“Basal area” in the original equation of plant dominance (Equation 1) was replaced by substituting the formulated regression equation and plant dominance was calculated. Here, crown area statistics for each mangrove species obtained by on-screen digitization of drone images

and GE satellite images on ArcMap v.10.3 were used as individual tree crown area. Plant dominance values obtained from all three methods (conventional method, drone imagery method and GE satellite imagery method) were compared and percentage deviations and average percentage deviations of RS-based methods (drone imagery method and GE satellite imagery method) were calculated taking the conventional method as the reference. Here, percentage deviations and average percentage deviations of plant dominance were calculated according to the mangrove species studied and the type of mangrove vegetation, respectively.

### Data Analysis

As this is a preliminary study, we just wanted to show what the level of accuracy is, of using remote sensing methods to determine plant dominance. Therefore, all raw data collected for each parameter were checked for parametric assumptions. The Shapiro-Wilk normality test was performed to check the normality of the data. The data were then transformed to log values, square root values and arc-sin values and normality was checked. As the data were not normally distributed even under such transformation, nonparametric analysis was selected. Therefore, the Spearman rank correlation test was performed to check whether there is a significant correlation between the basal area and the individual tree crown area as Spearman correlation is strong enough to study the correlation between the real basal area and the crown area. When mentioning the accuracy of using remote sensing methods (X %), (100-X) is the error of the method. That is mentioned for each method (ground truthing was conducted for each plot) and to increase the clarity, a new text was added to mention the error of each.

The statistical significance of analyses was considered at a 95% confidence interval and  $P < 0.05$ . All the statistical analyses were performed using R.4.2.3 statistical software whereas ArcMap v.10.3 area statistics were used to measure mangrove tree crown area in drone images and GE satellite images.

## RESULTS AND DISCUSSION

Maps of crown area of monospecific and mixed mangrove vegetation created using ArcMap v.10.3 are shown in Figures 3 and 4. Despite the presence of *Excoecaria agallocha* in the M2 plot, *Ceriops tagal* dominated in all three monospecific vegetation plots (M1, M2, M3). The crown area of *C. tagal* is 370 m<sup>2</sup>,

248 m<sup>2</sup> and 350 m<sup>2</sup> respectively for the M1, M2 and M3 plots. Hence, monospecific vegetation is dominated by *C. tagal*. Regarding mixed vegetation stands (X1, X2, X3), six true mangrove species *Avicennia marina*, *Bruguiera gymnorrhiza*, *C. tagal*, *E. agallocha*, *Lumnitzera racemosa*, and *Rhizophora mucronata* were found. *B. gymnorrhiza* dominated in X1 with a crown area of 81 m<sup>2</sup>, while *C. tagal* dominated in X2 with a 140 m<sup>2</sup> crown area. The X3 plot was dominated by *A. marina* with a 318 m<sup>2</sup> crown area. The total area of the plot could not be occupied by the tree crowns due to two main reasons, viz., the presence of dead crowns and trees (specially *C. tagal*) and leaning trees and crowns.

Plant dominance values calculated using the three methods (conventional method, drone imagery method, and GE satellite imagery method) are shown in Table 1. According to the results, the drone imagery method can be used without an error and with 13.98% average error, for monospecific mangrove vegetation and mixed mangrove vegetation respectively, whereas, the GE satellite imagery method can be used with 2.15% and 57.85% average error for monospecific mangrove vegetation and mixed mangrove vegetation, respectively.

Plant dominance values for both monospecific and mixed vegetation stands determined by RS-based methods (drone imagery method and GE satellite imagery method) have deviated from the conventional method because, in RS-based methods, only the surface attributes of the vegetation are detected. This may lead to underestimation of plant dominance. For both vegetation types in the mangrove forest, the drone imagery method has shown the least average percentage deviation in determination of plant dominance, compared to the GE satellite imagery method, because drone imagery possesses high resolution compared to GE satellite imagery.

Considering the determination of plant dominance in mangrove forests by the drone imagery method, monospecific vegetation has exhibited results almost similar to the conventional method, while mixed vegetation stands have exhibited a deviation from the conventional method. Results indicate that, under RS-based methods, monospecific vegetation has shown less error in the determination of plant dominance than mixed vegetation stands. It is evident that monospecific vegetation possesses a simple structure without (or with less) stratification and low biodiversity, whereas mixed vegetation possesses a complex community structure with a high level of stratification, overlapped tree crowns and high biodiversity. Hence, detection of the understory



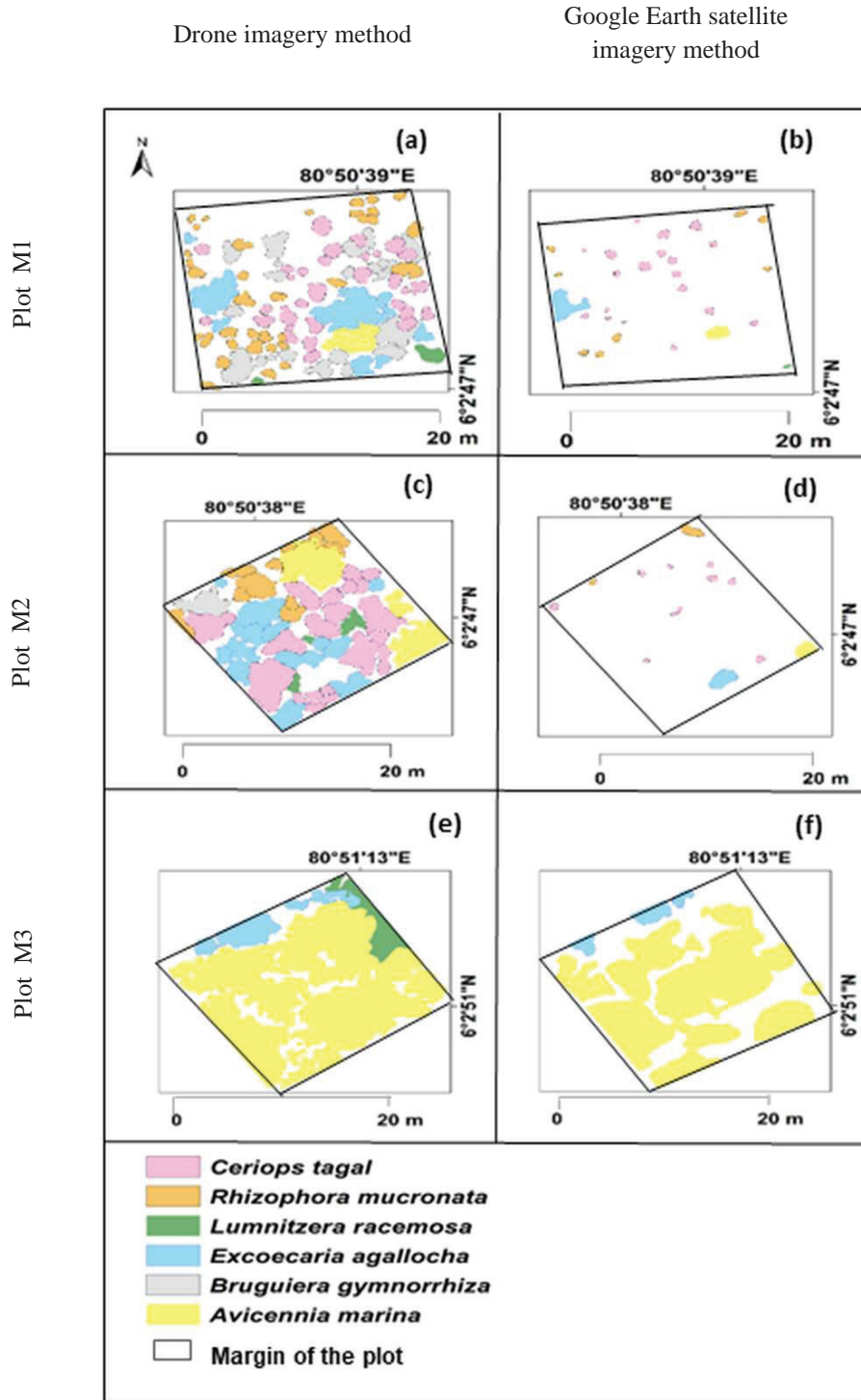


**Figure 4:** Maps showing the crown area of mangrove species in each mixed plot according to the drone imagery method and Google Earth satellite imagery method.

**Table 1:** Plant dominance values for each plot (species-wise) determined by the imagery method.

Plot	species	Plant dominance			Percentage deviation of plant dominance from conventional method (%)	
		Conventional method	Drone imagery method	Google Earth satellite imagery method	Drone imagery method	Google Earth satellite imagery method
M1	<i>Ceriops tagal</i>	1	1	1	0%	0%
M2	<i>Ceriops tagal</i>	0.62	0.62	0.61	0%	6%
	<i>Excoecaria agallocha</i>	0.38	0.38	0.37	0%	2.6%
M3	<i>Ceriops tagal</i>	1	1	1	0%	0%
X1	<i>Bruguiera gymnorrhiza</i>	0.27	0.27	0	0%	100%
	<i>Excoecaria agallocha</i>	0.27	0.23	0.07	14.8%	74%
	<i>Ceriops tagal</i>	0.22	0.22	0.13	0%	41%
	<i>Rhizophora mucronata</i>	0.16	0.16	0.12	0%	25%
	<i>Avicennia marina</i>	0.06	0.06	0.03	0%	50%
	<i>Avicennia officinalis</i>	0.01	0	0	100%	100%
	<i>Lumnitzera racemosa</i>	0.01	0.01	0.01	0%	0%
	<i>Ceriops tagal</i>	0.40	0.40	0.29	0%	28%
X2	<i>Excoecaria agallocha</i>	0.30	0.23	0.10	23.3%	67%
	<i>Rhizophora mucronata</i>	0.14	0.10	0.07	28.6%	50%
	<i>Avicennia marina</i>	0.09	0.09	0.08	0%	11.1%
	<i>Bruguiera gymnorrhiza</i>	0.04	0.04	0	0%	100%
	<i>Lumnitzera racemosa</i>	0.03	0.03	0	0%	100%
X3	<i>Avicennia marina</i>	0.89	0.86	0.85	3.4%	4.5%
	<i>Lumnitzera racemosa</i>	0.07	0.05	0	28.6%	100%
	<i>Excoecaria agallocha</i>	0.04	0.03	0.01	25%	75%

Source: based on data analysis.

(M1: Monospecific vegetation plot No.1, M2: Monospecific vegetation plot No.2, M3: Monospecific vegetation plot No.3, X1: Mixed vegetation plot No.1, X2: Mixed vegetation plot No.2, X3: Mixed vegetation plot No.3)

by the RS-based method is interrupted due to the presence of strata at different levels and overlapped crowns. Therefore, crown area in mixed vegetation stands has been underestimated. As a result, plant dominance has also been underestimated in mixed vegetation stands. Therefore, determination of plant dominance using the drone imagery method for mixed vegetation stands in mangrove forests showed an average error of 13.98%. Moreover, the effect of wind and leaning trees also provide reasons for the underestimation of plant dominance.

GE satellite images were downloaded at a time close to the period when drone images have been captured. All drone images and GE satellite images were captured during the time between January to September in 2022.

Hence, possible errors that can result due to temporal changes between GE satellite images and drone images were avoided. Mangrove species were easily identified from drone images using crown attributes including crown color, crown texture and crown size. Regarding GE satellite images, identification of different mangrove species using the above mentioned crown attributes was challenging due to some obvious technical difficulties in GE satellite imagery method (Madarasinghe *et al.*, 2020c), such as the high number of unidentifiable prominent crowns/margins due to comparatively less detail in GE images than in drone images. Therefore, in the GE satellite imagery method, crown area was underestimated regardless of the vegetation type. However, the results revealed that, between these two

RS-based methods, the drone imagery method is more accurate in the determination of plant dominance than the GE satellite imagery method, for inaccessible mangrove forests. Even so, the GE satellite imagery method can be applied as an alternative method to the drone imagery method when determining plant dominance in mangrove forests.

Moreover, the results of the Spearman rank correlation test revealed that there is a weak positive correlation ( $P < 0.05$ ,  $r = 0.132$ ) between the basal area and the individual tree crown area of mangrove species.

## CONCLUSION

The results of the present study suggest the applicability and accuracy of RS-based methods (drone imagery method and GE satellite imagery method) in the determination of plant dominance in dense, inaccessible mangrove forests. According to the results, RS-based methods could be used as an alternative method to the conventional basal area-based method of determining plant dominance in mangrove forests, with different accuracy levels. The drone imagery method can be used with 100% and 86.02% average accuracies respectively for monospecific mangrove vegetation and mixed mangrove vegetation respectively, whereas the GE satellite imagery method can be used with 97.85% and 42.15% average accuracies for monospecific mangrove vegetation and mixed mangrove vegetation, respectively. Therefore, this RS-based method could be used in determining plant dominance in dense mangrove forests.

## Acknowledgement

The authors wish to thank the FSPI-SEDRIC project for the financial support and the Department of Botany, Faculty of Science, University of Ruhuna, Sri Lanka for providing great support for this study.

## REFERENCES

Conchedda, G., Durieux, L., & Mayaux, P. (2008). An object-based method for mapping and change analysis in mangrove ecosystems. *ISPRS Journal of Photogrammetry and Remote Sensing* 63(5): 578-589. <https://doi.org/10.1016/j.isprsjprs.2008.04.002>

De Silva, W., & Amarasinghe, M.D. (2021). Potential use of mangroves for coastal protection: A case study from Sri Lanka. *Journal of the Indian Society of Coastal Agricultural Research* 39(1): 41-51. <https://doi.org/10.54894/JISCAR.39.2.2021.110687>

Fadrique, B., Santos-Andrade, P., Farfan-Rios, W., Salinas, N.,

Silman, M., & Feeley, K.J. (2021). Reduced tree density and basal area in Andean forests are associated with bamboo dominance. *Forest ecology and management* 480: 118648. <https://doi.org/10.1016/j.foreco.2020.118648>

Gillespie, T.W., Foody, G.M., Rocchini, D., Giorgi, A.P., & Saatchi, S. (2008). Measuring and modelling biodiversity from space. *Progress in physical geography* 32(2): 203-221. <https://doi.org/10.1016/j.ecoinf.2010.06.001>

He, K.S., Bradley, B.A., Cord, A.F., Rocchini, D., Tuanmu, M.N., Schmidtlein, S., Turner, W., Wegmann, M., & Pettorelli, N. (2015). Will remote sensing shape the next generation of species distribution models?. *Remote Sensing in Ecology and Conservation* 1(1): 4-18. <https://doi.org/10.1002/rse2.7>

Hillebrand, H., Bennett, D.M., & Cadotte, M.W. (2008). Consequences of dominance: a review of evenness effects on local and regional ecosystem processes. *Ecology* 89(6): 1510-1520. <https://doi.org/10.1890/07-1053.1>

Jayatissa, L. P., Dahdouh-Guebas., & Koedam, N. (2002). A review of the floral composition and distribution of mangroves in Sri Lanka. *Botanical Journal of the Linnean Society*, 138(1), 29-43. DOI:10.1046/j.1095-8339.2002.00002.x

Kerr, J.T. & Ostrovsky, M. (2003). From space to species: ecological applications for remote sensing. *Trends in Ecology & Evolution* 18(6): 299-305. [https://doi.org/10.1016/S0169-5347\(03\)00071-5](https://doi.org/10.1016/S0169-5347(03)00071-5)

Kuenzer, C., Ottinger, M., Wegmann, M., Guo, H., Wang, C., Zhang, J., Dech, S., & Wikelski, M. (2014). Earth observation satellite sensors for biodiversity monitoring: potentials and bottlenecks. *International Journal of Remote Sensing* 35(18): 6599-6647. <https://doi.org/10.1080/01431161.2014.964349>

Long, B.G. & Skewes, T.D. (1996). A technique for mapping mangroves with Landsat TM satellite data and geographic information system. *Estuarine, Coastal and Shelf Science* 43(3): 373-381. <https://doi.org/10.1006/ecss.1996.0076>

Madarasinghe, S.K., Amarasinghe, Y.W.P., Liyanage, C.H., Gunathilake, H.M.S.A.T., Jayasingha, J.A.I.K., Jayasingha, M., Priyankara, W.K.L., Kodikara, K.A.S., Koedam, N., Dahdouh-Guebas, F. & Jayatissa, L.P. (2020b). Retrospective study on changes in Dondra lagoon (2006-2017) resulting from tsunami impact and post-tsunami development. *Journal of Coastal Conservation* 24: 1-11. <https://doi.org/10.1007/s11852-020-00777-1>

Madarasinghe, S.K., Yapa, K.K., Satyanarayana, B., Udayakantha, P.M.P., Kodikara, S. & Jayatissa, L.P. (2020a). Inland irrigation project causes disappearance of coastal lagoon: the trajectory of Kalametiya lagoon, Sri Lanka from 1956 to 2016. *Coastal Management* 48(3): 188-209. <https://doi.org/10.1080/08920753.2020.1747914>

Madarasinghe, S.K., Yapa, K.K.A.S., & Jayatissa, L.P. (2020). Google Earth imagery coupled with on-screen digitisation for urban land use mapping: case study of Hambantota, Sri Lanka. *Journal of the National Science Foundation of Sri Lanka*. 48(4): 357 -366. <http://dx.doi.org/10.4038/>

- jnsfsr.v48i4.9795
- Nagendra H. (2001). Using remote sensing to assess biodiversity. *International journal of remote sensing* 22(12): 2377-2400. <https://doi.org/10.1080/01431160117096>
- Nandy, S. & Kushwaha, S.P.S. (2011). Study on the utility of IRS 1D LISS-III data and the classification techniques for mapping of Sunderban mangroves. *Journal of Coastal Conservation* 15(1): 123-137. <https://doi.org/10.1007/s11852-010-0126-z>
- Pau, S. & Dee, L.E. (2016). Remote sensing of species dominance and the value for quantifying ecosystem services. *Remote Sensing in Ecology and Conservation* 2(3): 141-151. <https://doi.org/10.1002/rse2.23>
- Pau, S., Edwards, E.J. & Still, C.J. (2013). Improving our understanding of environmental controls on the distribution of C3 and C4 grasses. *Global Change Biology* 19(1): 184-196. <https://doi.org/10.1111/gcb.12037>
- Priyashantha, A.K.H. & Taufikurahman, T. (2020). Mangroves of Sri Lanka: Distribution, status and conservation requirements. *Tropical Plant Research* 7(3): 654-668. <https://doi.org/10.22271/tpr.2020.v7.i3.083>
- Purnamasayangasukasih, P.R., Norizah, K., Ismail, A.A. & Shamsudin, I. (2016). A review of uses of satellite imagery in monitoring mangrove forests. In: *IOP Conference Series: Earth and Environmental Science*, vol. 37, Kuala Lumpur, Malaysia, 3–14 April. <https://doi.org/10.1088/1755-1315/37/1/012034>
- Purvis, A. & Hector, A. (2000). Getting the measure of biodiversity. *Nature* 405(6783): 212-219. <https://doi.org/10.1038/35012221>
- Schroeder, T.A., Hamann, A., Wang, T. & Coops, N.C. (2010). Occurrence and dominance of six Pacific Northwest conifer species. *Journal of Vegetation Science* 21(3): 586-596. <https://doi.org/10.1111/j.1654-1103.2009.01163.x>
- Skidmore, A.K., et al. (2015). Environmental science: Agree on biodiversity metrics to track from space. *Nature* 523(7561): 403-405. <https://doi.org/10.1038/523403a>
- Turner, B.L., et al. (2003). A framework for vulnerability analysis in sustainability science. *Proceedings of the national academy of sciences*, volume 100, June 5. pp.8074-8079. <https://doi.org/10.1073/pnas.1231335100>
- Wang, L., Jia, M., Yin, D., & Tian, J. (2019). A review of remote sensing for mangrove forests: 1956–2018. *Remote Sensing of Environment* 231. 111223. <https://doi.org/10.1016/j.rse.2019.111223>
- Warren, S.D., Alt, M., Olson, K.D., Irl, S.D., Steinbauer, M.J., & Jentsch, A. (2014). The relationship between the spectral diversity of satellite imagery, habitat heterogeneity, and plant species richness. *Ecological Informatics* 24: 160-168. <https://doi.org/10.1016/j.ecoinf.2014.08.006>

## RESEARCH ARTICLE

### Structural Engineering

# Simplification of large-scale solid element model for seismic structural response analysis of buildings

HMSC Rathnasiri, JASC Jayasinghe\* and AJ Dammika

*Department of Civil Engineering, Faculty of Engineering, University of Peradeniya, Peradeniya, Sri Lanka.*

Submitted: 28 April 2024; Revised: 21 November 2024; Accepted: 28 November 2024

**Abstract:** The seismic response analysis of large-scale structural systems, including integrated earthquake simulations for urbanized cities, requires developing complex numerical models with over 10 million solid elements. However, such detailed models are often computationally intensive and time-consuming. Therefore, simplified models are necessary to efficiently assess the seismic response of structures in the time domain during the early stages of analysis. The authors are proposing a meta-modelling theory in which a simple mass-spring model (MSM) is constructed from a large-scale solid-element model. This paper presents examples of converting a three-dimensional solid element model to a one-dimensional MSM, which is denoted as the consistent mass-spring model (CMSM) in the viewpoint of structural mechanics. The performance of the proposed CMSM is compared with conventional MSM and the frequency-adaptive lumped mass-stick model (LMSM). For comparison, three-storey symmetrical and unsymmetrical (T-shaped and L-shaped) reinforced concrete (RC) buildings are selected. Numerical time history simulations are carried out to check the suitability of the proposed CMSM for three sets of ground motions. The proposed CMSMs solve the same physical problem as the solid element model, using suitable mathematical approximations, and show very good agreement with those of the solid models. The first three natural frequencies of the CMSM were found to match those of the solid element model for both symmetric and asymmetric RC buildings in the study, demonstrating the high accuracy of the developed MSM. It is also shown that such a simplified model is used as an alternative to a large-scale solid element model to estimate the overall responses of the structure at the initial stage of large-scale analysis.

**Keywords:** Continuum mechanics, mass-spring models, meta-modeling, seismic structural response analysis, structural mechanics.

## INTRODUCTION

Modern modelling software enables us to automatically construct a solid element model using the data from Computer-Aided-Design (CAD) (Riaz *et al.*, 2021; Hori *et al.*, 2023). For a complicated structure, the constructed solid element model has a degree of freedom (DOF) of a few ten or hundred thousand (Kettil & Wiberg, 2002; Tuñón-Sanjur *et al.*, 2007; Quinay *et al.*, 2011; Tuñón-Sanjur *et al.*, 2013; Kusakabe *et al.*, 2022) but the model has high quality as it has high fidelity to the target structure. However, it is not an easy task to use such a large-scale model for seismic structural analysis that is carried out in the time domain. Large computer resources are needed for the computation of analyzing the model, especially when non-linear material properties or a state of finite or large deformation are considered.

For an efficient numerical analysis in the time domain, it is vital to have a simpler model such as a frame element model (Kettil & Wiberg, 2002). However, it is not certain that the frame model that is determined by the method is used as an alternative to a solid element model which is automatically constructed from CAD data. It is rare to

\* Corresponding author ([supunj@eng.pdn.ac.lk](mailto:supunj@eng.pdn.ac.lk); [id https://orcid.org/0000-0003-1054-9358](https://orcid.org/0000-0003-1054-9358))



have an identical natural frequency for the frame model and the solid element model even for linear seismic structural analysis (Jayasinghe *et al.*, 2016; 2017). A solid element model uses Young’s modulus and Poisson’s ratio for linear isotropic elasticity, but Poisson’s ratio is fully ignored in a truss or beam theory which is the foundation of the frame model (Hori *et al.*, 2014).

To resolve the conflict between solid element model analysis and other analysis, the authors are proposing a new theory, called “meta-modelling” (Hori *et al.*, 2014; 2015a 2015b; Jayasinghe *et al.*, 2014; 2015a; 2015b; 2015c; 2015d; 2016), which regards structural mechanics (Hjelmstad, 2005; Zienkiewicz *et al.*, 2014) as a mathematical approximation of continuum mechanics (Gonzalez & Stuart, 2008; Reddy, 2013). The mathematical approximation is so smart that a spatially three-dimensional problem of continuum mechanics is reduced to a zero or one-dimensional problem, and it is shown that the accuracy loss due to the mathematical approximation is minimum when a structure or a structural component has a suitable configuration. There is a correlation between the accuracy of numerical analysis and the fidelity of the model (Jayasinghe *et al.*, 2015a; 2015b; 2015c).

This paper applies meta-modeling theory to develop a one-dimensional simplified model from a large-scale three-dimensional solid element model, enabling efficient seismic structural response analysis at the initial stages. A MSM is chosen as a simplified model, and a spatially three-dimensional problem of the seismic structural response is reduced to a spatially zero-dimensional problem. A key issue is the clarification of the advantages and disadvantages of using a simplified model as an alternative to a solid element model. Due to the rigorousness of the meta-modelling theory based on which it is constructed, the simplified model can provide accurate overall displacement behaviour.

The present paper is organized as follows. First, the significance of adopting a simpler numerical model compared to the complex solid element models for efficient numerical analysis is explained. In Section 2, the meta-modelling theory is explained using an energy theory or a Lagrangian of an MSM with a single mass point. It is shown that this Lagrangian is derived from that of continuum mechanics by making suitable mathematical approximations. The methodology for the development of the consistent mass-spring model (CMSM) using meta-modelling theory is explained in Section 3 along with the development of the conventional MSM and frequency

adaptive lumped mass-stick model (LMSM). Section 4 describes a numerical example to evaluate the seismic performance of the proposed CMSM compared to the conventional MSM and frequency adaptive LMSM. Symmetric and asymmetric (T-shaped and L-shaped) three-storey RC building structures are considered as the numerical examples to evaluate the seismic performance of the MSMs. The seismic performance is evaluated by comparing the natural frequency, peak acceleration, the storey drifts and floor displacements of CMSM with the conventional MSM and frequency adaptive LMSM. The major conclusion of the present study is made in Section 5.

**MATERIALS AND METHODS**

**Meta-modelling theory**

A single mass point MSM which consists of one mass and one spring is considered to explain the meta-modelling theory (Hori *et al.*, 2014), for a structure as shown in Figure 1.

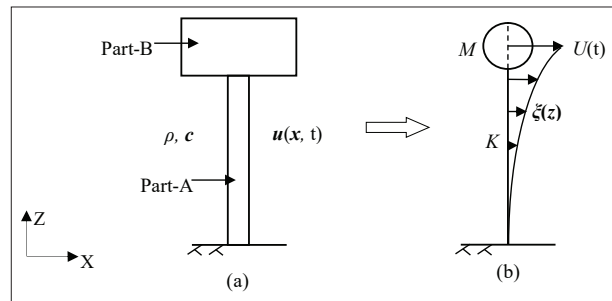


**Figure 1:** Highly mass concentrated structure

The structure is modeled as a linear MSM when the mass of part-A is negligible compared to that of part-B of the structure. A Lagrangian of this MSM is;

$$\mathcal{L}_s[U, V] = \mathcal{K}_s[V] - \mathcal{P}_s[U]. \tag{1}$$

Here,  $U$  and  $V$  are displacement and velocity of the mass in a particular direction, and  $\mathcal{K}_s$  and  $\mathcal{P}_s$  are the kinematic and strain energy defined as;

$$\begin{aligned} \mathcal{K}_s[V] &= \frac{1}{2}MV^2, \\ \mathcal{P}_s[U] &= \frac{1}{2}KU^2, \end{aligned} \tag{2}$$

where  $M$  is lumped mass and  $K$  is the spring constant for the lateral stiffness, and  $V = \dot{U}$ .

Since this structure is made of a certain material (steel, Reinforced Concrete (RC), or wood), the structure can be modeled according to the continuum mechanics (Gonzalez & Stuart, 2008; Reddy, 2013). That is, we consider a three-dimensional displacement vector function,  $\mathbf{u}$ . Assuming linear elasticity, we have the following Lagrangian;

$$\mathcal{L}_c[\mathbf{v}, \boldsymbol{\epsilon}] = \mathcal{K}_c[\mathbf{v}] - \mathcal{P}_c[\boldsymbol{\epsilon}], \quad \dots(3)$$

where  $\mathbf{v} = \dot{\mathbf{u}}$  is velocity and  $\boldsymbol{\epsilon} = \text{sym} \nabla \mathbf{u}$  is strain with dot and  $\nabla$  being the temporal and spatial derivatives, and with  $\text{sym}$  meaning the symmetric part, and  $\mathcal{K}_c$  and  $\mathcal{P}_c$  are;

$$\begin{aligned} \mathcal{K}_c[\mathbf{v}] &= \int_V \frac{1}{2} \rho \mathbf{v} \cdot \mathbf{v} \, dv, \\ \mathcal{P}_c[\boldsymbol{\epsilon}] &= \int_V \frac{1}{2} \boldsymbol{\epsilon} : \mathbf{c} : \boldsymbol{\epsilon} \, dv, \end{aligned} \quad \dots(4)$$

where  $\rho$  and  $\mathbf{c}$  are density and elasticity, with  $\cdot$  and  $:$  standing for the inner product and second-order contraction, respectively. The form of  $\mathcal{L}_s$  and  $\mathcal{L}_c$  given by Equations (1) and (3) are similar to each other, even though the functions and functionals are given by Equations (2) and (4) are utterly different.

The meta-modeling theory takes advantage of the similarity in the form of  $\mathcal{L}_s$  and  $\mathcal{L}_c$ , and derives  $\mathcal{L}_s$  from  $\mathcal{L}_c$ . The procedure of deriving  $\mathcal{L}_s$  from  $\mathcal{L}_c$  is simple, as we have to approximate the three-dimensional vector-valued function,  $\mathbf{u}$ . Indeed, if we approximate it as the product of an unknown temporal function,  $U(t)$ , and a known three-dimensional vector-valued function,  $\boldsymbol{\xi}(\mathbf{x})$ , as;

$$\mathbf{u}(\mathbf{x}, t) = U(t)\boldsymbol{\xi}(\mathbf{x}), \quad \dots(5)$$

then, substituting Equation (5) into  $\mathcal{L}_c$ , we obtain  $\mathcal{L}_s$ . Here, the mass and spring constants,  $M$  and  $K$ , are explicitly computed in terms of  $\rho$  and  $\mathbf{c}$  together with the assumed  $\boldsymbol{\xi}$ . That is,

$$\begin{aligned} M &= \int \rho \boldsymbol{\xi} \cdot \boldsymbol{\xi} \, dv, \\ K &= \int \nabla \boldsymbol{\xi} : \mathbf{c} : \nabla \boldsymbol{\xi} \, dv, \end{aligned} \quad \dots(6)$$

The derivation of  $\mathcal{L}_s$  from  $\mathcal{L}_c$  is made mathematically, without making any physical assumptions. The Lagrangian problem of a continuum model with  $\rho$  and

$\mathbf{c}$  ( $\mathcal{L}_c$ ) is reduced to another Lagrangian problem of an MSM of  $M$  and  $K$  ( $\mathcal{L}_s$ ), by using an approximated function of the displacement. Therefore, the solution of  $\mathcal{L}_s$  is regarded as an approximate solution of  $\mathcal{L}_c$ .

The meta-modelling theory is able to derive a bar model, a beam model or a plate model from a continuum model in the same manner as shown in the above, *i.e.*, substituting a suitably approximated displacement function into  $\mathcal{L}_c$  (Hjelmstad, 2005; Hori *et al.*, 2014; Zienkiewicz *et al.*, 2014). The key concept of this theory is that all the modeling solves the same physical problem of continuum mechanics but uses their own distinct mathematical approximations. According to this theory, therefore, it is guaranteed that when a simplified model is constructed by making use of natural frequencies and mode shapes of the continuum modelling, it will share the same fundamental dynamic characteristics as the continuum mechanics' model.

### Formulation of CMSM meta-modelling theory

We seek to construct a rigorous simplified model which shares the identical fundamental dynamic characteristics as those of the target solid element model; this simplified model is called Consistent Mass-Spring Model (CMSM).

This study is an extension of previous work done by Jayasinghe *et al.* (2015). The previous CMSM formulation is limited to only two mass points, but the current formulation is extended to  $n$  mass points, where  $n$  is a positive real integer. This improvement of CMSM will increase the accuracy of response. The previous formulation of CMSM is restructured by using a linear transformation matrix which transfers dynamic modes to approximate displacement functions to incorporate the effect of higher modes.

According to the meta-modelling theory, we consider an approximate displacement function of the following form;

$$\mathbf{u}(\mathbf{x}, t) = \sum_{\alpha=1}^n U^\alpha(t) \boldsymbol{\Phi}^\alpha(\mathbf{x}), \quad \dots(7)$$

where  $U^\alpha$  is a certain direction displacement component of the  $\alpha$ -th mass point and  $\boldsymbol{\Phi}^\alpha$  is an approximate displacement mode. By definition, a component of  $\boldsymbol{\Phi}^\alpha(\mathbf{x}^\alpha)$  corresponding to  $U^\alpha$  takes on a value of 1, with  $\mathbf{x}^\alpha$  being the location of the  $\alpha$ -th mass point, and  $\boldsymbol{\Phi}^\alpha(\mathbf{x}^\beta) = 0$  for  $\alpha \neq \beta$  which can be called requirement 1.

For simplicity, we substitute the approximate displacement ( $\mathbf{u}$ ) of Equation (7) into  $\mathcal{L}$  of Equation (3). Then, we obtain

$$\mathcal{L} = \sum_{\alpha, \beta=1}^n \frac{1}{2} m^{*\alpha\beta} \dot{U}^\alpha \dot{U}^\beta - \frac{1}{2} k^{*\alpha\beta} U^\alpha U^\beta, \quad \dots(8)$$

where,

$$m^{*\alpha\beta} = \int_V \rho \Phi^\alpha \Phi^\beta dv \text{ and } k^{*\alpha\beta} = \int_V \nabla \Phi^\alpha : \mathbf{c} : \nabla \Phi^\beta dv. \quad \dots(9)$$

The right side of Equation (8) is rewritten as

$$\sum_{\alpha=1}^n \frac{1}{2} M^\alpha (\dot{U}^\alpha)^2 + \sum_{\alpha, \beta=1 (\alpha \neq \beta)}^n M^{\alpha\beta} \dot{U}^\alpha \dot{U}^\beta - \sum_{\alpha, \beta=1 (\alpha \neq \beta)}^n \frac{1}{2} K^{\alpha\beta} (U^\alpha - U^\beta)^2 - \sum_{\alpha=1}^n \frac{1}{2} K^\alpha (U^\alpha)^2,$$

where

$$M^\alpha = m^{*\alpha\alpha}, \quad M^{\alpha\beta} = m^{*\alpha\beta}, \quad K^{\alpha\beta} = -k^{*\alpha\beta} \text{ and } K^\alpha = \sum_{\beta=1}^n k^{*\alpha\beta}.$$

According to Equation (8), it is straightforward to understand the necessity of a third spring for the MSM which consists of two mass points; see Figure 2 for a two point MSM. If we can choose a  $\Phi^\alpha$  so that  $M^{\alpha\beta}$  and  $K^\alpha$  vanish (requirement 2), then the above  $\mathcal{L}$  of Equation (8) becomes  $\mathcal{L}$  of the typical MSM which includes an equal number of linear springs and mass points.

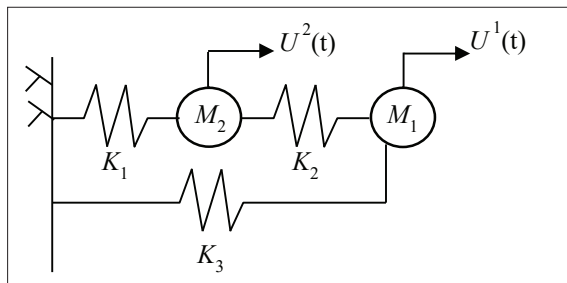


**Figure 2:** Schematic view of a CMSM consisting of two mass points

### Introduction of dynamic modes with linear transformation matrix

Dynamic mode shapes of a target problem need to be incorporated in the construction of a MSM, so that it shares the same dynamic fundamental characteristics with a continuum model. We suppose that an  $n$  number of dynamic modes  $\{\Psi^\alpha, \omega^\alpha\}$  ( $\alpha = 1, 2, 3, \dots, n$ ) are given;  $\Psi^\alpha$  and  $\omega^\alpha$  are mode shape and natural frequency of the  $\alpha$ -th mode respectively. By definition,  $\Psi^\alpha$  and  $\omega^\alpha$  satisfy;

$$\int_V \rho \Psi^\alpha \cdot \Psi^\beta dv = 0, \quad \int_V \nabla \Psi^\alpha : \mathbf{c} : \nabla \Psi^\beta dv = 0, \quad \dots(10)$$

and,

$$\rho(\omega^\alpha)^2 \Psi^\alpha + \nabla \cdot (\mathbf{c} : \nabla \Psi^\alpha) = 0, \quad \dots(11)$$

for  $\alpha \neq \beta$ .

Employing  $\mathcal{L}$  of Equation (3) and substituting the approximate displacement function ( $\mathbf{u} = \sum U^\alpha \Psi^\alpha$ ) into it, we can obtain,

$$\mathcal{L} = \sum_{\alpha, \beta=1}^n \frac{1}{2} m^\alpha (\dot{u}^\alpha)^2 - \frac{1}{2} k^\alpha (u^\alpha)^2, \quad \dots(12)$$

where,

$$m^\alpha = \int_V \rho \Psi^\alpha \Psi^\alpha dv \text{ and } k^\alpha = \int_V \nabla \Psi^\alpha : \mathbf{c} : \nabla \Psi^\alpha dv. \quad \dots(13)$$

As a result of the orthogonality property of dynamic mode shapes, Equation (10), dynamic modes do not produce coupling terms in Equation (12). Additionally, due to Equation (11), it is readily seen that  $m^\alpha$  and  $k^\alpha$  of Equation (13) satisfy;

$$(\omega^\alpha)^2 m^\alpha = k^\alpha, \quad \dots(14)$$

for  $\alpha = 1, 2, 3, \dots, n$ . Note that, if  $\Psi^\alpha$  is replaced by  $\Psi'^\alpha = a \Psi^\alpha$ , we have

$$m'^\alpha = c^2 m^\alpha \text{ and } k'^\alpha = c^2 k^\alpha, \quad \dots(15)$$

which still satisfies

$$(\omega^\alpha)^2 m'^\alpha = k'^\alpha \quad \dots(16)$$

Furthermore, note that;

$$\mathbf{u}(\mathbf{x}, t) = \sum_{\alpha=1}^n u'^\alpha(t) \boldsymbol{\Psi}'^\alpha(\mathbf{x}) = \sum_{\alpha=1}^n u^\alpha(t) \boldsymbol{\Psi}^\alpha(\mathbf{x}). \quad \dots(17)$$

Pure dynamic modes can satisfy neither requirement 1 nor requirement 2 which are mentioned above. In general, it is not possible to find  $\{\boldsymbol{\Phi}^\alpha\}$  which satisfies both requirements; thus, we need to find a suitable linear combination of  $\{\boldsymbol{\Psi}^\alpha\}$  that satisfies, at least, requirement 1. To this end, we consider the following combination.

$$\mathbf{U}^\alpha = \sum_{\beta=1}^n t^{\alpha\beta} \mathbf{u}^\beta \quad \text{and} \quad \boldsymbol{\Phi}^\alpha = \sum_{\beta=1}^n (t^{\alpha\beta})^{-1} \boldsymbol{\Psi}^\beta, \quad \dots(18)$$

where  $[t^{\alpha\beta}]$  is a linear transformation matrix with  $[t^{\alpha\beta}]^{-1}$  being the inverse of  $[t^{\alpha\beta}]$ .

Then, Equation (9) is rewritten as.

$$m^{*\alpha\beta} = \sum_{\gamma, \beta, \alpha=1}^n m^\gamma (t^{\alpha\gamma})^{-1} (t^{\beta\gamma})^{-1} \quad \text{and}$$

$$k^{*\alpha\beta} = \sum_{\gamma, \beta, \alpha=1}^n k^\gamma (t^{\alpha\gamma})^{-1} (t^{\beta\gamma})^{-1} \quad \dots(19)$$

To determine the components of  $[t^{\alpha\beta}]$ , we introduce a vector  $[\boldsymbol{\Xi}^\alpha]$ , which consists of zeros and ones, zero for mass points not on  $z = z^\alpha$  and one for the mass point on  $z = z^\alpha$ . Here,  $z^\alpha$  is the location of  $\alpha$ -th mass point along the axial direction of a target problem, and then we can compute,

$$(t^{\alpha\gamma})^{-1} = [\boldsymbol{\Xi}^\alpha] [\boldsymbol{\Psi}^\gamma(z^\alpha)]^{-1} \quad \dots(20)$$

Here,  $[\boldsymbol{\Psi}^\gamma(z^\alpha)]$  is a regular square matrix with  $[\boldsymbol{\Psi}^\gamma(z^\alpha)]^{-1}$  being the inverse of  $[\boldsymbol{\Psi}^\gamma(z^\alpha)]$ .  $\boldsymbol{\Psi}^\gamma(z^\alpha)$  is a displacement component along a fixed direction for the MSM of the  $\gamma$ -th dynamic mode at the  $\alpha$ -th mass point location. It is clear that coupling mass and stiffness terms of mass and stiffness matrices should be there to assure the consistency of the MSM.

## Application of CMSM for building structures and comparative study

### Problem setting for building structures

A symmetric and asymmetric three-storey RC building (Figure 3 and Figure 5) is considered in the present study to develop the Mass-spring models described in Section 3. The selected three-storey RC building consists of square columns having cross-section dimensions of 0.35 m x 0.35 m and a uniform slab thickness of 0.15 m. The elastic modulus, Poisson's ratio, and density of the concrete are 24 GPa, 0.2, and 2000 kg m<sup>-3</sup>, respectively. Three different earthquake ground motions are selected to perform the time history analysis. Figure 4 shows the acceleration time histories of the selected earthquake ground motions. All the ground motions are applied in the X-direction of the symmetric and asymmetric three-storey RC buildings in the time history analysis.

### Construction of MSMs

First, 3D finite element models of the symmetric and asymmetric three-storey RC buildings are developed using FE software. Modal analysis is performed to

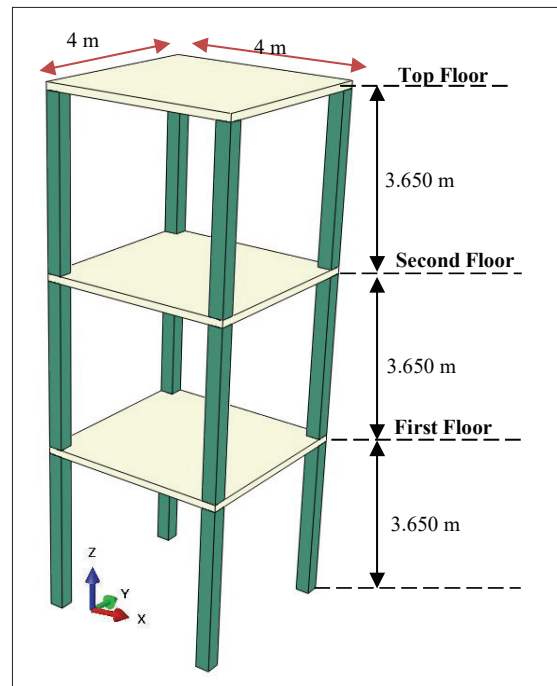


Figure 3: Selected symmetric building

obtain the necessary undamped natural frequencies and the mode shapes of the symmetric and asymmetric three-storey RC buildings. Figure 6, depict the mode shapes of the symmetric three-storey RC buildings. The obtained mode shapes are then used to develop the low-fidelity MSMs considered in this study. Time history analysis is performed to determine the displacement and acceleration response of the developed low-fidelity MSMs. The spring stiffness is determined using the static pushover analysis of the 3D finite element (FE) model.

The mass and stiffness matrices of the CMSM, as well as the mass matrix of the frequency adaptive LSM, are then determined using *Mathematica* code. The tributary area consideration method is used to compute the mass matrix of the conventional MSM. Then, *Mathematica* coding is developed based on the Newmarks' method to determine the displacement and acceleration of the low-fidelity MSMs. Finally, the drift ratio and peak acceleration of the MSMs are compared with the 3D solid model to investigate the utilization of the low-fidelity models of the structures, compared to the 3D solid models.

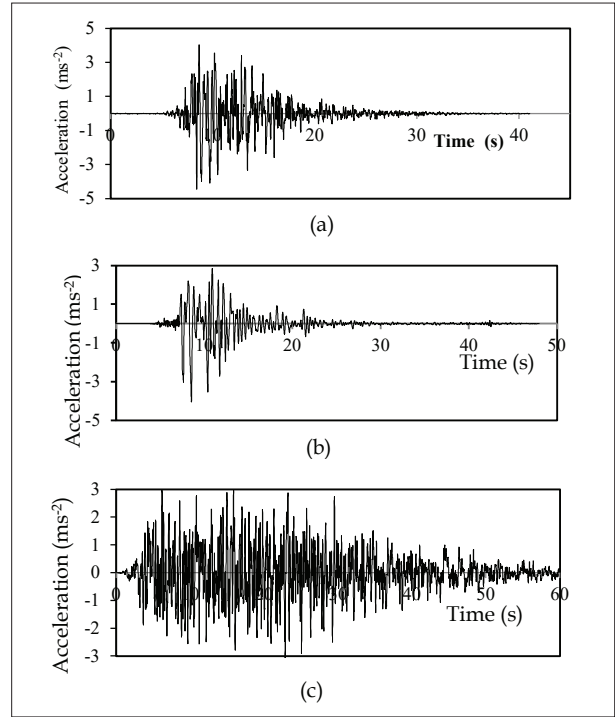


Figure 4: Selected Ground Motions (a) 1st (b) 2nd (c) 3rd

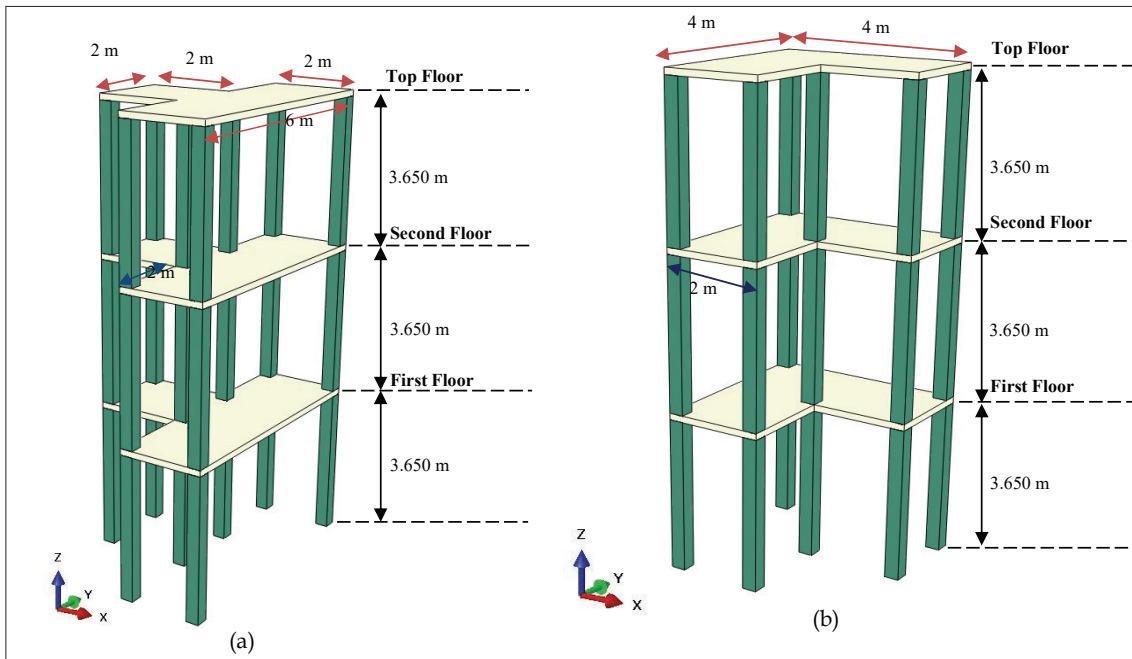


Figure 5: Selected asymmetrical buildings: (a) T-Shape (b) L-Shape

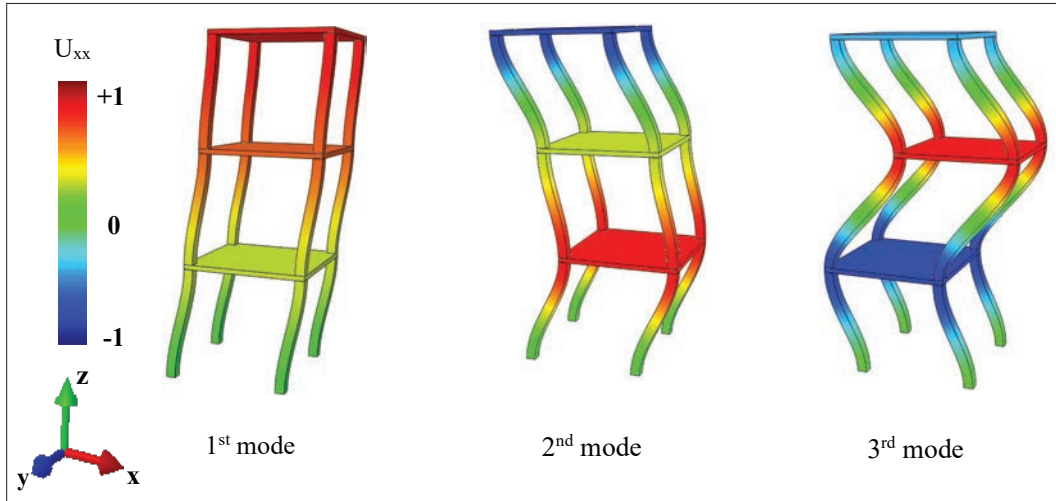


Figure 6: Mode shapes in x-direction of the symmetric three-storey RC building

## RESULTS AND DISCUSSION

### Comparison of the natural frequency of MSMs

The natural frequency, drift ratio, and peak acceleration of the mass point in the low-fidelity MSMs are compared with those of the solid model to evaluate the significance and potential advantages of using low-fidelity models over solid models. First, to evaluate the consistency of the developed MSMs for symmetric and asymmetric three-storey RC buildings, their natural frequencies are compared with those of the solid model (Table 1).

The natural frequencies of the conventional MSM and the frequency adaptive LSM show a marginal error compared to the natural frequencies of the solid element model. Moreover, the frequency-adaptive LSM outperforms the conventional MSM in terms of natural frequencies. However, the first three natural frequencies of the CMSM coincide with the corresponding natural frequencies of the solid element model for symmetric and asymmetric RC buildings considered in the study. These findings confirm the consistency of the developed CMSM with the solid model.

Table 1: Natural frequencies comparison in x-direction between the CMSM and other MSMs

Building type	Symmetric building			Asymmetric building L-shaped			Asymmetric building T-shaped			
	1	2	3	1	2	3	1	2	3	
Mode Number (x-direction)										
Conventional MSM	Solid model / (Hz)	2.33	6.60	9.80	3.03	8.71	13.02	3.02	8.69	13.20
	Frequency (Hz)	2.39	6.66	9.53	3.20	8.87	12.60	3.16	8.75	12.43
	Error (%)	2.58	0.91	2.76	5.61	1.84	3.23	4.64	0.69	5.83
Frequency adaptive LSM	Frequency (Hz)	2.36	6.62	9.61	3.11	8.72	12.67	3.11	8.73	12.72
	Error (%)	1.29	0.30	1.94	2.64	0.11	2.69	2.98	0.46	3.64
CMSM	Frequency (Hz)	2.33	6.60	9.80	3.03	8.71	13.02	3.02	8.69	13.20
	Error (%)	0	0	0	0	0	0	0	0	0

**Comparison of the peak acceleration and storey drifts**

The damages to the building structures can be estimated based on the peak displacement, peak velocity, peak acceleration response, and maximum drift ratio under seismic loading. The present study considered the peak acceleration response and drift ratio of the symmetric and asymmetric three-storey RC buildings to estimate the damage under seismic loading. Figure 7 shows the response of the symmetrical three-storey RC building from the time history analysis using the second and third earthquake ground motions. It can be identified that the conventional MSM has more or less the same response as the frequency-adaptive LMSM with regard to peak

acceleration and drift ratio. Moreover, the conventional MSM and the frequency-adaptive LMSM depict a significant variation between their seismic responses compared to the solid element model. Therefore, adopting the conventional MSMs and the frequency-adaptive LMSM to determine the seismic response of the solid element model yields less accurate results. However, the peak acceleration and the drift ratio response of the CMSM model due to the seismic loading have coincided with the solid element model. Therefore, the developed CMSM for the symmetric three-storey RC building can be used to determine the seismic response of the symmetrical three-storey RC building instead of adopting the solid model.

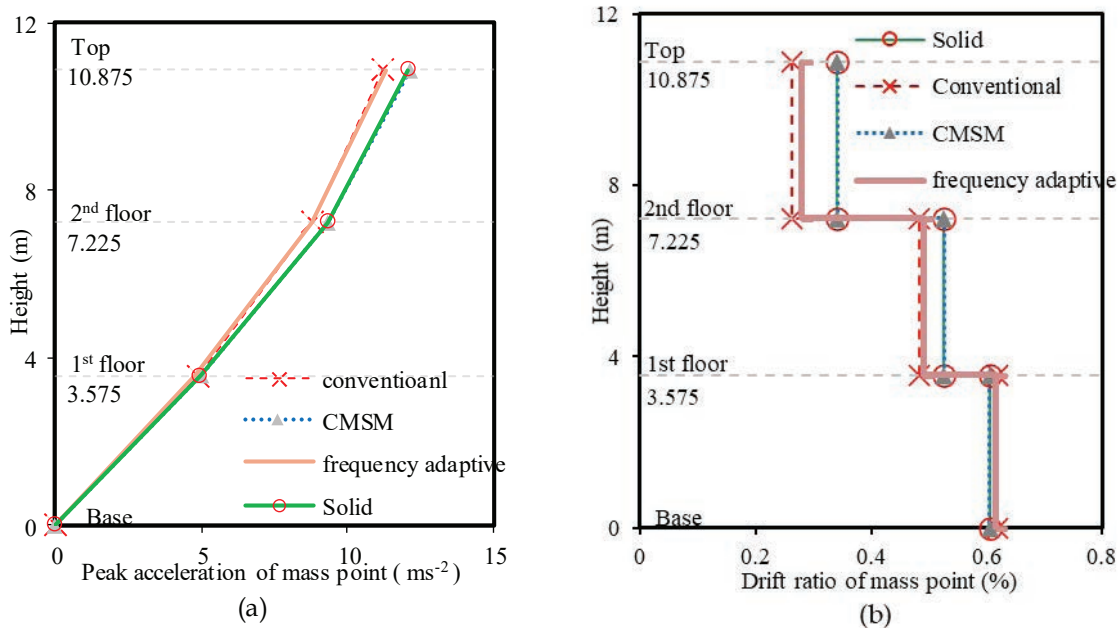


**Figure 7:** Response of symmetrical building: (a) peak acceleration for second ground motion and (b) drift ratio for third ground motion

Figure 8 and Figure 9 show the peak acceleration and drift ratio responses of the L-shaped and T-shaped three-storey RC buildings for the 2<sup>nd</sup> and 3<sup>rd</sup> earthquake ground motions.

According to Figures 8 and 9, the peak acceleration and drift ratio responses of the conventional MSM and the frequency adaptive LMSM differ significantly from the peak acceleration and drift ratio responses of the solid element model for both L-shaped and T-shaped

asymmetrical buildings. The frequency-adaptive LMSM produces more accurate results compared to the conventional MSM. However, the peak acceleration and drift ratio response of the CMSM almost coincides with the peak acceleration and drift ratio of the solid model. Therefore, the developed CMSM can be used to determine the seismic response of the L-shaped and T-shaped asymmetrical buildings instead of the solid element model.

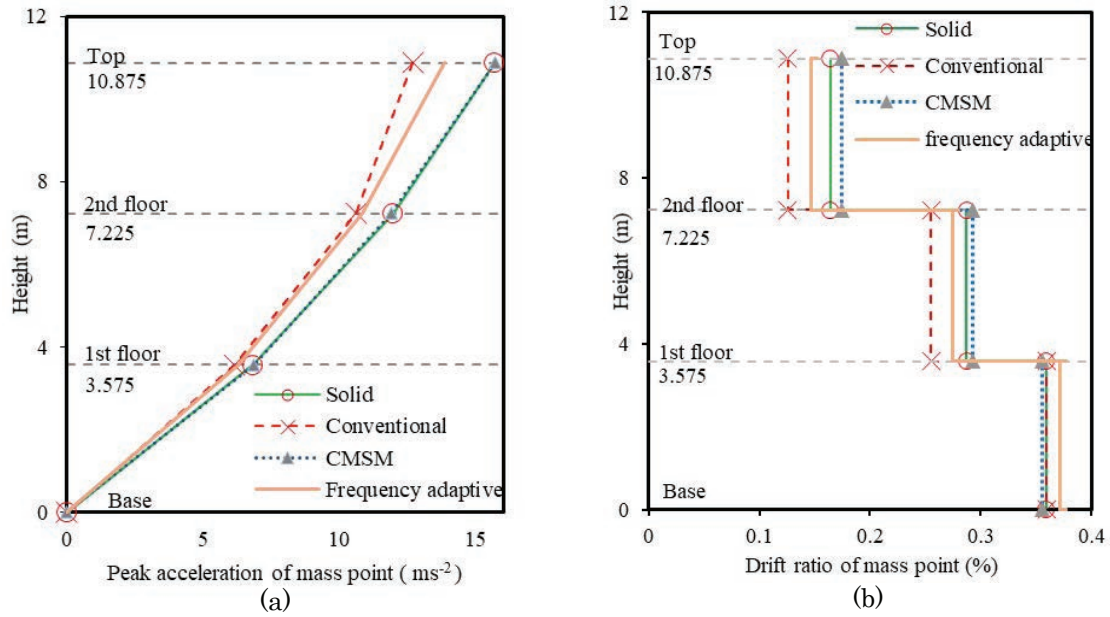


**Figure 8:** Response of L-shaped asymmetrical building: (a) peak acceleration for second ground motion and (b) drift ratio for third ground motion

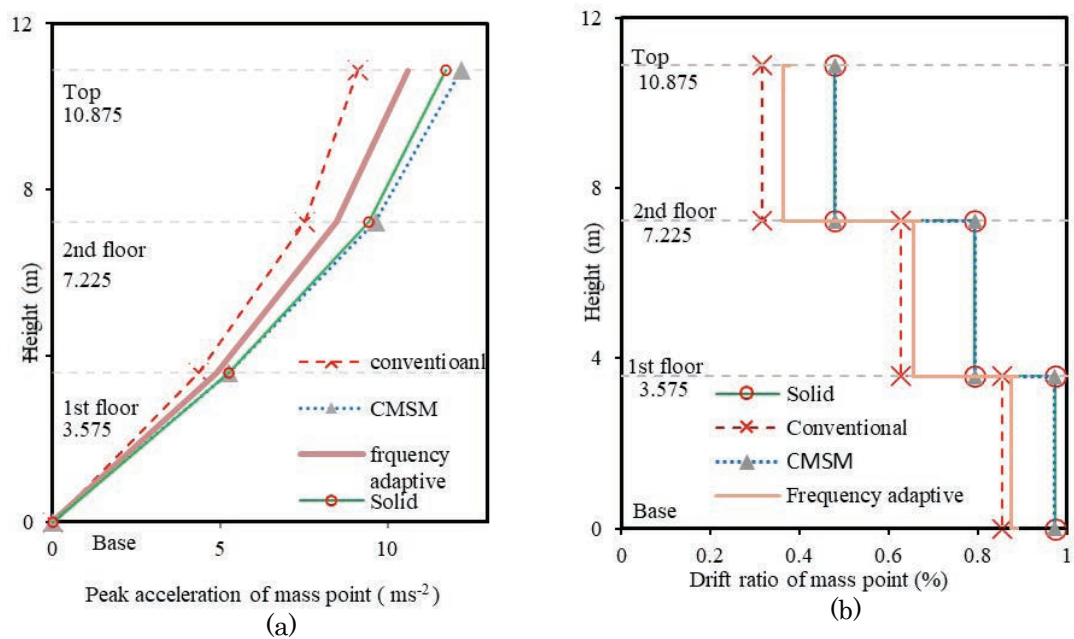


**Figure 9:** Response of T-shaped asymmetrical building: (a) peak acceleration for second ground motion and (b) drift ratio for third ground motion

As per the significant comparison, it is evident that conventional MSMs and frequency-adaptive LMSM yield less accurate results compared to the solid element model. However, the developed CMSM in the present study produces almost the same results as the solid element model for both symmetrical and asymmetrical three-storey RC buildings. Therefore, the developed CMSM can be used to evaluate the seismic response

of both symmetric and asymmetric three-storey RC buildings considered in the present study instead of using the solid element model. Table 2 illustrates the percentage of error in the peak acceleration response and drift ratio from the developed CMSMs for each floor of the symmetric and asymmetric three-storey RC buildings considered in the study.

**Table 2:** Percentage of error in peak acceleration and maximum drift ratio of CMSM with the solid model

Symmetric building						
Ground motions	1 <sup>st</sup>		2 <sup>nd</sup>		3 <sup>rd</sup>	
Peak Values	Acc. / ms <sup>-2</sup>	Drift ratio (%)	Acc. / ms <sup>-2</sup>	Drift ratio (%)	Acc. / ms <sup>-2</sup>	Drift ratio (%)
3rd floor/ (10.95m)	0.11	0.20	0.21	0.07	0.48	0.20
2nd floor/ (7.30m)	0.37	0.01	0.13	0.03	0.03	0.10
1st floor/ (3.65m)	0.21	0.07	0.14	0.05	0.19	0.03
L-shaped building						
Ground motions	1 <sup>st</sup>		2 <sup>nd</sup>		3 <sup>rd</sup>	
Peak Values	Acc. / ms <sup>-2</sup>	Drift ratio (%)	Acc. / ms <sup>-2</sup>	Drift ratio (%)	Acc. / ms <sup>-2</sup>	Drift ratio (%)
3rd floor/ (10.95m)	2.35	8.87	3.85	8.95	0.76	6.12
2nd floor/ (7.30m)	1.54	3.75	2.36	4.67	1.10	1.89
1st floor/ (3.65m)	1.82	1.02	0.15	1.61	0.40	1.03
T-shaped building						
Ground motions	1 <sup>st</sup>		2 <sup>nd</sup>		3 <sup>rd</sup>	
Peak Values	Acc. / ms <sup>-2</sup>	Drift ratio (%)	Acc. / ms <sup>-2</sup>	Drift ratio (%)	Acc. / ms <sup>-2</sup>	Drift ratio (%)
3rd floor/ (10.95m)	0.24	0.10	0.13	0.23	0.29	0.06
2nd floor/ (7.30m)	0.38	0.03	0.12	0.14	0.01	0.11
1st floor/ (3.65m)	0.48	0.11	0.07	0.03	0.87	0.00

When compared to the symmetric building and T-shaped asymmetrical building, the L-shaped asymmetrical building has the largest error percentages for both peak acceleration and maximum drift ratio across all levels. This is due to the torsional irregularity of the L-shaped building which caused the torsional mode which should be considered in the development of the CMSM. However, T-shaped buildings are not subject to any torsional response due to the application of the earthquake ground motion through the centre of the stiffness. Therefore, it is evident that the developed CMSM can be used to determine the seismic response of the symmetric and asymmetric three-storey RC buildings considered in the study instead of using the solid model.

## CONCLUSION

In this paper, the authors propose a systematic method for the rigorous development of a simplified 1D model based on the solid element model. This model is entitled CMSM. The consistency of CMSM is assured by implementing the meta-modelling theory in the construction process of CMSM. According to the meta-modelling theory, additional springs are incorporated in CMSM to guarantee consistency with that of the solid element model. The proposed CMSM can incorporate any number of dynamic mode shapes of a target structure to improve the accuracy of the response.

The performance of the proposed MSM is compared with the available MSMs, such as the conventional MSM and the frequency-adaptive LMSM. The target building types are three-storey symmetrical and L-shaped and T-shaped asymmetrical RC building structures. The seismic response is evaluated by comparing the peak displacement, the peak acceleration, and the maximum drift ratio of each floor level. The study found that the first three natural frequencies of the CMSM align closely with those of the solid element model for both symmetric and asymmetric RC buildings. A comparative analysis further demonstrates that the CMSM shows excellent agreement with the solid element model for these structures. Additionally, the peak acceleration and drift ratio responses of the CMSM show good agreement with those of the solid element model. Therefore, it can be concluded that the proposed CMSM can solve the same physical problem of the solid element model using suitable mathematical approximations. However, an L-shaped asymmetric RC building has a small deviated response compared to the solid element model. This is due to the neglect of the torsional modes of vibrations in the construction of all MSMs. The T-shaped asymmetrical building provides a better response to the application of the ground motions along the symmetric axis of the building in all MSMs.

The proposed CMSM needs to be extended to non-linear analysis, which will result in more benefits by saving computational resources at the initial stage of design. At least, it is straightforward to apply the meta-modelling to obtain an incremental response of a non-linear elastoplastic structure. Furthermore, by incorporating the torsional mode into the MSM formulation process, the selected MSMs can be improved for seismic response analysis of asymmetric building structures.

## REFERENCES

- Ali, A., Hayah, N. A., Kim, D., & Cho, S. G. (2014). Probabilistic seismic assessment of base-isolated NPPs subjected to strong ground motions of the Tohoku earthquake. *Nuclear Engineering and Technology*, 46(5), 699–706. <https://doi.org/10.5516/NET.09.2014.030>
- Bose, M. K., Soni, R. S., Mahajan, S. C., & Kakodkar, A. (Eds.). (1996). Strain energy concept for developing lumped mass stick model of complex structures. In *Proceedings of the 11th World Conference on Earthquake Engineering*. Pergamon. Acapulco, Mexico, June 23–28.
- Chopra, A. K. (2012). *Dynamics of structures: Theory and applications to earthquake engineering* (4th ed.). Prentice Hall.
- Clough, R. W., & Penzien, J. (1975). *Dynamics of structures*. McGraw-Hill.
- Gonzalez, O., & Stuart, A. M. (2008). *A first course in continuum mechanics* (Cambridge texts in applied mathematics, No. 42). Cambridge University Press.
- Halabian, A. M., El Naggar, M. H., & Vickery, B. J. (2002). Nonlinear seismic response of reinforced-concrete free-standing towers with application to TV towers on flexible foundations. *Structural Design of Tall and Special Buildings*, 11(1), 51–72. <https://doi.org/10.1002/tal.190>
- Halabian, A. M., & Kabiri, S. (2011). Effect of foundation flexibility on ductility reduction factors for R/C stack-like structures. *Earthquake Engineering & Engineering Vibration*, 10(2), 277–290. <https://doi.org/10.1007/s11803-011-0065-1>
- Hjelmstad, K. D. (2005). *Fundamentals of structural mechanics* (2nd ed.). Boston, MA: Springer. <https://doi.org/10.1007/b137547>
- Hori, M., & Ichimura, T. (2023). *Integrated earthquake simulation* (1st ed.). Abingdon, Oxon: CRC Press. <https://doi.org/10.1201/9781003149798-1>
- Hori, M., Ohtani, H., Jayasinghe, J. A. S. C., Meddegadara, L., Ichimura, T., & Fujita, K. (2015). Automated model construction for integrated earthquake simulation. In *15th International Conference on Civil, Structural and Environmental Engineering Computing*, Prague, Czech Republic.
- Hori, M., Tanaka, S., Wijerathne, L., & Ichimura, T. (2015). Meta-Modeling for Consistent Seismic Response Analysis. *Proceedings of the 5th ECCOMAS Thematic Conference on Computational Methods in Structural Dynamics and Earthquake Engineering*, Crete Island, Greece.
- Hori, M., Wijerathne, L., Ichimura, T., & Tanaka, S. (2014). Meta-Modeling for Constructing Models Consistent with Continuum Mechanics. *Journal of Japan Society of Civil Engineers*, 2(1), 269–275.
- Huang, Y.-N., Whittaker, A. S., & Luco, N. (2010). Seismic performance assessment of base-isolated safety-related nuclear structures. *Earthquake Engineering and Structural Dynamics*, 39(13), 1421–1442. <https://doi.org/10.1002/eqe.1038>
- Jadhav, M. B., & Jangid, R. S. (2004). Response of base-isolated liquid storage tanks. *Shock and Vibration*, 11, 33–45. <https://doi.org/10.1155/2004/276030>
- Jayasinghe, J. A. S. C., Hori, M., Riaz, M. R., Wijerathne, M. L. L., & Ichimura, T. (2017). Conversion between solid and beam element solutions of finite element method based on meta-modeling theory: Development and application to a ramp tunnel structure. *Earthquake Engineering and Engineering Vibration*, 16(2), 297–309. <https://doi.org/10.1007/s11803-017-0383-z>
- Jayasinghe, J. A. S. C., Hori, M., Riaz, M. R., & Wijerathne, M. L. L. (2015). Meta-Modeling-Based Consistent Mass Spring Model for Seismic Response Analysis of Bridge Structure. *Journal of Japan Society of Civil Engineers*, 71(2), I\_137-I\_148.
- Jayasinghe, J. A. S. C., Hori, M., Riaz, M. R., Tamechika, N., Maddegadara, L., & Ichimura, T. (2015). Construction of consistent mass spring model based on meta-modeling theory for simplification of solid element model for seismic

- analysis. *Proceedings of the 6th International Conference on Structural Engineering and Construction Management*, Kandy, Sri Lanka.
- Jayasinghe, J. A. S. C., Hori, M., Riaz, M. R., Tamechika, N., Wijerathne, M. L. L., & Ichimura, T. (2016). Application of Meta-Modeling for Quality Assurance of Automated High Fidelity Bridge Structure Models. *Journal of Japan Society of Civil Engineers*, 72(4), 1\_98–1\_109.
- Jayasinghe, J. A. S. C., Tanaka, S., Wijerathne, L., Hori, M., & Ichimura, T. (2015). Conversion Between Solid and Beam Element Solutions of Finite Element Method Based on Meta-Modeling. *Proceedings of the 2nd International Conference on Civil and Building Engineering Informatics*, Tokyo, Japan.
- Jayasinghe, J. A. S. C., Tanaka, S., Wijerathne, L., Hori, M., & Ichimura, T. (2014). Rigorous Conversion of Solid and Beam Element Solutions Based on Meta-Modeling. *Journal of Japan Society of Civil Engineers*, 70(2), 223–233.
- Jayasinghe, J. A. S. C., Tanaka, S., Wijerathne, L., Hori, M., & Ichimura, T. (2015). Automated Construction of Consistent Lumped Mass Model for Road Network. *Journal of Japan Society of Civil Engineers*, 71(4), I\_547–I\_556.
- Kettill, P., & Wiberg, N. E. (2002). Application of 3D solid modeling and simulation programs to a bridge structure. *Engineering with Computers*, 18(2), 160–169. <https://doi.org/10.1007/s003660200014>
- Krawinkler, H., & Senevirathna, G. D. P. K. (1998). Pros and cons of a pushover analysis for seismic performance evaluation. *Engineering Structures*, 20(4–6), 452–464.
- Kusakabe, R., Ichimura, T., Fujita, K., Hori, M., & Wijerathne, L. (2022). Scalable large-scale multi-physics earthquake simulation on multiple GPUs with stabilization. *Journal of Computational Science*, 61, 101619. <https://doi.org/10.1016/j.jocs.2022.101619>
- Lee, H., Roh, H., Youn, J., & Lee, J. S. (2012). Frequency Adaptive Lumped-Mass Stick Model and Its Application to Nuclear Containment Structure. *Proceedings of the Fifteenth World Conference on Earthquake Engineering*, Lisbon, Portugal.
- Lee, H., Ou, Y.-C., Roh, H., & Lee, J. S. (2015). Simplified model and seismic response of integrated nuclear containment system based on frequency adaptive lumped-mass stick modeling approach. *KSCE Journal of Civil Engineering*, 19(6), 1757–1766. <https://doi.org/10.1007/s12205-014-1295-3>
- Malhotra, P. K. (1997). Method for seismic base isolation of liquid-storage tanks. *Journal of Structural Engineering*, 123(1), 113–116. [https://doi.org/10.1061/\(ASCE\)0733-9445\(1997\)123:1\(113\)](https://doi.org/10.1061/(ASCE)0733-9445(1997)123:1(113))
- Moussa, L., & Ali, Z. (2010). Approximate Earthquake Analysis for Regular Base Isolated Buildings Subjected to Near Fault Ground Motions. *Proceedings of the World Congress on Engineering 2010 (Vol. II)*, London, U.K., June 30 – July 2.
- Mwafy, A. M., & Elnashai, A. S. (2001). Static pushover versus dynamic collapse analysis of RC buildings. *Engineering Structures*, 23(5), 407–424. [https://doi.org/10.1016/S0141-0296\(00\)00068-7](https://doi.org/10.1016/S0141-0296(00)00068-7)
- Paraskeva, T. S., Kappos, A. J., & Sextos, A. G. (2006). Extension of modal pushover analysis to seismic assessment of bridges. *Earthquake Engineering & Structural Dynamics*, 35(10), 1269–1293. <https://doi.org/10.1002/eqe.582>
- Quinay, P. E. B., Ichimura, T., Hori, M., Nishida, A., & Yoshimura, S. (2013). Seismic structural response estimates of a fault-structure system model with fine resolution using multiscale analysis with parallel simulation of seismic-wave propagation. *Bulletin of the Seismological Society of America*, 103(3), 2094–2110. <https://doi.org/10.1785/0120120216>
- Quinay, P. E. B., Ichimura, T., Hori, M., Wijerathne, M. L. L., & Nishida, A. (2011). Seismic structural response analysis considering fault-structure system: Application to nuclear power plant structures. *Progress in Nuclear Science and Technology*, 2, 516–523.
- Reddy, J. N. (2013). *An introduction to continuum mechanics* (2nd ed.). Cambridge: Cambridge University Press.
- Reinhorn, A. M., Oikonomou, K., Roh, H., Schiff, A., & Kempner, L. (2011). Modeling and seismic performance evaluation of high voltage transformers and bushings.
- Riaz, M. R., Motoyama, H., & Hori, M. (2021). Review of soil-structure interaction based on continuum mechanics theory and use of high-performance computing. *Geosciences*, 11(2), 72. <https://doi.org/10.3390/geosciences11020072>
- Roh, H., Lee, H., & Lee, J. S. (2013). New lumped-mass-stick model based on modal characteristics of structures: Development and application to a nuclear containment building. *Earthquake Engineering and Engineering Vibration*, 12(2), 307–317. <https://doi.org/10.1007/s11803-013-0173-1>
- Roh, H., Oliveto, N. D., & Reinhorn, A. M. (2012). Experimental test and modeling of hollow-core composite insulators. *Nonlinear Dynamics*, 69(4), 1651–1663. <https://doi.org/10.1007/s11071-012-0376-4>
- Seleemah, A. A., & El-Sharkawy, M. (2011). Seismic response of base isolated liquid storage ground tanks. *Ain Shams Engineering Journal*, 2(1), 33–42. <https://doi.org/10.1016/j.asej.2011.05.001>
- Takada, T., & Yamaguchi, K. (2002). Two-step seismic limit state design procedure based on non-linear LFRD and dynamic response analyses. *Structural Safety*, 24(4), 397–415.
- Tuñón-Sanjur, L., Orr, R. S., Tinic, S., & Ruiz, D. P. (2007). Finite element modeling of the AP1000 nuclear island for seismic analyses at generic soil and rock sites. *Nuclear Engineering and Design*, 237(12–13), 1474–1485. <https://doi.org/10.1016/j.nucengdes.2006.10.006>
- Varma, V., Reddy, G. R., Vaze, K. K., & Kushwaha, H. S. (2002). Simplified approach for seismic analysis of structures. *International Journal of Structural Stability and Dynamics*, 2(2), 207–225. <https://doi.org/10.1142/S021945540200052X>
- Villaverde, R. (1987). Simplified approach for the seismic analysis of equipment attached to elastoplastic structures. *Nuclear Engineering and Design*, 103, 267–279.
- Wilson, J. L. (2003). Earthquake response of tall reinforced concrete chimneys. *Engineering Structures*, 25(1), 11–24. [https://doi.org/10.1016/S0141-0296\(02\)00098-6](https://doi.org/10.1016/S0141-0296(02)00098-6)
- Zienkiewicz, O. C., Taylor, R. L., & Fox, D. D. (2014). *The finite element method for solid and structural mechanics* (7th ed.). Oxford, Waltham, Mass.: Butterworth-Heinemann.

## RESEARCH ARTICLE

# Deep Learning

## Athlete body power and strength estimation using skeleton point cloud

H Rangala<sup>1</sup>, S Samaraweera<sup>1</sup>, KD Sandaruwan<sup>1\*</sup>, TA Weerasinghe<sup>1</sup> and DC Ranasinghe<sup>2</sup>

<sup>1</sup> University of Colombo School of Computing, 35, Reid Avenue, Colombo 7, Sri Lanka.

<sup>2</sup> Center for Sports and Exercise Medicine, Department of Allied Health Sciences, Faculty of Medicine University of Colombo, Colombo, Sri Lanka.

Submitted: 05 July 2024; Revised: 20 November 2024; Accepted: 27 November 2024

**Abstract:** Vertical jump assessment is one of the most frequently used techniques to evaluate lower limb strength and power in the context of strength and conditioning. Countermovement jump (CMJ) and squat jump (SJ) have been recognized as the most valid and reliable vertical jump tests to assess body power and strength. The traditional method requires professional involvement and equipment for parameter assessment. In the context of college athletes, it is not practical to acquire direct supervision from coaches and use laboratory-based equipment such as force plates. Hence, the main objective of this study is to reduce the physical involvement in the traditional method by developing a system to identify lower body power and strength, which can be handled at an athlete's own pace. Thus, we propose a single camera system that captures athlete skeleton joint variation from the lateral view to identify the accuracy of CMJ and SJ along with measurements for power, maximum jump height, reactive strength index, and ground reaction force. These performance parameter values are measured using a rule-based model developed with motion equations and skeleton joint variations. The biomechanics of the exercises are identified based on the clinically accepted jump protocol. The experimental results show that the system identifies athlete biomechanics with an accuracy of 91.7% for CMJ and an accuracy of 95.8% for SJ. Also, the system measures maximum jump height with a standard error of 0.88 cm.

**Keywords:** Biomechanics, countermovement jump, moveNet, Skeleton point cloud, Squat jump.

## INTRODUCTION

Lower body strength and power identification provide valuable insights into different capacities such as an athlete's movement coordination and timing. This information can be used in connection with the art of coaching to maximize athlete training program effectiveness. But training an athlete's power and strength to improve his/her sport performance is a challenging aspect of coaching. In the traditional strength and power identification process, sports instructors offer expert advice, monitoring correctness of counter movement jump and squat jump along with parameter measurements such as maximum height jumped by the athlete. In the local context, the most fundamental method of identifying athletes' performance is the jump and reach test. However, due to inability to take accurate and reliable measurements, several researchers have proposed laboratory and field-based methods such as force plates and contact mats, to replace the use of jump and reach test for measuring athletes' power and strength. However, many athletes tend to be involved in sports without identification of their body capacities due to issues such as difficulty in acquiring expensive equipment and obtaining the involvement of domain

\* Corresponding author ([kdsandaruwan@gmail.com](mailto:kdsandaruwan@gmail.com);  <https://orcid.org/0000-0002-1473-1125>)



experts (Velloso *et al.*, 2013). If athletes are not routinely assessed to identify body powers, their performance capacities will not be identified properly. Even though athletes try to use limited resources, it is crucial to perform strength and power jumps in clinically accepted procedures because jumps without proper guidance have a consequential impact on jump adherence and technique (O'Reilly *et al.*, 2017). With the increasing availability of portable devices such as laptops and mobile phones with sensing features, studies have proposed many self-assessment approaches with use of wearable and nonwearable sensors. Human action recognition (HAR) has attracted the attention of research communities in the computer vision area in recent years. Use of action recognition has made tremendous progress in the strength and conditioning context, such as AI based physical fitness training, self-assessment of body capacities, and sport-specific movement analysis. The introduction of low-cost depth sensors like Microsoft Kinect and Orbbec Astra Pro and pose estimation methods such as the moveNet model have made the use of human action recognition easier. The primary motivation for this research study is to propose a solution for athletes to routinely self-assess their lower body power and strength along with feedback for the correctness of counter movement jump (CMJ) and squat jump (SJ) by using a full body tracking approach. The goal of this research is to reduce the professional involvement for physical inspection in the strength and power estimation of athletes and minimize the subjectiveness that happens when taking measurements.

### Related work

Recent technological advances have sparked interest in the research community to use different technologies in the strength and conditioning context (Gallagher & Heymsfield, 2023). Much research has been conducted and many commercial applications developed to provide virtual physical fitness training. Some of the physical fitness solutions that are built without any external sensor hardware are Fitness Expert, Adidas micoach, Abs & core, AndAndo (Kranz *et al.*, 2013). However, there are only a limited number of studies conducted in self-assessment of an athlete's body capacities. Suchomel *et al.* (2016) have presented that an athlete's muscular strength is highly correlated to running, superior jumping and other sport specific performances. The related work of our study is classified into two categories. Those are the studies related to an athlete's biomechanical identification and work related to performance parameter identification of athletes.

### Performance parameter identification

In the local context, the most fundamental method of identifying an athletes' performance is the jump and reach test. However, due to inability to take accurate and reliable measurements in this method, several researchers have proposed laboratory and field-based technologies. In a study, Beckham *et al.* (2012) discussed the identification of an athlete's strength using a force platform by considering flight time and net pulse as the performance parameters. Even though force plates allow the athletes to collect high-quality data such as maximal strength, rate of force development, and explosive performance, they are complex devices, which makes it difficult to master their use in field-based assessments. Whitmer *et al.* (2015) have proposed contact mats to estimate athletes vertical jump height. The contact mat calculates the vertical jump height similarly to a force plate, which is commonly used in laboratory settings. Glatthorn *et al.* (2011) have pointed out that the validity of contact mat measurement degrades due to the fact that feet are not directly in contact with the sports surface. Hence, they have proposed optjump photocells, which use the athlete's jump flight time to calculate jump height. An athlete's device contact time is estimated using the time where the laser beam is broken and the flight time as the period where the laser beam is broken. However, due to the difficulty in handling the proposed devices in the field, many studies have focused on inertial sensors. Wearable and minimally invasive sensors have seen a surge in popularity in recent years, as they can provide useful information for athletes' functional evaluation in sports. Risk analysis and performance enhancement can be refined through wearable devices in sports applications (Franchini *et al.*, 2022). A study has proposed a method to predict jump heights, including jumps with simple rotations using a single inertial measuring unit (IMU) (King & Paulson, 2007). In order to track a full body motion, it is required to use several inertial sensors. Without the use of markers on the human body, it is now possible to analyze the motions of humans in a natural context of activity. The development and availability of accessible and easy-to-use motion capture technologies are aided by these new motion analysis approaches (King & Paulson, 2007). According to the literature, most of the studies have proposed solutions to identify maximum jump height and ground reaction force (GRF). Mascherini *et al.* (2019) have concluded that several parameters should be evaluated at the same time as vertical jump height in order to have a correct functional assessment of athletes and healthy non-sporting subjects.

## Biomechanical identification

Biomechanics is the study and science of the way in which the structure of biological creatures responds to exterior forces and stimuli (Lu & Chang, 2012). Pueo (2016) has proposed a method that uses high tech cameras that can visualize an athlete in 3D space. Chang *et al.* (2007) have used a 3-axis accelerometer incorporated into a workout glove to detect hand movement of weight-lifting athletes. In this approach, the accuracy of the exercise is not considered. The work is limited only to recognizing the exercise based on highest likelihood. In a study, Lu *et al.* (2021) have proposed a method to recognize the human lower limb vertical jump phases using bidirectional LSTM and convolutional LSTM. This work limits the vertical jump phase based on previously trained jump phases. Abdur Rahman *et al.* (2013) have proposed a multimedia interactive therapy environment for children having physical disabilities. The study focuses only on elbow joint variation and compares angle calculation with a conventional device called a goniometer. Ding *et al.* (2015) have developed a platform for Free-weight Exercise Monitoring using RFIDs, which determines what exercise a user is undertaking based on the frequency of the weight's movements. Even though the proposed work identifies the free weight exercise, this work fails to identify the correctness of the kinematics with time. The aforementioned methods have focused on movement recognition. Several studies have used skeletal point tracking to evaluate certain stances used in sports like taekwondo (Fernando *et al.*, 2024) and badminton (Krishnaram *et al.*, 2024). However, a mechanism for identifying the biomechanics of counter movement jump and squat jump using self-assessment technologies has not yet been explored. With the invention of the depth camera, clear information on 3D structural views was received. Cameras with depth sensors such as Microsoft Kinect, RealSense, and Orbbec Astra Pro have been used for human skeleton joint tracking (Farooq & Won, 2015). Some studies show the use of multiple cameras for motion capture, particularly useful in sports and neurorehabilitation settings (Bianchi *et al.*, 2023). Sapinski *et al.* (2019) have proposed a method to recognize seven basic emotional states utilizing body movement tracked using Microsoft Kinect. Lai *et al.* (2017) have used multiple acceleration sensors and gyroscopes to identify body motion patterns. Bajpai & Joshi (2021) have proposed a model named moveNet which is a predictive 14 neural network that identifies skeleton joints of humans. Hence, we intend to evaluate which method out of the moveNet model and Orbbec camera is best suited for tracking counter movement jump and

squat jump, and provide a solution to assess lower body power and strength at athlete's own pace, including both biomechanics and performance variables.

## MATERIALS AND METHODS

As mentioned in the previous section, there are no studies that have been conducted using skeleton tracking to carry out the biomechanical assessment and performance parameters simultaneously to estimate lower body power and strength of athletes. One of the main objectives of this study is to identify the correctness of countermovement jump and squat jump by using a biomechanical model in combination with the quantitative measurements for power, maximum jump height, ground reaction force, and reactive strength index identified, using a model named performance parameter model.

### Identify clinically accepted jump biomechanics and parameters

Initially, the clinically accepted procedure of estimating athlete body power and strength was obtained by referring to the journals suggested by domain experts. According to Markovic *et al.* (2004), countermovement jump and squat jump have shown high reliability and validity in testing lower limb performance. The jump protocol presented by Petrigna *et al.* (2019) was taken as the clinically accepted procedure for a countermovement jump and a squat jump. These instructions are transformed into an approach which uses the skeleton joint data of an athlete. Table 1 represents the derived transformations. The left side of the table contains the clinical procedure of countermovement jump and the right side represents the procedure in terms of skeleton joint variation.

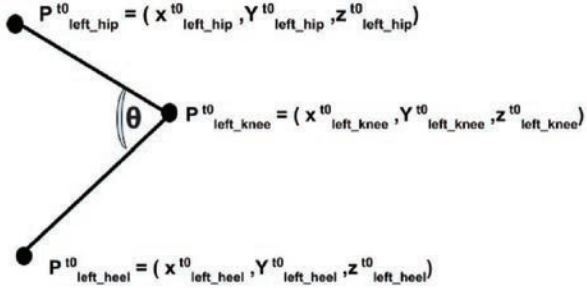
### Skeleton tracking technology selection

According to the literature, depth cameras and pose estimation models have shown a high reliability for markerless motion capturing applications (D'Haene *et al.*, 2024). In this study both the approaches are used to track countermovement jump and squat jump. The MoveNet pose estimation model and the skeleton tracking algorithm of the Orbbec astra camera was chosen to evaluate accuracy for the skeleton tracking method. The athlete's movement along the coronal plane is tracked with the variation of  $x$  coordinate, movement along the sagittal plane is tracked with the variation of  $y$  coordinate, and the movement along the transverse plane is tracked using the  $z$  coordinate. In order to determine the accuracy of the skeleton detection algorithm in the

camera, a code was implemented to calculate the angles between the joints. After analyzing the skeleton joint angles for the movement of an athlete in the erect position (straight knees) and downward movement until the knee angles are approximately 90°, it was found that the joint

values predicted from the skeleton detection algorithm in the depth camera was not consistent with the speed of the jump. Figure 1 represents the plot of left knee angle (red), right knee angle (blue) variations with time and the difference of those angles (green).

**Table 1:** Transformation of counter movement jump

Clinical and theoretical evaluation	Skeleton point cloud mapping
<p><b>Biomechanical assessment</b></p>  <p data-bbox="177 1081 483 1108">Straight legs and spine at start time</p>	<p data-bbox="730 596 1098 623">A 3D point at <math>t_n</math> time in <math>i^{\text{th}}</math> joint is noted as</p> $P^i_{t_n} = (x^i_{t_n}, Y^i_{t_n}, z^i_{t_n})$ <ul data-bbox="730 688 1214 716" style="list-style-type: none"> <li>• Consider hip, knee, heel joint points at starting time <math>t_0</math></li> </ul> $P^{t_0}_{\text{left\_hip}} = (x^{t_0}_{\text{left\_hip}}, y^{t_0}_{\text{left\_hip}}, z^{t_0}_{\text{left\_hip}})$ $P^{t_0}_{\text{right\_hip}} = (x^{t_0}_{\text{right\_hip}}, y^{t_0}_{\text{right\_hip}}, z^{t_0}_{\text{right\_hip}})$ $P^{t_0}_{\text{left\_knee}} = (x^{t_0}_{\text{left\_knee}}, y^{t_0}_{\text{left\_knee}}, z^{t_0}_{\text{left\_knee}})$ $P^{t_0}_{\text{right\_knee}} = (x^{t_0}_{\text{right\_knee}}, y^{t_0}_{\text{right\_knee}}, z^{t_0}_{\text{right\_knee}})$ $P^{t_0}_{\text{left\_heel}} = (x^{t_0}_{\text{left\_heel}}, y^{t_0}_{\text{left\_heel}}, z^{t_0}_{\text{left\_heel}})$ $P^{t_0}_{\text{right\_heel}} = (x^{t_0}_{\text{right\_heel}}, y^{t_0}_{\text{right\_heel}}, z^{t_0}_{\text{right\_heel}})$ <ul data-bbox="730 1003 1257 1031" style="list-style-type: none"> <li>• Calculate angle between three 3D vectors of hip, knee, heel</li> </ul>  <p data-bbox="730 1409 1145 1436">A 3D point at time <math>t_n</math> in the <math>i^{\text{th}}</math> joint is noted as P</p> $a = P^{t_0}_{\text{left\_knee}} P^{t_0}_{\text{left\_hip}}$ $b = P^{t_0}_{\text{left\_heel}} P^{t_0}_{\text{left\_knee}}$ $a \cdot b =  a  *  b  * \cos(\theta)$ $\cos(\theta) = \frac{a \cdot b}{ a  *  b }$ <ul data-bbox="730 1675 1342 1745" style="list-style-type: none"> <li>• Calculate the angle between three 3D vectors of hip, knee, heel joints</li> <li>• Calculate the angle between three 3D vectors of neck</li> </ul>

**Clinical and theoretical evaluation**

**Biomechanical assessment**

Downward movement until knee angles are flexed (approximately) 90°

Check for the maintenance of this posture for at least 2s.



Knee angles are flexed  $\approx 90^\circ$

**Parameter assessment**

Start calculating the time duration between the subject's take-off ( $t_3$ ) and touch down ( $t_4$ )

Calculate the maximum height jumped

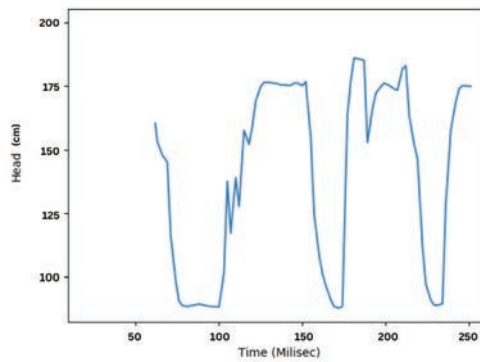
Calculate the maximum force generated by lower limbs during landing

**Skeleton point cloud mapping**

- Calculate the angle between three 3D vectors of the hip, knee, and heel joints
- Calculate the angle between three 3D vectors of knee, mid spin, neck
- Need to check whether the joint positions are fixed within the considered time.

Process  $y_{head}^{10}$  point coordinates of the head joint

- Identify time  $t_2$  when head joint's y values are changing
- Identify time  $t_3$  when head joint's y value is maximum
- Identify time  $t_4$  when heel joint's y values become stable



Represents the raw data of the head joint's y plane variation with time when Counter Movement Jump is performed

- Calculate the maximum force generated by using following motion equations and Newtonian law formula

Acceleration  $a = F / m$ , Velocity  $V = u + at$ , Displacement  $s = (1 / 2)(v - u)t$ ,

Power  $P = FV$

**Biomechanical assessment**

After landing, the end position should be the same as the starting.

Since the biomechanical assessment of the end position is similar to the starting position, the mapping identified in the starting position will be used in this phase

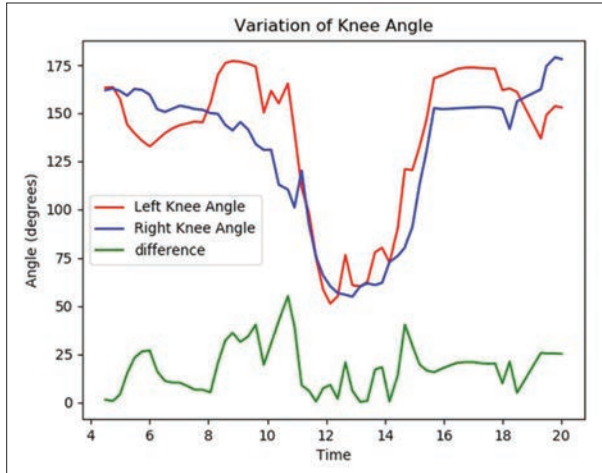


Figure 1: Variation of knee angles in low cost depth camera

Since the graphical representation showcases some higher angle differences for left and right knee angles, the moveNet pose estimation model had better accuracy. Figure 4 represents the plot of the left knee angle (red), right knee angle (blue) variations with time and the difference of those angles (green) by using the moveNet model for countermovement jump and squat jump.

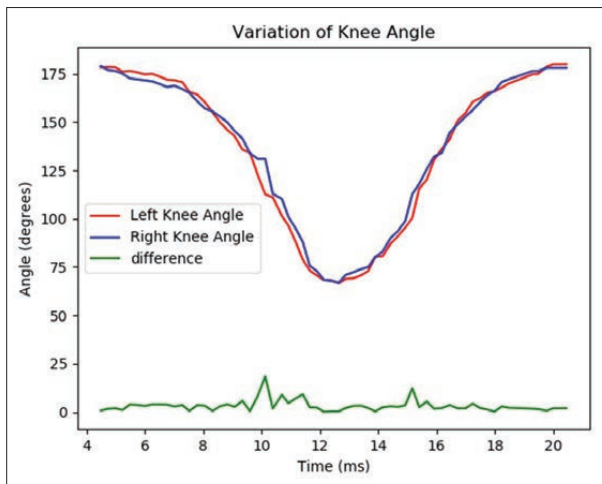


Figure 2: Variation of knee angles with time in moveNet model

The depth camera and moveNet model evaluation was conducted using an evaluation metric. The sum of all the angle differences throughout the movement is calculated using the metric. The metric, average joint difference, is defined in equation 1,

$$d_{avg} = \frac{\sum_{i=1}^N \|LK_{orbec,i} - RK_{orbec,i}\|}{N} \dots(1)$$

In particular, after calculating joint angles using the skeleton point cloud received from the depth camera and the moveNet model, we compared the left knee angle and the corresponding right knee angle for all frame updates N, respectively named  $LK_{orbec,i}$  and  $RK_{orbec,i}$ . And the moveNet returned a low average of joint angle differences. Hence the moveNet model was chosen for tracking the athlete’s skeleton in real time.

**Biomechanical model development**

The rule based approach is used to construct the two models, performance parameter model and biomechanical model. The main reason for using a rule based approach is to capture the knowledge of human experts and journals in a specialized domain (sport science) and embody it within a computational model. Hence the knowledge is encoded as rules. The identified transformations are used to develop the biomechanical model. The angle between two lines in 2D space is equal to the angle subtended by the two vectors which are parallel to those lines. The angle between the two vectors  $a = (x1,y1)$ ,  $b = (x2,y2)$  are calculated using the equations 2 and 3.

$$a \cdot b = |a| * |b| * \cos(\theta) \dots(2)$$

$$\cos(\theta) = \frac{a \cdot b}{|a| * |b|} \dots(3)$$

**Performance parameter model development**

Movement within sport is considered to measure the parameters quantitatively. The concept of linear motion is applied to identify the maximum height jumped by the athlete. When performing countermovement jump and squat jump, it is assumed that all parts of the athlete are moved at the same speed during flight time. Newton’s second law is used to identify the power generated by the athlete. According to the theory, the acceleration of an athlete during the flight time of the two jumps is proportional to the size of the force and inversely proportional to the athlete’s body mass ( $F = ma$ ). The takeoff time is identified using the presence and absence of ankle lift. Since the ankle lift movement occurs along the y plane, the instance where the values of the ankle joint start to change and joint y value comes to the value initial state was used. The maximum height jumped by the athlete is calculated using a function accepting an

array of values for ankle joint y plane variation, takeoff time, flight time and scale as inputs. The average of left ankle variation and right ankle variation is taken as the maximum height. The following equations are used to calculate performance parameters:  $Power =$

Energy/time,  $Reactive\ strength\ index = \text{jump height} / \text{time for jump}$ ,  $Upward\ acceleration = \text{jump height} / (\text{time for jump} * 2)$ , and  $GRF = (\text{Upward acceleration} * \text{weight}) + (\text{weight} * 9.8)$

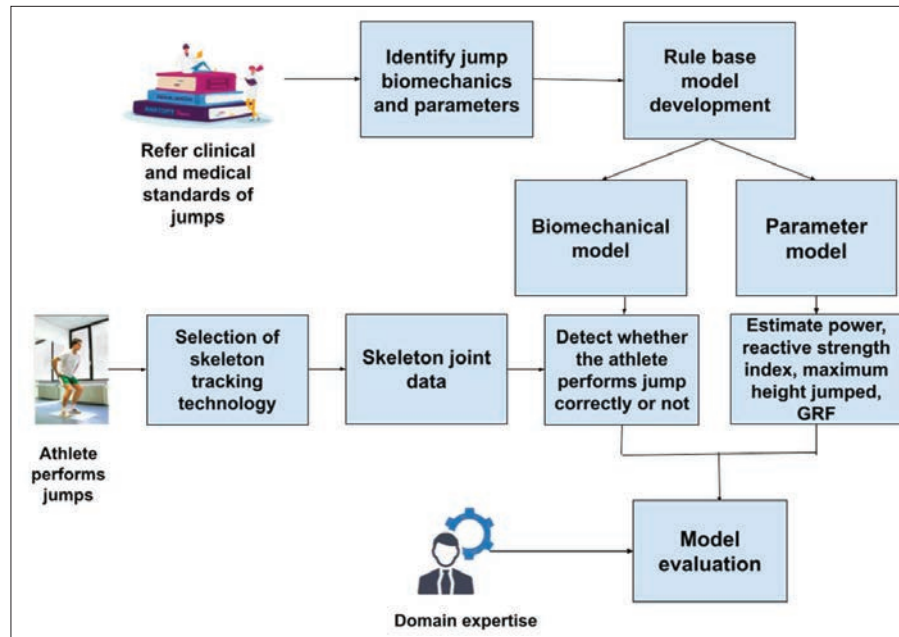


Figure 3: Overview of the research workflow

### High-level research design

The proposed solution is a combination of biomechanical assessment and performance parameter assessment. These two assessments are performed by developing two rule-based models separately. The high level architecture of this study depicts the step-wise procedure of concluding the study. Finally, the two models are fine-tuned based on the feedback from domain experts. The Figure 3 represents the overview of the research workflow.

### Athlete classification based on sport domain

This stage represents an application of the use of power and strength calculated from the proposed system. According to previous studies, athletes have shown different strength and power levels based on their sport domain. In this study, Kmeans clustering was used to

identify whether there is a clear separation of athletes based on their strength and power values. The reason for the use of K-means algorithm is its adaptation to new examples and its ability to warm-start the positions of centroids.

## RESULTS AND DISCUSSION

As discussed, both the biomechanical assessment and performance parameter assessment are focused in this study. The skeleton joint variation obtained from the moveNet pose estimation model is used as input for the biomechanical model and performance parameter model. When the model is executed, it continuously returns the joint values at 30+ FPS as lists for each joint updation, as shown in Figure 4 below. Each list has 17 array values representing each joint. The code outputs an athlete's video along with the correct skeleton joints.

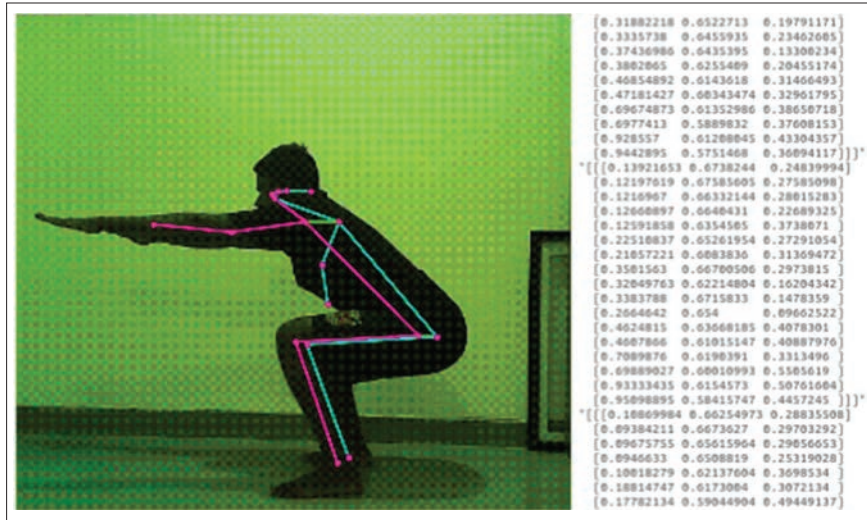


Figure 4: A snapshot of the MoveNet model outputs for CMJ running at 30+ FPS

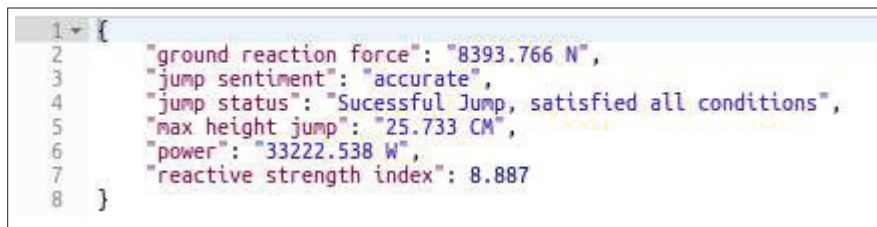


Figure 5: Computational output for an athlete’s counter-movement jump

Finally, the joint values received from the moveNet model are fed into the performance parameter model and biomechanical model. Additionally, the athlete’s body weight needs to be taken as an input to measure performance parameters. The parameters that have been calculated are ground reaction force, maximum jump height, power, and reactive strength capacity. In addition to these parameters, jump status is identified. The computational output of a Netball player when performing countermovement jump is represented in Figure 5

The accuracy of the proposed system is identified with the involvement of domain experts. A set of subjects were evaluated as they performed the CMJ and SJ in front of the camera and the domain experts. The evaluation results obtained from the system are compared with the

evaluation results of a domain expert to conclude how accurate the system output is. Domain experts observed the jump and clinically analyzed the accuracy of the jumps. Further, the strength and power measurements were taken with the help of a sport instructor. Then the results of our study were compared against the expert opinion and the model fine tuned.

### Subjects

Twenty five (25) subjects including 10 male athletes (university hockey team) and 14 female athletes (university netball team), 20 - 25 years of age, were enrolled to volunteer for the model evaluation. The average age of subjects is 23.7. The selection was done with the help of a domain expert.

**Jump protocol**

An indoor space at the sports complex of the University of Colombo was used for experimental tests. Since the moveNet model produces only sagittal (x) plane and coronal (y) plane values, to avoid the effect from transverse (z) plane variation, the athlete was asked to perform the jumps at a predefined position where the distance between the camera and the subject was 2 m and camera was placed 65 cm above and parallel to the floor. At the beginning, the weight of each subject was measured and they were asked to warm up for 5 minutes. And then they were instructed to perform counter-movement jump and squat jump barefoot. While athletes perform jumps one after the other, the jump height was measured using a tape attached to the wall. Athletes were asked to apply some liquid in their hand and were asked to touch the wall at their maximum jump point. The difference between normal touch point and maximum touch point was taken as the ground truth for maximum jump height parameter.

**Evaluation of the biomechanical model**

In this research a confusion matrix-based evaluation was used to clarify the accuracy of the biomechanical model. The model was evaluated separately for counter movement jump (CMJ) and squat jump (SJ). Then the model was fine-tuned based on domain expert opinion and was re-evaluated. Subjects are binary classified based on the correctness of their jump. Thus the confusion matrix presents four possible outcomes derived by comparing model output and domain experts feedback. The following is the list of terminology used in the confusion matrix.

True Positive (TP) - the case where the model output is that subject performs the jump correctly and the domain expert confirms the subject actually does.

True negative (TN) - the case where the model output is that the subject does not perform correctly and the domain expert confirms that the subject actually does not perform correctly.

False positive (FP) - the case where the model output is that the subject performs correctly and the domain expert clarifies the subject does not perform correctly.

False negative (FN) - the case where the model output is that the subject does not perform jumps correctly and the domain expert clarifies the subject performs correctly.

The confusion matrix for CMJ and SJ of the initial evaluation, the accuracy of the biomechanical model for CMJ before fine tuning is 79.2% and the mis-classification rate is 20.8%. The accuracy of the biomechanical model for SJ before fine tuning is 83.3% and the mis-classification rate is 16.7%.

To achieve better accuracy, the biomechanical model was fine-tuned. According to the domain expert feedback, an additional rule was added to the model where it checked the forward-leaning of athletes. The confusion matrix for the fine-tuned model is represented in Table 2 and Table 3 respectively. The accuracy of the biomechanical model for CMJ after fine tuning is 91.7%  $(8+14) / 24*100\%$  and the mis-classification rate is 8.3%  $(1+1) / 24*100\%$ . The accuracy of the model for SJ after fine tuning is 95.8%  $(10+13) / 24 * 100\%$  and the mis-classification rate is 4.2%  $(0+1)/24* 100\%$ .

**Table 2:** Confusion matrix for cmj after model fine tuning

		Computational output	
		Positive (correct jump)	Negative (incorrect jump)
Domain expert opinion	Positive (correct jump)	TP = 8	FN = 1
	Negative (incorrect jump)	FP = 1	TN = 14

**Table 3:** Confusion matrix for sj after model fine tuning

		Computational output	
		Positive (correct jump)	Negative (incorrect jump)
Domain expert opinion	Positive (correct jump)	TP = 10	FN = 1
	Negative (incorrect jump)	FP = 0	TN = 13

### Evaluation of the performance parameter model

In this research, an athlete's four parameters were identified using skeleton joint variation. Those are the power, maximum jump height, reactive strength capacity, and GRF. The maximum jump height parameter is evaluated by comparing the value given by the proposed system and the value calculated using the jump and reach test where a measuring tape was attached to the wall and the athlete was asked to touch the maximum reach point. The average standard error between the computed values and clinical methods is used to evaluate the performance parameter model. The calculated absolute standard error for jump height variable is 0.88 cm. In the performance parameter model, parameter values are estimated only if the biomechanical model detects that an athlete's jump has an accurate jump movement.

### Athlete classification based on sport domain

This phase is an application of the data computed using the proposed models. All the data of athletes whose jump status was identified as correct were considered for classification. K means clustering was applied to cluster athlete data. Figure 6 represents the two clearly separated clusters. When manually analyzed, it can be seen that red spots represent the hockey players and purple spots represent the netball players.

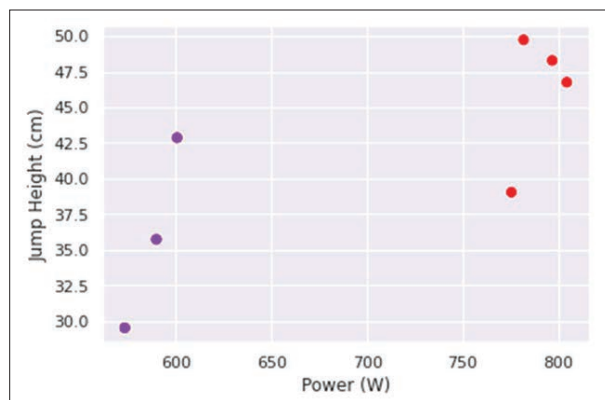


**Figure 6:** Classification of hockey players (red) and netball players (purple) using power and maximum jump height

According to Thomas *et al.* (2017), netball players have been classified as strong and weak based on their power and jump height values. Our study used these parameter values as a reference to classify athletes based on their parameter values calculated using our proposed solution.

Based on the available literature, this is a novel approach to identify body power and strength in athletes using skeleton tracking. A rule-based model was created to identify the counter movement jump and squat jump accuracy of athletes and to quantitatively measure power, reactive strength capacity, maximum jump height and ground reaction force simultaneously. The first objective of this research is to identify an appropriate skeleton tracking technology to accurately track counter movement jump and squat jump. In this research a low-cost depth camera named Orbbec Astra Pro and a pose estimation model named moveNet were evaluated for skeleton joint tracking. Based on the accuracy, the moveNet pose estimation model was chosen for skeleton joint tracking of athletes. The next objective of this study is to investigate how skeleton joint data can be used to measure body assessment parameters used in strength and power estimation. Initially, knowledge about clinically and medically accepted procedures for determining power and strength was obtained through literature. Then transformations were used to convert clinical approaches to a method that used skeleton joint variation with time. Two-rule based models were proposed based on the derived transformations to identify athletes performance parameters and biomechanics respectively. After fine tuning the biomechanical model, an accuracy of 95.8% and a mis-classification rate of 4.2% was achieved. Hence, better accuracy was able to be achieved in the biomechanical model. An additional rule was added to the model based on the domain expert's feedback. In the performance parameter model, the maximum jump height was estimated with a standard error deviation of 1.7 cm. However, the standard error deviation is comparatively higher than the approaches proposed by O'Reilly *et al.* (2017) and Kranz *et al.* (2013). In this study only the athlete's jump height could be evaluated due to the unavailability of force plates in local context to test GRF and other two parameters.

### CONCLUSION

Identification of body power and strength is a widely discussed topic in the field of sports science. The most frequently used vertical jump tests to assess body capacities are countermovement jump and squat jump. This research was focused on identifying athlete body power and strength using skeleton joint tracking which can be handled at the athlete's own pace. The system demonstrates a high level of accuracy in identifying athlete biomechanics, achieving 91.7% accuracy for countermovement jumps and 95.8% accuracy for squat jumps. This shows that the model is reliable and effective

in analyzing and distinguishing the biomechanics of the mentioned jumps performed by athletes. The model's ability to measure maximum jump height with a standard error of 0.88 cm suggests a high degree of precision. This study also gives insights into different athletes showing different body power and strength levels based on the sport. A clear classification can be observed in body power and strength levels of netball players vs hockey players.

Furthermore, this model can be used in connection with learning approaches such as machine learning along with some additional data such as body temperature, and heart rate to identify more hidden patterns and information in athletes' performances. Future work should explore methods to enhance the 3D spatial accuracy of the model for better capturing and analyzing the athlete's movements. Additionally, the proposed system can be developed into a user application that is compatible with a portable device such as a laptop or a smartphone.

## REFERENCES

- Abdur Rahman, M., Qamar, A. M., Ahmed, M. A., Ataur Rahman, M., & Basalamah, S. (2013). Multimedia interactive therapy environment for children having physical disabilities. *Proceedings of the 3rd ACM Conference on International Conference on Multimedia Retrieval*, 313–314. <https://doi.org/10.1145/2461466.2461515>
- Bajpai, R., & Joshi, D. (2021). Movenet: A deep neural network for joint profile prediction across variable walking speeds and slopes. *IEEE Transactions on Instrumentation and Measurement*, 70, 1–11. <https://doi.org/10.1109/TIM.2020.3035655>
- Beckham, G. K., Lamont, H. S., Sato, K., Ramsey, M. W., Haff, G. G., & Stone, M. H. (2012). Isometric strength of powerlifters in key positions of the conventional deadlift. *Journal of Trainology*, 1(2), 32–35. [https://doi.org/10.17338/trainology.1.2\\_32](https://doi.org/10.17338/trainology.1.2_32)
- Bianchi, F., Mantiuk, R., & Ghiasi, S. (2023). Scalable software architecture for multi-camera motion capture: Application in sports and neurorehabilitation. *Journal of Biomechanics*, 122, 20–30. <https://doi.org/10.1016/j.jbiomech.2023.113728>
- Chang, K.-H., Chen, M. Y., & Canny, J. (2007). Tracking free-weight exercises. In *International Conference on Ubiquitous Computing* 19–37. Springer. [https://doi.org/10.1007/978-3-540-74853-3\\_2](https://doi.org/10.1007/978-3-540-74853-3_2)
- D'Haene, M., Chorin, F., Colson, S. S., Guérin, O., Zory, R., & Piche, E. (2024). Validation of a 3D markerless motion capture tool using multiple pose and depth estimations for quantitative gait analysis. *Sensors*, 24(22), Article 7105. <https://doi.org/10.3390/s24227105>
- Ding, H., Shangguan, L., Yang, Z., Han, J., Zhou, Z., Yang, P., Xi, W., & Zhao, J. (2015). FEMO: A platform for free-weight exercise monitoring with RFIDs, *Proceedings of the 13th ACM Conference on Embedded Networked Sensor Systems*. 141–154. <https://doi.org/10.1145/2809695.2809708>
- Farooq, A., & Won, C. S. (2015). A survey of human action recognition approaches that use an RGB-D sensor. *IEIE Transactions on Smart Processing and Computing*, 4(4), 281–290. <https://doi.org/10.5573/IEIESPC.2015.4.4.281>
- Fernando, W. M. U., Sandaruwan, K. D., & Athapaththu, A. M. K. B. (2024). Evaluation of Taekwondo Poomsae movements using skeleton points. *Journal of the National Science Foundation of Sri Lanka*, 52(1), 143–156. <https://doi.org/10.4038/jnsfsr.v52i1.11986>
- Franchini, E., Brito, C. J., & Artioli, G. G. (2022). Weight loss in combat sports: Physiological, psychological and performance effects. *Journal of the International Society of Sports Nutrition*, 19(1), 4. <https://doi.org/10.1186/s12970-021-00483-5>
- Gallagher, D., & Heymsfield, S. B. (2023). Assessing body composition in athletes: Methods and applications. *Journal of Biological Chemistry*, 299(8), 102354. <https://doi.org/10.1016/j.jbc.2023.102354>
- Glatthorn, J. F., Gouge, S., Nussbaumer, S., Stauffacher, S., Impellizzeri, F. M., & Maffiuletti, N. A. (2011). Validity and reliability of Optojump photoelectric cells for estimating vertical jump height. *Journal of Strength and Conditioning Research*, 25(2), 556–560. <https://doi.org/10.1519/JSC.0b013e3181cc242f>
- King, B. A., & Paulson, L. D. (2007). Motion capture moves into new realms. *Computer*, 40(9), 13–16. <https://doi.org/10.1109/MC.2007.326>
- Kranz, M., Möller, A., Hammerla, N., Diewald, S., Plötz, T., Olivier, P., & Roalter, L. (2013). The mobile fitness coach: Towards individualized skill assessment using personalized mobile devices. *Pervasive and Mobile Computing*, 9(2), 203–215. <https://doi.org/10.1016/j.pmcj.2012.06.002>
- Krishnam, N., Ahamed, J., Sathyamoorthy, N., Sandaruwan, K. D., & Athapaththu, A. M. K. B. (2024). Skeletal point analysis to determine the accuracy of forehand smash shots played by badminton players. *Journal of the National Science Foundation of Sri Lanka*, 52(1), 125–142. <https://doi.org/10.4038/jnsfsr.v52i1.12141>
- Lai, C.-F., Hwang, R.-H., & Lai, Y.-H. (2017). An intelligent body posture analysis model using multi-sensors for long-term physical rehabilitation. *Journal of Medical Systems*, 41(4), 1–15. <https://doi.org/10.1007/s10916-017-0711-4>
- Lu, T.-W., & Chang, C.-F. (2012). Biomechanics of human movement and its clinical applications. *The Kaohsiung Journal of Medical Sciences*, 28(2), S13–S25. <https://doi.org/10.1016/j.kjms.2011.08.004>
- Lu, Y., Wang, H., Qi, Y., & Xi, H. (2021). Evaluation of classification performance in human lower limb jump phases of signal correlation information and LSTM models. *Biomedical Signal Processing and Control*, 64, 102279. <https://doi.org/10.1016/j.bspc.2021.102279>
- Markovic, G., Dizdar, D., Jukic, I., & Cardinale, M. (2004). Reliability and factorial validity of squat and countermovement jump tests. *Journal of Strength and Conditioning Research*, 18(3), 551–555. <https://doi.org/10.1519/00124278-200408000-00028>

- Mascherini, G., Marella, M., Bosi, P., Radini, M., Spicuglia, P., Gulisano, M., & Francia, P. (2019). Can the vertical jump height measure the lower limbs muscle strength. *Italian Journal of Anatomy and Embryology*, *124*(1), 107–112. <https://doi.org/10.13128/ijae-25474>
- O'Reilly, M. A., Whelan, D. F., Ward, T. E., Delahunt, E., & Caulfield, B. (2017). Technology in strength and conditioning tracking lower-limb exercises with wearable sensors. *Journal of Strength & Conditioning Research*, *31*(6), 1726–1736. <https://doi.org/10.1519/JSC.0000000000001852>
- Petrigna, L., Karsten, B., Marcolin, G., Paoli, A., D'Antona, G., Palma, A., & Bianco, A. (2019). A review of countermovement and squat jump testing methods in the context of public health examination in adolescence: Reliability and feasibility of current testing procedures. *Frontiers in Physiology*, *10*, Article 1384. <https://doi.org/10.3389/fphys.2019.01384>
- Pueo, B. (2016). High-speed cameras for motion analysis in sports science. *Journal of Human Sport and Exercise*, *11*(1), 53–73. <https://doi.org/10.14198/jhse.2016.111.06>
- Sapinski, T., Kamińska, D., Pelikant, A., & Anbarjafari, G. (2019). Emotion recognition from skeletal movements. *Entropy*, *21*(7), Article 646. <https://doi.org/10.3390/e21070646>
- Suchomel, T. J., Nimphius, S., & Stone, M. H. (2016). The importance of muscular strength in athletic performance. *Sports Medicine*, *46*(10), 1419–1449. <https://doi.org/10.1007/s40279-016-0486-0>
- Thomas, C., Comfort, P., Jones, P. A., & Dos' Santos, T. (2017). A comparison of isometric mid-thigh pull strength, vertical jump, sprint speed, and change-of-direction speed in academy netball players. *International Journal of Sports Physiology and Performance*, *12*(7), 916–921. <https://doi.org/10.1123/ijsp.2016-0240>
- Velloso, E., Bulling, A., Gellersen, H., Ugulino, W., & Fuks, H. (2013). Qualitative activity recognition of weightlifting exercises. *Proceedings of the 4th Augmented Human International Conference*, 116–123. <https://doi.org/10.1145/2459236.2459256>
- Whitmer, T. D., Fry, A. C., Forsythe, C. M., Andre, M. J., Lane, M. T., Hudy, A., & Honnold, D. E. (2015). Accuracy of a vertical jump contact mat for determining jump height and flight time. *Journal of Strength and Conditioning Research*, *29*(4), 877–881. <https://doi.org/10.1519/JSC.0000000000000542>

## RESEARCH ARTICLE

### Biotechnology

# Establishment and evaluation of real-time PCR based SELEX platform for the identification of protein binding aptamers: A pilot study in Sri Lanka

AI Abeykoon<sup>1\*</sup>, KMN Kumarasinghe<sup>1</sup>, NV Chandrasekharan<sup>2</sup> and PMTB Wickramasinghe<sup>3</sup>

<sup>1</sup> Department of Pre-Clinical Sciences, Faculty of Medicine, General Sir John Kotelawala Defence University, Ratmalana, Sri Lanka.

<sup>2</sup> Department of Chemistry, Faculty of Science, University of Colombo, Colombo, Sri Lanka.

<sup>3</sup> Department of Biochemistry and Clinical Chemistry, Faculty of Medicine, University of Kelaniya, Kelaniya, Sri Lanka.

Submitted: 01 March 2024; Revised: 26 October 2024; Accepted: 12 December 2024

**Abstract:** Aptamers are single-stranded DNA (ssDNA) affinity reagents capable of substituting conventional antibodies in processes of molecular recognition. Their higher affinities, lower costs of production and longer shelf lives of aptamers are making them increasingly popular and replacing conventional antibodies in the fields of diagnostics and therapeutics. Systematic evolution of ligands by exponential enrichment (SELEX) is a well-established and efficient technology for generation of aptamers with high affinity against various targets including whole cells, isolated proteins, and small molecules. This study is the first to report efforts in exploring SELEX for isolating protein-binding aptamers using a quantitative PCR and NGS-based approach in a local context. A low-cost selection platform was developed by coating microwell plates with human serum albumin, the target protein of interest, for quantitative and qualitative solid phase immunoassays. Changes in affinity and diversity were monitored through analysis of amplification plots, melt curves, remelt curves and high-resolution melt curve (HRM). Following eight selection cycles, the enriched DNA was subjected to high-throughput sequencing, and the two most abundant sequences were identified. The sequences were evaluated through in-silico binding assays, which resulted in comparable binding affinities expected for aptamers. Among the monitoring techniques, the amplification curve analysis was a valuable tool in understanding changes in pool affinity. Although the melt curve initially lacked sufficient resolution in the early stages of SELEX, the re-melt curve and HRM analysis accurately reflected pool diversity during this time. Thus, we demonstrate that it is feasible to use locally available technology for the successful development of aptamers. This

highlights the potential to produce affinity reagents locally on a commercial scale in the future.

**Keywords:** PCR, protein binding aptamers, SELEX platform.

## INTRODUCTION

Aptamers are single-stranded deoxyribonucleic acids (ssDNA) or ribonucleic acids (ssRNA) that can bind target molecules with high affinity and specificity. Depending on the sequence of nucleotides, aptamers can fold into unique and distinct three-dimensional conformations, which can bind to target molecules with high affinity and selectivity. Systematic evolution of ligands by exponential enrichment (SELEX) is a well-established technology for generating synthetic DNA and/or RNA molecules with high affinity against various targets, including whole cells, isolated proteins, and small molecules. These designer DNA or RNA molecules are alternatives to antibodies in developing theranostics in biomedical research (Ellington & Szostak, 1990; Tuerk & Gold, 1990).

Aptamers offer significant advantages over antibodies in many aspects. They can be developed against almost any target. Moreover, their high thermal stability, relatively high resistance to both biological and chemical degradation, and low cost of production are just a few

\* Corresponding author (isuruabeykoon@kdu.ac.lk;  <https://orcid.org/0000-0002-2189-1004>)



This article is published under the Creative Commons CC-BY-ND License (<http://creativecommons.org/licenses/by-nd/4.0/>). This license permits use, distribution and reproduction, commercial and non-commercial, provided that the original work is properly cited and is not changed in anyway.

of the many superior qualities, which make aptamers preferable to antibodies (Famuko *et al.*, 2007).

Aptamer research is a fast-developing field with an annual revenue valued at USD 151 million in 2021 and projected to reach USD 342 million by 2026 (Markets & Markets, 2022). Despite this significant global trend, Sri Lanka is lagging behind in aptamer research even though the country possesses adequate technology to engage in SELEX and aptamers. This paper discusses the initial efforts and challenges in the establishment of the SELEX platform for the first time in Sri Lanka, paving the way for the future development of a wide array of aptamers with applications in both diagnostics and therapeutics.

## MATERIALS AND METHODS

### Design and preparation of ssDNA library

The initial library design was based on the work published by Percze *et al.* in 2017. A 50 pmol sample of the library was dissolved in 100  $\mu$ L of selection buffer and the solution incubated at 95 °C for 5 min in a heat block. The heated library was then immediately cooled by placing it on ice for 15 min. Prior to binding, the library was allowed to equilibrate to room temperature.

### Optimization of PCR for amplification of ssDNA library

All PCR reactions were conducted in a volume of 20  $\mu$ L. An initial denaturing step at 95 °C for 5 min was followed by twenty cycles of the standard PCR protocol, with a denaturing step at 95 °C for 10 s, an annealing step at 63 °C for 10 s, and an extension step at 72 °C for 10 s. A final extension step was performed at 72 °C for 1 min.

The optimized conventional PCR cycling parameters and reagent concentrations/volume were used as a baseline for the optimization of quantitative PCR. Template concentrations ranging from 1 $\mu$ M to 10<sup>-8</sup> $\mu$ M were tested.

### Optimization of biotin/streptavidin-based ssDNA generation

Following this procedure, streptavidin-coated magnetic Dyna beads (MagSi-STA by Magtivio) were used for the generation of single-stranded DNA.

A 100  $\mu$ L sample of the PCR product was added to prepared beads and pulse vortexed for 10 s and then

incubated at room temperature for 30 min. The solution was then briefly centrifuged, and the supernatant discarded. Next, 250  $\mu$ L of water was added, pulse vortexed, briefly centrifuged, and the supernatant discarded to remove unbound sequences. The beads were then resuspended in 5  $\mu$ L of 0.15M NaOH and incubated for 3 min. The supernatant was carefully separated and neutralized with 2.5  $\mu$ L of 0.3M HCl. The solution was then stored at 4 °C until further use.

Generation of ssDNA was confirmed through 4% agarose gel electrophoresis (50V for 60 min).

### Selection procedure/target binding assay

A 50 pmol (50  $\mu$ L of 10  $\mu$ M) sample of the library was dissolved in 100  $\mu$ L of binding buffer. The library solution was heat-denatured and snap-cooled in ice for 15 min. Before binding, the library was allowed to equilibrate to room temperature.

The prepared library was added to human serum albumin (HSA) (Sigma Aldrich) coated microtiter plate wells and incubated for 1 h. The supernatant was then removed, and the wells were washed thoroughly three times with 200  $\mu$ L of PCR grade water to remove any unbound sequences.

Elution of bound sequences was conducted using a Qiagen DNA mini kit with slight modifications described below.

To a sample well, 100  $\mu$ L of buffer ATL was added and incubated at room temperature for 30 min with occasional vortexing. Next, 100  $\mu$ L of buffer AL was added and thoroughly mixed by vortexing for 15 s. The mixture was then incubated for 10 min at room temperature. A 200  $\mu$ L volume of absolute ethanol was added to the well and vortexed for 15 s. The mixture was then placed in a minicolumn provided by the manufacturer and centrifuged at 6000 x g for 1 min. The flow-through was discarded and the column was placed in a new collecting tube. A volume of 500  $\mu$ L of buffer AW1 was added and centrifuged at 6000 x g for 1 min. The flow-through was discarded and the column was placed in a new collecting tube. Next, 500  $\mu$ L of buffer AW2 was added and the tube was centrifuged at 20,000 x g for 3 min. The flow-through was discarded and the column was placed in a new collecting tube. Finally, 100  $\mu$ L of PCR grade water was added, incubated for 1 min and centrifuged at 6000 x g for 1 min. The flow-through was carefully separated and stored at 4 °C until further use.

**Table 1:** Stringency changes across SELEX cycles

SELEX Cycle number	Num. of washes	Incubation time (minutes)	Incubating temperature (°C)	Use of shaking platform
I	1	60	25	No
II	2	45	25	No
III	3	45	45	No
IV	4	30	45	No
V	5	15	45	Yes
VI	6	15	45	Yes
VII	6	10	45	Yes
VIII	6	10	55	Yes

### Conducting SELEX cycles

A SELEX cycle involves incubating the prepared library with the target, extracting the bound fraction, PCR amplifying the bound fraction, and generating ssDNA. The stringency of each cycle of SELEX was gradually increased to isolate stronger binders for the target. Stringency improvement was achieved through two main aspects: (i) changes in selection conditions, and (ii) inclusion of negative selection cycles.

Changes in time, temperature parameters, and the number of washes were the main approaches to improving stringency during selection (see Table 1). In addition, as higher cycle numbers were reached, incubation was done on a shaking platform with the frequency gradually increasing with each cycle.

### Monitoring SELEX process

#### *Quantification of the bound fraction*

A real-time PCR assay was developed to quantify target-bound oligonucleotides from each SELEX cycle. Quantitative PCR was performed on the Rotor Gene Q PCR system with a reaction volume of 20  $\mu$ l. The reaction mixture consisted of 10  $\mu$ l of x2 SYBR Green PCR Master mix, 2  $\mu$ l of 10  $\mu$ M unlabeled forward and reverse primers, and 2  $\mu$ l of DNA template (target-bound oligonucleotides washed after each cycle). Two dilutions of  $10^4$ -fold and  $10^5$ -fold per sample were analyzed, each in duplicates for SELEX cycles II-IV. For SELEX cycles 5 and 6,  $10^5$ -fold and  $10^6$ -fold dilutions were used, respectively. The cycling conditions were pre-incubation at 95 °C for 5 minutes, initial denaturation at 95 °C for 10 s, annealing at 63 °C for 10 s, and extension at 72 °C for 10 s concluded by a final elongation at 72 °C for 1 min.

### *Melt curve analysis*

PCR-amplified products from each SELEX cycle were subjected to gradual melting in the quantitative PCR system. For analysis, the sample temperature was gradually increased from 50 °C to 95 °C at a step rate of 0.3 °C/min. Changes in fluorescence intensity were monitored continuously, and melting peaks were calculated with the cycler software (Rotor-Gene Q software).

### *NGS sequencing*

The aptamer pools were amplified by PCR and NGS libraries were prepared by nick repair and barcoding using IonXpress™ barcode adapters (ThermoFisher Scientific, USA). The NGS templates of the libraries were prepared by clonal amplification of barcoded libraries using the Ion OneTouch™ 2 System. The amplified libraries were enriched using the Ion One Touch ES enrichment system, and the template positive ion sphere particles were loaded onto an Ion 540 chip and sequenced using the Ion Genestudio S5 system at Genelabs Medical (Pvt) Ltd., Sri Lanka. The Ion Torrent Suite™ software was used for data analysis including the generation of the Fastq file, which was used for further downstream analysis.

### *In silico target binding assay*

3D structures of the first two aptamer sequences derived from the sequencing results were generated using the Builder GUI menu in PyMOL 2.5.4 (<http://www.pymol.org>). The sense DNA strands were folded using sculpt models and the generated files were exported as PDB files. The plasma-derived human serum albumin was selected as the target protein and its PDB file was downloaded from the protein data bank (5z0b; <https://www.rcsb.org>).

org/structure/5z0b). The sequence TCGTCTGCTCCG TCCAATACCCCGGCTTTGGTTTAGAGGTAGTT GCTCATTACTTGTACGCTCCGGATGTTTGGTG TGAGGTCGTGC-3' was used as the reference sequence. The ZDOCK server<sup>1</sup> was used to identify aptamer-protein binding. The PDB files of the aptamers and target proteins were submitted to the ZDOCK server. All amino acids in the target protein were selected for the analysis, and the probable binding complexes were determined with the ZDOCK score. Further, the likelihood of the sequences being aptamers was measured using the PPAI web server<sup>2</sup> and prediction scores were calculated using the optimal threshold value of 0.44 to predict true protein-aptamer pairs.

### Comparative wet lab binding assay

A selection platform for ssDNA aptamers was prepared by immobilizing HSA in microtiter plate wells (Nunc-Immuno™ Microtiter™ 96 well solid plates – Thermo Scientific).

An unselected DNA aptamer library was used as the negative control and the HSA binding ssDNA sequence, reported in the literature (referred to as aptamer 1), was used as the positive control.

A 2 µl sample of a 1000 pmol/µl library was dissolved in 98 µl of binding buffer to prepare a 100 µl solution of 20 pmol/µl. The diluted library was then incubated at 95 °C for 5 min in a heat block and immediately cooled by placing it on ice for 15 min. The library was allowed to equilibrate to room temperature, before binding.

A 200 pmol (20µl of 100 pmol/µl) sample of aptamers 1 (positive control) and 2 (test sequence) were dissolved separately in 80 µl of binding buffer to prepare a 100 µl solution of 20 pmol/µl. The aptamer solutions were then incubated at 95 °C for 5 min in a heat block and then immediately cooled by placing it on ice for 15 min. Before binding, the aptamer solutions were allowed to equilibrate to room temperature.

The controls and test samples were incubated in the albumin-coated plates on a shaking incubator for 30 min at room temperature.

A 50 µl sample was aspirated from each well and stored at 4 °C until further use. The already optimized real-time PCR assay was used to quantify ssDNA before and after binding.

## RESULTS AND DISCUSSION

### Optimization of PCR for amplification of ssDNA library

A template concentration of  $1 \times 10^{-4}$  µM was identified as the ideal concentration for obtaining a well-defined band on the agarose gel. An annealing temperature of 63 °C produced clear bands after twenty rounds of standard PCR cycles (Figure 1).

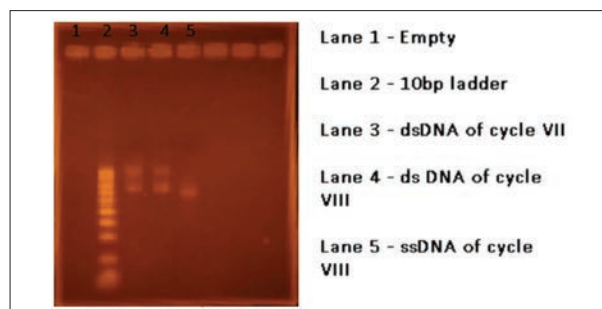


**Figure 1:** Gel electrophoresis in 4% agarose. Lane 1: empty lane, Lane 2: 10 bp ladder, Lane 3: dsDNA of cycle VII, Lane 4: dsDNA of cycle 8, and Lane 5: ssDNA of cycle 8.

### Optimization of quantitative PCR for amplification of ssDNA library

The optimized conventional PCR cycling parameters and reagent concentrations/volume provided efficient amplification in the quantitative PCR setup at template concentrations of  $1 \times 10^{-4}$  µM (Figure 2).

### Melt curve analysis

The melt curve analysis of PCR amplified products from each SELEX cycle (I to VIII) demonstrated a narrowing of peaks and a shift in peak towards higher temperatures indicating a reduction in pool diversity (Figure 3).

### In silico target binding assay

Both sequences selected through NGS data analysis yielded comparable ZDOCK scores (Table 2) and interactions with HSA protein (Figure 6). The PPAI server analysis for the two sequences yielded a score of 0.47 predicting the sequences as probable binders for the defined target.

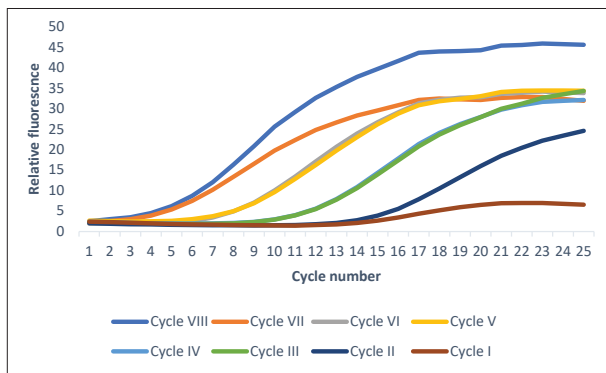


Figure 2: Amplification curves for dilutions of ssDNA library

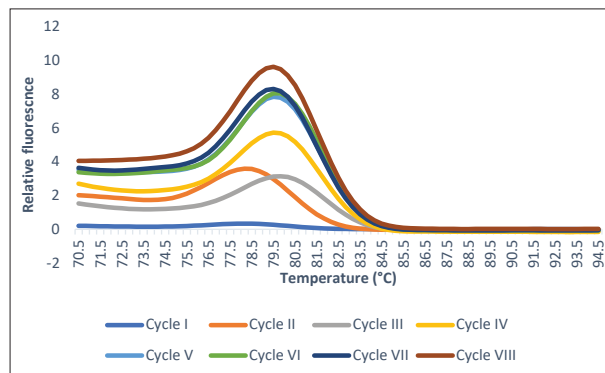


Figure 4: Re-melt curve analysis of SELEX cycles I-VIII

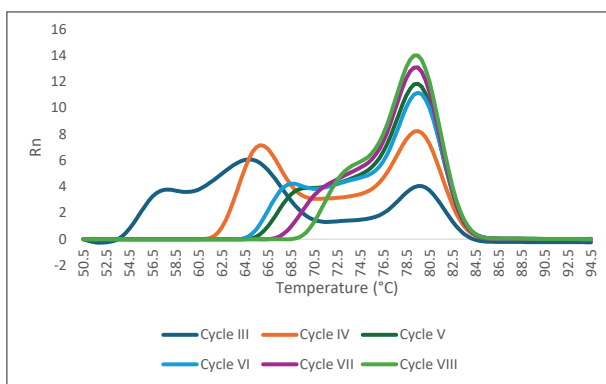


Figure 3: Melt curve analysis of SELEX cycles III to VIII

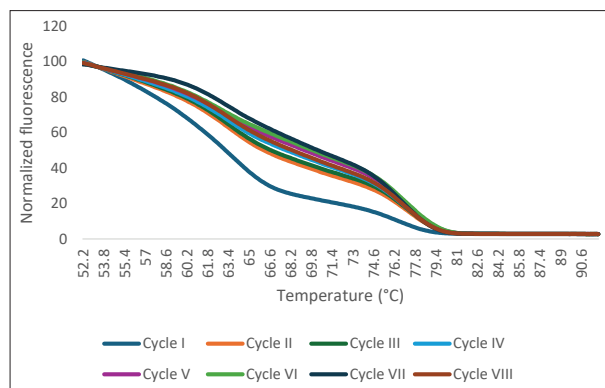


Figure 5: Normalized HRM analysis of SELEX cycles I-VIII

Table 2: Sequences of selected aptamers, their frequencies, ZDOCK, PPAI results

Sequence	Count	ZDOCK score	PPAI results	
			Prediction result <sup>a</sup>	Prediction score <sup>b</sup>
Seq 1 AGAGGAAAGCGGAGGCGTAGTGGTT	123	1067.844	Yes	0.47
Seq 2 CCCATAGAGAGGAAAGCGGAGGCGTAGTGGTT	85	1190.363	Yes	0.47

<sup>a</sup> Prediction result ('yes' represents that it is an aptamer, and 'no' represents that it is not an aptamer)

<sup>b</sup> Prediction score (the probability that the sequence is an aptamer)

### Wet lab analysis

The respective Ct values obtained for original and post incubation ssDNA are presented in Table 3.

The DNA concentrations were calculated using a

standard curve (Supplementary Figure 1) generated for serial dilutions of the ssDNA library. The threshold cycle numbers from three independent experiments were averaged, and the standard deviation was calculated for each concentration analyzed (Table 4).

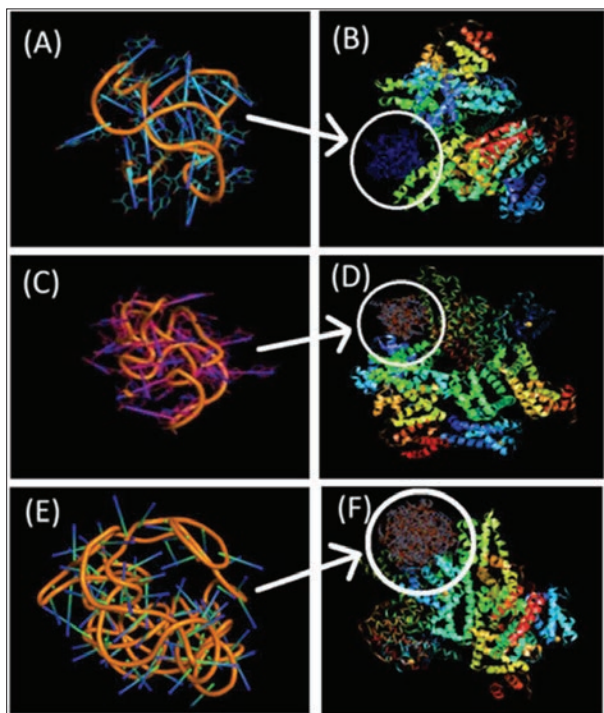


**Figure 6:** 3-D modelling and ZDOCK interaction of selected DNA sequences with target protein HSA.

- (A) scrambled unrestricted structure of aptamer sequence 01
- (B) ZDOCK interaction of sequence 01 with albumin
- (C) scrambled unrestricted structure of aptamer sequence 02
- (D) ZDOCK interaction of sequence 02 with albumin
- (E) scrambled unrestricted structure of control sequence
- (F) ZDOCK interaction of control sequence with albumin.

**Table 3:** DNA concentration and Ct values for samples at pre-incubation and post-incubation

Series number	Content	Ct	$\Delta$ Ct
1	Positive control/Aptamer 1 (Pre incubation)	22.531	~3
2	Positive control/Aptamer 1 (Post incubation)	25.421	
3	Test sequence/Aptamer2 (Pre incubation)	18.737	~1
4	Test sequence/Aptamer 2 (Post incubation)	19.884	
5	Negative control/Library (Pre incubation)	15.711	~0
6	Negative control/Library (Post incubation)	15.593	

**Table 4:** Average threshold cycles and standard deviation for ssDNA library dilutions

DNA concentration ( $\mu$ M)	Negative logarithmic derivative of concentration	Average Ct'	SD
$1 \times 10^{-8}$	8	19.40	6.6
$1 \times 10^{-7}$	7	14.27	1.1
$1 \times 10^{-6}$	6	12.20	2.9
$1 \times 10^{-5}$	5	11.10	4.0
$1 \times 10^{-4}$	4	10.34	3.8

Monitoring SELEX is crucial to ensure the isolation of aptamer sequences with high affinity and specificity towards a defined target. In this experiment, an aptamer library was enriched towards human serum albumin through eight cycles of SELEX. The process utilized real-time PCR-based approaches for both amplification and monitoring. Amplification plots were considered in affinity assessments of aptamer pools from cycles I to VIII. The first reported use of quantitative PCR in SELEX monitoring was by Adali *et al.* (2013) where the selected fraction of aptamers in every cycle of SELEX was quantified. The optimized qPCR allowed for the detection of aptamers ranging from 5 pg to 0.02 pg with a 98.7% efficiency (Adali *et al.*, 2013). In contrast, comparison studies by Mencin *et al.* (2014) using non-saturating SYBR Green based quantification revealed some significant drawbacks of the assay. The higher affinity of SYBR Green towards AT compared to GC resulted in a low copy number when selection was directed towards GC-rich motifs enrichment. This effect was even more prominent in the latter cycles of SELEX giving a fourfold difference compared to the fluorescence-based assay results. This study highlights the usefulness of a saturation dye for ssDNA quantification in SELEX experiments (Mencin *et al.*, 2014). Our experiment targeting HSA used saturating SYBR green (Promega) for the generation of amplification signals since the final sequence was not known at the start of the experiment. The initial cycle of SELEX is known to yield minimal sequences demonstrating a drastic reduction in DNA quantity (Mencin *et al.*, 2014; Song *et al.*, 2017). Our findings were in agreement with this, demonstrating extremely low bound fractions in SELEX cycle I. However, from cycles II to VIII, a gradual increase in the bound fraction was observed, reflecting a gradual increase in the pool's affinity towards the target.

Dynamics of diversity changes across the SELEX process were evaluated through melt curve, re-melt curve, and HRM analysis. Melt curve analysis is frequently used to assess RT-PCR amplicon length and product purity in dye-based RT-PCR assays. The melt profile and dissociation kinetic properties of double-stranded DNA depend on factors such as sequence composition, length and concentration of products. This approach has been explored as a monitoring tool for SELEX to determine reductions in diversity across advancing selection cycles. Theoretically, a near Gaussian peak is expected for the melting profile of the library, where narrowing of the peak is expected with advancing cycles due to the reduction of diversity. In a comparison study of monitoring approaches, Mencin *et al.* (2014) observed this phenomenon starting with a library of a normal distribution, with a gradual reduction of the peak width occurring up to cycle four. In subsequent cycles, well defined melting peaks were observed and the peaks of cycles seven and nine were almost super imposed, reflecting the convergence of library diversity towards a specific sequence. Our experiment targeting HAS used melt curve analysis, which revealed a gradual convergence of melt profile peaks towards a specific temperature. A bimodal distribution was observed in SELEX cycles III-VIII as exemplified in many previous reports of melt curve analysis (Mencin *et al.*, 2014; Luo *et al.*, 2017; Song *et al.*, 2017). A gradual increase in peak temperature was observed across SELEX cycles confirming a reduction in pool diversity.

Vanbraband *et al.* (2014) reported the use of melting curve analysis after a short re-annealing step known as remelt curve analysis (rMCA) as a useful tool for diversity analysis in enrichment monitoring. Conventional melt curves of the amplified products were obtained by increasing the temperature from 60 °C to 95 °C. Reannealing was performed at 70 °C for 1 minute followed by a second melting analysis (remelting) from 70 °C to 95 °C at 0.5 °C/s. During this stringent re-annealing phase, both hetero- and homoduplexes were formed with their proportions depending on the sequence diversity. As the diversity of SELEX pools decreased, more homoduplexes were observed in the reannealing phase shifting the obtained rMCA melting temperatures and providing crucial information on enrichment in terms of diversity (Vanbraband *et al.*, 2014). In contrast to Vanbraband's findings our study in the temperature range of 70 °C to 95 °C revealed a single peak. However, across SELEX cycles a clear shift in peak temperature was observed reflecting pool enrichment. These changes were evident in the initial stages of SELEX highlighting the importance of remelt curve analysis as a monitoring tool over conventional melt curve analysis.

HRM analysis is an advanced version of conventional melt curve analysis where sequence-related melting profiles revealing single nucleotide changes are generated (Farrar *et al.*, 2017). Unlike the classical melt curve, HRM analysis monitors melting differences in temperature gaps of less than 0.5 °C, generating a comparatively higher density of data points per 1 °C. Such enriched data can provide information on subtle differences in sequences. The use of HRM analysis and the availability of HRM data on the library behavior across SELEX cycles are sparse. This experiment presents early reports on using HRM analysis as a monitoring tool. Melting profile changes were observed even in the early stages of SELEX with HRM, whereas conventional amplification plots or melt curve analysis failed to detect such early changes. A gradual shift in the melting profile further reflected the gradual enrichment of the library pool.

The affinity was monitored based on unbound fraction determination. This method of affinity determination was employed to avoid practical limitations associated with determinations of the bound fraction of aptamers. Such bound fraction quantifications require the separation of the aptamer-target complex from the binding platform and/or isolation of DNA from the target, both of which carry risks of yielding lower quantities of aptamer, thereby affecting the final affinity calculations. In contrast, determination of original and unbound aptamer concentrations could be conducted by directly sampling the original and unbound solutions, thereby allowing for a more accurate measure of affinity.

The ssDNA library used as the negative control produced similar Ct values for both initial incubating and unbound fractions implying that negligible binding has occurred and that the concentration of the initial incubating DNA and final unbound fractions remained consistent. The positive control in this experiment had a Ct of 22.5 (rounded to the first decimal) for the initial incubation concentration. The Ct value for the post-incubation eluted sample was 25.4, resulting in a Ct difference of nearly 3, suggesting that a significant amount of the initial incubating DNA had bound to the coated well. The Ct difference for the test sequence used was 1.2 (Table 3) indicating a significant binding of the test sequence compared to the negative control.

The first round of NGS on the aptamer library selected from the final SELEX cycle identified 540 potential sequences of aptamers. Among these, there were 432 unique sequences each appearing once, 36 unique sequences appearing twice, and approximately 40 sequences appearing three or more times (see Supplementary Table 1). This is consistent with previous

literature on NGS results from final SELEX cycles targeting various protein targets where over  $\approx 100$  different sequences have been identified as potential binders (Schütze *et al.*, 2011; Stoltenburg & Strehlitz, 2018; Cho *et al.*, 2010). Two sequences with the highest frequencies were selected for further in silico testing.

Both sequences yielded comparable ZDOCK scores, with the probability of the selected sequences being an aptamer identified as 0.44 for each. The PPAI server predicted the two sequences as probable.

## CONCLUSION

The PCR system allows for both pool amplification and monitoring of SELEX, simultaneously. Among the monitoring techniques, the amplification plot analysis has revealed a valuable tool in understanding pool affinity changes. Additionally, melt curve, re-melt curve and HRM analysis have provided insights into pool diversity across SELEX. Although the melt curve lacked sufficient resolution during the initial stages of SELEX, the re-melt curve and HRM analysis accurately reflected pool diversity changes during these early stages. Sequencing results from NGS analysis reflected this enrichment of the aptamer library, resulting in a binding sequence with comparable binding affinity.

Therefore, the authors suggest the possibility of using local resources to identify protein binding DNA aptamers. They further recommend improvements to the SELEX procedure by utilizing NGS analysis during the early cycles to achieve better selection. Finally, they suggest further characterization of selected sequences through association/dissociation kinetic assessments.

## REFERENCES

- Aiswarya, P. U., Gopika, R., Jinju, J., Malavika, M. K., Franklin, J., Jinu, G. (2023). Aptamers: Features, synthesis and applications. *Chemistry and Biodiversity*, 20(10). <https://doi.org/10.1002/cbdv.202301008>
- Avcı-Adalı, M., Wilhelm, N., Perle, N., Stoll, H., Schlensak, C., & Wendel, H.P. (2013). Absolute quantification of cell-bound DNA aptamers during SELEX. *Nucleic Acid Therapeutics*, 23(2), 125–30. <https://doi.org/10.1089/nat.2012.0406>
- Cho, M., Xiao, Y., Nie, J., Stewart, R., Csordas, A.T., Oh, S.S. (2010). Quantitative selection of DNA aptamers through microfluidic selection and high-throughput sequencing. *Proceedings of the National Academy of Sciences of the United States of America*, 107(35), 15373–8. <https://doi.org/10.1073/pnas.1009331107>
- Ellington, A.D., Szostak, J.W. (1990). In vitro selection of RNA molecules that bind specific ligands. *Nature*, 346(6287), 818–22. <https://doi.org/10.1038/346818a0>
- Famulok, M., Hartig, J.S., Mayer, G. (2007). Functional aptamers and aptazymes in biotechnology, diagnostics, and therapy. *Chemical Reviews*, 107, 3715–43. <https://doi.org/10.1021/cr0306743>
- Farrar, J. S. & Wittwer, C. T. (2017). High-resolution melting curve analysis for molecular diagnostics. In G. P. Patrinos (Ed.), *Molecular Diagnostics* (3rd ed., pp. 79–102). Academic Press.
- Luo, Z., He, L., Wang, J., Fang, X., Zhang, L. (2017). Developing a combined strategy for monitoring the progress of aptamer selection. *Analyst*, 142(17), 3136–3139. <https://doi.org/10.1039/c7an01131h>
- Markets and Markets. (2022). Aptamers market revenue trends and growth drivers. <https://www.marketsandmarkets.com/Market-Reports/aptamers-technology-market-1167.html>
- Mencin, N., Šmuc, T., Vraničar, M., Mavri, J., Hren, M., Galeša, K. (2014). Optimization of SELEX: Comparison of different methods for monitoring the progress of in vitro selection of aptamers. *Journal of Pharmaceutical and Biomedical Analysis*, 91, 151–159. <https://doi.org/10.1016/j.jpba.2013.12.031>
- Schütze, T., Wilhelm, B., Greiner, N., Braun, H., Peter, F., Mörl, M. (2011). Probing the SELEX process with next-generation sequencing. *PLoS One*, 6(12), 1–10. <https://doi.org/10.1371/journal.pone.0029604>
- Song, M.S., Sekhon, S.S., Shin, W.R., Kim, H.C., Min, J., Ahn, J.Y., Kim, Y.H. (2017). Detecting and discriminating shigella sonnei using an aptamer-based fluorescent biosensor platform. *Molecules*, 22(825). <https://doi.org/10.3390/molecules22050825>
- Stoltenburg, R., Strehlitz, B. (2018). Refining the results of a classical SELEX experiment by expanding the sequence data set of an aptamer pool selected for protein A. *international journal of molecular science*, 19(2), 642. <https://doi.org/10.3390/ijms19020642>
- Tuerk, C., Gold, L. (1990). Systematic evolution of ligands by exponential enrichment. RNA ligands to bacteriophage T4 DNA polymerase. *Science*, 249(4968), 505–510. <https://doi.org/10.1126/science.2200121>
- Vanbrabant, J., Leirs, K., Vanschoenbeek, K., Lammertyn, J., Michiels, L. (2014). reMelting curve analysis as a tool for enrichment monitoring in the SELEX process. *Analyst*, 139(3):589–595. <https://doi.org/10.1039/c3an01884a>

## RESEARCH ARTICLE

### Internet of Things

# Enhanced privacy-preserving federated convivial learning for internet of medical things (IoMT) through blockchain-enabled trust Q-learning

Sudharson K<sup>1\*</sup>, G Babu<sup>2</sup>, R Santhiya<sup>3</sup> and CS Anita<sup>1</sup>

<sup>1</sup> Department of Artificial Intelligence and Machine Learning, RMD Engineering College, Kavaraipettai, Tamil Nadu 601206, India.

<sup>2</sup> Department of Bio-Medical Engineering, SRM Easwari Engineering College, Ramapuram, Chennai, Tamil Nadu 600089, India.

<sup>3</sup> Department of Computer Science and Engineering, Saveetha Engineering College, Thandalam, Chennai, Tamil Nadu 602105, India.

Submitted: 02 March 2024; Revised: 16 September 2024; Accepted: 06 December 2024

**Abstract:** Personalized treatment and remote monitoring have been made possible by the quick uptake of internet of medical things (IoMT) devices, which have completely changed the healthcare industry. That being said, there are a lot of security and privacy issues with this expansion. While resolving certain privacy issues, current federated learning techniques cannot guarantee complete security and trust amongst involved IoMT devices. We offer the privacy-preserving federated convivial learning (FCL) platform, designed specifically for internet of medical things applications, to close this gap. The present study presents a trust-based Q-learning model powered by blockchain technology, which improves data privacy by restricting model training to approved devices only. Our solution promotes trustworthy and cooperative interactions amongst IoMT devices without sacrificing privacy by incorporating the principles of convivial learning. Comparing experimental results to traditional federated learning techniques, improved privacy protection is 92.4% and increased model accuracy is 94.7%. The advancement of IoMT technology and safe data sharing are made possible by this framework, which also makes healthcare systems safer and more effective.

**Keywords:** Blockchain, convivial learning, internet of medical things and trust Q-learning, privacy-preserving

## INTRODUCTION

The internet of medical things, or IoMT, revolutionizes healthcare by enabling real-time data gathering, analysis,

and utilization for improved patient care. It does this by linking medical devices to digital systems. IoMT is transforming the way healthcare professionals manage and provide care, from wearable health monitors like smartwatches to cutting-edge equipment for remote monitoring and individualized therapies. However, the quick development of IoMT has highlighted a significant challenge: making sure that the enormous volumes of sensitive data being exchanged and gathered stay private and secure. The issue for research is the growing susceptibility of healthcare systems to data breaches, which compromise patient safety and confidence in addition to causing financial losses.

The effectiveness of traditional security measures and centralized data management strategies in reducing these threats has been demonstrated. By enabling IoMT devices to cooperatively build machine learning models without exchanging raw data, federated learning—a decentralized approach to model training—offers a possible remedy. Federated learning has shown promise, but scalability, security, and trust issues remain, particularly in the highly sensitive and networked IoMT setting.

The minimal number of studies on trust and cooperation between IoMT devices in federated learning highlights the research gap. The coordination of existing models is primarily dependent on a central server, which

\* Corresponding author (susankumar@gmail.com;  <https://orcid.org/0000-0002-2923-8990>)



This article is published under the Creative Commons CC-BY-ND License (<http://creativecommons.org/licenses/by-nd/4.0/>). This license permits use, distribution and reproduction, commercial and non-commercial, provided that the original work is properly cited and is not changed in anyway.

leaves them open to cyber-attacks and single-point failures. Additionally, whereas blockchain technology has demonstrated a great deal of promise for data security and integrity, little is known about how it may be used to improve trust and decentralization in federated learning for IoMT.

The unique privacy-preserving federated convivial learning (FCL) architecture that this study proposes to bridge the gaps between blockchain technology and the trust-based Q-learning model is significant. By integrating trust mechanisms and limiting the participation of unauthorized and unreliable devices in model training, this framework promotes safe, decentralized collaboration across IoMT devices. To create more safe and efficient healthcare systems, the study intends to proactively improve data privacy, security, and trust in IoMT networks by fusing blockchain technology with federated learning.

### Related work

The internet of medical things (IoMT) signifies the convergence of medical devices with our digital world, allowing healthcare professionals to collect, analyze, and utilize health data in unprecedented ways. IoMT devices, ranging from wearable health monitors to specialized devices for remote patient monitoring, have evolved significantly in recent years (Srivastava *et al.*, 2022). However, this growth poses a challenge—ensuring the privacy and security of shared and collected data. This concern is particularly crucial given historical data breaches in healthcare, which result in financial implications and jeopardize patient trust and safety.

Federated learning has emerged as a promising solution, enabling model training without centralizing data (Nguyen *et al.*, 2022). This nascent technology faces challenges despite its potential, especially with the healthcare sector's increasing reliance on IoMT devices and the growing cyber-attack instances. Recognizing these limitations requires a more rigorous and innovative approach to addressing data privacy and security concerns.

Convivial learning aims to embed trust and collaboration in federated learning (Bano *et al.*, 2023). Additionally, the potential of blockchain technology, known for ensuring data integrity and transparency, still needs to be explored in the IoMT context. Integrating these principles could proactively establish a foundation of trust and collaboration within the entire IoMT ecosystem.

IoMT has solidified its position in healthcare, enabling personalized patient care and efficient remote monitoring. The overview of IoMT devices showcased their potential in health monitoring and diagnostics (Srivastava *et al.*, 2022), emphasizing their crucial role in chronic disease management and timely interventions. IoMT's potential in telehealth services was highlighted as a crucial bridge between patients and physicians, especially in geographically isolated regions (Gajarawala & Pelkowski, 2021). The findings underscore IoMT's transformative role in facilitating seamless communication and healthcare delivery.

Interoperability challenges in IoMT were discussed, underlining the need for a standardized framework to facilitate seamless data sharing without compromising patient data integrity (Wagan *et al.*, 2022). A study explored the economic implications of IoMT adoption in healthcare, projecting potential cost savings through reduced hospital readmissions and efficient resource utilization (Rani *et al.*, 2023). The discussion underscored the ethical considerations associated with IoMT, emphasizing the delicate balance between technological advancements and patient rights (Gerke *et al.*, 2020).

The introduction highlighted the role of federated learning in training models on decentralized data, demonstrating its potential to enhance accuracy while ensuring data localization (Nguyen *et al.*, 2022). Privacy-preserving capabilities were explored, introducing techniques to enhance model privacy without compromising accuracy (Yan *et al.*, 2023). The discussion on the scalability of federated learning (Bano *et al.*, 2023) emphasized challenges like communication overhead and proposed techniques for scalability. Secure aggregation in federated learning was explored to ensure confidentiality during the aggregation process (Zheng *et al.*, 2023). In a comprehensive review, the challenges and opportunities of applying federated learning in healthcare were examined (Majeed *et al.*, 2022). The authors underscored the necessity for domain-specific adjustments to accommodate the unique requirements of healthcare.

Blockchain's fundamental principles and potential applications in healthcare were discussed, covering use cases such as patient record management and drug traceability (Ghosh *et al.*, 2023). The proposal introduced a framework for IoMT devices based on blockchain technology (Rafique *et al.*, 2023). The emphasis was placed on blockchain's pivotal role in maintaining data integrity and mitigating the risks associated with unauthorized access. In a paper (Almalki *et al.*, 2022), the

authors introduced a lightweight blockchain architecture tailored for IoMT devices. They highlighted its efficiency in ensuring real-time data storage and retrieval. The exploration focused on blockchain’s contribution to bolstering patient trust in IoMT devices. It was suggested that transparent data management and tamper-proof records could cultivate confidence among patients in adopting IoMT devices (Rahmani *et al.*, 2022).

In summary, while there are evident advancements and innovations in IoMT, federated learning, and blockchain, the integration of these technologies remains in its nascent stages. This literature review underscores the potential of these combinations, particularly in ensuring patient data privacy and security.

## MATERIALS AND METHODS

### Proposed FCL approach

The proposed methodology introduces an advanced federated convivial learning (FCL) framework to address privacy, security, and collaboration challenges in the internet of medical things (IoMT). The system architecture adopts a multi-layered approach that integrates IoMT devices, communication protocols, federated learning, trust dynamics, and blockchain technology. The layers of the system are designed to enhance data security, decentralized collaboration, and trust management, providing robust healthcare solutions while ensuring data privacy.

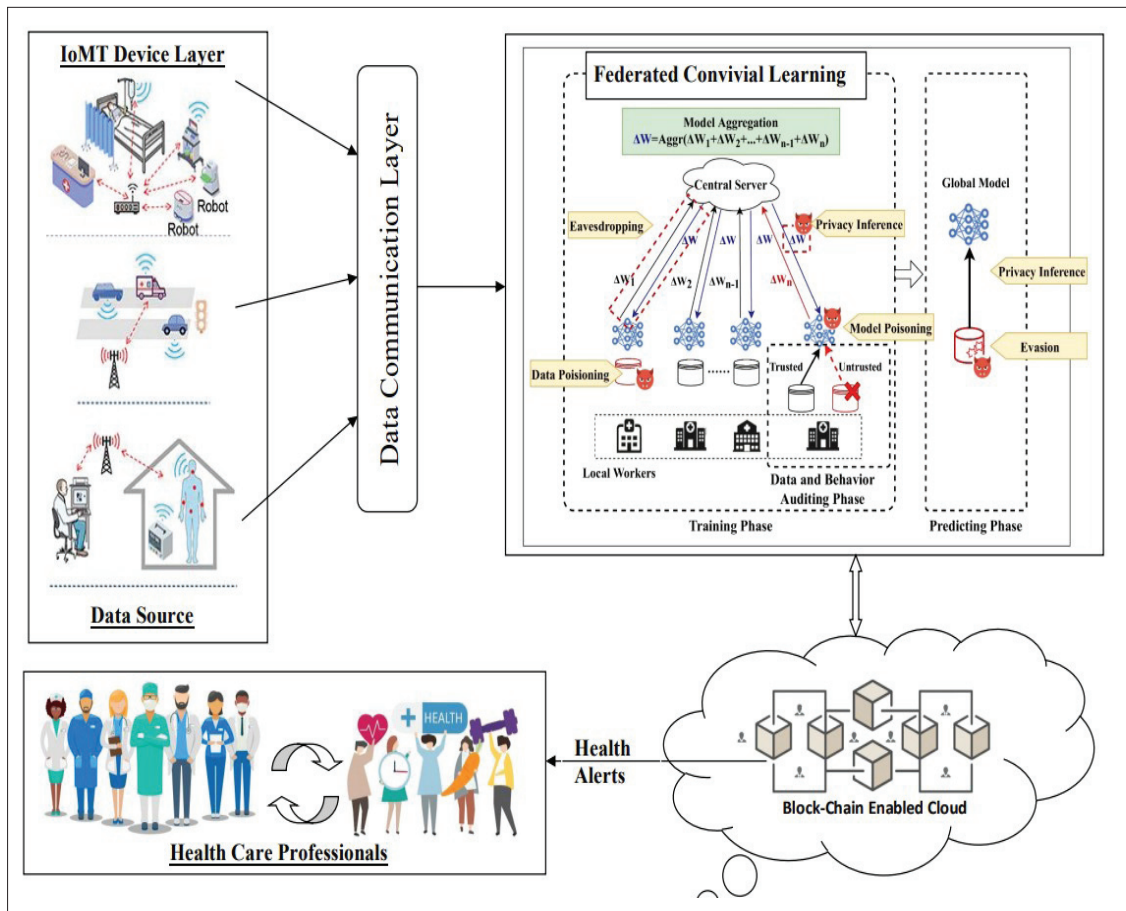


Figure 1: Federated convivial learning (FCL) Architecture

## System architecture

The architecture consists of five core layers:

- IoMT layer:** This foundational layer includes IoMT devices that gather medical data, storing it locally to preserve patient privacy. Each IoMT device acts as a node with its own dedicated storage system.
- Communication layer:** This layer establishes encrypted communication channels between IoMT devices, ensuring that all data transfers are protected from unauthorized access. Encryption functions  $E(\text{data})$  and decryption functions  $D(\text{data})$  secure the information exchanged within the network.
- Federated convivial learning (FCL) layer:** This layer enables collaborative model updates across IoMT devices. By promoting decentralized peer-to-peer interactions, devices can train models locally while securely sharing updates with trusted peers. This setup maintains data privacy by preventing exposure of raw data and ensures efficient collaborative learning (Sudharson *et al.*, 2022).
- Blockchain layer:** Blockchain technology is integrated to ensure transparency and immutability. Smart contracts process trust evaluations, and a decentralized ledger records all interactions between IoMT devices. This ensures that only authorized devices participate in the federated learning process, thus improving system security (Mohammed, 2023).
- Application layer:** In this layer, predictions and insights generated by the trained models are processed and used for healthcare applications. The application layer demonstrates the practical outcomes of the FCL framework, providing secure, privacy-preserving healthcare insights in real-time.

### Federated convivial learning

Federated Convivial Learning (FCL) is a key extension of federated learning that focuses on fostering trust and friendly interactions between IoMT devices. Unlike traditional federated learning, where a central server controls synchronization, FCL decentralizes trust and promotes collaboration among devices (Soner *et al.*, 2022).

The core mathematical model of FCL distributes trust among devices:

$$M_{\text{central}} = \sum_{i=1}^N w_i M_i$$

Here,  $M$  represents the global model,  $N$  is the number of participating devices,  $M_i$  is the model trained locally by device  $i$ , and  $w_i$  is the trust weight assigned to each device, reflecting its credibility.

**Collaborative inference:** Each device trains its model independently but shares inferences rather than raw data, maintaining privacy (Sudharson & Arun, 2022). If  $D_i$  is the datasets of device  $i$ , the collaborative inference function  $F_i$  for device  $i$  can be expressed as:

$$F_{\text{collab}} = \alpha F_i(D_i) + (1 - \alpha) F_j(D_j)$$

where  $F_j$  is the inference function for device  $j$ , and  $\alpha$  is the collaboration weight.

**Decentralized updates:** FCL-enabled devices share model updates with trusted peers rather than central servers, minimizing single points of failure (Hai *et al.*, 2022). The model update from device  $i$  to  $j$  can be written as:

$$U_{j_{\text{new}}} = \beta U_i + (1 - \beta) U_j$$

where  $\beta$  is the influence factor representing how much of  $U_i$  is incorporated into  $U_j$ 's update.

### Trust Q-Learning and blockchain integration

Trust management is governed by Trust Q-Learning, a reinforcement learning approach designed to build trust relationships among IoMT devices. Blockchain integration ensures the permanence and verifiability of these trust scores (Murugeswari *et al.*, 2023).

Each device's **state**  $S_{i,t}$  is defined by its recent interactions and data quality. Devices choose actions  $A_{i,t}$ , such as sharing model updates or seeking collaboration. Positive rewards  $R_{i,t} = f(S_{i,t}, A_{i,t})$ , are assigned for trustworthy interactions, while malicious actions are penalized.

The Q-value for a state-action pair is updated using the following formula:

$$Q_{i,t}(S_{i,t}, A_{i,t}) = (1 - \lambda) Q_{i,t-1}(S_{i,t-1}, A_{i,t-1}) + \lambda [R_{i,t} + \gamma \max_a Q_{i,t}(S_{i,t}, a)]$$

where  $\lambda$  is the learning rate and  $\gamma$  is the discount factor. Blockchain-based **smart contracts** adjust trust scores dynamically using:

$$T_{i_{\text{new}}} = T_{i_{\text{old}}} + \kappa (I_{i_{\text{new}}} - T_{i_{\text{new}}})$$

where  $\kappa$  is the adjustment rate, and  $I_{i_{\text{new}}}$  is the interaction score.

Before a device can participate in FCL, its trustworthiness is verified on the blockchain, ensuring that only trusted devices are allowed to collaborate (Veerasathpurush et al., 2023).

### Privacy-preserving mechanisms

FCL incorporates several privacy-preserving techniques to ensure that sensitive healthcare data remains secure during the learning process:

- **Local model training:** Each device trains its model using local data  $D_i$ , preserving privacy by avoiding centralized data sharing.
- **Differential privacy:** Noise is added to the updates before they are shared to ensure that the original data cannot be reconstructed. The differentially private model update  $U_{i\_private}$  is:

$$U_{i\_private} = U_i + G(0, \sigma^2)$$

where  $G(0, \sigma^2)$  is Gaussian noise with mean 0 and variance  $\sigma^2$

- **Homomorphic encryption:** Devices can share encrypted data without revealing the raw information. If  $E(data)$  represents encrypted data, the system allows operations like:

$$E(data_1) \oplus E(data_2) = E(data_1 + data_2)$$

- **Secure aggregation:** Multiple devices share their encrypted updates, which are then aggregated securely without individual updates being revealed. The secure aggregated update  $U_{agg}$  is:

$$U_{agg} = \sum_{i=1}^N U_{i\_private}$$

### Trust establishment and convivial learning

Building trust is essential for effective collaboration. Each device is assigned an initial trust score  $T_{i0}$ , based on prior interactions. After each interaction, trust scores are updated using the following formula:

$$T_{i\_new} = (1 - \alpha) \times T_{i\_old} + \alpha \times I_{ij} \text{ Where } \alpha (0 < \alpha < 1)$$

where  $I_{ij}$  represents the interaction score between devices  $i$  and  $j$ , and  $\alpha$  is the trust update factor. Devices with high trust scores are prioritized for collaboration, while those with low trust scores may face penalties, such as reduced collaboration weights or exclusion from the learning process.

---

### Algorithm

---

```

Initialize trust scores ( $w_i$ ) for each device
Initialize models ( $M_i$ ) for each device
Initialize trust update parameter  $\alpha$ 
Initialize collaboration factor  $\beta$ 
Repeat until convergence:
  for each device  $i$ :
    Select a peer device  $j$  to collaborate with
    # Collaborative Inference
    •  $F_{collab} = \alpha F_i(D_i) + (1 - \alpha) F_j(D_j)$ 
    # Trust-Weighted Collaboration
    •
     $M_{i\_updated} = \beta \times T_j \times M_i + (1 - \beta \times T_j) \times M_j$ 
    # Calculate interaction score
     $I_{ij} = \text{measure\_interaction\_quality}(i, j)$ 
    # Update trust scores
    •  $T_{i\_new} = (1 - \alpha) \times T_{i\_old} + \alpha \times I_{ij}$ 
    # Implement privacy-preserving mechanisms (e.g.,
    differential privacy, homomorphic encryption)
    # Penalty for Distrust
    for each device  $i$ :
      if  $T_i < T_{min}$ :
        reduce_collaboration_weight( $i$ )
    # Evaluate models, convergence criteria, and
    update model parameters
    # Deploy trained models for medical predictions and
    applications
    
```

---

The FCL framework addresses key challenges in decentralized learning by combining privacy-preserving mechanisms, trust management, and blockchain technology. The architecture enables secure, scalable, and efficient learning across IoMT networks, ensuring that sensitive medical data remains private.

The trust-based collaborative approach ensures that devices contribute to the learning process based on their trustworthiness. The use of blockchain further enhances system transparency, ensuring that only authorized devices are part of the network.

Future work will focus on improving the scalability of the FCL framework for large-scale IoMT networks, addressing communication overhead, and further refining trust dynamics to enhance collaboration and security.

## Experimental setup

### Dataset description

The dataset used in this study was collected from various internet of medical things (IoMT) devices, including wearable health monitors and electronic medical records. It consisted of 500,000 entries, each containing 20 features representing key health metrics such as heart rate, oxygen saturation, step count, and sleep duration. Each entry was associated with a timestamp and a device ID, enabling traceability of the data source (Gadekallu *et al.*, 2023).

Before the dataset was used in model training, several preprocessing steps were applied to ensure data quality. First, normalization was performed to scale all feature values uniformly, ensuring that different variables were comparable. Second, missing values were handled by employing mean imputation, and records with a high percentage of missing data were removed. Finally, outlier detection was conducted to identify and remove anomalous data points, which could otherwise distort the model's performance. The dataset was then split into 80% training data and 20% testing data, ensuring that the model evaluation was conducted on previously unseen data.

### Baseline comparisons

To ensure a comprehensive evaluation of the Trust-Based FCL framework, we compared it with three established federated learning methods:

**Standard federated averaging (FedAvg):** FedAvg is a basic federated learning method that averages local model updates from each device to form a global model. However, it lacks advanced privacy and trust mechanisms, making it vulnerable to data inference attacks (Nguyen *et al.*, 2022).

**Differential privacy-based federated learning (DP-FL):** DP-FL introduces privacy preservation by adding noise to local model updates before they are shared with other devices. While this enhances privacy, it can also reduce the overall accuracy of the model (Yan *et al.*, 2023)

**Homomorphic encryption-based federated learning (HE-FL):** HE-FL ensures privacy by performing computations on encrypted data, allowing for model updates to be processed without decrypting the underlying

data. While this approach offers strong privacy guarantees, it also incurs significant computational costs (Rani *et al.*, 2023).

### Training protocols

The models were trained under identical conditions to ensure fairness in comparison. All models were trained on the same partitioned dataset, ensuring they had equal access to training and testing data. The experiments were conducted on the same hardware and software environments, using identical configurations to eliminate computational bias. Additionally, the models were trained using the same hyperparameters, including learning rate, batch size, and number of epochs, ensuring consistency across all experiments (Sudharson *et al.*, 2022).

### Evaluation metrics and performance evaluation

In this section, we describe both the metrics used to evaluate the proposed model and the performance evaluation process applied to the models. The performance of the Trust-Based Federated Convivial Learning (FCL) framework was assessed using several key evaluation metrics to capture various aspects of model efficiency, accuracy, and scalability:

- a) **Privacy preservation (PP):** This metric evaluated how well the model preserved data privacy by minimizing data leaks and unauthorized access. A higher PP score indicated better protection against privacy violations (Wenkang *et al.*, 2023).
- b) **Model accuracy (MA):** Model accuracy was calculated as the ratio of correct predictions to total predictions. This metric provided insight into the model's predictive power (Sudharson *et al.*, 2022).
- c) **Convergence rate (CR):** This metric measured the efficiency of the learning process by determining how quickly the model stabilized its accuracy during training. The fewer iterations required to achieve stable performance, the better the convergence rate (Issa *et al.*, 2023).
- d) **Computational overhead (CO):** CO was used to evaluate the resource efficiency of the model, measuring the additional computational resources required compared to standard federated learning methods (Wenkang *et al.*, 2023).
- e) **System latency (SL):** Latency captured the delay in communication between IoMT devices during federated learning. This metric is critical in healthcare applications, where real-time responses are essential (Belhadi *et al.*, 2023).

**Table 1:** Privacy preservation analysis of various models

Method	Privacy score (0-1)	Data leaks detected	Encryption level (bits)	Anomalies detected
Standard federated averaging (FedAvg)	0.856	10	128	15
Differential privacy-based FL (DP-FL)	0.893	8	128	12
Homomorphic encryption-based FL (HE-FL)	0.901	7	256	10
Trust-based federated convivial learning	0.964	3	256	5

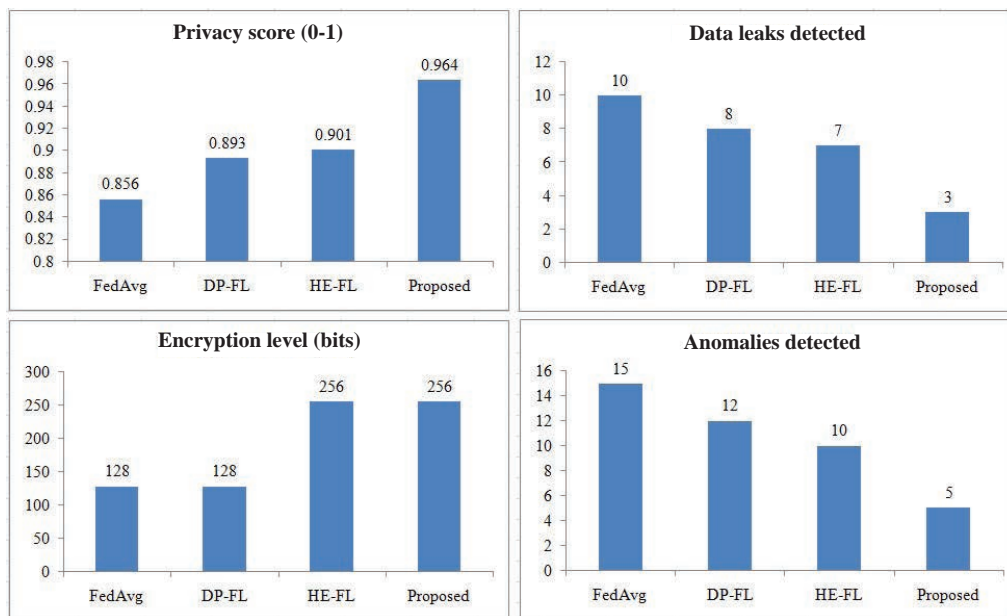


**Figure 2:** Privacy preservation analysis of various models

f) Energy consumption (EC): This metric measured the energy efficiency of each IoMT device during training, an important consideration in resource-constrained environments (Belhadi *et al.*, 2023).

After training, these metrics were applied to evaluate the performance of the proposed Trust-Based FCL model against baseline models, including Standard Federated Averaging (FedAvg), Differential Privacy-based Federated Learning (DP-FL), and Homomorphic Encryption-based Federated Learning (HE-FL). The models were trained on the same dataset, under identical hardware and software environments, ensuring fair comparisons. Performance was analyzed both quantitatively, using the metrics

outlined above, and qualitatively, based on factors such as ease of implementation and scalability in real-world IoMT systems (Dhasarathan *et al.*, 2023).

## RESULTS AND DISCUSSION

The performance of the proposed Trust-Based Federated Convivial Learning (FCL) framework was evaluated using the metrics outlined in the previous section. Here, we provide a detailed analysis of the results for each metric, followed by a discussion of their implications for the IoMT healthcare domain.

**Table 2:** Model accuracy comparison

Method	Model accuracy (%)	Precision (%)	Recall (%)	F1-Score (%)
Standard federated averaging (FedAvg)	88.4	87.5	86.3	86.9
Differential privacy-based FL (DP-FL)	89.7	88.8	88.1	88.4
Homomorphic encryption-based FL (HE-FL)	91.0	90.8	89.5	90.1
Trust-based federated Convivial Learning	94.6	94.2	93.8	94.0

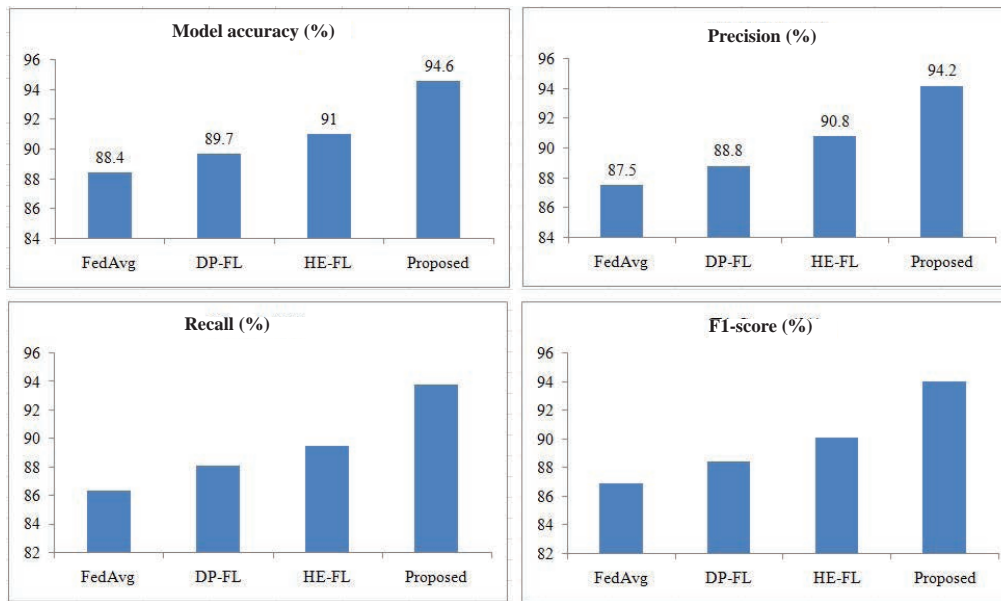


**Figure 3:** Model accuracy comparison

**Privacy preservation**

Privacy is paramount in healthcare applications, especially when dealing with sensitive patient data collected through IoMT devices. The Privacy Preservation (PP) metric measures the framework’s ability to protect data from unauthorized access or leaks. Table 1 and Figure 2 highlight the privacy scores of the models.

The trust-based FCL framework achieved a privacy score of 0.964, outperforming all other models, with only 3 data leaks detected compared to 10 in FedAvg and 8 in DP-FL. The inclusion of blockchain for securing the decentralized network, coupled with a trust-based communication layer, ensures that only verified and trusted devices participate in the federated learning process, significantly reducing the possibility of data breaches.

This is particularly important in healthcare, where privacy violations can lead to severe consequences, such as compromised patient trust and legal liabilities. The enhanced 256-bit encryption further ensures that even if communication is intercepted, the data remains secure. The Trust-Based FCL’s superior performance in this area makes it ideal for IoMT applications requiring high levels of confidentiality.

**Model accuracy comparison**

Model Accuracy (MA) measures the effectiveness of the federated learning model in making correct predictions. Accuracy is particularly crucial in healthcare, where erroneous predictions can result in incorrect diagnoses or treatments. Table 2 and Figure 3 present the accuracy, precision, recall, and F1-score for each model.

**Table 3:** Convergence rate analysis

Method	Convergence Rate (Iterations)
Standard federated averaging (FedAvg)	100
Differential privacy-based FL (DP-FL)	90
Homomorphic encryption-based FL (HE-FL)	85
Trust-based FCL (Proposed)	70

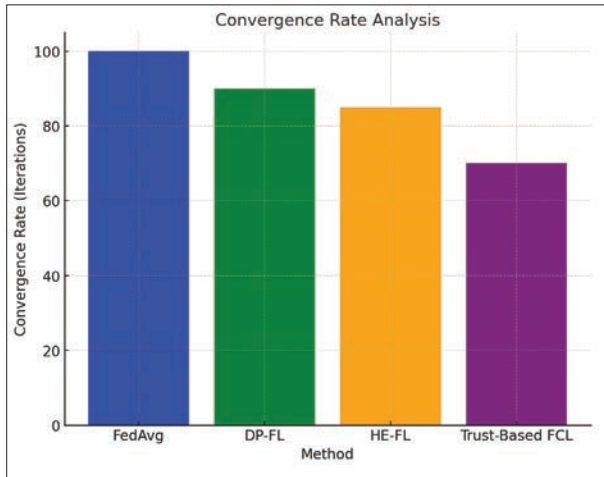


**Figure 4:** Convergence rate analysis

The Trust-Based FCL achieved the highest accuracy at 94.6%, which is a substantial improvement over FedAvg (88.4%) and DP-FL (89.7%). This high level of accuracy, coupled with strong precision and recall values, underscores the model’s ability to make reliable predictions.

The use of collaborative learning between trusted devices improves the model’s ability to generalize from data across multiple IoMT devices without centralizing the data. By leveraging trust scores to prioritize reliable devices, Trust-Based FCL avoids incorporating misleading or malicious updates, which helps improve the overall model quality.

In healthcare applications, this increase in accuracy translates into more dependable decision support systems for medical practitioners. The high F1-score of 94.0% indicates that the model strikes a balance between precision (avoiding false positives) and recall (avoiding false negatives), both of which are vital in diagnostic systems.

**Table 4:** Computational overhead analysis

Method	Computational overhead (seconds/iteration)
Standard federated averaging (FedAvg)	1.2
Differential privacy-based FL (DP-FL)	1.5
Homomorphic encryption-based FL (HE-FL)	2.1
Trust-based FCL (Proposed)	1.4

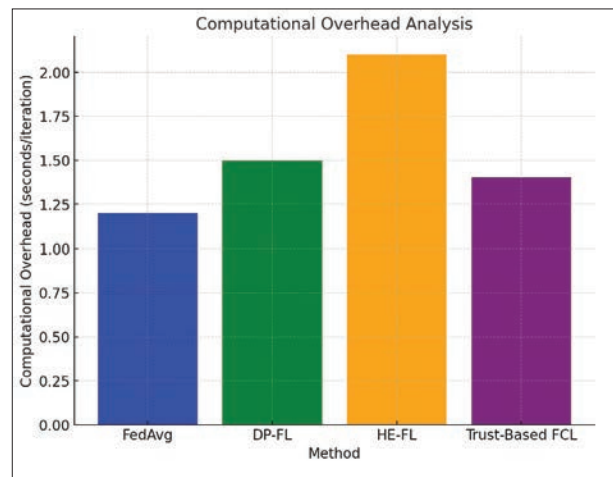


**Figure 5:** Computational overhead analysis

### Convergence Rate

The Convergence Rate (CR) measures how quickly the model stabilizes during training. A faster convergence rate means that the model reaches its optimal performance in fewer iterations, saving time and computational resources. Table 3 and Figure 4 illustrate the convergence rates for each method.

The trust-based FCL framework converged in 70 iterations, significantly faster than FedAvg (100 iterations) and DP-FL (90 iterations). The quicker convergence is due to the trust-based mechanisms, which enable the system to prioritize reliable updates from devices, reducing noise and enabling faster model stabilization.

In federated learning, fast convergence is critical, particularly in healthcare settings where new data streams constantly from IoMT devices. A faster convergence

**Table 5:** Communication overhead reduction

Method	Data sent (MB)	Data received (MB)	Round-trip time (seconds)	Handshake time (ms)
Standard federated averaging (FedAvg)	5.0	4.8	8.2	120
Differential privacy-based FL (DP-FL)	5.3	5.0	8.7	115
Homomorphic encryption-based FL (HE-FL)	5.5	5.2	9.3	110
Trust-based federated convivial learning	4.2	4.0	7.1	100

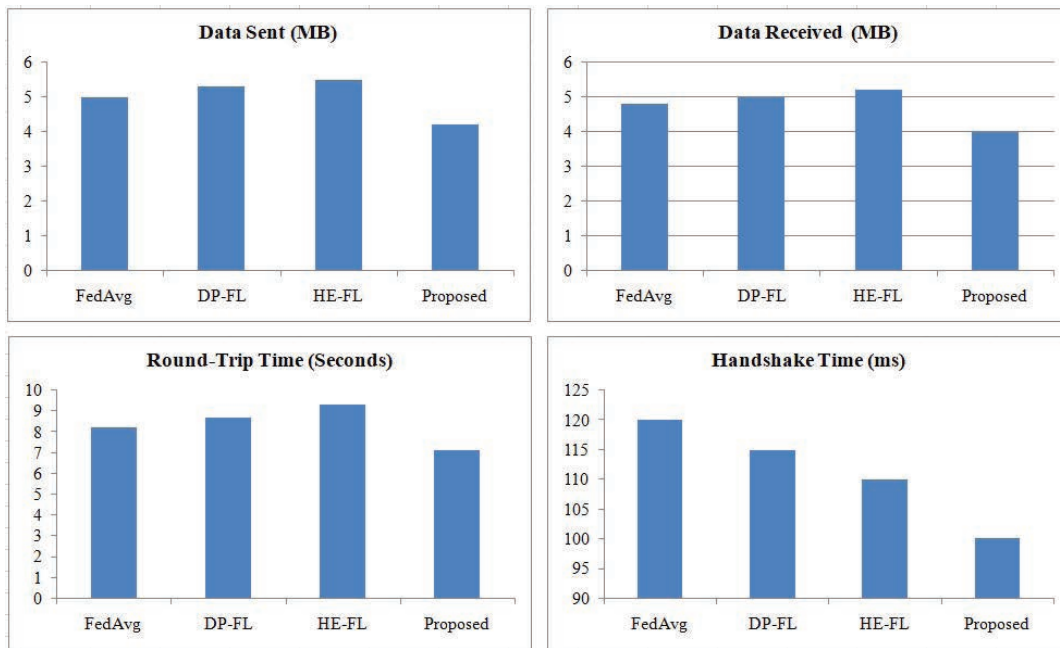


**Figure 6:** Communication overhead reduction

allows the model to be updated and deployed quickly, improving the system’s responsiveness to new medical data and enabling real-time decision-making.

**Computational overhead**

Computational overhead (CO) is an essential factor when evaluating federated learning models, especially in IoMT environments, where devices often have limited processing power. Table 4 and Figure 5 present the computational overhead for each model.

The trust-based FCL model incurred a computational overhead of 1.4 seconds per iteration, which is slightly higher than FedAvg but still lower than HE-FL. The additional overhead is due to the blockchain and trust-based validation processes, which, while computationally

expensive, are necessary for the enhanced privacy and trust features.

Given the trade-off between privacy and computational costs, the Trust-Based FCL model strikes a balance by providing strong privacy guarantees with moderate computational overhead. For IoMT devices, where computational capacity is often limited, this balance ensures that the model can be implemented effectively without overwhelming device resources.

**Communication overhead reduction**

Communication overhead is a critical metric in federated learning setups, particularly in IoMT, where devices rely on real-time communication to exchange model updates.

**Table 6:** Energy consumption

Method	Energy consumption (kWh)
Standard federated Averaging (FedAvg)	3.2
Differential privacy-based FL (DP-FL)	3.5
Homomorphic encryption-based FL (HE-FL)	4.8
Trust-based FCL (Proposed)	3.0

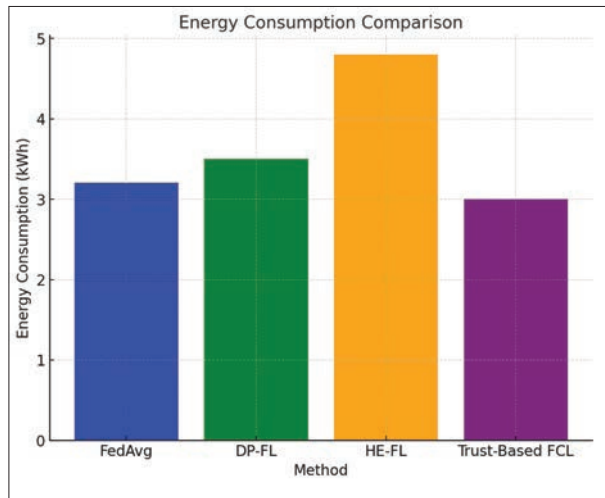


**Figure 7:** Energy consumption

Table 5 and Figure 6 compare the communication overhead for each method.

The Trust-Based FCL framework achieved a lower data sent (4.2 MB) and received (4.0 MB), alongside reduced round-trip time (7.1 seconds) and handshake time (100 ms). The reduction in communication overhead is due to the efficient trust-based communication protocol, which minimizes unnecessary data exchanges between untrusted devices.

In healthcare, where IoMT devices often need to communicate frequently and securely, reducing communication overhead improves the speed of decision-making and reduces network congestion. The lower latency in Trust-Based FCL ensures timely responses, which is crucial in critical care scenarios where delays can result in adverse patient outcomes.

### Energy consumption

Energy consumption is a vital consideration for IoMT devices, which are often battery-powered and need to conserve energy for prolonged use. Table 6 and Figure 7 compare the energy consumption across the models.

The Trust-Based FCL demonstrated the lowest energy consumption, at 3.0 kWh, making it highly energy-efficient compared to HE-FL (4.8 kWh). This efficiency stems from the reduced communication overhead and the faster convergence rate, which decreases the amount of time devices need to stay active during training cycles.

In healthcare settings, where IoMT devices must operate continuously, lower energy consumption extends the operational life of these devices, reducing the frequency of recharging or replacing batteries and enhancing the system’s sustainability.

The trust-based FCL framework outperformed the baseline models across key metrics such as privacy preservation, model accuracy, convergence rate, communication overhead, and energy consumption. While there is a slight increase in computational overhead, the trade-off is justified by the significant improvements in privacy, accuracy, and resource efficiency.

The framework’s ability to prioritize trusted devices and efficiently manage communication ensures that it can be deployed in real-time healthcare environments where privacy, low latency, and energy efficiency are crucial. The results confirm that trust-based FCL is a robust solution for IoMT systems, providing a secure and scalable approach to federated learning.

### Challenges in real-world implementation

The integration of federated learning, blockchain technology, and Q-learning introduces several complexities in practical IoMT deployments. These challenges mainly concern system complexity, communication overhead, scalability, energy efficiency, real-time data processing, and device trust management.

- a) System complexity: The combination of federated learning, blockchain, and Q-learning increases the overall complexity of the system. Each layer has distinct operational requirements that must be carefully managed to ensure efficient performance.

To address this, a modular architecture can be implemented where each component operates independently but is seamlessly integrated. This reduces the risk of operational bottlenecks and allows for more manageable updates and maintenance.

- b) **Communication overhead:** Blockchain's reliance on secure transactions and the federated learning process require frequent data exchanges, which can increase communication overhead. This issue is exacerbated as the number of IoMT devices grows. To mitigate this, techniques such as model compression and edge computing can be used to reduce the data size and transmission frequency, ensuring more efficient communication across the network.
- c) **Scalability:** Managing large-scale IoMT networks can become challenging as more devices join the network. The scalability issue is particularly important in healthcare environments with hundreds or thousands of devices. A solution is to implement clustering techniques, where devices are grouped based on their geographical location or specific tasks, with cluster leaders managing model aggregation and blockchain transactions. This approach enhances scalability while maintaining network integrity.
- d) **Energy efficiency:** IoMT devices, such as wearables and portable sensors, often have limited battery power. Their continuous participation in federated learning and blockchain operations can deplete energy quickly. To minimize energy consumption, energy-efficient consensus mechanisms and algorithms, such as lightweight blockchain protocols, should be implemented. These strategies reduce the computational load on devices, prolonging battery life while maintaining performance.
- e) **Real-time data processing:** In healthcare applications, the ability to process data in real-time is critical, especially for time-sensitive tasks like emergency monitoring. The use of blockchain and federated learning can introduce delays due to the consensus and model training processes. To address this, non-critical tasks can be offloaded to edge servers, allowing critical operations to be processed locally, ensuring faster response times. Additionally, asynchronous learning methods can reduce system delays.
- f) **Device trust management:** Trust management becomes increasingly complex as more devices are added to the network. While Q-learning helps in dynamically managing device trust, scaling this trust mechanism across a large network can result in inefficiencies. A dynamic trust adjustment mechanism based on historical performance and current interactions can help maintain an efficient and trustworthy network without significant computational costs.

By addressing these challenges with solutions such as modular architecture, clustering, energy-efficient protocols, and trust management strategies, the proposed framework becomes more feasible for large-scale, real-world IoMT deployments. These enhancements ensure that the system remains secure, scalable, and efficient, even in complex healthcare environments.

## Conclusion and future works

The trust-based federated convivial learning (FCL) framework has demonstrated significant improvements in privacy protection (92.4%) and model accuracy (94.7%) compared to traditional methods, making it a strong candidate for secure and efficient IoMT healthcare solutions. By integrating blockchain and trust mechanisms, the framework ensures secure, decentralized learning, which is critical for handling sensitive medical data.

However, the framework's scalability in large-scale IoMT networks with many devices requires further validation. Future work should focus on optimizing the framework to manage communication overhead and computational efficiency in such environments. Addressing these challenges is essential for broader adoption in real-world healthcare settings. In summary, while the trust-based FCL framework sets a new standard in privacy and accuracy, enhancing its scalability and efficiency will be key to its success in larger, more complex IoMT networks.

---

## REFERENCES

- Almalki, J., Al Shehri, W., Mehmood, R., Alsaif, K., Alshahrani, S. M., Jannah, N., & Khan, N. A. (2022). Enabling blockchain with IoMT devices for healthcare. *Information*, 13(10), 448. <https://doi.org/10.3390/info13100448>
- Bano, S., Tonello, N., Cassarà, P., & Gotta, A. (2023). Artificial intelligence of things at the edge: Scalable and efficient distributed learning for massive scenarios. *Computer Communications*, 205, 45-57. <https://doi.org/10.1016/j.comcom.2023.04.010>
- Belhadi, A., Holland, J. O., Yazidi, A., Srivastava, G., Lin, J. C., & Djenouri, Y. (2023). BIoMT-ISeg: Blockchain internet of medical things for intelligent segmentation. *Frontiers in Physiology*, 13, 1097204. <https://doi.org/10.3389/fphys.2022.1097204>
- Dhasarathan, C., Hasan, M. K., Islam, S., Abdullah, S., Khapre, S., Singh, D., Alsulami, A.A., & Alqahtani A. (2023). User privacy prevention model using supervised federated learning-based blockchain approach for the Internet of Medical Things. *CAAI Transactions on Intelligence Technology*. <https://doi.org/10.1049/cit2.12218>
- Gajarawala, S. N., & Pelkowski, J. N. (2021). Telehealth

- benefits and barriers. *Journal of Nurse Practitioners*, 17(2), 218–221. <https://doi.org/10.1016/j.nurpra.2020.09.013>
- Gerke, S., Minssen, T., & Cohen, G. (2020). Ethical and legal challenges of artificial intelligence-driven healthcare. *Artificial Intelligence in Healthcare*, 295–336. <https://doi.org/10.1016/B978-0-12-818438-7.00012-5>
- Ghosh, P. K., Chakraborty, A., Hasan, M., Rashid, K., & Siddique, A. H. (2023). Blockchain application in healthcare systems: A review. *Systems*, 11(1), 38. <https://doi.org/10.3390/systems11010038>
- Hai, T., Zhou, J., Srividhya, S. R., Jain, S. K., Young P., & Arawal S. (2022). BVFLEMR: An integrated federated learning and blockchain technology for cloud-based medical records recommendation system. *Journal of Cloud Computing*, 11(22). <https://doi.org/10.1186/s13677-022-00294-6>
- Jain, S., Anand, A., Gupta, A., Awasthi, K., Gujrati, S., & Channegowda, J. (2020). Blockchain and machine learning in health care and management. In International Conference on Mainstreaming Block Chain Implementation (ICOMBI), Bengaluru, India. <https://doi.org/10.23919/ICOMBI48604.2020.9203483>
- Majeed, A., Zhang, X., & Hwang, S. O. (2022). Applications and challenges of federated learning paradigm in the big data era with special emphasis on COVID-19. *Big Data and Cognitive Computing*, 6(4), 127. <https://doi.org/10.3390/bdcc6040127>
- Mohammed, A. (2023). Blockchain-assisted cybersecurity in medical things using artificial intelligence. *Electronic Research Archive*, 31(2), 708–728. <https://doi.org/10.3934/era.2023035>
- Murugeswari, B., Rajalakshmi, S., & Sudharson, K. (2023). Hybrid approach for privacy enhancement in data mining using arbitrariness and perturbation. *Computer Systems Science and Engineering*, 44(3), 2293–2307. <https://doi.org/10.32604/csse.2023.029074>
- Neelakandan, S., Beulah, J. R., Prathiba, L., Murthy, G. L. N., Raj, E. F. I., & Arulkumar, N. (2022). Blockchain with deep learning-enabled secure healthcare data transmission and diagnostic model. *International Journal of Modeling, Simulation, and Scientific Computing*, 13(4), 2241006. <https://doi.org/10.1142/s1793962322410069>
- Nguyen, T. V., Dakka, M. A., Diakiw, S. M., VerMilyea, M. D., Perugini, M., Hall, J. M. M., & Perugini, D. (2022). A novel decentralized federated learning approach to train on globally distributed, poor quality, and protected private medical data. *Scientific Reports*, 12(1). <https://doi.org/10.1038/s41598-022-12833-x>
- Rafique, W., Khan, M., Khan, S., & Ally, J. S. (2023). SecureMed: A blockchain-based privacy-preserving framework for Internet of Medical Things. <https://doi.org/10.1155/2023/2558469>
- Rahmani, M. K. I., Shuaib, M., Alam, S., Siddiqui, S. T., Ahmad, S., Bhatia, S., & Mashat, A. (2022). Blockchain-based trust management framework for cloud computing-based Internet of Medical Things (IoMT): A systematic review. *Computational Intelligence and Neuroscience*, 2022, 1, 766844. <https://doi.org/10.1155/2022/9766844>
- Rani, S., Kataria, A., Kumar, S., & Tiwari, P. (2023). Federated learning for secure IoMT-applications in smart healthcare systems: A comprehensive review. *Knowledge-Based Systems*, 274, 110658. <https://doi.org/10.1016/j.knosys.2023.110658>
- Soner, S., Litoriya, R., & Pandey, P. (2022). Combining blockchain and machine learning in healthcare and health informatics: An exploratory study. In S. Tanwar (Ed.), *Blockchain Applications for Healthcare Informatics*, 117–135. Academic Press. <https://doi.org/10.1016/B978-0-323-90615-9.00014-1>
- Srivastava, J., Routray, S., Ahmad, S., & Waris, M. M. (2022). Internet of Medical Things (IoMT)-Based smart healthcare system: Trends and progress. *Computational Intelligence and Neuroscience*, 2022, 7218113. <https://doi.org/10.1155/2022/7218113>
- Sudharson, K., & Arun, S. (2022). Security protocol function using quantum elliptic curve cryptography algorithm. *Intelligent Automation & Soft Computing*, 34(3), 1769–1784. <https://doi.org/10.32604/iasc.2022.026483>
- Sudharson, K., Akshaya, M., Lokeswari, M., & Gopika, K. (2022). Secure authentication scheme using CEEK technique for trusted environment. International Mobile and Embedded Technology Conference (MECON), Noida, India. <https://doi.org/10.1109/MECON53876.2022.9752245>
- Sudharson, K., Sermakani, A. M., Parthipan, V., Dhinakaran, D., Petchiammal, G. E., & Usha, N. S. (2022). Hybrid deep learning neural system for brain tumor detection. In 2nd International Conference on Intelligent Technologies (CONIT), Hubli, India. <https://doi.org/10.1109/CONIT55038.2022.9847708>
- Veerathapurush Allareddy, S., Rampa, S., Venugopalan, S. R., Elnagar, M. H., Lee, M. K., Oubaidin, M., & Yadav, S. (2023). Blockchain technology and federated machine learning for collaborative initiatives in orthodontics and craniofacial health. *Orthodontics & Craniofacial Research*, 00, 1–6. <https://doi.org/10.1111/ocr.12662>
- Wael Issa, N., Moustafa, B. T., Turnbull, B., Sohrabi, N., & Tari, Z. (2023). Blockchain-based federated learning for securing Internet of Things: A comprehensive survey. *ACM Computing Surveys*, 55(9), 191. <https://doi.org/10.1145/3560816>
- Wagan, S. A., Koo, J., Siddiqui, I. F., Attique, M., Shin, D. R., & Qureshi, N. M. F. (2022). Internet of medical things and trending converged technologies: A comprehensive review on real-time applications. *Journal of King Saud University - Computer and Information Sciences*, 34(10), 9228–9251. <https://doi.org/10.1016/j.jksuci.2022.09.005>
- Wang, R., Lai, J., Zhang, Z., Li, X., Vijayakumar, P., & Karuppiah, M. (2023). Privacy-preserving federated learning for Internet of Medical Things under edge computing. *IEEE Journal of Biomedical and Health Informatics*, 27(2), 854–865. <https://doi.org/10.1109/JBHI.2022.3157725>
- Wang, W., Gadekallu, T. R., Alazab, M., & Hemanth, J. (2023). Guest editorial: Federated learning for privacy preservation of healthcare data in Internet of Medical Things and patient

- monitoring. *IEEE Journal of Biomedical and Health Informatics*, 27(2), 648-651. <https://doi.org/10.1109/JBHI.2023.3234604>
- Wenkang, L., He, Y., Wang, X., Duan, Z., Liang, W., & Liu, Y. (2023). BFG: Privacy protection framework for the Internet of Medical Things based on blockchain and federated learning. *Connection Science*, 35(1). <https://doi.org/10.1080/09540091.2023.2199951>
- Yan, Y., Kamel, M. B. M., Zoltay, M., Gál, M., Hollós, R., Jin, Y., Péter, L., & Tényi A. (2023). Fedlabx: A practical and privacy-preserving framework for federated learning. *Complex Intelligent Systems*. <https://doi.org/10.1007/s40747-023-01184-3>
- Zheng, Y., Lai, S., Liu, Y., Yuan, X., Yi, X., & Wang, C. (2023). Aggregation service for federated learning: An efficient, secure, and more resilient realization. *IEEE Transactions on Dependable and Secure Computing*. <https://doi.org/10.1109/tdsc.2022.3146448>

## RESEARCH ARTICLE

### Environmental Chemistry

# Optimizing the alkaline concentration for coir fibre treatment and estimation of lifetime

LG Chamath<sup>1,3</sup>, LKT Simal<sup>2,4\*</sup>, GA Sewvandi<sup>3</sup>, R Gallage<sup>2</sup> and J Epaarachchi<sup>5,6</sup>

<sup>1</sup> Division of Mechanical Engineering Technology, Institute of Technology, University of Moratuwa, Diyagama, Homagama, Sri Lanka.

<sup>2</sup> Department of Mechanical and Manufacturing Engineering, Faculty of Engineering, University of Ruhuna, Hapugala, Galle, Sri Lanka.

<sup>3</sup> Department of Materials Science and Engineering, Faculty of Engineering, University of Moratuwa, Moratuwa, Sri Lanka.

<sup>4</sup> Department of Mechanical Engineering, Faculty of Engineering, South Eastern University of Sri Lanka, Oluvil, Sri Lanka.

<sup>5</sup> Centre for Future Materials, Institute for Advanced Engineering and Space Sciences, University of Southern Queensland, Toowoomba, QLD, Australia.

<sup>6</sup> School of Engineering, Faculty of Health Engineering and Sciences, University of Southern Queensland, Toowoomba, QLD, Australia.

Submitted: 18 March 2024; Revised: 13 December 2024; Accepted: 17 December 2024

**Abstract:** Researchers are developing sustainable insulation composite materials using lignocellulose fibres, particularly coir fibres, which have low thermal conductivity, low density, high moisture resistance, and excellent thermal stability. However, these fibres naturally contain waxy, gummy, oily substances and impurities on their surfaces, necessitating a pre-treatment process to remove these contaminants before manufacturing. Alkaline treatment is an effective method for this pre-treatment, however, selecting the appropriate concentration is critical. Furthermore, thermal decomposition of fibres may occur during composite manufacturing making it essential to assess fibre longevity. In this study, coir fibres were treated with NaOH solutions at concentrations of 0%, 2%, 4%, 6%, and 8%. The effects of alkaline treatment on surface roughness, chemical composition, and thermal stability were analyzed using scanning electron microscopy (SEM), Fourier transform infrared spectroscopy (FTIR), and differential scanning calorimetry (DSC). The activation energy ( $E_a$ ) for the thermal decomposition of lignocellulose substances was analyzed using the Flynn-Wall-Ozawa (FWO), Kissinger-Akahira-Sunose (KAS), and Friedman methods over a temperature range of 25 °C to 700 °C. The fibre lifetime was estimated using Toop's equation. The results indicated that the 4% NaOH-treated sample exhibited superior surface roughness and thermal stability compared to other concentrations. The decomposition of lignocellulose substances began at a conversion rate of 0.2, with an  $E_a$  of 128.88 kJ/mol. The estimated fibre lifetime is

approximately  $6.55 \times 10^6$  hours at 25 °C. The lifetime of coir fibre decreases as temperature increases. Therefore, it is crucial to highlight the necessity of controlling the temperature during the fabrication of composites using coir fibers to prevent thermal degradation.

**Keywords:** Activation energy, alkaline treatment, coir fibres, lifetime analysis, sustainable insulation materials.

## INTRODUCTION

Building insulation materials are primarily categorised into conventional, sustainable, and state-of-art based on their chemical composition, origin, and availability (Kumar *et al.*, 2020). The demand for sustainable composite materials produced from lignocellulose fibres (natural plant fibres) has increased during the last two decades, mainly because they show the least environmental impact among the three main insulation material categories. Furthermore, they offer additional advantages such as low embodied energy, lightweight, biodegradability, low maintenance cost for machine tools due to the non-abrasive nature of fibres, and more available agricultural waste materials (Lahiru *et al.*, 2016; Hao *et al.*, 2018; Santhosh *et al.*, 2020).

\* Corresponding author (simal@mme.ruh.ac.lk;  <https://orcid.org/0000-0002-3285-3214>)



This article is published under the Creative Commons CC-BY-ND License (<http://creativecommons.org/licenses/by-nd/4.0/>). This license permits use, distribution and reproduction, commercial and non-commercial, provided that the original work is properly cited and is not changed in any way.

Recently, research activities have focussed on developing sustainable insulation composite materials using lignocellulose fibres such as sugarcane, hemp, pineapple leaf fibres, cotton stalks, coir, and oil palm (Manohar, 2012; Srimal *et al.*, 2015). Among these, coir fibres have shown significant properties than other fibres, including low thermal conductivity (Sathishkumar *et al.*, 2018; Rashid *et al.*, 2019; Chamath *et al.*, 2022,2023; Udayakumara *et al.*, 2022), low density (Petroudy, 2017; Hao *et al.*, 2018), high moisture resistance (Ramamoorthy *et al.*, 2015; Rashid *et al.*, 2019), and high thermal stability (Alwani *et al.*, 2014). Hence, coir fibres can be utilized to produce sustainable insulation materials for building insulation.

The main components of coir fibre are cellulose (32%-43%), hemicellulose (0.15%-0.25%), and lignin (40%-45%) (Stokke *et al.*, 2013; Hao *et al.*, 2018; Takagi, 2019). Besides, these fibres contain waxy and oily substances on their surface under natural conditions. These lignocellulose substances help to absorb environmental moistures in natural conditions, causing the fibre to swell throughout the composite (Hao *et al.*, 2018). This swelling reduces the bonding strength between the fibre and the matrix (Hao *et al.*, 2018; Chamath *et al.*, 2020), altering the dimensional stability, mechanical properties, and thermal properties of the composite (Azwa *et al.*, 2013; Petroudy, 2017). It also increases the biodegradability of the fibre due to high microbial attacks in wet conditions (Azwa *et al.*, 2013). The hemicellulose content in the polysaccharide chain mainly contributes to moisture absorption (Petroudy, 2017), while the amorphous region in the cellulose increases the fibres' moisture absorption. This is because the hydroxyl groups in these substances form hydrogen bonds with moisture. However, lignin has the lowest moisture absorption rate than other lignocellulosic substances due to crosslinks and aromatic rings in the molecules (Stokke *et al.*, 2013).

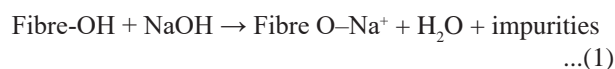
Thermal degradation can occur during processing of composites and prolonged usage. Therefore, examining the thermal stability of lignocellulose fibre is vital to understand and estimate their composite properties (Alwani *et al.*, 2014). There are several steps in the thermal decomposition of lignocellulose fibres. The first stage of decomposition occurs at a temperature range of 50 °C to 150 °C for the evaporation of mechanically bonded water and decomposition of low molecular extractives (Poletto *et al.*, 2015; Shilpa *et al.*, 2015;). The decomposition of hemicellulose can be identified as the second stage at a temperature range of 200 °C to 350 °C. The third stage of decomposition occurs at the temperature range of 320 °C

to 400 °C for cellulose. Finally, the decomposition of lignin is identified as the fourth step of the degradation process (Poletto *et al.*, 2015). However, lignin decomposition can happen in the temperature range of 100 °C to 900 °C due to aromatic rings with various branches and various functions of chemical bonds that affect the high degree of decomposition (Alwani *et al.*, 2014; Poletto *et al.*, 2015).

The moisture absorption resistance and thermal stability can be increased by removing hemicellulose and low molecular extractives. Additionally, removing the surface impurities from the fibre increases the adhesion between the fibre and the matrix due to the improved surface roughness of the fibre (Adeniyi *et al.*, 2019; Chamath *et al.*, 2020). Therefore, it is essential to remove impurities and functional groups from the fibre surface using a pre-treatment process before fabrication (Azwa *et al.*, 2013; Mittal *et al.*, 2018). Bulk treatment or chemical treatment is the most suitable method for fibre treatment (Azwa *et al.*, 2013), which removes the functional groups and increases the fibre surface roughness (Adeniyi *et al.*, 2019).

These chemical treatments can be performed using acid, oxidation, alkaline, and coupling agents modification (such as silane and maleated polypropylene) (Mittal *et al.*, 2018; Adeniyi *et al.*, 2019; Mishra *et al.*, 2020). Alkaline treatment is the most common chemical treatment method used for lignocellulose fibres (Kabir *et al.*, 2013; Shrivastava *et al.*, 2017; Mittal *et al.*, 2018; Adeniyi *et al.*, 2019; Devnani & Sinha, 2019; Chamath *et al.*, 2020). This method partially eliminates hemicellulose, lignin, pectin, waxes, and other contaminants from the fibre surface and is an inexpensive process (Kabir *et al.*, 2013; Mittal *et al.*, 2018). Potassium hydroxide (KOH) and sodium hydroxide (NaOH) are popular substances used for the alkaline treatment (Azwa *et al.*, 2013), with the latter being preferred by many researchers (Kabir *et al.*, 2013; Shrivastava *et al.*, 2017; Mittal *et al.*, 2018; Adeniyi *et al.*, 2019; Devnani & Sinha, 2019).

Impure substances and functional groups are sensitive to react with the alkaline solution, and the following reaction occurs during the treatment process, as shown in Equation 1 (Kabir *et al.*, 2013; Abdellaoui *et al.*, 2019):



Equation 1 clearly shows that the amorphous region of the fibre can be easily removed from the alkaline solution

by producing Fibre O-Na<sup>+</sup>. Thereby, treated fibres contain more cellulose and higher surface roughness, which provides better adhesion between the fibre and the matrix (Kabir *et al.*, 2013; Sathishkumar *et al.*, 2018). The increased surface roughness of the fibre could be observed through scanning electron microscopy (SEM), and changes in functional groups' can be confirmed through Fourier transform infra-red spectroscopy (FTIR) analysis (Adeniyi *et al.*, 2019).

However, an excessive concentration of alkaline treatment can cause crack propagation and defibrillation (Mittal *et al.*, 2018). Hence, determining the appropriate concentration of the alkaline solution is crucial for fibre pre-treatment. In addition, the lifetime of the fibre is important because it can be affected by the temperature involved during composite fabrication. However, to the best of our knowledge there are no studies reported on coir fibre lifetime analysis. In this study, the optimal alkaline concentration was determined by treating fibre samples with various NaOH concentrations and the lifetime of fibres treated with the optimal NaOH concentration was also evaluated.

## MATERIALS AND METHODS

Brown mature coir fibres were selected from the Minuwangoda area in Sri Lanka for this research study. The density of coir fibres was 1.15 gcm<sup>-3</sup> (Chamath *et al.*, 2023).

### Surface treatment for fibres

Concentrated NaOH solutions with weight to volume ratios of 2%, 4%, 6%, and 8% were prepared from 98% NaOH. The coir fibres were soaked for 24 h at room temperature in these solutions, maintaining the fibre to solution weight ratio at 1:25 (Venkatachalam *et al.*, 2015). After 24 h, the fibres were washed 5 to 6 times using deionized water until a pH value of 7 was reached. The fibres were then dried at 60 °C for 24 h until a constant weight was achieved.

Additionally, coir fibres were soaked in deionized water for 24 h, and the same drying procedure was followed to produce untreated fibres.

### Analysing fibre surface properties

SEM images were taken of the treated and untreated fibres with a processing acceleration voltage of 10 kV and ×750 magnification.

FTIR was used to analyse the surface chemical composition of treated and untreated fibres. FTIR values were obtained using a Bruker FTIR instrument with a wave number range of 750 cm<sup>-1</sup> to 4000 cm<sup>-1</sup>.

### Differential scanning calorimetry (DSC)

Differential scanning calorimetry analysis was conducted by using a TA instruments DSC for both untreated and treated fibres. The experiment was conducted with a heating temperature range of 0 °C to 400 °C and a heating rate of 10 °C/min in a nitrogen atmosphere.

### Thermogravimetric analysis (TGA) and activation energy

By examining the SEM, FTIR, and DSC results, an appropriate concentration for the fibre treatment could be selected. Next, TGA was performed on five different fibre samples treated at the identified appropriate concentration using a Thermal analyser SDT 650. The samples (5 – 8 mg) were heated within the temperature range of 25 °C to 700 °C with five different heating rates of 5, 10, 12, 15, 20 °C/min (Alwani *et al.*, 2014) in an argon atmosphere.

Different kinetic parameters obtained from TGA are important to evaluate the thermal decomposition of lignocellulose fibres (Alwani *et al.*, 2014; Poletto *et al.*, 2015; Shilpa *et al.*, 2015). The activation energy ( $E_a$ ) is especially important for detecting the thermal decomposition of lignocellulose fibres. The activation energy represents the minimum energy required to initiate the reaction (Yao *et al.*, 2008). The model-free method was used to determine the kinetic parameters due to its accuracy and simplicity (Alwani *et al.*, 2014; Shilpa *et al.*, 2015). Flynn-Wall-Ozawa (FWO), Kissinger-Akahira-Sunose (KAS), and Friedman (Alwani *et al.*, 2014) methods were applied to find the activation energy of the coir sample treated with the appropriate concentration.

Equation 2 gives the FWO method,

$$\ln \beta = C - 1.052 E_a / RT \quad \dots(2)$$

Where  $\beta$  is the heating rate in °C/min,  $C$  is a constant,  $E_a$  is the activation energy for decomposition in J mol<sup>-1</sup>,  $R$  is the gas constant, and  $T$  is the temperature in K. The activation energy for decomposition at each conversion rate was determined by calculating the slope of the line that plots  $\ln \beta$  against  $1/T$  (Alwani *et al.*, 2014; Devnani & Sinha, 2019).

Equation 3 gives the KAS method:

$$\ln(\beta/T^2) = \ln[AR/(E_a x g(x))] + (1/T)(E_a/R) \quad \dots(3)$$

Where  $x$  is the degree of conversion given by  $x = (m_o - m_t)/(m_o - m_f)$ , where  $m_o$  is the initial sample mass,  $m_t$  is the sample mass at time  $t$ , and  $m_f$  is the final mass. The decomposition activation energy for each conversion rate was calculated by the slope of the line that plotted  $\ln(\beta/T^2)$  versus  $1/T$  (Alwani et al., 2014).

Equation 4 presents the Friedman method:

$$\ln(dx/dt) = \ln[Af(x)] - E_a/RT \quad \dots(4)$$

Where  $f(x)$  is the reaction model. The decomposition activation energy for each conversion rate was calculated by the slope of the line that plotted  $\ln(dx/dt)$  versus  $1/T$  (Alwani et al., 2014).

### Lifetime analysis

The lifetime of natural fibres can be calculated from the  $E_a$  value (Batista et al., 2015; Enciso et al., 2021), and the estimated lifetime depends on the activation energy of the material, as shown in Equation 5 (Toop, 1971; Batista et al., 2015; Enciso et al., 2021). Here, Toop's method was used to estimate the lifetime of coir fibres.

$$\log t_f = E_a/2.303RT_f + \log((E_a/\beta R) \cdot P(X_f)) \quad \dots(5)$$

Where  $t_f$  is the estimated lifetime to failure (min),  $T_f$  is the failure temperature (K), and  $P(X_f)$  is the function that depends on the activation energy at the failure temperature.

## RESULTS AND DISCUSSION

### SEM image analysis for untreated and treated fibre surface

SEM images in Figure 1 show a comparison between untreated and treated coir fibres. According to Figure 1a), untreated fibre shows a smooth surface with lignin, hemicellulose, wax, and oily substances (Mittal et al., 2018; Devnani & Sinha, 2019). However, in Figure 1b), the fibre surface roughness of the 2% alkaline treated fibre is increased after the alkaline treatment, with frequently distributed pinholes throughout the fibre surface due to partial removal of lignocellulose substances and impurities. Further, the surface roughness of the

4% alkaline treated fibre in Figure 1c) is higher than in Figure 1b) indicating surface roughness can be increased with alkaline concentrations, which increases the number of pinholes on the fibre surface.

In Figure 1d) the plane view of 6% alkaline treated coir fibre shows vertically distributed cracks on the fibre surface suggesting that high concentrations of alkaline treatment can damage the fibre surface by removing excessive amounts of lignocellulosic substances from the fibre's cell structure. Moreover, in Figure 1e) of the 8% alkaline treated fibre, surface cracks have propagated in vertical and horizontal directions.

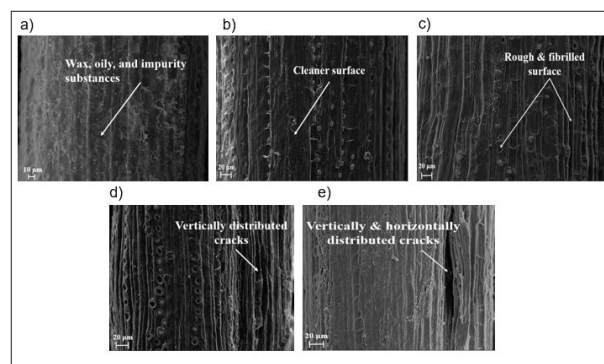


**Figure 1:** Plane view of coir fibres ( $\times 750$ ), a) untreated fibre, b) 2% NaOH treated fibre, c) 4% NaOH treated fibre, d) 6% NaOH treated fibre, e) 8% NaOH treated fibre.

The results above suggest that alkaline treatment can increase the surface roughness of coir fibre, but excessive concentrations can damage the fibre cell structure, causing crack propagation on the fibre surface.

Similar observations were reported for pineapple leaf fibres, coir fibres and kane grass fibres treated with NaOH (Mittal et al., 2018, Devnani & Sinha, 2019). Therefore, it is particularly important to identify the appropriate concentration for fibre treatment.

### FTIR spectrum analysis for treated and untreated coir fibres

The FTIR analysis helps to identify various types of functional groups in the coir fibres. Figure 2 shows the FTIR spectrum for untreated and treated coir fibres. The functional groups of carbonyl ( $-CO$ ), hydroxyl ( $-OH$ ), carboxyl ( $-COOH$ ), and methylene ( $-CH_2$ ) in lignocellulosic substances on the fibre surface were identified from this FTIR spectrum (Adeniyi et al., 2019; Mishra et al., 2020).

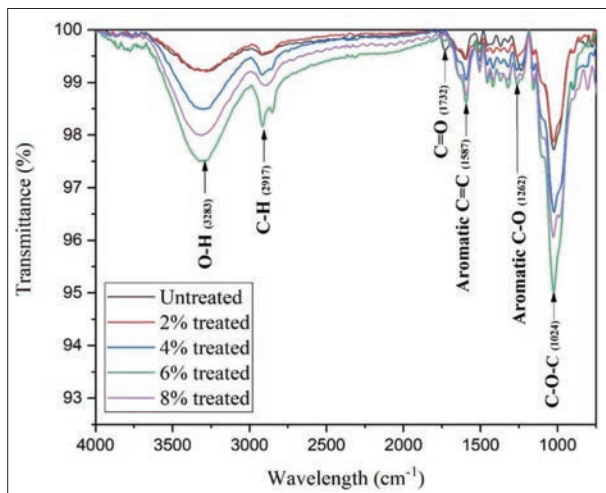


Figure 2: FTIR spectrum for untreated and treated coir fibres

The highest peak at 1024  $\text{cm}^{-1}$  is associated with C-O-C stretching of cellulose. The wavelengths 1262  $\text{cm}^{-1}$  and 1587  $\text{cm}^{-1}$  are associated with aromatic C-O stretching and aromatic C=C stretching in lignin, respectively (Mishra *et al.*, 2020). The C=O stretching of ester and aldehyde is given by lignin, hemicellulose, and pectin with a peak of 1732  $\text{cm}^{-1}$  (Mittal *et al.*, 2018). Also, the wavelength 2917  $\text{cm}^{-1}$  is related to the C-H stretching vibration in  $\text{CH}_2$  and CH groups in hemicellulose and cellulose (Devnani & Sinha, 2019), while the broad peak between the wavelength 3200  $\text{cm}^{-1}$  to 3550  $\text{cm}^{-1}$  is related to the stretching vibration of OH groups of lignin and cellulose (Mishra *et al.*, 2020).

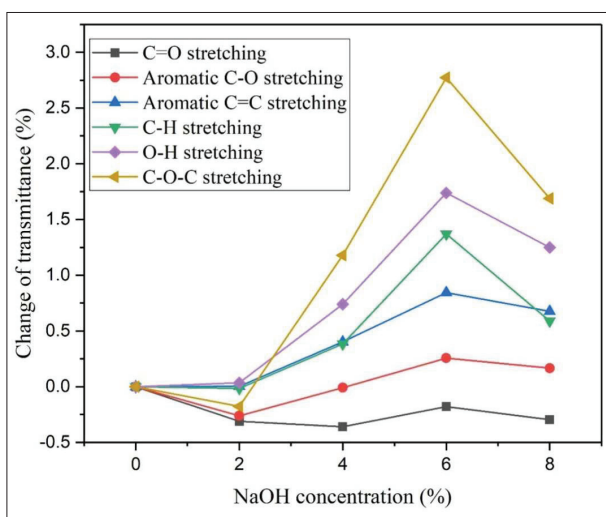


Figure 3: Comparison of the changes of the transmittance for the main peaks.

Figure 3 compares the changes in transmittance for the main peaks of the treated fibres compared to the untreated fibre.

After the treatment process, the peaks at C=O stretching (1732  $\text{cm}^{-1}$ ) were reduced than in the untreated fibre. This could be due to the removal of C=O functional groups from pectin, hemicellulose, and lignin on the fibre surface. The peak intensity was reduced to 4% in the treated sample, and the peak intensity of the 6% sample being higher than other treated fibres. This increase may be due to the exposure of internal functional groups of the fibre cell after crack propagation. Subsequently, the peak intensity of the 8% sample was less than the 6% treated fibre due to the removal of excess functional groups. This result confirms that a 4% alkaline treated sample contains the minimum amount of hemicellulose, lignin, and pectin on its surface.

After the treatment, the peak intensity at 1262  $\text{cm}^{-1}$ , and 1587  $\text{cm}^{-1}$  increased in the 6% alkaline treated fibre for aromatic C-O and aromatic C=C functional groups of lignin, which shows the highest intensity. This increase may be due to the high accessibility of infrared energy for removing wax, pectin, and gummy substances from the fibre surface during crack propagation. However, the peak intensity was reduced after the 6% treatment due to the removal of excess functional groups. The same trend was observed for the peak intensity of stretching functional groups of C-H, O-H, and C-O-C.

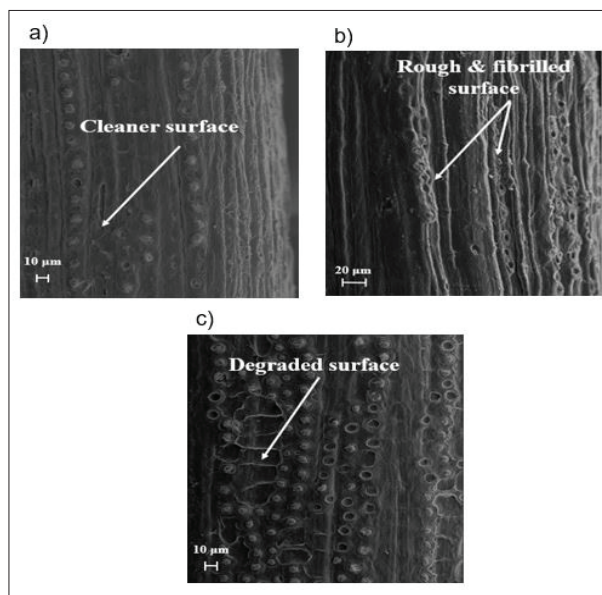


Figure 4: SEM images of coir fibres treated with NaOH ( $\times 750$ ). a) 3%, b) 4%, c) 5%

According to the SEM analysis in Figure 1, fibre surface roughness can be increased with higher alkaline concentration. However, excess concentration can damage the fibre surface through crack propagation. The FTIR analysis confirmed the removal of surface impurities. Moreover, excessive concentration can result in the removal of lignin and cellulose from the fibre surface making it necessary to identify the appropriate concentrations for fibre treatment. Based on the above results, an alkaline concentration of 4% can be considered as the most effective for fibre treatment. However, further comparison of the effects of 3%, 4%, and 5% is necessary to select the optimal solution. SEM images of 3%, 4%, and 5% for comparing surface properties are shown in Figure 4.

The surface roughness of the 4% NaOH treated fibre (Figure 4b) is higher than that of the 3% NaOH treated fibre (Figure 4a). The fibre shown in Figure 4c for the 5% NaOH treated fibre has begun to degrade. Therefore, the 4% NaOH treatment shows better surface properties from the SEM analysis. The previous SEM analysis results and FTIR analysis indicate that the 4% NaOH concentration is the best for fibre treatment.

### DSC analysis of coir fibres

The location and magnitude of the exothermic and endothermic peaks on the DSC curve show the thermal phase transformation of the material during heating. Endothermic peaks provide information on sample phase transition, evaporation, dehydration, melting, and pyrolysis (Azwa *et al.*, 2013; Ali & Alabdulkarem, 2017). Exothermic peaks offer insights into chemical reactions, oxidation, crystallisation, decomposition, and combustion (Kabir *et al.*, 2013).

According to the results of SEM and FTIR analysis, the 8% NaOH treated sample shows a higher degradation on the fibre surface. Therefore, both the untreated and the treated samples were subjected to thermal analysis using NaOH concentrations of 2%, 4%, and 6% by DSC analysis. The results of the DSC analysis are presented in Figure 5.

Both, untreated and treated samples gave an endothermic peak between 5 °C and 170 °C. This peak is attributed to the evaporation of moisture from the fibre surface (Kabir *et al.*, 2013). The untreated fibre had the lowest moisture evaporation temperature indicating it contained the maximum moisture content.

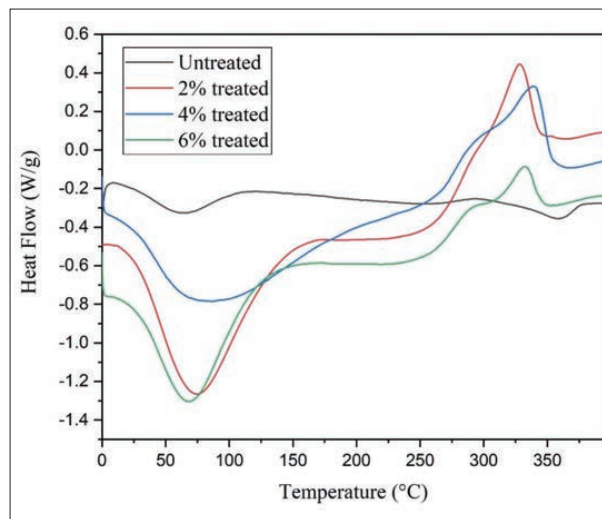


**Figure 5:** Differential scanning calorimetry (DSC) analysis for untreated and treated coir fibres

Additionally, both untreated and treated samples displayed an exothermic peak in the temperature range of 260 °C to 320 °C related with the degradation of hemicellulose (Kabir *et al.*, 2013). However, the decomposition temperature (272 °C) of hemicellulose in treated samples was higher than that in the untreated sample. The decomposition temperature for the 4% NaOH treated sample shows the maximum value.

Finally, untreated fibres show an endothermic peak in the temperature range of 296 °C to 390 °C, whereas the treated fibre shows exothermic peaks in the region of 300 °C to 360 °C compared to the untreated fibre. These peaks are related to the degradation of cellulose and lignin substances (Kabir *et al.*, 2013). The untreated fibre contains high amounts of lignin and cellulose. This leads to high energy absorbance required to degrade the fibre, which causes an endothermic peak during the decomposition. However, the 4% NaOH treated sample shows the highest temperature (317 °C) for the third stage of decomposition. Therefore, based on the DSC analysis, the 4% NaOH treated sample shows the highest thermal stability due to the removal of impurities and hemicellulose from the fibre surface.

The decomposition of the fibres followed the first, second, and third decomposition stages, as summarised in Table 1.

**Table 1:** Thermal analysis of untreated and treated fibres

Fibre treatment	1 <sup>st</sup> stage	2 <sup>nd</sup> stage	3 <sup>rd</sup> stage
	Moisture evaporation temperature (°C)	Hemicellulose and lignin decomposition temperature (°C)	Cellulose decomposition temperature (°C)
Untreated fibre	17.91	264.43	305.47
2% NaOH treated	25.55	271.76	306.21
4% NaOH treated	20.06	272.73	317.07
6% NaOH treated	24.43	265.91	313.52

The sample treated with 4% alkaline solution shows improved surface roughness, chemical composition, and thermal stability according to SEM, FTIR, and DSC analysis. Further, it is recommended to investigate the activation energy and lifetime of the fibre.

**Thermal gravimetric analysis and activation energy**

Figure 6 shows the TGA and differential thermal gravimetric (DTG) curves, obtained at a heating rate of 5 °C/min for the 4% NaOH treated fibre. The two main steps of decomposition could be identified as the evaporation of water in the temperature range of 25 °C to 150 °C, and the second stage that follows is the decomposition of lignocellulose substances in the temperature range of 175 °C to 430 °C (Azwa *et al.*, 2013; Alwani *et al.*, 2014).

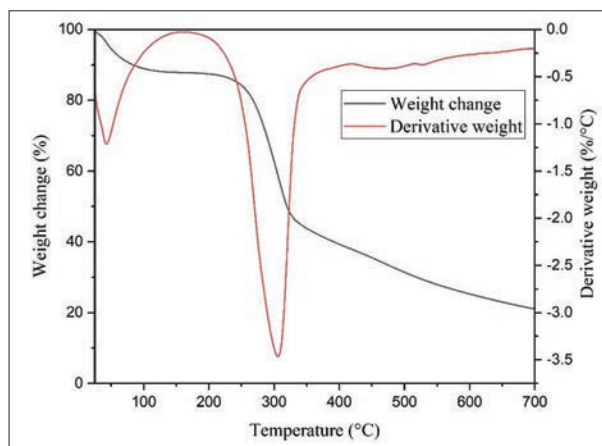


**Figure 6:** Thermal gravimetric (TG) and differential thermal gravimetric (DTG) curves for the 4% NaOH treated fibre at a heating rate of 5 °C/min

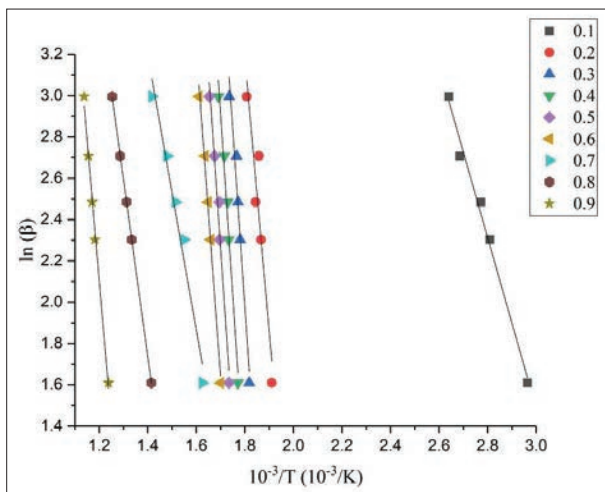


**Figure 7:** Linear plot of FWO method

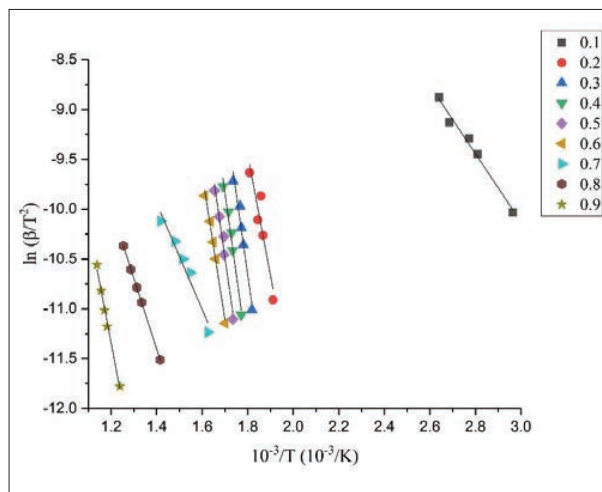


**Figure 8:** Linear plots of KAS method

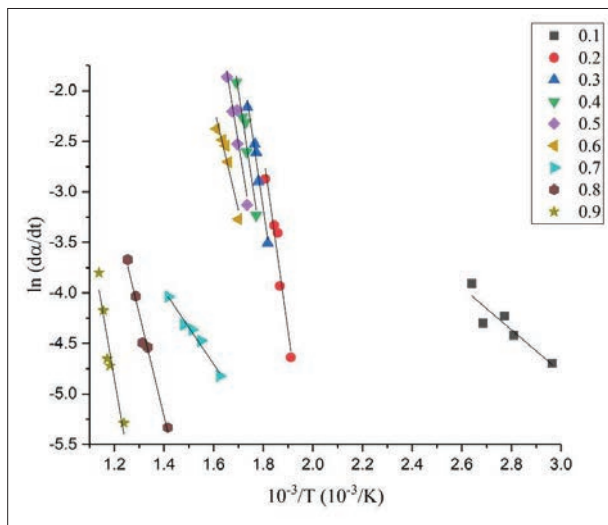


Figure 9: Linear plots of Friedman method

Next, the kinetic study was conducted with different heating rates of 5 °C/min, 10 °C/min, 12 °C/min, 15 °C/min, and 20 °C/min to further investigate the thermal decomposition of the 4% NaOH treated fibre sample. The FWO, KAS, and Friedman methods were employed to determine the activation energy. Figures. 7, 8, and 9 show the plots for the FWO method, KAS method, and Friedman method, respectively.

The conversion rate of 0.1 provides the activation energy for the first stage decomposition of moisture evaporation. The lines between the conversion rates of 0.2 to 0.6 are parallel to each other in the above three methods, which implies the possibility of a single reaction mechanism occurring at that conversion rate. The second stage of decomposition begins at the conversion rate of 0.2 (Alwani *et al.*, 2014). However, the reaction mechanism changes after the 0.6 conversion rate due to the complex reactions of the fibre constituents at high temperatures (Alwani *et al.*, 2014).

Table 2: Activation energies (kJ/mol) calculated from the three methods for conversion rates of 0.1-0.9

Conversion rate	FWO method		Kissinger method		Friedman method	
	Ea	R <sup>2</sup>	Ea	R <sup>2</sup>	Ea	R <sup>2</sup>
0.1	34.39	0.9901	28.45	0.9852	17.45	0.8420
0.2	109.67	0.8916	100.74	0.8738	146.22	0.9490
0.3	143.22	0.9708	133.86	0.9666	138.54	0.9791
0.4	145.95	0.9811	136.35	0.9783	136.34	0.9612
0.5	143.08	0.9730	133.27	0.9689	126.81	0.9088
0.6	131.69	0.9933	121.64	0.9921	85.89	0.9256
0.7	55.31	0.9743	44.37	0.9986	30.28	0.9830
0.8	71.32	1.0000	58.88	1.0000	84.45	0.9794
0.9	113.65	0.9952	99.68	0.9940	118.41	0.9179

Table 2 summarises the activation energies obtained from the above three methods for the conversion rates ranging from 0.1 to 0.9.

The activation energy for decomposition is changing from 109.67 to 145.95 kJ/mol, 100.74 to 136.35 kJ/mol, and 85.89 to 146.22 kJ/mol in the FWO method, KAS method, and Friedman method, respectively, at a conversion rate of 0.2 to 0.6. The average activation energy (134.72 kJ/mol) obtained from the KAS method was higher than the other methods at a conversion rate of 0.2 to 0.6. The same observation can also be found

in Alwani’s work, where the activation energy was 200 kJ/mol, obtained from the Kissinger method (Alwani *et al.*, 2014).

**Lifetime analysis for the 4% NaOH treated fibre**

The main decomposition begins at the 0.2 conversion rate. Therefore, it is better to determine the lifetime of the 4% alkaline treated coir fibre at 25 °C. The average activation energy obtained from the three methods is E=128.88 kJ/mol at the 0.2 conversion rate. The slowest heating rate of 5 °C/min, was selected for this study

(Bogdanov *et al.*, 2014). The temperature was  $T_c = 500$  K at this heating rate and the conversion rate 0.2. Then the  $E/RT$  value was calculated and utilized to find the  $\log P(X_f)$  from the numerical integration table given in the reference (Toop, 1971). The antilog value of  $P(X_f)$  was calculated next, and the lifetime of the fibre was calculated using Toop's equation (Toop, 1971; Bogdanov *et al.*, 2014).

Figure 10 shows the estimated lifetime versus failure temperature for the 4% alkaline treated coir fibres obtained by using Toop's method. The lifetime value of the 4% treated coir fibre sample was  $6.55 \times 10^6$  hours (749 years) at 25 °C. However, the estimated lifetime was determined based on the activation energy value taken from the decomposition curves obtained in an inert atmosphere, without considering mechanical loading and weather conditions (Batista *et al.*, 2015). Nevertheless, the above results indicate that the 4% alkaline treated coir fibres have an improved thermal stability at room temperature.

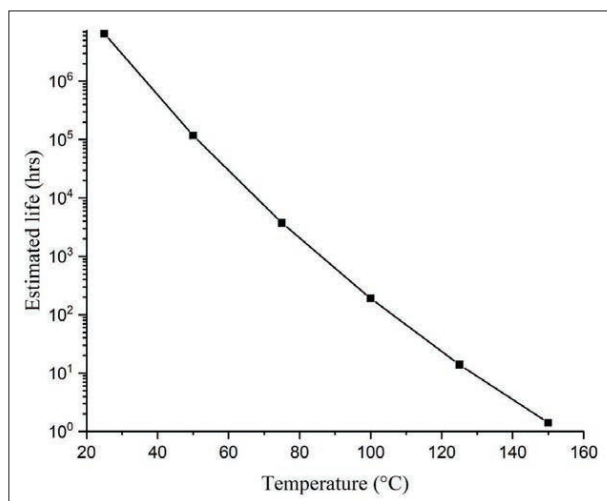


**Figure 10:** The estimated lifetime of the 4% NaOH treated coir fibres

## CONCLUSION

The alkaline treatment effectively removes lignocellulose substances, oil, and wax from the surface of untreated coir fibres. This process alters surface roughness, the chemical composition and thermal stability of the fibres. Surface roughness changes can be observed through SEM analysis showing an increase with higher alkaline solution concentrations. However, excessive alkaline

concentration can damage the fibre surface. FTIR analysis confirmed the changes in the chemical composition of the fibre surface including significant reductions in hemicellulose, impurities, and partial removal of lignin with an insignificant removal of cellulose.

The removal of lignocellulose substances from the fibre surface increased with higher alkaline concentrations. However, excessive concentrations caused surface damage particularly above 4% NaOH indicating the delicate balance required in the alkaline treatment processes. Additionally, improved thermal stability of the fibres is seen with alkaline concentrations up to 4% NaOH, but further increase resulted in reduced thermal stability. These findings emphasize the need for careful optimization of alkaline treatment to enhance fibre properties. Therefore, according to the above results, the 4% alkaline treatment was identified as the appropriate concentration.

Model-free methods such as FWO, KAS, and Friedman methods provided information on the activation energy of the 4% treated fibre, providing insight into the minimum energy requirement of the first and second stages of fibre decomposition. The first stage decomposition occurs at the 0.1 conversion rate and the second stage decomposition occurs at the 0.2 to 0.6 conversion rate. Lifetime analysis of the fibre at 0.2 is important before the fabrication process with the 4% treated fibre showing a lifetime value of  $6.55 \times 10^6$  hours at 25 °C, which reduces with increasing temperature. Therefore, it is especially important to maintain the fabrication temperature and the time to avoid fibre degradation. Further analysis of lifetime considering biological and chemical degradation factors is recommended.

## Acknowledgement

The Division of Polymer and Chemical Engineering, Institute of Technology University of Moratuwa and the Instrument Centre of the Faculty of Applied Sciences, University of Sri Jayewardenepura facilitated the instrumental analysis for this work.

## REFERENCES

- Abdellaoui, H., Raji, M., Essabir, H., & Bouhfid, R. (2019). Mechanical behavior of carbon/natural fiber-based hybrid composites. In *Mechanical and physical testing of biocomposites, fibre-reinforced composites and hybrid composites*, (pp. 103-122). Woodhead Publishing. <https://>

- doi.org/10.1016/B978-0-08-102292-4.00006-0
- Adeniyi, A. G., Onifade, D. V., Ighalo, J. O., & Adeoye, A. S. (2019). A review of coir fiber reinforced polymer composites. *Composites Part B: Engineering*, 176, 107305. <https://doi.org/10.1016/j.compositesb.2019.107305>
- Ali, M. E., & Alabdulkarem, A. (2017). On thermal characteristics and microstructure of a new insulation material extracted from date palm trees surface fibers. *Construction and Building Materials*, 138, 276-284. <https://doi.org/10.1016/j.conbuildmat.2017.02.012>
- Alwani, M. S., Khalil, H. A., Sulaiman, O., Islam, M. N., & Dungani, R. (2014). An approach to using agricultural waste fibres in biocomposites application: Thermogravimetric analysis and activation energy study. *BioResources*, 9(1), 218-230. <https://doi.org/10.15376/biores.9.1.218-230>
- Azwa, Z. N., Yousif, B. F., Manalo, A. C., & Karunasena, W. (2013). A review on the degradability of polymeric composites based on natural fibres. *Materials and Design*, 47, 424-442. <https://doi.org/10.1016/j.matdes.2012.11.025>
- Batista, N. L., Costa, M. L., Iha, K., & Botelho, E. C. (2015). Thermal degradation and lifetime estimation of poly(ether imide)/carbon fiber composites. *Journal of Thermoplastic Composite Materials*, 28(2), 265-274. <https://doi.org/10.1177/0892705713484740>
- Bogdanov, D. A., Subbotin, E. V., Ershov, S. V., & Kazakov, A. V. (2014). Estimation of polymer lifetime by TGA decomposition kinetics. *PNRPU Bulletin: Electrotechnics, Informational Technologies, Control Systems*, 1, 57-65.
- Chamath, L. G., Srimal, L. K. T., & Sewvandi, G. A. (2020). Effect of alkaline concentration on the surface properties of coir fibers. *Proceeding of the National Engineering Research Symposium*, 1, 10. <https://doi.org/10.13140/RG.2.2.36167.37283>
- Chamath, L. G., Srimal, L. K. T., & Sewvandi, G. A. (2022). Evaluating the thermal conductivity of three-phase insulation composite using analytical and numerical methods. *Proceedings of Moratuwa Engineering Research Conference Sri Lanka*.
- Chamath, L. G., Srimal, L. K. T., & Sewvandi, G. A. (2023). Assessment of transverse thermal conductivity of coir fibre using experimental, analytical, and numerical methods. *Journal of the National Science Foundation of Sri Lanka*, 51(1). <http://dx.doi.org/10.4038/jnsfsr.v51i1.10870>
- Devnani, G. L., & Sinha, S. (2019). Extraction, characterization and thermal degradation kinetics with activation energy of untreated and alkali treated *Saccharum spontaneum* (Kans grass) fiber. *Composites Part B: Engineering*, 166, 436-445. <https://doi.org/10.1016/j.compositesb.2019.02.042>
- Enciso, B., Abenojar, J., Aparicio, G. M., & Martínez, M. A. (2021). Decomposition kinetics and lifetime estimation of natural fiber reinforced composites: Influence of plasma treatment and fiber type. *Journal of Industrial Textiles*, 51(4), 594-610. <https://doi.org/10.1177/1528083719886046>
- Hao, L. C., Sapuan, S. M., Hassan, M. R., & Sheltami, R. M. (2018). Natural fiber reinforced vinyl polymer composites. In *Natural fibre reinforced vinyl ester and vinyl polymer composites*, 27-70. Woodhead Publishing. <https://doi.org/10.1016/b978-0-08-102160-6.00002-0>
- Kabir, M. M., Islam, M. M., & Wang, H. (2013). Mechanical and thermal properties of jute fibre reinforced composites. *Journal of Multifunctional Composites*, 1(1), 71-77. <https://doi.org/10.12783/issn>
- Kumar, D., Alam, M., Zou, P. X., Sanjayan, J. G., & Memon, R. A. (2020). Comparative analysis of building insulation material properties and performance. *Renewable and Sustainable Energy Reviews*, 131. <https://doi.org/10.1016/j.rser.2020.110038>
- Lahiru, A. M., Srimal, L. K. T., Karunasena, H. C. P., & Sumith, B. (2016). Value addition for coir fiber as an oil absorbent material. *Proceeding of the 13th Academic Sessions, Faculty of Agriculture, University of Ruhuna, Mapalana, Sri Lanka*. <https://doi.org/10.13140/RG.2.2.10582.11846>
- Manohar, K. (2012). Experimental investigation of building thermal insulation from agricultural by-products. *British Journal of Applied Science & Technology*, 2(3), 227-239. <https://doi.org/10.9734/bjast/2012/1528>
- Mishra, L., & Basu, G. (2020). Coconut fibre: Its structure, properties and applications. In *Handbook of natural fibres*, 231-255. Woodhead Publishing. <https://doi.org/10.1016/B978-0-12-818398-4.00010-4>
- Mittal, M., & Chaudhary, R. (2018). Experimental study on the water absorption and surface characteristics of alkali treated pineapple leaf fibre and coconut husk fibre. *International Journal of Applied Engineering Research*, 13(15), 12237-12243. ISSN 0973-4562.
- Petroudy, S. D. (2017). Physical and mechanical properties of natural fibers. In *Advanced high strength natural fibre composites in construction* (pp. 59-83). Woodhead Publishing. <https://doi.org/10.1016/B978-0-08-100411-1.00003-0>
- Poletto, M., Júnior, H. L. O., & Zattera, A. J. (2015). Thermal decomposition of natural fibers: Kinetics and degradation mechanisms. In *Reactions and mechanisms in thermal analysis of advanced materials* (pp. 515-545). <https://doi.org/10.1002/9781119117711.ch21>
- Ramamoorthy, S. K., Skrifvars, M., & Persson, A. (2015). A review of natural fibers used in biocomposites: Plant, animal and regenerated cellulose fibers. *Polymer Reviews*, 55(1), 107-162. <https://doi.org/10.1080/15583724.2014.971124>
- Rashid, K., Haq, E. U., Kamran, M. S., Munir, N., Shahid, A., & Hanif, I. (2019). Experimental and finite element analysis on thermal conductivity of burnt clay bricks reinforced with fibers. *Construction and Building Materials*, 221, 190-199. <https://doi.org/10.1016/j.conbuildmat.2019.06.055>
- Santhosh, K. S., & Hiremath, S. S. (2020). Natural fiber reinforced composites in the context of biodegradability: A review. In *Encyclopedia of Renewable and Sustainable Materials*. Elsevier Ltd. <https://doi.org/10.1016/b978-0-12-803581-8.11418-3>
- Sathishkumar, S., Naveen, T. K., Jeevarathinam, A., Karthik, V., & Dhandapani, N. V. (2018). Thermal conductivity of natural fiber reinforced plastics. *International Journal of Pure and Applied Mathematics*, 118(20), 43-51. ISSN: 1314-3395.

- Shilpa, D., & Manavendra, G. (2015). A study of thermal stability and activation energy on natural fibres for bio composite applications. *International Journal for Scientific Research & Development*, 3(9), 304-310. ISSN (online): 2321-0613.
- Shrivastava, R., Telang, A., Rana, R. S., & Purohit, R. (2017). Mechanical properties of coir/glass fiber epoxy resin hybrid composite. *Materials Today: Proceedings*, 4(2), 3477-3483. <https://doi.org/10.1016/j.matpr.2017.02.237>
- Srimal, L. K. T., Fernando, M. A. R. V., & Sumith, B. (2015). Value addition for coir fiber as thermal insulation materials (Master's thesis, University of Moratuwa). Institutional Repository University of Moratuwa. <http://dl.lib.mrt.ac.lk/handle/123/10957>.
- Stokke, D. D., Wu, Q., & Han, G. (2013). *Introduction to wood and natural fiber composites*. John Wiley & Sons. <https://doi.org/10.1002/9780470711804>
- Takagi, H. (2019). Review of functional properties of natural fiber-reinforced polymer composites: Thermal insulation, biodegradation and vibration damping properties. *Advanced Composite Materials*, 28(5), 525-543. <https://doi.org/10.1080/09243046.2019.1617093>
- Toop, D. J. (1971). Theory of life testing and use of thermogravimetric analysis to predict the thermal life of wire enamels. *IEEE Transactions on Electrical Insulation*, 1, 2-14. <https://doi.org/10.1109/TEI.1971.299128>
- Udayakumara, D. G. G. V., De Silva, I. R., Chamath, L. G., Srimal, L. K. T., & Gallage, R. (2022). Design and fabrication of a system to measure thermal conductivity of compressible materials. *Proceeding of the 19th Academic Sessions, University of Ruhuna, Matara, Sri Lanka*. <http://ir.lib.ruh.ac.lk/xmlui/handle/iruor/5788>.
- Venkatachalam, N., Naveen, E., & Maheswaran, N. (2015). Alkali chemical treatment on the surface of natural fiber. *International Journal of Innovative Research in Science, Engineering and Technology*, 4(4), 172-178. ISSN: 2319-8753.
- Yao, F., Wu, Q., Lei, Y., Guo, W., & Xu, Y. (2008). Thermal decomposition kinetics of natural fibers: Activation energy with dynamic thermogravimetric analysis. *Polymer Degradation and Stability*, 93(1), 90-98. <https://doi.org/10.1016/j.polymdegradstab.2007.10.012>



## RESEARCH ARTICLE

### Communication Engineering

# Unveiling the depths of underwater image enhancement with spatial blended CNN: Diving into clarity

R Ahila Priyadharshini\*, S Arivazhagan and K Ramajeyam  
Mepco Schlenk Engineering College, Mepco Nagar, Sivakasi, Tamil Nadu 626005, India.

Submitted: 29 July 2024; Revised: 05 December 2024; Accepted: 09 December 2024

**Abstract:** This study introduces a pioneering approach called spatial blended convolutional neural network (SBCNN) tailored specifically for enhancing the visual quality of underwater images. Traditional methods often struggle with the challenges posed by underwater environments, such as light absorption, scattering, and colour distortion. SBCNN addresses these challenges by combining spatial techniques with convolutional neural networks (CNNs), leveraging the strengths of both approaches. The architecture of SBCNN is designed to effectively capture spatial details and structural information inherent in underwater images. It incorporates spatial CNN branches, which are specialized components dedicated to analyse and enhance spatial features within the image. By integrating these spatial branches with traditional CNN layers, SBCNN can effectively address the unique characteristics of underwater imagery. To assess the performance of SBCNN, the study conducted comprehensive experimental evaluations using three different datasets: UIEB, EUVP, and UFO-120 and quantitative metrics such as peak signal-to-noise ratio (PSNR), mean square error (MSE), and Structural Similarity Index (SSIM) were utilized to compare the results with existing methods. The findings from these evaluations demonstrated significant improvements achieved by SBCNN over traditional techniques, indicating its effectiveness in enhancing the visual quality of underwater images. Furthermore, to validate the generalizability of the proposed method, cross-dataset testing was conducted on the EUVP ImageNet dataset and UIEB dataset.

**Keywords:** Contrast enhancement, Contrast stretching, convolution neural network, deep learning, Homomorphic filtering, underwater images.

## INTRODUCTION

Underwater image enhancement is a field of research focused on improving the quality and visibility of images captured in underwater environments. Underwater imaging presents unique challenges due to the interaction of light with water. These challenges include light absorption, scattering, and colour distortion, which degrade the visible quality of underwater images. When light enters the water, it undergoes absorption by water molecules and dissolved substances. Different wavelengths of light are absorbed to different extents, resulting in colour changes and loss of originality in underwater images. As a result, underwater scenes often appear dominated by shades of blue or green, making it difficult to accurately perceive and differentiate objects (Ancuti *et al.*, 2012). Scattering is another significant challenge in underwater imaging. When light encounters suspended particles, plankton, and other impurities in the water, it scatters in different directions. This scattering causes a reduction in contrast, making objects appear blurry or hazy, and reducing the visibility of fine details. As a result, underwater images often lack sharpness and low clarity, making it more challenging to discern objects and structures (Liu *et al.*, 2019). In addition to absorption and scattering, water also introduces haze and reduces contrast in underwater images. Haze is caused by the presence of suspended particles and dissolved organic matter, which scatter light

\* Corresponding author (rahila@mepcoeng.ac.in;  <https://orcid.org/0000-0001-9265-4842>)



This article is published under the Creative Commons CC-BY-ND License (<http://creativecommons.org/licenses/by-nd/4.0/>). This license permits use, distribution and reproduction, commercial and non-commercial, provided that the original work is properly cited and is not changed in any way.

and create a hazy appearance. This haze further reduces visibility and limits the depth perception in underwater scenes. Overcoming these challenges and enhancing underwater images is crucial for various applications. In scientific research, underwater images provide valuable information about marine ecosystems, species behaviour, and environmental changes (Prasath & Kumanan 2020). By improving the visibility and quality of these images, researchers can extract more accurate data and gain a better understanding of underwater environments. In fields such as underwater archaeology, enhanced images enable the documentation and analysis of submerged artifacts and structures, aiding in the preservation and interpretation of our cultural heritage.

Over the years, researchers have explored both traditional methods and deep learning methods to address this problem. Traditional image enhancement methods can be divided into two categories: physical models and non-physical models. Physical models attempt to restore an image to its original state, while non-physical models enhance the image without attempting to restore it. Newer deep learning-based image enhancement methods can be divided into two categories: convolutional neural network (CNN)-based models and generative adversarial network (GAN)-based models. CNN-based models learn to enhance images by analyzing a large dataset of images. GAN-based models use two neural networks to compete, one network trying to generate realistic images and the other network trying to distinguish between real and fake images.

Initially, traditional methods aim to address challenges in underwater imagery, such as colour casts, low contrast, and haze caused by light absorption and scattering. For instance, Hitam *et al.* (2013) proposed an adaptive histogram equalization technique specifically designed for underwater image enhancement. Unlike traditional histogram equalization, which applies a single transformation to the entire image, this method adaptively divides the image into smaller regions and performs histogram equalization independently in each region. By considering the local characteristics of an image, this approach can effectively enhance the contrast and visibility of the underwater images. Bianco *et al.* (2015) adopted a colour correction technique that considers the physical properties of light absorption in water. It models the light absorption process using the properties of water, and uses this information to estimate and correct the colour cast in underwater images. By considering the specific wavelengths of light absorbed by water, this method can effectively restore true colours and enhance the visual quality of underwater images. In

the work proposed by Abin *et al.* (2021), a fusion-based technique that combines information from multiple underwater images to enhance visual quality was proposed. By capturing multiple images with different exposure settings or from different viewpoints, this method overcomes the limitations of a single image and extracts more accurate scene detail. The captured images were aligned and fused using advanced image-fusion algorithms, resulting in an enhanced image with improved colour, contrast, and visibility. Zhou *et al.* (2022) developed a retinex theory, which aims to decompose an image into its reflectance and illumination components, to enhance underwater images. This approach employs multiscale analysis to capture both local and global image information. By manipulating the illumination component, which represents global lighting conditions, this method can alleviate the colour cast and significantly improve the overall appearance of underwater images. The approach of Muniraj and Dhandapani (2021) drew inspiration from image-dehazing techniques and adapted them for underwater image enhancement. It is assumed that the degradation of underwater images is similar to the effects of atmospheric haze in land-based images. This method employs dehazing algorithms to estimate and remove underwater haze, thereby enhancing the contrast, clarity, and visibility of underwater images. It considers the unique characteristics of underwater scenes and properties of light scattering in water.

Traditional methods struggle to address the complex combination of light absorption, scattering, and colour distortion in severely degraded underwater images. Their simplistic enhancement techniques often fail to recover details from such images. Basic colour correction methods (*e.g.*, white balance adjustment) often fall short in underwater conditions because they cannot accurately restore colours in images with severe wavelength-dependent absorption, especially when red wavelengths are completely lost. Many traditional methods rely on manually tuned parameters (*e.g.*, filter sizes, contrast enhancement levels), which can be difficult to optimize for different underwater conditions. This manual tweaking makes it hard to automate the enhancement process for a wide variety of images

In recent years, deep learning has gained significant popularity due to its effectiveness in various image processing tasks, including computer vision, image segmentation, pattern recognition, and image enhancement (Priyadharshini *et al.*, 2021, 2023; Arun *et al.*, 2024). CNN-based algorithms focus on preserving the original underwater image, while GAN-based approaches are designed to enhance the perceptual quality

of the images. However, the need for a large number of labelled images poses a challenge in real-world deep learning-based underwater image enhancement (Yang *et al.*, 2019). Hashisho *et al.* (2019) developed a real-time underwater image-enhancement model based on an end-to-end deep neural network. Their approach utilized a U-Net architecture with skip connections to capture both low- and high-level image features, resulting in an accurate enhancement. Although the model achieved real-time performance and showed practical applicability, a drawback of this method is its dependence on large-scale annotated datasets, which can be time consuming and resource intensive. Consequently, the generalizability of this model to diverse underwater conditions is limited.

With the advent of deep convolutional neural networks, Li *et al.* (2020) proposed a deep learning-based method for enhancing underwater images using underwater scene priors. By incorporating these priors into their deep neural network architecture, they successfully improved visibility and restored colour in underwater images. However, one drawback of this approach is its limited effectiveness when applied to underwater scenarios with different characteristics. WaterNet is a deep learning-based approach proposed by Li *et al.* (2020) for underwater image enhancement. It utilizes a fully convolutional network (FCN) architecture to enhance the visual quality of underwater images. WaterNet effectively enhances the image clarity, colour correction, and overall visibility by training on a large dataset of paired underwater and reference images. Underwater convolutional neural network (UWCNN) is another deep learning method for underwater image enhancement introduced by Anwar *et al.* (2018). UWCNN employs a deep convolutional neural network with skip connections to capture and restore both low-level and high-level features in underwater images. By incorporating skip connections, the UWCNN effectively preserves fine details during the enhancement process. This model was trained using a dataset of paired underwater and reference images to learn the mapping between degraded and enhanced image domains.

GAN-based methods, such as underwater GAN, proposed by Wang *et al.* (2019), leverage an adversarial learning framework to generate realistic and visually pleasing enhanced images. GAN-based methods produce visually appealing enhancements by capturing the statistical properties of the underwater scenes. In addition, CycleGAN, proposed by Du *et al.* (2021), is another popular deep learning model used for underwater image enhancement. CycleGAN is an image-to-image translation model that can learn mappings between

different domains without requiring paired training data. By training on unpaired datasets of underwater and reference images, CycleGAN can learn to transform underwater images to resemble the characteristics of reference images, thereby effectively enhancing the visibility and overall quality of underwater images. While GANs offer significant potential in underwater image enhancement, their limitations such as the need for large datasets, training instability, potential artifacts, and computational complexity must be carefully considered and mitigated in practical applications.

In this study, we propose a spatial blended convolutional neural network (SB-CNN) technique by leveraging deep learning, specifically convolutional neural networks in combination with the traditional spatial enhancement technique, to enhance underwater images. The main contributions of this study are as follows.

- Integration of deep CNN architecture with spatial enhancement technique to enhance image quality by preserving consistent colouring, structural similarity of scene content, and image sharpness.
- Experiments are conducted using spatial techniques and deep learning techniques individually as well as in a combined manner.
- Experiments, conducted on widely used datasets such as UEIB, UFO-120, and EUVP, demonstrate that our method delivers competitive performance while ensuring interpretability.
- Cross validation on different datasets is carried out to prove the potential efficiency of this approach

---

## MATERIALS AND METHODS

In this section, the datasets used for the experimentation, the proposed deep CNN architectures and the concept of transforming underwater images with spatial blended CNN enhancement are discussed.

### UIEB dataset

The underwater image enhancement benchmark (UIEB) dataset comprises raw underwater images alongside their corresponding pseudo-reference images, which are used as a standard for evaluating real-world underwater image enhancement. For each raw image, the pseudo-reference is selected from results produced by various UIE algorithms, aiming to identify the best possible enhancement. The subjective quality evaluation study of Li *et al.* involved gathering 890 raw underwater images and their associated mean opinion scores (MOSS)

through repeated assessments. This dataset offers a wide range of underwater scenes, showcasing diverse image content, resolutions, and quality degradation patterns (Li *et al.*, 2020). Furthermore, the dataset also includes an additional set of 60 challenging images, which play a vital role in evaluating the efficacy of image enhancement algorithms. The sample images of UIEB dataset are shown in Figure 1.

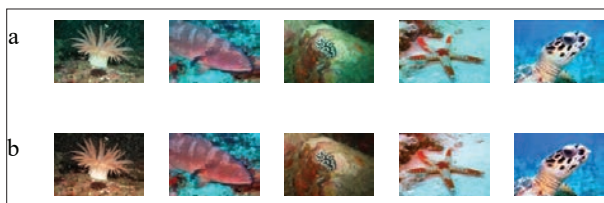


Source: Li *et al.*, 2020

**Figure 1:** Sample images of UIEB dataset (a) raw images (b) reference images

### UFO-120 dataset

The UFO-120 dataset is a specialized collection of underwater images designed for research and development in the field of underwater image enhancement and restoration. It was developed to address the challenges posed by underwater environments, such as colour distortions, poor visibility, and noise, which degrade image quality due to the scattering and absorption of light underwater (Jahidul Islam *et al.*, 2020). Each image is accompanied by an associated ground truth image, resulting in a collection of 120 ground truth images. The images showcase a diverse range of underwater scenes, encompassing different settings, lighting conditions, and subject matter. The sample images of UFO-120 dataset are shown in Figure 2.



Source: Islam *et al.*, 2020

**Figure 2:** Sample images of UFO-120 dataset (a) low-resolution distorted images (b) high-resolution ground truth images

### EUVP dataset

The enhanced underwater visual perception (EUVP) dataset contains an extensive collection of both paired

and unpaired underwater images, including around 12,000 paired underwater dark, underwater ImageNet and underwater scenes and 8,000 unpaired samples. These images exhibit a wide range of perceptual quality, spanning from low to high. The dataset was created using seven different cameras, capturing images under diverse lighting conditions and water types. To generate distorted images from high-quality ones, the authors (Islam *et al.*, 2020) utilized a learned underwater distortion model based on CycleGAN, ensuring realistic representation of underwater visual degradation. The EUVP underwater scene dataset includes various real and synthetic underwater environments like coral reefs, marine life, and wrecks, showcasing typical underwater challenges such as colour distortion, low contrast, and lighting issues. The EUVP ImageNet dataset consists of underwater-degraded images derived from ImageNet (a large-scale visual database for object recognition) scenes. These images have been artificially degraded to simulate underwater conditions. In this dataset, clear ImageNet images are transformed to mimic underwater distortions such as colour degradation, blurring, and contrast reduction: mimicking light attenuation in water. The EUVP underwater dark dataset contains underwater images captured in dimly lit or deep-sea environments where natural light is minimal or absent. These images exhibit extreme darkness, low contrast, and significant noise. The sample images of EUVP underwater scene dataset are shown in Figure 3.



Source: Islam *et al.*, 2020

**Figure 3:** Sample images of EUVP underwater scene dataset (a) Input images (b) Ground truth images

### Proposed SBCNN approach

This research work deals with two different approaches: non-physical model enhancement methods and transforming underwater images with spatial blended CNN enhancement methods for underwater image enhancement.

### Proposed spatial enhancement methods

The proposed methodology aims to improve the visual quality of underwater images using a combination of

techniques, as shown in Figure 4. The methodology consisted of several interconnected stages. In the first stage, colour correction (Tarhate, 2020) was applied to address colour distortion issues commonly found in underwater images. This step mitigates the distortions caused by the absorption and scattering of light in water, thereby restoring the original colour of the scene. White balancing involves both eliminating unwanted colour casts and adjusting white light to appear cooler. According to the white patch theory, the white balance algorithm relies on the maximum value of the combined blue, green, and red channels to adjust colours. Padding is then applied by adding empty pixels around the image's edges to preserve its original dimensions, ensuring the image's size and shape remain intact. Gamma correction is applied to control the overall brightness of an image, improving results when the image appears too dark or overly bright. The gamma value is typically set to 0.7 based on observation. The mathematical formula for gamma correction is shown in equation 1:

$$F' = 255 \times \left(\frac{F}{255}\right)^\gamma \quad \dots(1)$$

where  $F'$  represents the corrected intensity,  $F$  is the original intensity, and  $\gamma$  is the gamma value.

Unsharp masking (USM) is a popular technique used to enhance image sharpness. Despite the name, it is designed to make an image look sharper by increasing the contrast along edges and fine details. The formula for

unsharp masking is shown in equation 2:

$$F_s = F + \beta(F - G * F) \quad \dots(2)$$

where:  $F_s$  is the sharpened image,  $G * F$  is the blurred (Gaussian-filtered) version of the image. In this work,  $\beta$  (scaling factor controlling the sharpness intensity) is set as 1.

Homomorphic filtering (Seow & Asari, 2004) is used to enhance image quality further. This technique operates in the frequency domain by modifying the amplitudes of the frequency components in the image. Homomorphic filtering improves the clarity and detail of underwater images by selectively amplifying specific frequency ranges. The subsequent stage focuses on fusion, in which multiple images or image components are combined to create a single composite image with improved visual quality. Fusion techniques help integrate information from different images captured under varying conditions, reduce noise, enhance details, and improve the overall image quality. The fusion used here is average fusion. Finally, contrast stretching (Samir, 2020) was employed to address the poor contrast that is often observed in underwater images. This technique expands the range of intensity values in an image and improves the contrast and object visibility in underwater scenes. To evaluate the performance of the methodology, full-reference metrics (Guo *et al.*, 2022) were utilized to objectively measure the image quality.

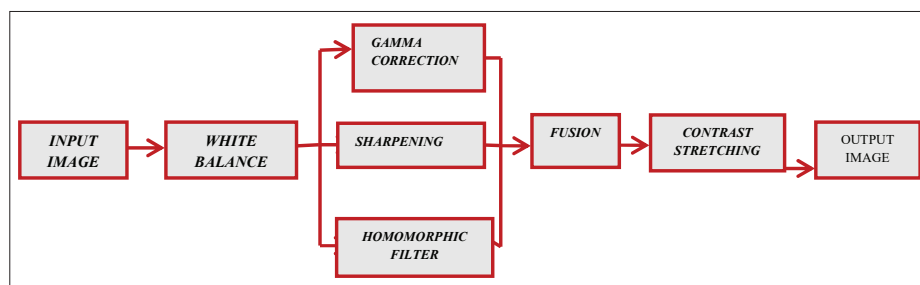


**Figure 4:** Block diagram of proposed spatial enhancement technique

### Proposed spatial blended CNN enhancement method

A novel method called spatial blended CNN is introduced for enhancing the sharpness and detail of images. The approach involves blending information from different scales to improve spatial resolution. The CNNs are used in this approach for feature extraction at different scales. The CNN learns to identify key features such as edges,

textures, and other details from the input image. These features are extracted at various resolutions, which are then combined to form a sharper, more detailed output. Feature maps from different scales are concatenated along the channel dimension. This approach preserves all information from each scale, giving the network more flexibility. The spatial blended CNN architecture stands out by omitting normalization techniques and

fully connected layers, providing a unique approach to enhance underwater images. Normalization layers (Batch Normalization) are often used to stabilize training and accelerate convergence. However, they may inadvertently suppress or distort fine image details, which are critical for high-quality image enhancement tasks. By omitting normalization, the architecture retains the raw range of feature values, potentially preserving subtle details crucial for the enhancement process. Fully connected

layers are typically used for tasks like classification or regression, where global image context is more relevant than spatial relationships. For image-to-image tasks like enhancement, spatial relationships and local features are more important. Fully connected layers, being inherently global, can lead to loss of spatial details. Instead, the architecture likely relies on convolutional layers that retain spatial information. The spatial blended CNN enhancement method is illustrated in Figure 5.

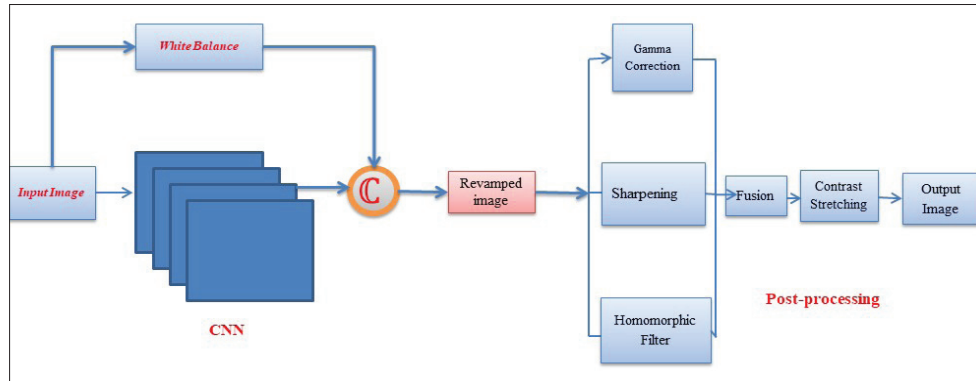


Figure 5: Block diagram of proposed spatial blended CNN enhancement method

The method starts by preprocessing the input images. The images were resized to standardized dimensions of  $256 \times 256$  pixels. To address colour distortion, red and blue channels are corrected with respect to green channel. First the RGB channels are normalized using the equation 3.

$$C'_i = C_i \times \frac{m_{Gray}}{m_{C_i}} \quad \dots(3)$$

Where  $C'_i$ : The normalized value of the colour channel  $i$  (either Red, Green, or Blue).

$C_i$ : The original value of the colour channel  $i$ .

$m_{Gray}$ : The mean of the grayscale version of the image.

$m_{C_i}$ : The mean of the colour channel  $i$ .

Then the colours in red and blue channels are corrected using equation 4 and 5 respectively.

$$R = C_R - 0.3(m_{C_G} - m_{C_R})C_G(1 - C_R) \quad \dots(4)$$

$$B = C_B - 0.3(m_{C_G} - m_{C_B})C_G(1 - C_B) \quad \dots(5)$$

This colour correction step aims to restore accurate colour information and enhance overall visual quality.

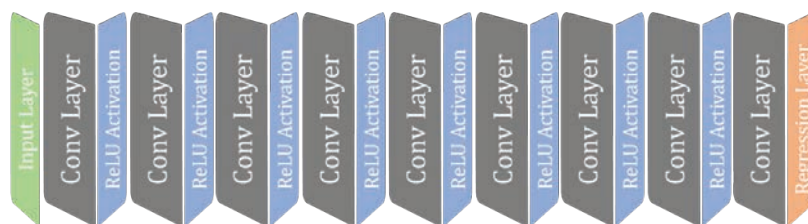


Figure 6: Proposed CNN architecture

Following the preprocessing stage, the method incorporates a deep CNN architecture, as shown in Figure 6, to learn the complex mapping between the original and enhanced images. A CNN consists of eight convolutional layers, typically followed by rectified linear unit (ReLU) activation, which introduces nonlinearity into the network. A regression layer is then added with the ninth convolutional layer to enable direct image enhancement. In each convolutional layer 128 filters with size  $3 \times 3$  are used. By training the CNN with 600 epochs and a batch size of 128, the model learned to extract high-level features and generate enhanced images with improved visibility, reduced colour distortion, and enhanced overall quality. The learning rate is set as 0.001. Once the CNN model is trained, it is used to predict the enhanced images of the original underwater inputs. To further refine the quality of the predicted images, a series of post processing techniques were applied (Mousavi *et al.*, 2023). These techniques include gamma correction to adjust pixel intensities, unsharp masking to enhance image sharpness, and contrast stretching to expand the dynamic range of the pixel values. The combination of these techniques results in enhanced underwater images with improved brightness, contrast, and visual appeal.

The training method involves pairing each input image with a corresponding reference image that serves as the target for training. The root mean square error (RMSE) is used as the loss function to measure the discrepancy between the enhanced and target images (Anwar *et al.*, 2018). The RMSE loss function is represented by equation 6,

$$RMSE = \sqrt{\frac{1}{MNO} \sum_{i,j,k=1}^{M,N,O} [h(x) - y(x)]^2} \quad \dots(6)$$

where  $M$ ,  $N$ , and  $O$  denote the height, width, and number of channels in the image, respectively. The variables  $i$ ,  $j$ , and  $k$  represent the coordinates within the three dimensions of the image.  $h(x)$  represents the original image, and  $y(x)$  represents the output image from CNN. The summation is performed over all pixel locations in the image.

## RESULTS AND DISCUSSION

In this study, a method for enhancing underwater images is developed using a combination of spatial analysis and deep learning. Experiments were conducted to evaluate the effectiveness of the proposed approach by using three datasets: UIEB, UFO-120, and EUVP. The method was compared with existing techniques, and the results were

measured using various metrics, such as PSNR, SSIM. This method showed significant improvements in image quality, reduced artifacts, and enhanced detail. A visual inspection confirmed the effectiveness of this approach.

### Metrics

We performed a quantitative evaluation of the output of spatial blended CNN using well-established metrics commonly used in previous studies. These metrics include the mean square error (MSE), peak signal-to-noise ratio (PSNR), and structural similarity index (SSIM). The PSNR metric quantifies the similarity between an image  $x$  and a reference image  $y$  by calculating the mean-squared error (MSE) between them. The PSNR is given in equation 7:

$$PSNR(x, y) = 10 \log_{10} \left[ \frac{256^2}{mse(x, y)} \right] \quad \dots(7)$$

In this formula, MSE measures the average squared difference between the pixel values of  $x$  and  $y$ . The PSNR measures the ratio of the maximum possible pixel value squared ( $256^2$  for an 8-bit image) to MSE. A higher PSNR value indicates greater similarity and better reconstruction quality between the images. The structural similarity index (SSIM) compares image patches based on their luminance, contrast, and structure. It quantifies the similarity between two images,  $x$  and  $y$ , using equation 8.

$$SSIM(x, y) = \frac{((2\mu_x\mu_y+c_1)(2\sigma_{xy}+c_2))}{[(\mu_x^2+\mu_y^2+c_1)(\sigma_x^2+\sigma_y^2+c_2)]} \quad \dots(8)$$

In this equation,  $\mu$  represents the mean value,  $\sigma^2$  represents the variance, and  $\sigma_{xy}$  represents the cross-correlation between images  $x$  and  $y$ . The constants  $c_1$  and  $c_2$  are included to ensure numerical stability and are calculated as  $c_1 = (255 \times 0.01)^2$  and

An SSIM value of 1 signifies identical images (which are undesirable in image enhancement); it should not be excessively low. In most cases, an SSIM value between 0.5 and 1 is considered desirable, striking a balance between preserving image structure and achieving desired enhancements.

### Analysis

In this section, we analyze our proposed approach and evaluate its performance both qualitatively and quantitatively. We compare the results of our spatial approach and white balancing CNN with the Spatial Blended CNN in Table 1, 2, and 3. Additionally, we

compare the performance of the spatial blended CNN with four state-of-the-art methods on the underwater image datasets mentioned earlier, as shown in Table 4 and 5. To assess the effectiveness of our method, we use a separate test set comprising two different dataset images that were not used during the training of the colour model in the spatial blended CNN pipeline. The results presented in the tables clearly demonstrate that the spatial blended CNN outperforms all other methods in terms of the MSE, PSNR, and SSIM metrics, establishing itself as the top-performing technique for underwater image enhancement on the above mentioned datasets.

### Spatial approach

A spatial approach mentioned in Figure 4 was employed to enhance underwater images by applying various filters. These filters aimed to address issues such as low contrast, colour distortion, and noise. The results of the enhancement process were evaluated using several metrics, which are presented in Table 1. Additionally, a sample output image is provided to visually demonstrate the improvements achieved through the spatial approach. The sample image enhanced using this approach is shown in Figure 7.

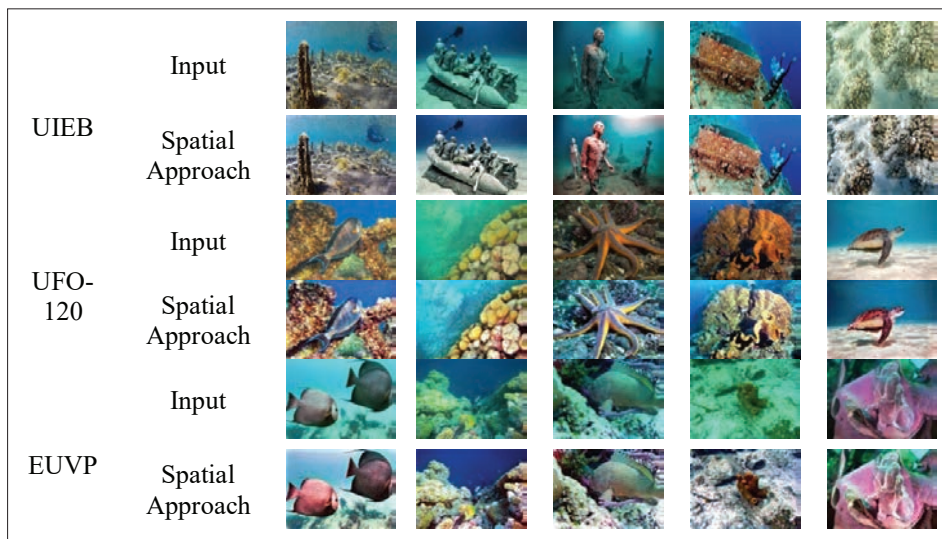


Figure 7: Sample enhanced image using spatial approach with different dataset

When evaluated on the EUVP test image dataset, the method achieves better PSNR, MSE, and SSIM results compared to the UIEB and UFO-120 datasets.

Table 1: Evaluation metrics for spatial approach

Dataset	Spatial approach		
	MSE ( $\times 10^3$ )	PSNR	SSIM
UIEB	1.292	17.542	0.7197
UFO-120	1.220	17.043	0.719
EUVP	1.179	18.641	0.7961

### White balancing CNN

A white balancing CNN was developed to enhance underwater images by improving their colour accuracy and reducing colour casts caused by water’s properties. This approach is similar to SB-CNN without post processing. The CNN was trained using a dataset of RGB underwater images and corresponding ground truth images with white balance adjustments. The trained network was then used to enhance new underwater images, resulting in improved colour accuracy and reduced colour casts. Figure 8 displays the output image generated by the white balancing CNN, and Table 2 provides a summary of the evaluation metrics. The white balancing CNN exhibited

effectiveness in enhancing underwater images, yielding higher PSNR and SSIM values, as well as lower MSE values, compared to the spatial approach. Notably, when examining the performance across different datasets, the EUVP dataset consistently yielded superior results compared with the UIEB and UFO-120 datasets within the white balancing CNN network.

**Table 2:** Evaluation metrics for white balancing CNN approach

Datasets	White balancing CNN		
	MSE ( $\times 10^3$ )	PSNR	SSIM
UIEB	0.831	19.721	0.758
UFO-120	1.102	18.659	0.752
EUVP	0.738	21.178	0.778

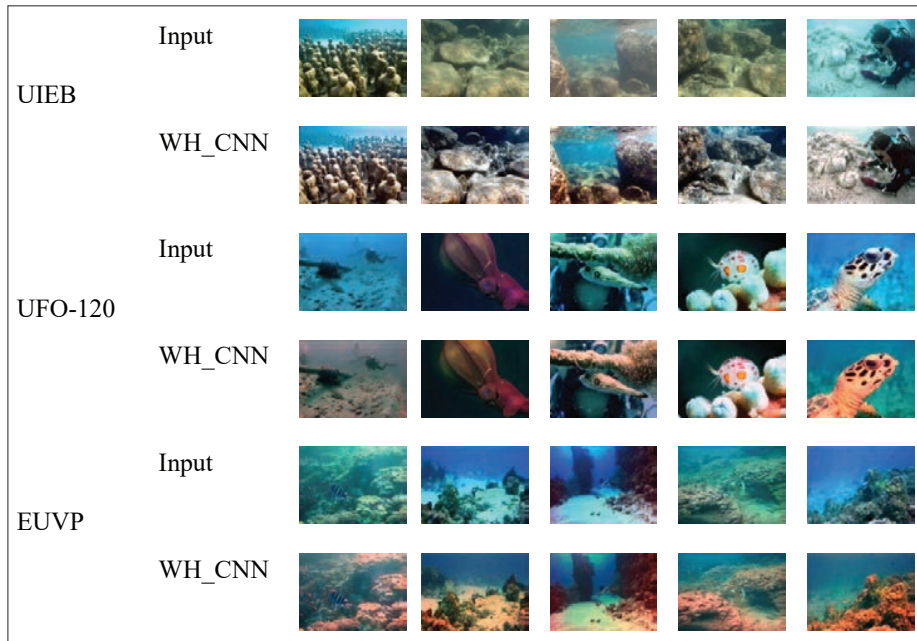


**Figure 8:** Sample enhanced image using white balancing CNN with different datasets

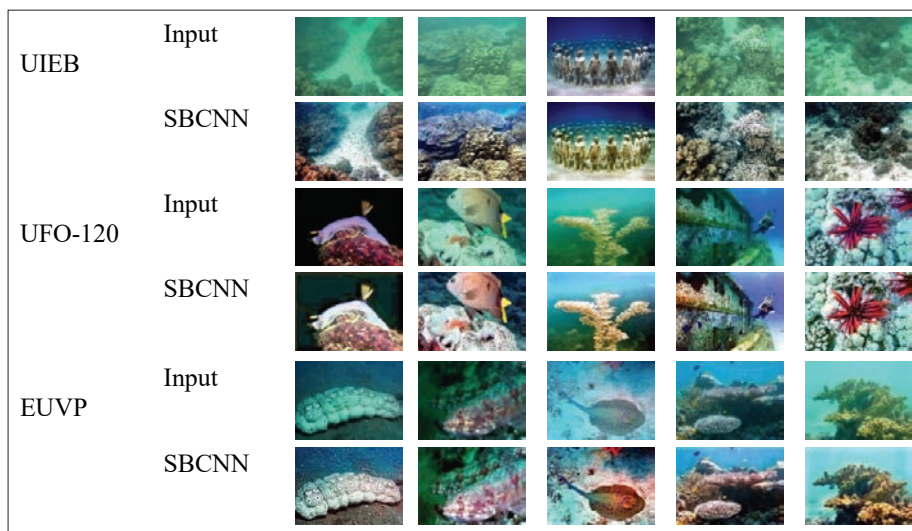


**Figure 9:** Sample enhanced image using spatial blended CNN with different datasets

### Spatial blended CNN

The spatial blended CNN shown in Fig 5 is used to enhance underwater images, combining spatial processing techniques with convolutional neural networks. The sample image enhanced using this approach is shown in Figure 9. Table 3 displays the evaluation metrics for the spatial blended CNN. The results in Table 3 demonstrate the effectiveness of the spatially blended CNN in enhancing underwater images. The higher PSNR and SSIM values, along with the lower MSE values, indicate improved image quality, better similarity to the reference images, and reduced errors. Notably, the spatial blended CNN performed exceptionally well on the EUVP, UIEB, and UFO-120 datasets, producing high-quality images comparable to the reference images. These results clearly establish the superiority of the spatial blended CNN over both the spatial approach and white balancing CNN in the arena of underwater image enhancement. Figure 10 depicts the visual comparison of different underwater image enhancement methods adopted in this work.

**Table 3:** Evaluation metrics for spatial blended CNN

Datasets	Spatial blended CNN		
	MSE ( $\times 10^3$ )	PSNR	SSIM
UIEB	0.341	22.879	0.871
UFO-120	0.202	25.212	0.800
EUVP	0.160	26.380	0.789

**Table 4:** Performance comparison of SBCNN with existing approaches.

Dataset	Metrics	WaterNet (Li et al 2020)	FUnIE- GAN (Islam et al 2020)	Deep SESR (Jahidul et al 2020)	Shallow- UWnet (Naik et al 2021)	FUnIE- GAN-UP (Islam et al 2020)	UGAN (Fabbri et al 2018)	UGAN-P (Fabbri et al 2018)	iDehaze (Mousavi et al 2023)	SBCNN
UIEB	MSE ( $\times 10^3$ )	0.843	0.824	0.803	0.890	-	-	-	1.062	<b>0.341</b>
	PSNR	19.110	19.130	19.260	18.990	-	-	-	17.960	<b>22.878</b>
	SSIM	0.790	0.730	0.730	0.670	-	-	-	0.800	<b>0.871</b>
UFO-120	MSE ( $\times 10^3$ )	0.293	0.231	<b>0.153</b>	0.198	0.299	0.238	0.248	1.217	0.202
	PSNR	23.120	24.720	<b>26.460</b>	25.200	23.290	24.23	24.110	17.550	25.212
	SSIM	0.730	0.740	0.780	0.730	0.670	0.690	0.690	0.720	<b>0.800</b>
EUVP	MSE ( $\times 10^3$ )	0.226	0.142	0.193	<b>0.104</b>	0.196	0.155	0.155	0.322	0.16
	PSNR	24.430	26.190	25.300	<b>27.390</b>	25.210	26.530	26.530	23.010	26.379
	SSIM	0.820	0.820	0.810	0.830	0.780	0.800	0.800	<b>0.840</b>	0.789

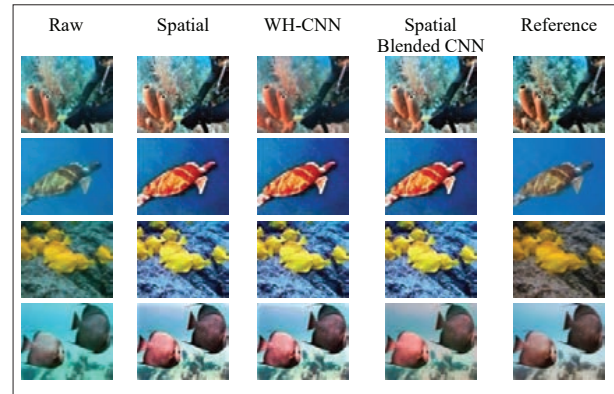


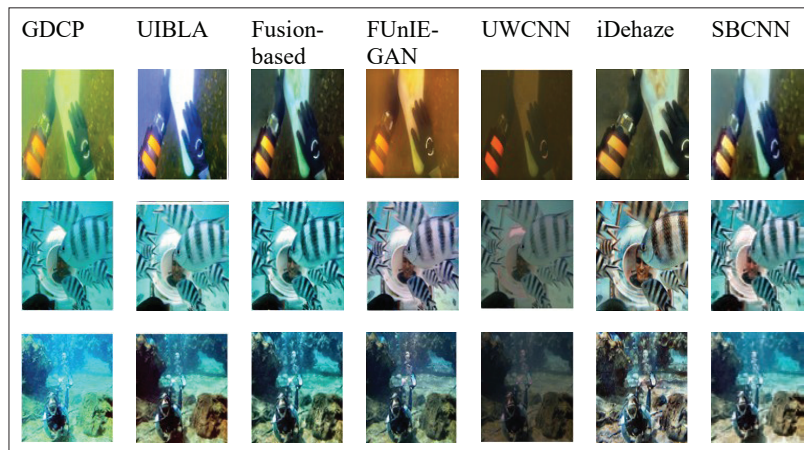
**Figure 10:** visual comparison of different underwater image enhancement methods including spatial approach, white balance CNN, and spatial blended CNN

While the spatial approach may have obtained lower metric scores, it demonstrated exceptional performance in enhancing the image quality. In contrast, the white-balancing CNN achieved a higher overall image quality. However, it is a spatially blended CNN that has proven to be the most effective method for producing high-quality images that closely resemble the reference images. The spatial blended CNN achieved higher metrics, indicating superior image quality. To further evaluate its performance, a comparison can be made between the metrics (PSNR and SSIM) and visual quality of the spatial blended CNN with other existing methods.

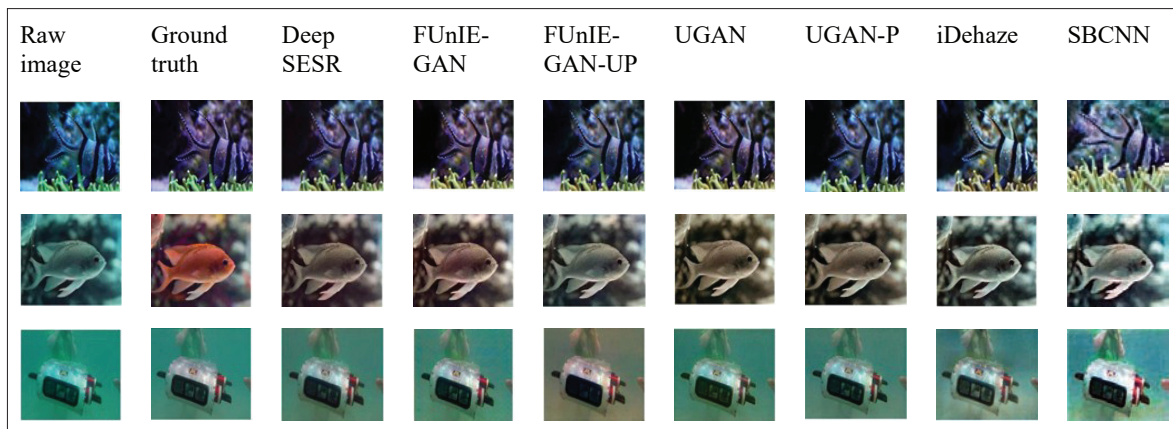
This comprehensive assessment will provide a more comprehensive understanding of the effectiveness of spatial blended CNN’s in enhancing underwater images.

Table 4 presents a comprehensive comparison between the spatial blended CNN and various existing methods, including WaterNet, FUnIE-GAN, deep SESR, Shallow-UWNet, UGAN and iDehaze. In terms of SSIM, the SBCNN showed a slight advantage over Shallow-UWNet, but it exhibited a relatively higher

standard deviation, indicating less stability in its results. The qualitative analysis on UIEB, EUVP and UFO-120 datasets are shown in Figures 11, 12 and 13 respectively. Interestingly, when specifically compared to WaterNet using the UIEB dataset, the SBCNN demonstrated more accurate SSIM results and higher stability. It is worth noting that the comparison with the UIEB dataset showed better results for the spatial blended CNN, while the average results of the approach were obtained by evaluating it with the UFO120 and EUVP datasets.



**Figure11:** Qualitative analysis on UIEB dataset. Existing approaches include Red Channel (Galdran *et al* 2015), GDCP (Peng *et al* 2018), UIBLA (Peng & Cosman 2017), Fusion-Based (Ancuti *et al* 2012), FUnIE-GAN (Islam *et al* 2020), UWCNN (Li *et al* 2020) and iDehaze (Mousavi *et al* 2023)



**Figure12:** Qualitative analysis on EUVP dataset. Existing approaches include deep SESR (Jahidul *et al* 2020), FUnIE-GAN and FUnIE-GAN-UP (Islam *et al* 2020), UGAN and UGAN-P (Fabbri *et al* 2018) and iDehaze (Mousavi *et al* 2023)

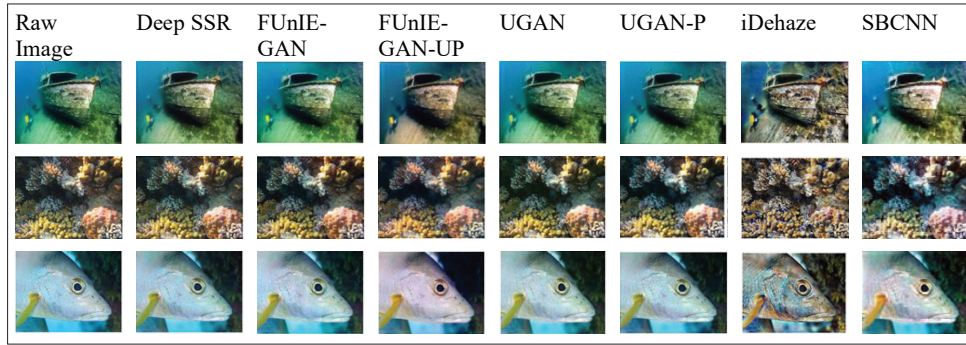


**Figure13:** Qualitative analysis on UFO-120 dataset. Existing approaches include Deep SESR (Jahidul *et al* 2020), FUnIE-GAN and FUnIE-GAN-UP (Islam *et al* 2020), UGAN and UGAN-P (Fabbri *et al* 2018) and iDehaze (Mousavi *et al* 2023)

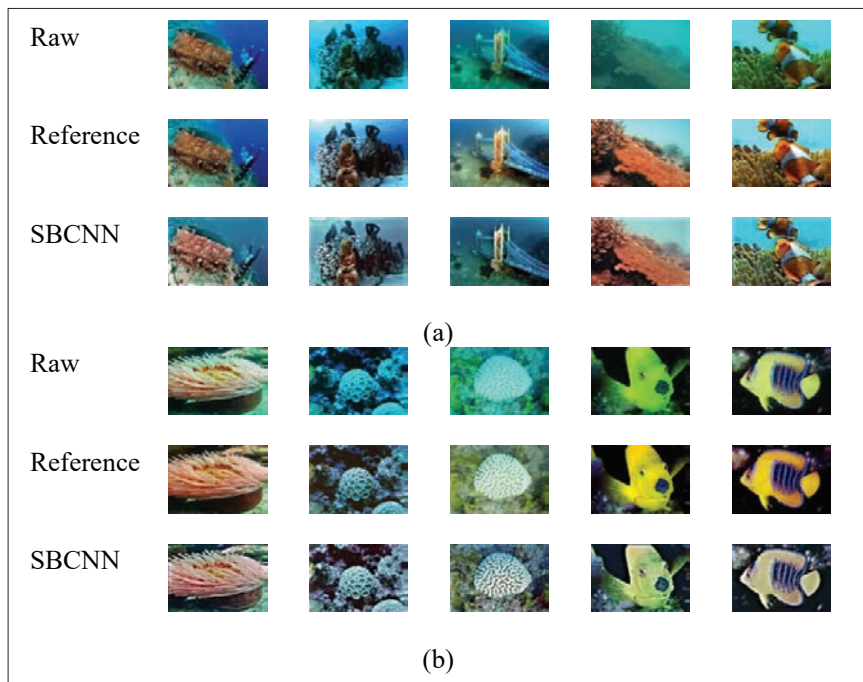


**Figure14:** Qualitative analysis of cross-validation on (a) UIEB dataset (b)EUVP ImageNet dataset

**Cross-dataset Testing**

The SBCNN trained on EUVP underwater scene dataset is evaluated with two extra datasets: the EUVP ImageNet dataset, containing underwater-degraded images derived from ImageNet database, and the UIEB dataset. By using these two distinct datasets in cross-testing, we can

more rigorously assess the model’s robustness, adjust hyperparameters as needed, and ensure that the enhanced images are consistent in quality across different types of underwater scenes. Figure 14 showcases the results of this cross-validation process, highlighting the performance and validation of the method in enhancing underwater images.

The cross-dataset testing results in Table 5 provide key quantitative insights into the SBCNN method's performance across the UIEB and EUVP ImageNet datasets. The lower mean squared error (MSE) values achieved on both datasets suggest that the SBCNN can closely reconstruct the ground truth images with minimal error, which is crucial for accurate underwater image enhancement. Specifically, the MSE value for the UIEB dataset is  $0.809 \times 10^3$ , while for the EUVP ImageNet dataset, it is slightly lower at  $0.782 \times 10^3$ . This small difference suggests a consistent performance across different underwater image sources, indicating the robustness of the method.

**Table 5:** Cross-dataset testing

Dataset	MSE ( $\times 10^3$ )	PSNR	SSIM
UIEB	0.809	20.429	0.8283
EUVP imagenet	0.782	20.717	0.7538

## CONCLUSION

In conclusion, the proposed method for enhancing underwater images demonstrates superior performance compared with existing techniques, as evidenced by improved objective metrics such as PSNR, MSE, and SSIM. By leveraging spatial processing techniques and a deep CNN architecture, this method effectively addresses common challenges in underwater imaging, including colour distortion, limited visibility, and scattered light, resulting in significant improvements in image quality. Moreover, innovative post-processing algorithms further refine the predicted images, enhancing brightness, contrast, and overall visual appeal. The combined use of deep learning techniques and spatial post-processing algorithms enables substantial improvements in colour accuracy, visibility, and overall image quality in the challenging domain of underwater imaging, making it a promising solution with diverse applications in marine research, underwater exploration, and related fields.

## REFERENCES

Abin, D., Gulabani, B., Joshi, C., Damle, S., & Gengaje, S. (2021). Fusion based approach for underwater image enhancement. *2021 International Conference on Communication Information and Computing Technology (ICCICT)*. <https://doi.org/10.1109/iccict50803.2021.9510127>

Ancuti, C., Ancuti, C.O., Haber, T., & Bekaert, P. (2012). Enhancing underwater images and videos by fusion. *Proceedings of the 2012 IEEE Conference on Computer Vision and Pattern Recognition, Providence, RI, USA*, <https://doi.org/10.1109/cvpr.2012.6247661>.

Anwar, S., Li, C., & Porikli, F. (2018). Deep underwater image enhancement. *arXiv preprint arXiv:1807.03528*.

Arun M., Visvaja K., & Vidhya A. (2024). Implementing underwater image enhancement algorithms on resource constrained devices. *The Journal of Ocean Technology, 19*(3), 100-116.

Bianco, G., Muzzupappa, M., Bruno, F., Garcia, R., & Neumann, L. (2015). A new color correction method for underwater imaging. *The International Archives of the Photogrammetry, Remote Sensing and Spatial Information Sciences, XL-5/W5*, 25-32. <https://doi.org/10.5194/isprsarchives-xl-5-w5-25-2015>

Du, R., Li, W., Chen, S., Li, C., & Zhang, Y. (2021). Unpaired underwater image enhancement based on cycleGAN. *Information, 13*(1), 1. <https://doi.org/10.3390/info13010001>

Fabbri, C., Islam, M. J., & Sattar, J. (2018). Enhancing underwater imagery using generative adversarial networks. *2018 IEEE International Conference on Robotics and Automation (ICRA)*. <https://doi.org/10.1109/icra.2018.8460552>

Galdran, A., Pardo, D., Picón, A., & Alvarez-Gila, A. (2015). Automatic red-channel Underwater Image Restoration. *Journal of Visual Communication and Image Representation, 26*, 132-145. <https://doi.org/10.1016/j.jvcir.2014.11.006>

Guo, P., He, L., Liu, S., Zeng, D., & Liu, H. (2022). Underwater image quality assessment: Subjective and objective methods. *IEEE Transactions on Multimedia, 24*, 1980-1989. <https://doi.org/10.1109/tmm.2021.3074825>

Hashisho, Y., Albadawi, M., Krause, T., & Freiherr von Lukas, U. (2019). Underwater Color Restoration using U-Net denoising autoencoder. *2019 11th International Symposium on Image and Signal Processing and Analysis (ISPA)*. <https://doi.org/10.1109/ispa.2019.8868679>

Hitam, M. S., Yussof, W. N., Awalludin, E. A., & Bachok, Z. (2013). Mixture contrast limited adaptive histogram equalization for Underwater Image Enhancement. *2013 International Conference on Computer Applications Technology (ICCAT)*. <https://doi.org/10.1109/iccat.2013.6522017>

Khanal, S. (2020). Contrast stretching. Medium. <https://samirkhanal35.medium.com/contrast-stretching-f25e7c4e8e33>

Islam, M. J., Xia, Y., & Sattar, J. (2020). Fast underwater image enhancement for improved visual perception. *IEEE Robotics and Automation Letters, 5*(2), 3227-3234. <https://doi.org/10.1109/lra.2020.2974710>

Jahidul Islam, M., Luo, P., & Sattar, J. (2020). Simultaneous enhancement and super-resolution of underwater imagery for improved visual perception. *Robotics: Science and Systems XVI*. <https://doi.org/10.15607/rss.2020.xvi.018>

Li, C., Anwar, S., & Porikli, F. (2020). Underwater scene prior

- inspired deep underwater image and video enhancement. *Pattern Recognition*, 98, 107038. <https://doi.org/10.1016/j.patcog.2019.107038>
- Li, C., Guo, C., Ren, W., Cong, R., Hou, J., Kwong, S., & Tao, D. (2020). An underwater image enhancement benchmark dataset and beyond. *IEEE Transactions on Image Processing*, 29, 4376–4389. <https://doi.org/10.1109/tip.2019.2955241>
- Li, C., Anwar, S., & Porikli, F. (2020). Underwater scene prior inspired deep underwater image and video enhancement. *Pattern Recognit.* 98, 107038.
- Liu, Y., Xu, H., Shang, D., Li, C., & Quan, X. (2019). An underwater image enhancement method for different illumination conditions based on color tone correction and fusion-based descattering. *Sensors*, 19(24), 5567. <https://doi.org/10.3390/s19245567>
- Mousavi, M., Estrada, R., & Ashok, A. (2023). iDehaze: Supervised underwater image enhancement and dehazing via physically accurate photorealistic simulations. *Electronics*, 12(11), 2352. <https://doi.org/10.3390/electronics12112352>
- Muniraj, M., & Dhandapani, V. (2021). Underwater image enhancement by combining color constancy and dehazing based on depth estimation. *Neurocomputing*, 460, 211–230. <https://doi.org/10.1016/j.neucom.2021.07.003>
- Naik, A., Swarnakar, A., & Mittal, K. (2021). Shallow-uwnet: compressed model for underwater image enhancement (student abstract). *Proceedings of the AAAI Conference on Artificial Intelligence*, 35(18), 15853–15854. <https://doi.org/10.1609/aaai.v35i18.17923>
- Peng, Y.-T., & Cosman, P. C. (2017). Underwater image restoration based on image blurriness and light absorption. *IEEE Transactions on Image Processing*, 26(4), 1579–1594. <https://doi.org/10.1109/tip.2017.2663846>
- Peng, Y.T., Cao, K., & Cosman, P.C. (2018). Generalization of the dark channel prior for single image restoration. *IEEE Trans. Image Process.* 27, 2856–2868
- Prasath, R., & Kumanan, T. (2020). Application of different techniques for underwater image processing- A systematic review. *IOP Conference Series: Materials Science and Engineering*, 925(1), 012034. <https://doi.org/10.1088/1757-899x/925/1/012034>
- Priyadharshini, R.A., Arivazhagan, S., & Arun, M. (2021). Ayurvedic medicinal plants identification: A comparative study on feature extraction methods. *Communications in Computer and Information Science*, 1377, 268–280. [https://doi.org/10.1007/978-981-16-1092-9\\_23](https://doi.org/10.1007/978-981-16-1092-9_23)
- Priyadharshini, R.A., Arivazhagan, S., & Arun, M. (2023). Crack recognition on concrete structures based on machine crafted and hand crafted features. *Expert Systems with Applications*, 228, 120447. <https://doi.org/10.1016/j.eswa.2023.120447>
- Priyadharshini, R.A., Arivazhagan, S., Pavithra, K.A., & Sowmya, S. (2024). An ensemble deep learning approach for underwater image enhancement, e-Prime - Advances in Electrical Engineering, Electronics and Energy, Volume 9, 2024, <https://doi.org/10.1016/j.prime.2024.100634>.
- Seow, M.-J., & Asari, V. K. (n.d.). (2024). Homomorphic processing system and ratio rule for color image enhancement. *2004 IEEE International Joint Conference on Neural Networks (IEEE Cat. No.04CH37541)*. <https://doi.org/10.1109/ijcnn.2004.1381031>
- Tarhate, S. (2020). Weight maps guided underwater image enhancement by fusion technique. *Bioscience Biotechnology Research Communications*, 13(14), 440–444. <https://doi.org/10.21786/bbrc/13.14/99>
- The UFO-120 dataset. The UFO-120 Dataset | Minnesota Interactive Robotics and Vision Laboratory. <https://irvlab.cs.umn.edu/resources/ufo-120-dataset>
- Wang, Nan, et al. UWGAN: underwater GAN for real-world underwater color restoration and dehazing. *arXiv preprint arXiv:1912.10269* (2019).
- Yang, M., Hu, J., Li, C., Rohde, G., Du, Y., & Hu, K. (2019a). An in-depth survey of underwater image enhancement and restoration. *IEEE Access*, 7, 123638–123657. <https://doi.org/10.1109/access.2019.2932611>
- Zhou, J., Yao, J., Zhang, W. et al. (2022). Multi-scale retinex-based adaptive gray-scale transformation method for underwater image enhancement. *Multimed Tools Appl* 81, 1811–1831. <https://doi.org/10.1007/s11042-021-11327-8>.

## List of Referees - Volume 52 (2024)

**Dr Piumi de A. Abeysundara**  
Dept. of Food Science and Technology  
Univ. of Sri Jayewardenepura

**Dr D. Sumith Abeysiriwardena**  
CIC Agribusiness (Pvt.) Ltd  
Sri Lanka

**Prof Asanga D. Ampitiyawatta**  
Dept. of Export Agriculture  
Sabaragamuwa Univ. of SL

**Prof Lidula N. Widanagama Arachchige**  
Dept. of Electrical Engineering  
Univ. of Moratuwa

**Prof Renuka N. Attanayake**  
Dept. of Plant and Molecular Biology  
Univ. of Kelaniya

**Prof Anoja P. Attanayake**  
Dept. of Biochemistry  
Univ. of Ruhuna

**Dr A. W. Suraj Chandana**  
Dept. of Sports Sciences and Physical  
Education  
Sabaragamuwa Univ. of SL

**Prof S. D. M. Chinthaka**  
Dept. of Chemistry  
Univ. of Sri Jayewardenepura

**Prof Enoka Corea**  
Dept. of Medical Microbiology &  
Immunology  
Univ. of Colombo

**Dr Asitha T. Cooray**  
Dept. of Chemistry  
Univ. of Sri Jayewardenepura

**Prof Warshi S. Dandeniya**  
Dept. of Soil Science  
Univ. of Peradeniya

**Prof Managala C. S. de Silva**  
Dept. of Zoology  
Univ. of Ruhuna

**Prof M. P. K. S. Kumudu de Silva**  
Dept. of Zoology  
Univ. of Ruhuna

**Dr Senuri de Silva**

**Prof Priyanjali T. de Zoysa**  
Dept. of Psychiatry  
Univ. of Colombo

**Prof Nelum Deshappriya**  
Dept. of Botany  
Univ. of Sri Jayewardenepura

**Prof R. Saman Dharmakeerthi**  
Dept. of Soil Science  
Univ. of Peradeniya

**Prof Sisira Ediriweera**  
Dept. of Science and Technology  
Uva Wellassa Univ.

**Dr Chamira U. S. Edussooriya**  
Dept. of Electronic &  
Telecommunication Engineering  
Univ. of Moratuwa

**Prof J. B. Ekanayake**  
Dept. of Electrical and Electronic  
Engineering  
Univ. of Peradeniya

**Dr K. K. W. Hasitha Erandi**  
Dept. of Mathematics  
Univ. of Colombo

**Prof T. Saminda P. Fernando**  
Dept. of Zoology  
The Open Univ. of SL

**Dr Samiru Gayan**  
Dept. of Electronic &  
Telecommunication Engineering  
Univ. of Moratuwa

**Prof Sudarshanee Geekiyanage**  
Dept. of Agricultural Biology  
Univ. of Ruhuna

**Dr D. R. Gimhani**  
Dept. of Biotechnology  
Wayamba Univ. of SL

**Prof G. M. Roshan I. Godaliyadda**  
Dept. of Electrical & Electronic  
Engineering  
Univ. of Peradeniya

**Prof K. B. Gunaherath**  
Dept. of Chemistry  
The Open Univ. of SL

**Dr K. Locana Gunaratna**  
Gunaratna Associates  
Sri Lanka

**Dr A. Danushi Gunasekera**  
Dept. Para Clinical Sciences  
Sir John Kotelawala Defence Univ.

**Dr Anjleen Hannak**  
Faculty of Biology and Chemistry  
Univ. of Bremen  
Germany

**Dr H. M. Sumudu T. Herath**  
Dept. of Civil Engineering  
Univ. of Moratuwa

**Prof H. M. Indika K. Herath**  
Dept. of Plantation Management  
Wayamba Univ. of SL

**Dr Chamod Hettiarachchi**  
Dept. of Civil Engineering  
Univ. of Moratuwa

**Prof Sanath Hettiarachchi**  
Dept. of Biological Sciences  
Rajarata Univ. of SL

**Dr A. Ilmudeen**  
Dept. of Management and I.T.  
South Eastern Univ. of SL

**Prof Cassim Iqbal**  
Park Lane, Rajagiriya

**Dr Chamnida Jayawardana**  
American National Business University  
USA

**Dr Upul Jayasinghe**  
Dept. Computer Engineering  
University of Peradeniya

**Prof K. G. L. R. Jayathunga**  
Dept. of Biosystem Technology  
Univ. of Sri Jayewardenepura

**Dr C. B. Jayawardana**  
American National Business University,  
USA

**Prof Gehan Jayasuriya**  
Dept. of Botany  
University of Peradeniya

**Mehmet Karakose**

**Dr Suneth Namal Karunarathna**  
Department of Computer Engineering  
University of Peradeniya

**Mrs Namalika Darshani Karunaratne**  
Department of Farm Animal Production  
& Health ..  
University of Peradeniya

**Dr N Karthikeyan**  
Dept. of Physics  
The Open University of SL

**Dr M. Kayanan**  
Dept. of Physical Science  
Univ. of Vavuniya

**Prof. Nuwan Kodagoda**  
SLIIT

**Prof K. A. Sunanda Kodikara**  
Dept. of Botany  
Univ. of Ruhuna

**Dr Renuka Kolandasamy**  
Dept. of Computer Science &  
Engineering  
KLEF  
India

**Prof Nisha Kottarachchi**  
Dept. of Biotechnology  
Wayamba University of SL

**Prof K.L. Wasantha Kumara**  
Department of Agricultural Biology  
University of Ruhuna

**Dr B. M. T. Kumarika**  
Dept. of Statistics and Computer  
Science  
Univ. of Kelaniya

**Prof. W. G. Shirani Manel Kumari**  
Department of Botany  
University of Ruhuna

**Prof Brijesh Kumbhani**  
IIT Ropar, India

**Prof W.G. Deepthi Lakmini Dept of  
Crop Science**  
Faculty of Agriculture  
University of Ruhuna

**Dr G.H. Jayantha Lanel**  
Dept. of Mathematics  
Univ. of Sri Jayewardenepura

**Dr Gayan C. Lankeshwara**  
School of Electrical Engineering &  
Computer Science  
Univ. of Queensland  
Australia

**Dr Thanuja Liyanage**  
Dept. of Soil Science  
Univ. of Ruhuna

**Dr Ruvini Liyanage**  
National Institute of Fundamental  
Studies

**Dr Veranja Liyanapathirana**  
Dept. of Microbiology  
University of Peradeniya

**Dr MDS Lokuhetti**  
World Health Organization

**Prof H. M. S. P. Madawala**  
Dept. of Botany  
University of Peradeniya

**Dr Pasan Maduranga**  
Dept. of Electrical & Electronic  
Engineering  
University of Peradeniya

**Dr B. G. D. A. Madushanka**  
Dept. of Mechanical Engineering  
The Open University of SL

**Prof Anuradha C. Mahasinghe**  
Dept. of Mathematics  
Univ. of Colombo

**Prof B. A. G. G. Mahendra**  
Dept. of Pathology  
Univ. of Kelaniya

**Dr Dimuthu S. Manamgoda**  
Dept. of Botany  
Univ. of Sri Jayewardenepura

**Abhilash S. Mandloi**  
Department of Electronics Engineering  
S. V. National Institute of Technology,  
Ihchhanath, Surat-395007 Gujarat,  
India

**Dr J. N. Munasinghe**  
Dept. of Town & Country Planning  
University of Moratuwa

**Dr M.I.S. Munaweera**  
Dept. of Chemistry  
Univ. of Sri Jayewardenepura

**Prof Chandrika Nanayakkara**  
Department of Plant Science University  
of Colombo

**Prof M.M.A.N. Navarathne**  
Postgraduate Institute of Science  
University of Peradeniya

**Dr Ledya Novamizanti**  
School of Electrical Engineering  
Telkom Univ.  
Indonesia

**Dr K Rasarie E Padmathilake**  
Dept. of Plant Sciences  
Rajarata University of SL

**Prof Priyani Paranagama**  
Department of Chemistry  
University of Kelaniya

**Prof Ranjith Pathirana**  
School of Agriculture  
Food and Wine  
University of Adelaide  
Australia

**Prof K. A. S. Pathirathne**  
Dept. of Chemistry  
University of Kelaniya

**Prof Asoka Pathiratne**  
Emeritus Professor  
University of Kelaniya  
Emeritus Prof. Ranjith Pathirana  
Univ. of Ruhuna

**Prof A.A.I. Perera**  
Department of Mathematics  
University of Peradeniya

**Dr Ishara Perera**  
Assistant Director  
Agricultural Department  
Agunakollapellasa

**Dr Chatumal Perera**  
Department of Electrical and Computer  
Engineering University of Toronto  
Canada

**Dr K.K.K.R. Perera**  
Department of Mathematics  
University of Kelaniya

**Prof SSN Perera**  
Dept. of Mathematics  
Univ. of Colombo

**Dr (Ms) I. T. S. Piyatilake**  
Dept. of Computational Mathematics  
University of Moratuwa

**Anil Audumbar Pise**  
University of the Witwatersrand  
City of Johannesburg Gauteng, South  
Africa

**Prof WTS Dammini Premachandra**  
Dept. of Zoology  
University of Ruhuna

**Dr U.M.B. Premarathne**  
NIFS

**Dr Mrs. J.M.K.J.J. Premaratha**  
Department of Livestock and Avian  
Science, Wayamba University

**Dr Mahesh Premarathna**  
National Institute of Fundamental  
Studies

**Prof S Priyadhasini**  
Department of Mathematics SK Arts  
and Science College Coimbatore, India

**Prof UGA Puswewala**  
Dept. of Civil Engineering  
University of Moratuwa

**Dr Kokila Ramanayaka**  
Dept. of Information Technology  
Univ. of Ruhuna

**Prof RRMPK Ranatunga**  
Dept. of Zoology  
Univ. of Sri Jayewardenepura

**Prof Roshan G. Ragel**  
Dept. of Computer Engineering  
University of Peradeniya

**Prof R.M.G. Rajapakse**  
Dept. of Chemistry  
University of Peradeniya

**Dr P. Rajarajeswari**  
Associate Professor  
Department of Mathematics Chikkanna  
Govt. Arts College Tiruppur, India

**Dr R.R.M. K. P. Ranatunga**  
Dept. of Zoology  
Univ. of Sri Jayewardenepura

**Prof A. L. Ranawake**  
Dept. of Agricultural Biology  
University of Ruhuna

**Dr Dineth S. Samarawickrama**  
Research Technologist  
Materials Technology Section  
ITI/NASTEC

**Prof Navaratnarajah Sathiparan**  
Dept. of Civil Engineering University  
of Jaffna, Sri Lanka

**Dr Vidura Vithana**

**Prof Upali Samarajeewa**  
Emeritus Professor  
Dept. of Food Science & Technology  
University of Peradeniya

**Prof G Asha Sewwandi**  
Dept. of Materials Science &  
Engineering Sciences  
Univ. of Moratuwa

**Dr R. A. S. P. Senanayake**  
Dept. of Plant & Molecular Biology  
University of Kelaniya

**Dr Chathurika Sewwandi Silva**  
Instrumentation and Automation  
Technology  
Faculty of Technology

**Prof W. L. Sumathipala**  
Nugegoda

**Dr Ramajeyam Tharshan**  
Dept of Mathematics & Statistics  
Univ of Jaffna

**Prof T.M. D. D. Thambavita**  
Dept. of Pharmacology  
University of Colombo

**Prof T. A. S. S. Thelijjagoda**  
SLIIT Malabe Campus  
Malabe

**Dr T. M. S. G. Tennekone**  
Director Research  
Link Natural Products

**Prof R. J. M. Uduporuwa**  
Department of Geography &  
Environmental Management  
Sabaragamuwa Univ. of SL

**Prof Preethi Udagama**  
Head / Dept. of Zoology and  
Environment Sciences  
University of Colombo

**Dr (Mrs) Isuru Udayangani  
Hewapathirana**  
Software Engineering Teaching Unit,  
University of Kelaniya

**Naoki Hirotsu**  
Dept. of Life Sciences  
University of Toyo  
Japan

**Prof Meththika Vithanage**  
Instrument Centre  
Faculty of Applied Sciences  
Univ. of Sri Jayewardenepura

**Dr S. M. Vidanagamachchi**  
University of Ruhuna

**Prof Kalaivani Vivehananthan**  
Dept. of Basic Sciences  
The Open University of SL

**Prof W. K. I. L. Wanniarachchi**  
Department of Physics  
Univ. of Sri Jayewardenepura

**Prof K. S. Wanniarachchi**  
Department of Civil and Environmental  
Engineering  
Univ. of Ruhuna

**Prof J. Wansapala**  
Department of Food Science  
& Technology  
Univ. of Sri Jayewardenepura

**Dr W.M.M.T.S. Weerakoon**  
Dept. of Electrical & Electronic  
Engineering, University of Peradeniya

**Prof Sriyani Wickramasinghe**  
Dept. of Biological Sciences  
Rajarata University of SL

**Dr Sanika Wijesekera**  
Dept. of Computer System Engineering  
SLIIT Malabe Campus

**Prof W. A. J. P. Wijesinghe**  
Dept. of Food Science and Technology  
Uva Wellassa Univ.

**Prof J.J. Wijetunge**  
Dept. of Civil Engineering  
University of Peradeniya

**Prof W. M. C. S. Wijesundera**  
Dept. of Zoology  
University of Peradeniya

**Dr Chaminda Wijesundara**  
Dept. of Zoology  
Univ. of Peradeniya

**Prof Swarna Wimalasiri**  
Dept. of Food Science & Technology  
University of Peradeniya

**Prof Surangi G. Yasawardene**  
Dept. of Anatomy  
Faculty of Medical Sciences  
Univ. of Sri Jayewardenepura

**Prof M. Siyamalan**  
Department of Computer Science  
University of Jaffna



## AUTHOR INDEX - VOL 52 – 2024

- Abayawansa KGR *see* Thilakarathne DS *et al.* (2024)
- Abeyaweera ND, Sivaruban A, Muruganathan A & Amarasinghe KP - Russell's viper (*Daboia russelii*) in the Jaffna peninsula, Sri Lanka bears signatures of incipient genetic divergence from the South Indian population **52**: 199-214 (2024)
- Abeykoon AI, Kumarasinghe KMN, Chandrasekharan NV & Wickramasinghe PMTB - Establishment and evaluation of real time PCR based SELEX platform for the identification of protein binding aptamers: A pilot study in Sri Lanka **52**: 493-500 (2024)
- Abeynayake S *see* Prathibhani MR *et al.* (2024)
- Ahamed J *see* Krishnaram N *et al.* (2024)
- Alkan BB *see* Alkan N *et al.* (2024)
- Alkan N, Pardo MC & Alkan BB - Comparison of methods for handling outliers in Cox regression model **52**: 59-68 (2024)
- Amarasena MDMCK & Wijeyaratne WMDN - Bioaccumulation and health risks of chromium and cadmium in *Basella alba* with emphasis on Urea, muriate of potash and triple super phosphate mixtures **52**: 371-383 (2024)
- Amarasinghe ADI, Wijewickrama DIH, De Fonseka IS, Lawanya MAD, Fernando WNS, Wishwanthi DAD, Senanayake G, Pushpakumara S & Ediri Arachchi WM - Structural brain network topology in migraine vs. healthy subjects: A graph theory study **52**: 321-330 (2024)
- Amarasinghe KP *see* Abeyaweera ND *et al.* (2024)
- Amirah Saeed Alharthi *see* Azam Zaka *et al.* (2024)
- Anita CS *see* Sudharson K *et al.* (2024)
- Arivazhagan S *see* Priyadarshi RA *et al.* (2024)
- Athapaththu AMKB *see* Fernando M *et al.* (2024)
- Athapaththu AMKB *see* Krishnaram N *et al.* (2024)
- Athapaththu AMSLK *see* Ranasinghe R *et al.* (2024)
- Attygalle DT *see* Deshani KAD *et al.* (2024)
- Azad R *see* Prathibhani MR *et al.* (2024)
- Azam Zaka, Riffat Jabeen, Amirah Saeed Alharthi & Hassan M. Aljohani - The modified control charts for monitoring the error detection of process control under different estimators **52**: 17-34 (2024)
- Aziz U *see* Khan H *et al.* (2024)
- Babu G *see* Sudharson K *et al.* (2024)
- Balasoorya D *see* Edirisinghe JC *et al.* (2024)
- Bandara CS *see* Perera RGSS *et al.* (2024)
- Bandara RMVV *see* Ranasinghe R *et al.* (2024)
- Bandara TMWJ *see* Kumara GRA *et al.* (2024)
- Bandularathne AMNN *see* Samarakoon SMTM *et al.* (2024)
- Buddhika PRM *see* Gunathilake SP *et al.* (2024)
- Chamath LG, Srimal LKT, Sewvandi GA, Gallage R & Epaarachchi J - Optimizing the alkaline concentration for coir fibre treatment and estimation of lifetime **52**: 515-525 (2024)
- Chaminda SP *see* Kanagasundaram G *et al.* (2024)
- Chandrasekharan NV *see* Abeykoon AI *et al.* (2024)
- Chen Bin, Quan YuXuan, Liu Ge, Li JianZhong, Nie GaoXing, Zhang YongChang, Shan ChenZe, Chen JunSen, Chen Rui, Chen Xi & Zhang MengWei - Predicting water content in engine oil using SPA-ISSA-BP methods **52**: 359-370 (2024)
- Chen JunSen *see* Chen Bin *et al.* (2024)
- Chen Rui *see* Chen Bin *et al.* (2024)
- Chen Xi *see* Chen Bin *et al.* (2024)
- Dammika AJ *see* Perera RGSS *et al.* (2024)
- Dammika AJ *see* Rathnasiri SC *et al.* (2024)

- Darshana KKN *see* Kalansuriya CM *et al.* (2024)
- Dassanayake ABN *see* Kanagasundaram G *et al.* (2024)
- Dassanayake BS *see* Gurunanthanan V *et al.* (2024)
- Daundasekera WB *see* Gnanapragasam SR & Daundasekera WB (2024)
- De Fonseka IS *see* Amarasinghe ADI *et al.* (2024)
- Deshani KAD, Attygalle DT & Hansen LL - Two level neuro-functional forecaster: A novel dynamic hybridization for functional data forecasting **52**: 81-91 (2024)
- Desikan K *see* Sarkarai D & Desikan K (2024)
- Dharmaratne PD *see* Malkanthi SN *et al.* (2024)
- Ediri Arachchi WM *see* Amarasinghe ADI *et al.* (2024)
- Edirisinghe JC, Ranjan H, Herath HMLK, Jayasinghe-Mudalige UK, Wijeratne M, Kuruppu V, Jayathilake C, Wijesuriya W, Somarathna K, Karunaratne S, Jayawardana S, Gunathilaka D & Balasooriya D - Impact of climate on tea yield: an empirical investigation from Sri Lanka **52**: 183-190 (2024)
- Epaarachchi J *see* Chamath LG *et al.* (2024)
- Faour A *see* Kasap P & Faour A (2024)
- Fernando HNS *see* Terensan S *et al.* (2024)
- Fernando M, Sandaruwan KD & Athapaththu AMKB - Evaluation of Taekwondo Poomsae movements using skeleton points † **52**: 143-156 (2024)
- Fernando WNS *see* Amarasinghe ADI *et al.* (2024)
- Gadiarachchi HW *see* Kumara GRA *et al.* (2024)
- Galabada H *see* Malkanthi SN *et al.* (2024)
- Gallage R *see* Chamath LG *et al.* (2024)
- Gamage BYI *see* Thilakarathne DS *et al.* (2024)
- Gayanjalee DA *see* Gunathilake SP *et al.* (2024)
- Geekiyanage S *see* Prathibhani MR *et al.* (2024)
- Gnanapragasam SR & Daundasekera WB - Meta-heuristic method to schedule vehicle routing with moving shipments at the cross-docking facility **52**: 169-181 (2024)
- Gunathilaka D *see* Edirisinghe JC *et al.* (2024)
- Gunathilake SP, Gayanjalee DA, Prathiraja DAS, Buddhika PRM, Weerathilake WADV & Rasika DMD - A preliminary study on milk composition of three buffalo breeds located in Polonnaruwa, Sri Lanka **52**: 103-111 (2024)
- Gunawardana WSN *see* Thilakarathne DS *et al.* (2024)
- Gurunanthanan V, Wijayarathne KB, Dassanayake BS, Mantilaka PG & Perera CS - Effective removal of Pb(II) ions using Fe<sub>3</sub>O<sub>4</sub>/MgO adsorbent: A comprehensive study **52**: 385-400 (2024)
- Hansen LL *see* Deshani KAD *et al.* (2024)
- Hassan M. Aljohani *see* Azam Zaka *et al.* (2024)
- Herath HMLK *see* Edirisinghe JC *et al.* (2024)
- Hewavitharana KHIK *see* Keerthana J *et al.* (2024)
- Jayarathne DC *see* Kalansuriya CM *et al.* (2024)
- Jayasekara L *see* Prathibhani MR *et al.* (2024)
- Jayasinghe JASC *see* Perera RGSS *et al.* (2024)
- Jayasinghe JASC *see* Rathnasiri SC *et al.* (2024)
- Jayasinghe-Mudalige UK *see* Edirisinghe JC *et al.* (2024)
- Jayathilake C *see* Edirisinghe JC *et al.* (2024)
- Jayawardana S *see* Edirisinghe JC *et al.* (2024)

- Jayawardena CL *see* Kanagasundaram G *et al.* (2024)
- Jayawardene CJ, Navaratna WCW & Senadheera JN - All Ramsey critical graphs for large cycles vs a complete graph of order six **52**: 113-123 (2024)
- K Sudharson, Babu G, Santhiya R & Anita CS - Enhanced privacy-preserving federated convivial learning for internet of medical things (IoMT) through blockchain-enabled trust Q-learning **52**: 501-514 (2024)
- Kalansuriya CM, Weerasingha RM, Jayaratne DC & Darshana KKN - Determination of noise level and acoustic analysis of toys for children in Sri Lanka market **52**: 191-197 (2024)
- Kalupahana RS *see* Thilakarathne DS *et al.* (2024)
- Kanagasundaram G, Dassanayake ABN, Jayawardena CL & Chaminda SP - Quantifying the relationship between uniaxial compressive strength and slake durability index in gneiss rocks: an experimental approach **52**: 243-255 (2024)
- Karunaratne DGBC *see* Kumara GRA *et al.* (2024)
- Kasap P & Faour AO - Maximum likelihood estimation for the two-parameter Maxwell distribution **52**: 441-458 (2024)
- Keerthana J, Hewavitharana KHIK & Wijesekara KB - Synthesis and characterization of biocomposite of bovine bone- based hydroxyapatite-poly (lactic acid)-maleic anhydride **52**: 271-279 (2024)
- Khan H, Aziz U, Koreshi ZU & Sheikh SR - Optimal fissile distribution in multiplying systems: Illustrative examples with Monte Carlo simulation and Pontryagin's maximum principle **52**: 69-80 (2024)
- Khazema Yousaf, Zernish Shabbir, Rasheeda Bashir, Syed Mohsin Raza, Saiqa Ilyas & Rukhama Haq - Prevalence and in silico analysis of p.D658G variant of WDR36 gene in patients affected with primary open angle glaucoma from Punjab Pakistan **52**: 35-44 (2024)
- Kodikara KAS *see* Samarakoon SMTM *et al.* (2024)
- Koreshi ZU *see* Khan H *et al.* (2024)
- Kottawatta KSA *see* Thilakarathne DS *et al.* (2024)
- Kottearachchi NS *see* Terensan S *et al.* (2024)
- Krishnam N, Ahamed J, Sathyamoorthy N, Sandaruwan KD & Athapaththu AMKB - Skeletal point analysis to determine the accuracy of forehand smash shots played by badminton players † **52**: 125-142 (2024)
- Kumara GRA, Medagedara ADT, Gadiarachchi HW, Karunaratne DGBC, Tennakone K, Rajapakse RMG & Bandara TMWJ - An electrical double-layer supercapacitor based on a biomass-activated charcoal electrode and ionic liquid with excellent charge-discharge cycle stability **52**: 331-341 (2024)
- Kumarasinghe KMN *see* Abeykoon AI *et al.* (2024)
- Kuruppu V *see* Edirisinghe JC *et al.* (2024)
- Lawanya MAD *see* Amarasinghe ADI *et al.* (2024)
- Li JianZhong *see* Chen Bin *et al.* (2024)
- Liu Ge *see* Chen Bin *et al.* (2024)
- Madarasinghe SK *see* Samarakoon SMTM *et al.* (2024)
- Malkanathi SN, Sathsara KGG, Dharmaratne PD & Galabada H - Proposed mix design improvements of compressed stabilized earth blocks (CSEB) with particle packing optimization and coir reinforcement **52**: 159-167 (2024)
- Mantilaka PG *see* Gurunathanan V *et al.* (2024)
- Medagedara ADT *see* Kumara GRA *et al.* (2024)
- Mendis MJL- Cycle structures with more than three nontrivial cycles of automorphisms of Latin squares **52**: 413-416 (2024)
- Muruganathan A *see* Abeyaweera ND *et al.* (2024)
- Mythili C *see* Ponram P *et al.* (2024)
- Navaratna WCW *see* Jayawardene CJ *et al.* (2024)
- Nie GaoXing *see* Chen Bin *et al.* (2024)
- Pardo MC *see* Alkan N *et al.* (2024)
- Perera CS *see* Gurunathanan V *et al.* (2024)

- Perera RGSS, Ruwanmali JHA, Thevega T, Jayasinghe JASC, Bandara CS & Dammika AJ - Thermal performance of glass facade under fire loading: a numerical approach **52**: 229-241 (2024)
- Ponram P, Mythili C, Selvakumar NC & Selwyn J Kumar A - Ergonomic assessment and gait analysis of a knee joint model with an active spring-reinforced centrally-rollable knee bypass support system **52**: 257-269 (2024)
- Prathibhani MR, Azad R, Ranaweera S, Jayasekara L, Ranawaka RAAK, Senanayake G, Abeynayake S & Geekiyanage S - Variation in plant morphology and leaf essential oil composition of a representative *Cinnamomum verum* collection from Sri Lanka† **52**: 3-16 (2024)
- Prathiraja DAS *see* Gunathilake SP *et al.* (2024)
- Priyadharshi RA, Arivazhagan S & Ramajeyam K- Unveiling the depths of underwater image enhancement with spatial blended CNN: Diving into clarity **52**: 527-540 (2024)
- Pushpakumara S *see* Amarasinghe ADI *et al.* (2024)
- Qin X *see* Wang Y *et al.* (2024)
- Quan YuXuan *see* Chen Bin *et al.* (2024)
- Rajapakse RMG *see* Kumara GRA *et al.* (2024)
- Ramajeyam K *see* Priyadharshi RA *et al.* (2024)
- Ranasinghe C *see* Rangala H *et al.* (2024)
- Ranasinghe R, Bandara RMVV & Athapaththu AMSLK -Symmetric encryption using snake graphs and supermagic covering **52**: 435-440 (2024)
- Ranawaka RAAK *see* Prathibhani MR *et al.* (2024)
- Ranawake AL & Shyamalee HAPA - Genetic diversity analysis of traditional and improved rice genotypes in Sri Lanka **52**: 215-227 (2024)
- Ranawake AL *see* Shyamalee HAPA & Ranawake AL (2024)
- Ranaweera S *see* Prathibhani MR *et al.* (2024)
- Ranaweera S *see* Prathibhani MR *et al.* (2024)
- Rangala H, Samaraweera S, Sandaruwan KD, Weerasinghe TA & Ranasinghe C - Athlete body power and strength estimation using skeleton point cloud **52**: 481-492 (2024)
- Ranjan H *see* Edirisinghe JC *et al.* (2024)
- Rasheeda Bashir *see* Khazeema Yousaf *et al.* (2024)
- Rasika DMD *see* Gunathilake SP *et al.* (2024)
- Rathnasiri SC, Jayasinghe JASC & Dammika AJ - Simplification of large-scale solid element model for seismic structural response analysis of buildings **52**: 469-480 (2024)
- Riffat Jabeen *see* Azam Zaka *et al.* (2024)
- Rukhama Haq *see* Khazeema Yousaf *et al.* (2024)
- Ruwanmali JHA *see* Perera RGSS *et al.* (2024)
- Saiqa Ilyas *see* Khazeema Yousaf *et al.* (2024)
- Samarakoon SMTM, Thilakarathne NDS, Wijayathilaka HD, Bandularathne AMNN, Madarasinghe SK & Kodikara KAS - Estimating plant dominance using field-measured structural parameters and remotely sensed data; A case study from Rekawa mangrove forest, southern coast of Sri Lanka **52**: 459-468 (2024)
- Samaraweera S *see* Rangala H *et al.* (2024)
- Sandaruwan KD *see* Fernando M *et al.* (2024)
- Sandaruwan KD *see* Krishnaram N *et al.* (2024)
- Sandaruwan KD *see* Rangala H *et al.* (2024)
- Santhiya R *see* Sudharson K *et al.* (2024)
- Sarkarai D & Desikan K - Computational analysis of diameter eccentricity based and hyper diameter eccentricity based indices for linear saturated monocarboxylic acids **52**: 311-320 (2024)
- Sathsara KGK *see* Malkanthi SN *et al.* (2024)
- Sathyamoorthy N *see* Krishnaram N *et al.* (2024)
- Selvakumar NC *see* Ponram P *et al.* (2024)

- Selwyn J Kumar A *see* Ponram P *et al.* (2024)
- Senadheera JN *see* Jayawardene CJ *et al.* (2024)
- Senanayake G *see* Amarasinghe ADI *et al.* (2024)
- Senanayake G *see* Prathibhani MR *et al.* (2024)
- Sewvandi GA *see* Chamath LG *et al.* (2024)
- Shan ChenZe *see* Chen Bin *et al.* (2024)
- Sharma N *see* Soni A & Sharma N (2024)
- Sheikh SR *see* Khan H *et al.* (2024)
- Shyamalee HAPA & Ranawake AL - Path coefficient analysis using traditional and improved rice genotypes for trait effect on grain yield **52**: 93-102 (2024)
- Shyamalee HAPA *see* Ranawake AL & Shyamalee HAPA (2024)
- Silva JN *see* Terensan S *et al.* (2024)
- Sivaruban A *see* Abeyaweera ND *et al.* (2024)
- Somarathna K *see* Edirisinghe JC *et al.* (2024)
- Soni A & Sharma N - An efficient and improved algorithm for generating an equivalent planar architecture of the data vortex switch **52**: 400-412 (2024)
- Srimal LKT *see* Chamath LG *et al.* (2024)
- Syed Mohsin Raza *see* Khazeema Yousaf *et al.* (2024)
- Tennakone K *see* Kumara GRA *et al.* (2024)
- Terensan S, Weerasena OVDSJ, Kottearachchi NS, Silva JN & Fernando HNS - Influence of cultivar selection on blast and brown spot diseases in rice: Molecular screening of blast resistance genes **52**: 343-358 (2024)
- Thevega T *see* Perera RGSS *et al.* (2024)
- Thilakarathne DS, Gamage BYI, Kottawatta KSA, Abayawansa KGR, Kalupahana RS & Gunawardana WSN -Decadal trends in antimicrobial susceptibility of *Escherichia coli* and *Salmonella* spp. in chicken from small-scale farm shops in Kandy district, Sri Lanka **52**: 419-433 (2024)
- Thilakarathne NDS *see* Samarakoon SMTM *et al.* (2024)
- Thilakasiri S *see* Wang Y *et al.* (2024)
- Thiruchchelvan N, Casonato S, Mikunthan G, Condron LM, Moukarzel R & Kularathna M - Prevalence and abundance of plant-parasitic nematodes associated with corn (*Zea mays* L.) in Anuradhapura, Sri Lanka **52**: 299-309 (2024)
- Thiruvaran T - Construction of an effective telephone bandwidth specifically for speaker recognition **52**: 283-298 (2024)
- Vidurapriya D *see* Wang Y *et al.* (2024)
- Wang Y, Vidurapriya D, Qin X & Thilakasiri S - The microstructure and the behaviour of low organic clayey soils in Sri Lanka **52**: 45-58 (2024)
- Weerasena OVDSJ *see* Terensan S *et al.* (2024)
- Weerasingha RM *see* Kalansuriya CM *et al.* (2024)
- Weerasinghe TA *see* Rangala H *et al.* (2024)
- Weerathilake WADV *see* Gunathilake SP *et al.* (2024)
- Wickramasinghe PMTB *see* Abeykoon AI *et al.* (2024)
- Wickramasinghe PMTB *see* Abeykoon AI *et al.* (2024)
- Wijayarathne KB *see* Gurunathanan V *et al.* (2024)
- Wijayathilaka HD *see* Samarakoon SMTM *et al.* (2024)
- Wijeratne M *see* Edirisinghe JC *et al.* (2024)
- Wijesekara KB *see* Keerthana J *et al.* (2024)
- Wijesuriya W *see* Edirisinghe JC *et al.* (2024)
- Wijewickrama DIH *see* Amarasinghe ADI *et al.* (2024)
- Wijayarathne WMDN *see* Amarasinghe ADI & Wijayarathne WMDN (2024)
- Wishwanthi DAD *see* Amarasinghe ADI *et al.* (2024)

Zernish Shabbir *see* Khazeema Yousaf *et al.* (2024)

Zhang MengWei *see* Chen Bin *et al.* (2024)

Zhang YongChang *see* Chen Bin *et al.* (2024)

**SUBJECT INDEX - VOL 52 – 2024****Activated carbon**

An electrical double-layer supercapacitor based on a biomass- activated charcoal electrode and ionic liquid with excellent charge-discharge cycle stability (Kumara GRA, Medagedara ADT, Gadiarachchi HW, Karunarathne DGBC, Tennakone K, Rajapakse RMG & Bandara TMWJ) **52**: 331-341 (2024)

**Activation energy**

Optimizing the alkaline concentration for coir fibre treatment and estimation of lifetime (Chamath LG, Srimal LKT, Sewvandi GA, Gallage R & Epaarachchi J) **52**: 515-525 (2024)

**Adsorption capacity**

Effective removal of Pb(II) ions using Fe<sub>3</sub>O<sub>4</sub>/MgO adsorbent: A comprehensive study (Gurunathanan V, Wijayarathne KB, Dassanayake BS, Mantilaka PG & Perera CS) **52**: 385-400 (2024)

**Alkaline treatment**

Optimizing the alkaline concentration for coir fibre treatment and estimation of lifetime (Chamath LG, Srimal LKT, Sewvandi GA, Gallage R & Epaarachchi J) **52**: 515-525 (2024)

**Antimicrobials**

Decadal trends in antimicrobial susceptibility of Escherichia coli and Salmonella spp. in chicken from small-scale farm shops in Kandy district, Sri Lanka (Thilakarathne DS, Gamage BYI, Kottawatta KSA, Abayawansa KGR, Kalupahana RS & Gunawardana WSN) **52**: 419-433 (2024)

**Anuradhapura**

Prevalence and abundance of plant-parasitic nematodes associated with corn (Zea mays L.) in Anuradhapura, Sri Lanka (Thiruchelvan N, Casonato S, Mikunthan G, Condrón LM, Moukarze R & Kularathna M) **52**: 299-309 (2024)

**Automorphism**

Cycle structures with more than three nontrivial cycles of automorphisms of Latin squares (Mendis MJL) **52**: 413-416 (2024)

**Autotopism**

Cycle structures with more than three nontrivial cycles of automorphisms of Latin squares (Mendis MJL) **52**: 413-416 (2024)

**Badminton forehand smash**

Skeletal point analysis to determine the accuracy of forehand smash shots played by badminton players † (Krishnam N, Ahamed J, Sathyamoorthy N, Sandaruwan KD & Athapaththu AMKB) **52**: 125-142 (2024)

**Biocomposite**

Synthesis and characterization of biocomposite of bovine bone- based hydroxyapatite-poly (lactic acid)-maleic anhydride (Keerthana J, Hewavitharana KHIK & Wijesekara KB) **52**: 271-279 (2024)

**Bioconcentration**

Bioaccumulation and health risks of chromium and cadmium in Basella alba with emphasis on Urea, muriate of potash and triple super phosphate mixtures (Amarasena MDMCK & Wijeyaratne WMDN) **52**: 371-383 (2024)

**Biomaterials**

Synthesis and characterization of biocomposite of bovine bone- based hydroxyapatite-poly (lactic acid)-maleic anhydride (Keerthana J, Hewavitharana KHIK & Wijesekara KB) **52**: 271-279 (2024)

**Biomechanics**

Athlete body power and strength estimation using skeleton point cloud (Rangala H, Samaraweera S, Sandaruwan KD, Weerasinghe TA & Ranasinghe DC) **52**: 481-492 (2024)

**Biomechanics**

Ergonomic assessment and gait analysis of a knee joint model with an active spring-reinforced centrally-rollable knee bypass support system (Ponram P, Mythili C, Selvakumar NC & Selwyn A, Kumar J) **52**: 257-269 (2024)

**Biomechanics**

Skeletal point analysis to determine the accuracy of forehand smash shots played by badminton players † (Krishnam N, Ahamed J, Sathyamoorthy N, Sandaruwan KD & Athapaththu AMKB) **52**: 125-142 (2024)

**Blast disease**

Influence of cultivar selection on blast and brown spot diseases in rice: Molecular screening of blast resistance genes (Terensan S, Weerasena OVD SJ, Kottearachchi NS, Silva JN & Fernando HNS) **52**: 343-358 (2024)

**Block diagram**

Cycle structures with more than three nontrivial cycles of automorphisms of Latin squares (Mendis MJL) **52**: 413-416 (2024)

**Blockchain**

Enhanced privacy-preserving federated convivial learning for internet of medical things (IoMT) through blockchain-enabled trust Q-learning (Sudharson K, Babu G, Santhiya R & Anita CS) **52**: 501-514 (2024)

**Bone tissue engineering**

Synthesis and characterization of biocomposite of bovine bone- based hydroxyapatite-poly (lactic acid)-maleic anhydride (Keerthana J, Hewavitharana KHIK & Wijesekara KB) **52**: 271-279 (2024)

**Brown spot disease**

Influence of cultivar selection on blast and brown spot diseases in rice: Molecular screening of blast resistance genes (Terensan S, Weerasena OVDSJ, Kottearachchi NS, Silva JN & Fernando HNS) **52**: 343-358 (2024)

**Buffalo milk**

A preliminary study on milk composition of three buffalo breeds located in Polonnaruwa, Sri Lanka (Gunathilake SP, Gayanjalee DA, Prathiraja DAS, Buddhika PRM, Weerathilake WADV & Rasika DMD) **52**: 103-111 (2024)

**Cadmium**

Bioaccumulation and health risks of chromium and cadmium in Basella alba with emphasis on Urea, muriate of potash and triple super phosphate mixtures (Amarasena MDMCK & Wijeyaratne WMDN) **52**: 371-383 (2024)

**Cancer**

Bioaccumulation and health risks of chromium and cadmium in Basella alba with emphasis on Urea, muriate of potash and triple super phosphate mixtures (Amarasena MDMCK & Wijeyaratne WMDN) **52**: 371-383 (2024)

**Chemisorption**

Effective removal of Pb(II) ions using Fe<sub>3</sub>O<sub>4</sub>/MgO adsorbent: A comprehensive study (Gurunathanan V, Wijeyaratne KB, Dassanayake BS, Mantilaka PG & Perera CS) **52**: 385-400 (2024)

**Chicken**

Decadal trends in antimicrobial susceptibility of Escherichia coli and Salmonella spp. in chicken from small-scale farm shops in Kandy district, Sri Lanka (Thilakarathne DS, Gamage BYI, Kottawatta KSA, Abayawansa KGR, Kalupahana RS & Gunawardana WSN) **52**: 419-433 (2024)

**Chromium**

Bioaccumulation and health risks of chromium and cadmium in Basella alba with emphasis on Urea, muriate of potash and triple super phosphate mixtures (Amarasena MDMCK & Wijeyaratne WMDN) **52**: 371-383 (2024)

**Cinnamomum verum collection**

Variation in plant morphology and leaf essential oil composition of a representative Cinnamomum verum collection from Sri Lanka† (Prathibhani MR, Azad R, Ranaweera S, Jayasekara L, Ranawaka RAAK, Senanayake G, Abeynayake S & Geekiyanage S) **52**: 3-16 (2024)

**Climate change**

Impact of climate on tea yield: an empirical investigation from Sri Lanka (Jayasinghe-Mudalige UK, Wijeratne M, Kuruppu V, Jayathilake C, Wijesuriya W, Somarathna K, Karunaratne S, Jayawardana S, Gunathilaka D & Balasooriya D) **52**: 183-190 (2024)

**Cluster analysis**

Influence of cultivar selection on blast and brown spot diseases in rice: Molecular screening of blast resistance genes (Terensan S, Weerasena OVDSJ, Kottearachchi NS, Silva JN & Fernando HNS) **52**: 343-358 (2024)

**Coconut coir**

Proposed mix design improvements of compressed stabilized earth blocks (CSEB) with particle packing optimization and coir

**Coir fibres**

Optimizing the alkaline concentration for coir fibre treatment and estimation of lifetime (Chamath LG, Srimal LKT, Sewvandi GA, Gallage R & Epaarachchi J) **52**: 515-525 (2024)

**Compatibilizer**

Synthesis and characterization of biocomposite of bovine bone- based hydroxyapatite-poly (lactic acid)-maleic anhydride (Keerthana J, Hewavitharana KHIK & Wijesekara KB) **52**: 271-279 (2024)

**Compressed stabilized earth blocks (CSEB)**

Proposed mix design improvements of compressed stabilized earth blocks (CSEB) with particle packing optimization and coir Reinforcement (Malkanathi SN, Sathsara K GK, Dharmaratne PD & Galabada H) **52**: 159-167 (2024)

**Compressive strength**

Proposed mix design improvements of compressed stabilized earth blocks (CSEB) with particle packing optimization and coir Reinforcement (Malkanathi SN, Sathsara K GK, Dharmaratne PD & Galabada H) **52**: 159-167 (2024)

**Continuum mechanics**

Simplification of large-scale solid element model for seismic structural response analysis of buildings (Rathnasiri SC, Jayasinghe JASC & Dammika AJ) **52**: 469-480 (2024)

**Contrast enhancement**

Unveiling the depths of underwater image enhancement with spatial blended CNN: Diving into clarity (Priyadarshi RA, Arivazhagan S & Ramajeyam K) **52**: 527-540 (2024)

**Contrast stretching**

Unveiling the depths of underwater image enhancement with spatial blended CNN: Diving into clarity (Priyadarshi RA, Arivazhagan S & Ramajeyam K) **52**: 527-540 (2024)

**Control charts**

The modified control charts for monitoring the error detection of process control under different estimators (Azam Zaka, Riffat Jabeen, Amirah Saeed Alharthi & Hassan M. Aljohani) **52**: 17-34 (2024)

**Convivial learning**

Enhanced privacy-preserving federated convivial learning for internet of medical things (IoMT) through blockchain-enabled trust Q-learning (Sudharson K, Babu G, Santhiya R & Anita CS) **52**: 501-514 (2024)

**Convolution neural network**

Unveiling the depths of underwater image enhancement with spatial blended CNN: Diving into clarity (Priyadarshi RA, Arivazhagan S & Ramajeyam K) **52**: 527-540 (2024)

**Correlation** Quantifying the relationship between uniaxial compressive strength and slake durability index in gneiss rocks: an experimental approach (Kanagasundaram G, Dassanayake ABN, Jayawardena CL & Chaminda SP) **52**: 243-255 (2024)

**Correlations**

The microstructure and the behaviour of low organic clayey soils in Sri Lanka (Wang Y, Vidurapriya D, Qin X & Thilakasiri S) **52**: 45-58 (2024)

**Cost-effectiveness**

Proposed mix design improvements of compressed stabilized earth blocks (CSEB) with particle packing optimization and coir Reinforcement (Malkanthi SN, Sathsara KGK, Dharmaratne PD & Galabada H) **52**: 159-167 (2024)

**Countermovement jump**

Athlete body power and strength estimation using skeleton point cloud (Rangala H, Samaraweera S, Sandaruwan KD, Weerasinghe TA & Ranasinghe DC) **52**: 481-492 (2024)

**Cox regression**

Comparison of methods for handling outliers in Cox regression model (Alkan N, Pardo MC & Alkan BB) **52**: 59-68 (2024)

**Cross-dock**

Meta-heuristic method to schedule vehicle routing with moving shipments at the cross-docking facility (Gnanapragasam SR & Daundasekera WB) **52**: 169-181 (2024)

**Crown area**

Estimating plant dominance using field-measured structural parameters and remotely sensed data; A case study from Rekawa mangrove forest, southern coast of Sri Lanka (Samarakoon SMTM, Madarasinghe SK, Thilakarathne NDS, Bandularathne AMNN, Wijayathilaka HD & Kodikara KAS) **52**: 459-468 (2024)

**Cultivar selection**

Influence of cultivar selection on blast and brown spot diseases in rice: Molecular screening of blast resistance genes (Terensan S, Weerasena OVDSJ, Kottearachchi NS, Silva JN & Fernando HNS) **52**: 343-358 (2024)

**Cycle structure**

Cycle structures with more than three nontrivial cycles of automorphisms of Latin squares (Mendis MJL) **52**: 413-416 (2024)

**Daboia russelii**

Russell's viper (*Daboia russelii*) in the Jaffna peninsula, Sri Lanka bears signatures of incipient genetic divergence from the South Indian population (Abeyaweera ND, Sivaruban A, Murugananthan A & Amarasinghe KP) **52**: 199-214 (2024)

**Daily intake of metals**

Bioaccumulation and health risks of chromium and cadmium in *Basella alba* with emphasis on Urea, muriate of potash and triple super phosphate mixtures (Amarasena MDMCK & Wijeyaratne WMDN) **52**: 371-383 (2024)

**Data vortex**

An efficient and improved algorithm for generating an equivalent planar architecture of the data vortex switch (Soni A & Sharma N) **52**: 401-412 (2024)

**Deep learning**

Unveiling the depths of underwater image enhancement with spatial blended CNN: Diving into clarity (Priyadarshi RA, Arivazhagan S & Ramajeyam K) **52**: 527-540 (2024)

**Derivative sampling**

Optimal fissile distribution in multiplying systems: Illustrative examples with Monte Carlo simulation and Pontryagin's maximum principle (Khan H, Aziz U, Koreshi ZU & Sheikh SR) **52**: 69-80 (2024)

**Diameter** Computational analysis of diameter eccentricity based and hyper diameter eccentricity based indices for linear saturated monocarboxylic acids (Sarkarai D & Desikan K) **52**: 311-320 (2024)

**Direct effect**

Path coefficient analysis using traditional and improved rice genotypes for trait effect on grain yield (Shyamalee HAPA & Ranawake AL) **52**: 931-102 (2024)

**Drone imagery**

Estimating plant dominance using field-measured structural parameters and remotely sensed data; A case study from Rekawa mangrove forest, southern coast of Sri Lanka (Samarakoon SMTM, Madarasinghe SK, Thilakarathne NDSD, Bandularathne AMNN, Wijayathilaka HD & Kodikara KAS) **52**: 459-468 (2024)

**Dynamic**

Two level neuro-functional forecaster: A novel dynamic hybridization for functional data forecasting (Deshani KAD, Attygalle DT & Hansen LL) **52**: 81-91 (2024)

**E. coli**

Decadal trends in antimicrobial susceptibility of Escherichia coli and Salmonella spp. in chicken from small-scale farm shops in Kandy district, Sri Lanka (Thilakarathne DS, Gamage BYI, Kottawatta KSA, Abayawansa KGR, Kalupahana RS & Gunawardana WSN) **52**: 419-433 (2024)

**Eccentricity**

Computational analysis of diameter eccentricity based and hyper diameter eccentricity based indices for linear saturated monocarboxylic acids (Sarkarai D & Desikan K) **52**: 311-320 (2024)

**EDX**

Quantifying the relationship between uniaxial compressive strength and slake durability index in gneiss rocks: an experimental approach (Kanagasundaram G, Dassanayake ABN, Jayawardena CL & Chaminda SP) **52**: 243-255 (2024)

**Engine oil**

Predicting water content in engine oil using SPA-ISSA-BP methods (Chen Bin, Quan YuXuan, Liu Ge, Li JianZhong, Nie GaoXing, Zhang YongChang, Shan ChenZe, Chen JunSen, Chen Rui, Chen Xi and Zhang MengWei) **52**: 359-370 (2024)

**Engineering properties**

The microstructure and the behaviour of low organic clayey soils in Sri Lanka (Wang Y, Vidurapriya D, Qin X & Thilakasiri S) **52**: 45-58 (2024)

**Environmental remediation**

Effective removal of Pb(II) ions using Fe<sub>3</sub>O<sub>4</sub>/MgO adsorbent: A comprehensive study (Gurunathanan V, Wijayarathne KB, Dassanayake BS, Mantilaka PG & Perera CS) **52**: 385-400 (2024)

**Equivalent planar architecture algorithm**

An efficient and improved algorithm for generating an equivalent planar architecture of the data vortex switch (Soni A & Sharma N) **52**: 401-412 (2024)

**Ergonomic assessment**

Ergonomic assessment and gait analysis of a knee joint model with an active spring-reinforced centrally-rollable knee bypass support system (Ponram P, Mythili C, Selvakumar NC & Selwyn A, Kumar J) **52**: 257-269 (2024)

**Finite element analysis**

Thermal performance of glass facade under fire loading: a numerical approach (Perera RGSS, Ruwanmali JHA, Thevega T, Jayasinghe JASC, Bandara CS & Dammika AJ) **52**: 229-241 (2024)

**Forecasting**

Two level neuro-functional forecaster: A novel dynamic hybridization for functional data forecasting (Deshani KAD, Attygalle DT & Hansen LL) **52**: 81-91 (2024)

**Frequency band shifting**

Construction of an effective telephone bandwidth specifically for speaker recognition (Thiruvaran T) **52**: 283-298 (2024)

**Functional data analysis**

Two level neuro-functional forecaster: A novel dynamic hybridization for functional data forecasting (Deshani KAD, Attygalle DT & Hansen LL) **52**: 81-91 (2024)

**Gait analysis**

Ergonomic assessment and gait analysis of a knee joint model with an active spring-reinforced centrally-rollable knee bypass support system (Ponram P, Mythili C, Selvakumar NC & Selwyn A, Kumar J) **52**: 257-269 (2024)

**GC-MS**

Variation in plant morphology and leaf essential oil composition of a representative *Cinnamomum verum* collection from Sri Lanka† (Prathibhani MR, Azad R, Ranaweera S, Jayasekara L, Ranawaka RAAK, Senanayake G, Abeynayake S & Geekiyana S) **52**: 3-16 (2024)

**Genetic algorithm**

Meta-heuristic method to schedule vehicle routing with moving shipments at the cross-docking facility (Gnanapragasam SR & Daundasekera WB) **52**: 169-181 (2024)

**glass facades**

Thermal performance of glass facade under fire loading: a numerical approach (Perera RGSS, Ruwanmali JHA, Thevega T, Jayasinghe JASC, Bandara CS & Dammika AJ) **52**: 229-241 (2024)

**Gneiss rock**

Quantifying the relationship between uniaxial compressive strength and slake durability index in gneiss rocks: an experimental approach (Kanagasundaram G, Dassanayake ABN, Jayawardena CL & Chaminda SP) **52**: 243-255 (2024)

**Goertzel's distribution**

Optimal fissile distribution in multiplying systems: Illustrative examples with Monte Carlo simulation and Pontryagin's maximum principle (Khan H, Aziz U, Koreshi ZU & Sheikh SR) **52**: 69-80 (2024)

**Google Earth satellite imagery**

Estimating plant dominance using field-measured structural parameters and remotely sensed data; A case study from Rekawa mangrove forest, southern coast of Sri Lanka (Samarakoon SMTM, Madarasinghe SK, Thilakarathne NDSD, Bandularathne AMNN, Wijayathilaka HD & Kodikara KAS) **52**: 459-468 (2024)

**Graph theory**

All Ramsey critical graphs for large cycles vs a complete graph of order six (Jayawardene CJ, Navaratna WCW & Senadheera JN) **52**: 113-123 (2024)

**Graph theory**

Structural brain network topology in migraine vs. healthy subjects: A graph theory study (Amarasinghe ADI, Wijewickrama DIH, De Fonseka IS, Lawanya MAD, Fernando WNS, Wishwanthi DAD, Senanayake G, Pushpakumara S & Ediri Arachchi WM) **52**: 321-330 (2024)

**Grey matter**

Structural brain network topology in migraine vs. healthy subjects: A graph theory study (Amarasinghe ADI, Wijewickrama DIH, De Fonseka IS, Lawanya MAD, Fernando WNS, Wishwanthi DAD, Senanayake G, Pushpakumara S & Ediri Arachchi WM) **52**: 321-330 (2024)

**Heterogeneous surface**

Effective removal of Pb(II) ions using Fe<sub>3</sub>O<sub>4</sub>/MgO adsorbent: A comprehensive study (Gurunathanan V, Wijayarathne KB, Dassanayake BS, Mantilaka PG & Perera CS) **52**: 385-400 (2024)

**Heuristic and traditional algorithms**

Maximum likelihood estimation for the two-parameter Maxwell distribution (Kasap P & Faouri AO) **52**: 441-458 (2024)

**High performance computing**

An efficient and improved algorithm for generating an equivalent planar architecture of the data vortex switch (Soni A & Sharma N) **52**: 401-412 (2024)

**Homomorphic filtering**

Unveiling the depths of underwater image enhancement with spatial blended CNN: Diving into clarity (Priyadarshi RA, Arivazhagan S & Ramajeyam K) **52**: 527-540 (2024)

**Hybrid**

Two level neuro-functional forecaster: A novel dynamic hybridization for functional data forecasting (Deshani KAD, Attygalle DT & Hansen LL) **52**: 81-91 (2024)

**Hydroxyapatite**

Synthesis and characterization of biocomposite of bovine bone- based hydroxyapatite-poly (lactic acid)-maleic anhydride (Keerthana J, Hewavitharana KHIK & Wijesekara KB) **52**: 271-279 (2024)

**Hyperaccumulation**

Bioaccumulation and health risks of chromium and cadmium in *Basella alba* with emphasis on Urea, muriate of potash and triple super phosphate mixtures (Amarasena MDMCK & Wijeyaratne WMDN) **52**: 371-383 (2024)

**Improved rice**

Path coefficient analysis using traditional and improved rice genotypes for trait effect on grain yield (Shyamalee HAPA & Ranawake AL) **52**: 931-102 (2024)

**Indirect effect**

Path coefficient analysis using traditional and improved rice genotypes for trait effect on grain yield (Shyamalee HAPA & Ranawake AL) **52**: 931-102 (2024)

**insulated glass panel**

Thermal performance of glass facade under fire loading: a numerical approach (Perera RGSS, Ruwanmali JHA, Thevega T, Jayasinghe JASC, Bandara CS & Dammika AJ) **52**: 229-241 (2024)

**Internet of medical Things and trust Q-learning**

Enhanced privacy-preserving federated convivial learning for internet of medical things (IoMT) through blockchain-enabled trust Q-learning (Sudharsan K, Babu G, Santhiya R & Anita CS) **52**: 501-514 (2024)

**Intra ocular pressure**

Prevalence and in silico analysis of p.D658G variant of WDR36 gene in patients affected with primary open angle glaucoma from Punjab Pakistan (Khazeema Yousaf, Zernish Shabbir, Rasheeda Bashir, Syed Mohsin Raza, Saiqa Ilyas and Rukhama Haq) **52**: 35-44 (2024)

**Iterative methods**

Maximum likelihood estimation for the two-parameter Maxwell distribution (Kasap P & Faouri AO) **52**: 441-458 (2024)

**Jaffna**

Russell's viper (*Daboia russelii*) in the Jaffna peninsula, Sri Lanka bears signatures of incipient genetic divergence from the South Indian population (Abeyaweera ND, Sivaruban A, Muruganathan A & Amarasinghe KP) **52**: 199-214 (2024)

**knee joint model**

Ergonomic assessment and gait analysis of a knee joint model with an active spring-reinforced centrally-rollable knee bypass support system (Ponram P, Mythili C, Selvakumar NC & Selwyn A, Kumar J) **52**: 257-269 (2024)

**knee support system**

Ergonomic assessment and gait analysis of a knee joint model with an active spring-reinforced centrally-rollable knee bypass support system (Ponram P, Mythili C, Selvakumar NC & Selwyn A, Kumar J) **52**: 257-269 (2024)

**laminated glass panel**

Thermal performance of glass facade under fire loading: a numerical approach (Perera RGSS, Ruwanmali JHA, Thevega T, Jayasinghe JASC, Bandara CS & Dammika AJ) **52**: 229-241 (2024)

**Lanka buffalo**

A preliminary study on milk composition of three buffalo breeds located in Polonnaruwa, Sri Lanka (Gunathilake SP, Gayanjalee DA, Prathiraja DAS, Buddhika PRM, Weerathilake WADV & Rasika DMD) **52**: 103-111 (2024)

**Latent transforming growth factor-beta Protein 2**

Prevalence and in silico analysis of p.D658G variant of WDR36 gene in patients affected with primary open angle glaucoma from Punjab Pakistan (Khazeema Yousaf, Zernish Shabbir, Rasheeda Bashir, Syed Mohsin Raza, Saiqa Ilyas and Rukhama Haq) **52**: 35-44 (2024)

**Latin square**

Cycle structures with more than three nontrivial cycles of automorphisms of Latin squares (Mendis MJL) **52**: 413-416 (2024) Antimicrobials

**Leaf essential oil composition**

Variation in plant morphology and leaf essential oil composition of a representative *Cinnamomum verum* collection from Sri Lanka† (Prathibhani MR, Azad R, Ranaweera S, Jayasekara L, Ranawaka RAAK, Senanayake G, Abeynayake S & Geekiyanage S) **52**: 3-16 (2024)

**Leaf morphology**

Variation in plant morphology and leaf essential oil composition of a representative *Cinnamomum verum* collection from Sri Lanka† (Prathibhani MR, Azad R, Ranaweera S, Jayasekara L, Ranawaka RAAK, Senanayake G, Abeynayake S & Geekiyanage S) **52**: 3-16 (2024)

**Lifetime analysis**

Optimizing the alkaline concentration for coir fibre treatment and estimation of lifetime (Chamath LG, Srimal LKT, Sewvandi GA, Gallage R & Epaarachchi J) **52**: 515-525 (2024)

**Long short-term memory (LSTM)**

Evaluation of Taekwondo Poomsae movements using skeleton points † (Fernando M, Sandaruwan KD & Athapaththu AMKB) **52**: 143-156 (2024)

**Low organic content**

The microstructure and the behaviour of low organic clayey soils in Sri Lanka (Wang Y, Vidurapriya D, Qin X & Thilakasiri S) **52**: 45-58 (2024)

**Machine errors**

The modified control charts for monitoring the error detection of process control under different estimators (Azam Zaka, Riffat Jabeen, Amirah Saeed Alharthi & Hassan M. Aljohani) **52**: 17-34 (2024)

**Machine learning (ML)**

Evaluation of Taekwondo Poomsae movements using skeleton points † (Fernando M, Sandaruwan KD & Athapaththu AMKB) **52**: 143-156 (2024)

**Machine learning**

Skeletal point analysis to determine the accuracy of forehand smash shots played by badminton players † (Krishnaram N, Ahamed J, Sathyamoorthy N, Sandaruwan KD & Athapaththu AMKB) **52**: 125-142 (2024)

**Maleic anhydride**

Synthesis and characterization of biocomposite of bovine bone- based hydroxyapatite-poly (lactic acid)-maleic anhydride (Keerthana J, Hewavitharana KHIK & Wijesekara KB) **52**: 271-279 (2024)

**Manufacturing process**

The modified control charts for monitoring the error detection of process control under different estimators (Azam Zaka, Riffat Jabeen, Amirah Saeed Alharthi & Hassan M. Aljohani) **52**: 17-34 (2024)

**Mass-spring models**

Simplification of large-scale solid element model for seismic structural response analysis of buildings (Rathnasiri SC, Jayasinghe JASC & Dammika AJ) **52**: 469-480 (2024)

**Mathematical model**

Skeletal point analysis to determine the accuracy of forehand smash shots played by badminton players † (Krishnaram N, Ahamed J, Sathyamoorthy N, Sandaruwan KD & Athapaththu AMKB) **52**: 125-142 (2024)

**Maximum likelihood**

Maximum likelihood estimation for the two-parameter Maxwell distribution (Kasap P & Faouri AO) **52**: 441-458 (2024)

**MCNP**

Optimal fissile distribution in multiplying systems: Illustrative examples with Monte Carlo simulation and Pontryagin's maximum principle (Khan H, Aziz U, Koreshi ZU & Sheikh SR) **52**: 69-80 (2024)

**Meat**

Decadal trends in antimicrobial susceptibility of Escherichia coli and Salmonella spp. in chicken from small-scale farm shops in Kandy district, Sri Lanka (Thilakarathne DS, Gamage BYI, Kottawatta KSA, Abayawansa KGR, Kalupahana RS & Gunawardana WSN) **52**: 419-433 (2024)

**Mediapipe**

Skeletal point analysis to determine the accuracy of forehand smash shots played by badminton players † (Krishnaram N, Ahamed J, Sathyamoorthy N, Sandaruwan KD & Athapaththu AMKB) **52**: 125-142 (2024)

**Meta-heuristic**

Meta-heuristic method to schedule vehicle routing with moving shipments at the cross-docking facility (Gnanapragasam SR & Daundasekera WB) **52**: 169-181 (2024)

**Meta-modeling**

Simplification of large-scale solid element model for seismic structural response analysis of buildings (Rathnasiri SC, Jayasinghe JASC & Dammika AJ) **52**: 469-480 (2024)

**Microstructure characteristics**

The microstructure and the behaviour of low organic clayey soils in Sri Lanka (Wang Y, Vidurapriya D, Qin X & Thilakasiri S) **52**: 45-58 (2024)

**Migraine**

Structural brain network topology in migraine vs. healthy subjects: A graph theory study (Amarasinghe ADI, Wijewickrama DIH, De Fonseka IS, Lawanya MAD, Fernando WNS, Wishwanthi DAD, Senanayake G, Pushpakumara S & Ediri Arachchi WM) **52**: 321-330 (2024)

**Milk fat**

A preliminary study on milk composition of three buffalo breeds located in Polonnaruwa, Sri Lanka (Gunathilake SP, Gayanjalee DA, Prathiraja DAS, Buddhika PRM, Weerathilake WADV & Rasika DMD) **52**: 103-111 (2024)

**Milk protein**

A preliminary study on milk composition of three buffalo breeds located in Polonnaruwa, Sri Lanka (Gunathilake SP, Gayanjalee DA, Prathiraja DAS, Buddhika PRM, Weerathilake WADV & Rasika DMD) **52:** 103-111 (2024)

**Minimum critical mass**

Optimal fissile distribution in multiplying systems: Illustrative examples with Monte Carlo simulation and Pontryagin's maximum principle (Khan H, Aziz U, Koreshi ZU & Sheikh SR) **52:** 69-80 (2024)

**Mitochondrial gene**

Russell's viper (*Daboia russelii*) in the Jaffna peninsula, Sri Lanka bears signatures of incipient genetic divergence from the South Indian population (Abeyaweera ND, Sivaruban A, Muruganathan A & Amarasinghe KP) **52:** 199-214 (2024)

**Modified maximum likelihood estimator**

The modified control charts for monitoring the error detection of process control under different estimators (Azam Zaka, Riffat Jabeen, Amirah Saeed Alharthi & Hassan M. Aljohani) **52:** 17-34 (2024)

**Molecular screening**

Influence of cultivar selection on blast and brown spot diseases in rice: Molecular screening of blast resistance genes (Terensan S, Weerasena OVDSJ, Kottearachchi NS, Silva JN & Fernando HNS) **52:** 343-358 (2024)  
monocarboxylic acids (Sarkarai D & Desikan K) **52:** 311-320 (2024)

**Monocarboxylic acids**

Computational analysis of diameter eccentricity based and hyper diameter eccentricity based indices for linear saturated monocarboxylic acids (Sarkarai D & Desikan K) **52:** 311-320 (2024)

**Monte Carlo simulation**

Maximum likelihood estimation for the two-parameter Maxwell distribution (Kasap P & Faouri AO) **52:** 441-458 (2024)

**MoveNet**

Athlete body power and strength estimation using skeleton point cloud (Rangala H, Samaraweera S, Sandaruwan KD, Weerasinghe TA & Ranasinghe DC) **52:** 481-492 (2024)

**Moving shipments**

Meta-heuristic method to schedule vehicle routing with moving shipments at the cross-docking facility (Gnanapragasam SR & Daundasekera WB) **52:** 169-181 (2024)

**MtDNA**

Russell's viper (*Daboia russelii*) in the Jaffna peninsula, Sri Lanka bears signatures of incipient genetic divergence from the South Indian population (Abeyaweera ND, Sivaruban A, Muruganathan A & Amarasinghe KP) **52:** 199-214 (2024)

**Multiple imputation**

Comparison of methods for handling outliers in Cox regression model (Alkan N, Pardo MC & Alkan BB) **52:** 59-68 (2024)

**Murrah**

A preliminary study on milk composition of three buffalo breeds located in Polonnaruwa, Sri Lanka (Gunathilake SP, Gayanjalee DA, Prathiraja DAS, Buddhika PRM, Weerathilake WADV & Rasika DMD) **52:** 103-111 (2024)

**Near-infrared spectroscopy**

Predicting water content in engine oil using SPA-ISSA-BP methods (Chen Bin, Quan YuXuan, Liu Ge, Li JianZhong, Nie GaoXing, Zhang YongChang, Shan ChenZe, Chen JunSen, Chen Rui, Chen Xi and Zhang MengWei) **52:** 359-370 (2024)

**Nematode diversity**

Prevalence and abundance of plant-parasitic nematodes associated with corn (*Zea mays* L.) in Anuradhapura, Sri Lanka (Thiruchelvan N, Casonato S, Mikunthan G, Condrón LM, Moukarze R & Kularathna M) **52:** 299-309 (2024)

**Neural network**

Predicting water content in engine oil using SPA-ISSA-BP methods (Chen Bin, Quan YuXuan, Liu Ge, Li JianZhong, Nie GaoXing, Zhang YongChang, Shan ChenZe, Chen JunSen, Chen Rui, Chen Xi and Zhang MengWei) **52:** 359-370 (2024)

**Neural network**

Two level neuro-functional forecaster: A novel dynamic hybridization for functional data forecasting (Deshani KAD, Attygalle DT & Hansen LL) **52:** 81-91 (2024)

**Neuroimaging**

Structural brain network topology in migraine vs. healthy subjects: A graph theory study (Amarasinghe ADI, Wijewickrama DIH, De Fonseka IS, Lawanya MAD, Fernando WNS, Wishwanthi DAD, Senanayake G, Pushpakumara S & Ediri Arachchi WM) **52:** 321-330 (2024)

**Nili-Ravi**

A preliminary study on milk composition of three buffalo breeds located in Polonnaruwa, Sri Lanka (Gunathilake SP, Gayanjalee DA, Prathiraja DAS, Buddhika PRM, Weerathilake WADV & Rasika DMD) **52**: 103-111 (2024)

**Noise level**

Determination of noise level and acoustic analysis of toys for children in Sri Lanka market (Kalansuriya CM, Weerasingha RM, Jayaratne DC & Darshana KKN) **52**: 191-197 (2024)

**Optical buffering**

An efficient and improved algorithm for generating an equivalent planar architecture of the data vortex switch (Soni A & Sharma N) **52**: 401-412 (2024)

**Optical interconnections**

An efficient and improved algorithm for generating an equivalent planar architecture of the data vortex switch (Soni A & Sharma N) **52**: 401-412 (2024)

**Optical packet switching**

An efficient and improved algorithm for generating an equivalent planar architecture of the data vortex switch (Soni A & Sharma N) **52**: 401-412 (2024) **52**: 401-412 (2024)

**Organic soils**

The microstructure and the behaviour of low organic clayey soils in Sri Lanka (Wang Y, Vidurapriya D, Qin X & Thilakasiri S) **52**: 45-58 (2024)

**Outliers**

Comparison of methods for handling outliers in Cox regression model (Alkan N, Pardo MC & Alkan BB) **52**: 59-68 (2024)

**panel ARDL**

Impact of climate on tea yield: an empirical investigation from Sri Lanka (Jayasinghe-Mudalige UK, Wijeratne M, Kuruppu V, Jayathilake C, Wijesuriya W, Somarathna K, Karunaratne S, Jayawardana S, Gunathilaka D & Balasooriya D) **52**: 183-190 (2024)

**Particle packing optimization**

Proposed mix design improvements of compressed stabilized earth blocks (CSEB) with particle packing optimization and coir Reinforcement (Malkanathi SN, Sathsara K GK, Dharmaratne PD & Galabada H) **52**: 159-167 (2024)

**Path analysis**

Path coefficient analysis using traditional and improved rice genotypes for trait effect on grain yield (Shyamalee HAPA & Ranawake AL) **52**: 931-102 (2024)

**PCR**

Establishment and evaluation of real time PCR based SELEX platform for the identification of protein binding aptamers: A pilot study in Sri Lanka (Abeykoon AI, Kumarasinghe KMN, Chandrasekharan NV & Wickramasinghe PMTB) **52**: 493-500 (2024)

**Peat**

The microstructure and the behaviour of low organic clayey soils in Sri Lanka (Wang Y, Vidurapriya D, Qin X & Thilakasiri S) **52**: 45-58 (2024)

**Percentile estimator**

The modified control charts for monitoring the error detection of process control under different estimators (Azam Zaka, Riffat Jabeen, Amirah Saeed Alharthi & Hassan M. Aljohani) **52**: 17-34 (2024)

**Phylogeny**

Russell's viper (*Daboia russelii*) in the Jaffna peninsula, Sri Lanka bears signatures of incipient genetic divergence from the South Indian population (Abeyaweera ND, Sivaruban A, Murugananthan A & Amarasinghe KP) **52**: 199-214 (2024)

**Plant dominance**

Estimating plant dominance using field-measured structural parameters and remotely sensed data; A case study from Rekawa mangrove forest, southern coast of Sri Lanka (Samarakoon SMTM, Madarasinghe SK, Thilakarathne NDSD, Bandularathne AMNN, Wijayathilaka HD & Kodikara KAS) **52**: 459-468 (2024)

**Plant-parasitic nematodes**

Prevalence and abundance of plant-parasitic nematodes associated with corn (*Zea mays* L.) in Anuradhapura, Sri Lanka (Thiruchelvan N, Casonato S, Mikunthan G, Condrón LM, Moukarze R & Kularathna M) **52**: 299-309 (2024)

**Poly (lactic acid)**

Synthesis and characterization of biocomposite of bovine bone- based hydroxyapatite-poly (lactic acid)-maleic anhydride (Keerthana J, Hewavitharana KHIK & Wijesekara KB) **52**: 271-279 (2024)

**Pontryagin maximum**

Optimal fissile distribution in multiplying systems: Illustrative examples with Monte Carlo simulation and Pontryagin's maximum principle (Khan H, Aziz U, Koreshi ZU & Sheikh SR) **52**: 69-80 (2024)

**Pratylenchus**

Prevalence and abundance of plant-parasitic nematodes associated with corn (*Zea mays* L.) in Anuradhapura, Sri Lanka (Thiruchelvan N, Casonato S, Mikunthan G, Condron LM, Moukarze R & Kularathna M) **52**: 209-309 (2024)

**Primary open angle glaucoma**

Prevalence and in silico analysis of p.D658G variant of WDR36 gene in patients affected with primary open angle glaucoma from Punjab Pakistan (Khazema Yousaf, Zernish Shabbir, Rasheeda Bashir, Syed Mohsin Raza, Saiqa Ilyas and Rukhama Haq) **52**: 35-44 (2024)

**Principle**

Optimal fissile distribution in multiplying systems: Illustrative examples with Monte Carlo simulation and Pontryagin's maximum principle (Khan H, Aziz U, Koreshi ZU & Sheikh SR) **52**: 69-80 (2024)

**Privacy-preserving**

Enhanced privacy-preserving federated convivial learning for internet of medical things (IoMT) through blockchain-enabled trust Q-learning (Sudharson K, Babu G, Santhiya R & Anita CS) **52**: 501-514 (2024)

**Protein binding aptamers**

Establishment and evaluation of real time PCR based SELEX platform for the identification of protein binding aptamers: A pilot study in Sri Lanka (Abeykoon AI, Kumarasinghe KMN, Chandrasekharan NV & Wickramasinghe PMTB) **52**: 493-500 (2024)

**QSPR**

Computational analysis of diameter eccentricity based and hyper diameter eccentricity based indices for linear saturated

**Radius**

Computational analysis of diameter eccentricity based and hyper diameter eccentricity based indices for linear saturated monocarboxylic acids (Sarkarai D & Desikan K) **52**: 311-320 (2024)

**Rainfall**

Impact of climate on tea yield: an empirical investigation from Sri Lanka (Jayasinghe-Mudalige UK, Wijeratne M, Kuruppu V, Jayathilake C, Wijesuriya W, Somarathna K, Karunaratne S, Jayawardana S, Gunathilaka D & Balasooriya D) **52**: 183-190 (2024)

**Ramsey critical graphs**

All Ramsey critical graphs for large cycles vs a complete graph of order six (Jayawardene CJ, Navaratna WCW & Senadheera JN) **52**: 113-123 (2024)

**Ramsey theory**

All Ramsey critical graphs for large cycles vs a complete graph of order six (Jayawardene CJ, Navaratna WCW & Senadheera JN) **52**: 113-123 (2024)

**Reflected power function distribution**

The modified control charts for monitoring the error detection of process control under different estimators (Azam Zaka, Riffat Jabeen, Amirah Saeed Alharthi & Hassan M. Aljohani) **52**: 17-34 (2024)

Reinforcement (Malkanathi SN, Sathsara KKG, Dharmaratne PD & Galabada H) **52**: 159-167 (2024)

**Rekawa mangrove forest**

Estimating plant dominance using field-measured structural parameters and remotely sensed data; A case study from Rekawa mangrove forest, southern coast of Sri Lanka (Samarakoon SMTM, Madarasinghe SK, Thilakarathne NDSD, Bandularathne AMNN, Wijayathilaka HD & Kodikara KAS) **52**: 459-468 (2024)

**Remote sensing**

Estimating plant dominance using field-measured structural parameters and remotely sensed data; A case study from Rekawa mangrove forest, southern coast of Sri Lanka (Samarakoon SMTM, Madarasinghe SK, Thilakarathne NDSD, Bandularathne AMNN, Wijayathilaka HD & Kodikara KAS) **52**: 459-468 (2024)

**Resistance**

Decadal trends in antimicrobial susceptibility of *Escherichia coli* and *Salmonella* spp. in chicken from small-scale farm shops in Kandy district, Sri Lanka (Thilakarathne DS, Gamage BYI, Kottawatta KSA, Abayawansa KGR, Kalupahana RS & Gunawardana WSN) **52**: 419-433 (2024)

**Rice cultivars**

Influence of cultivar selection on blast and brown spot diseases in rice: Molecular screening of blast resistance genes (Terensan S, Weerasena OVDSJ, Kottearachchi NS, Silva JN & Fernando HNS) **52**: 343-358 (2024)

**Robust Cox regression**

Comparison of methods for handling outliers in Cox regression model (Alkan N, Pardo MC & Alkan BB) **52**: 59-68 (2024)

**Salmonella spp.**

Decadal trends in antimicrobial susceptibility of Escherichia coli and Salmonella spp. in chicken from small-scale farm shops in Kandy district, Sri Lanka (Thilakarathne DS, Gamage BYI, Kottawatta KSA, Abayawansa KGR, Kalupahana RS & Gunawardana WSN) **52**: 419-433 (2024)

**Seismic structural response analysis**

Simplification of large-scale solid element model for seismic structural response analysis of buildings (Rathnasiri SC, Jayasinghe JASC & Dammika AJ) **52**: 469-480 (2024)

**SELEX platform**

Establishment and evaluation of real time PCR based SELEX platform for the identification of protein binding aptamers: A pilot study in Sri Lanka (Abeykoon AI, Kumarasinghe KMN, Chandrasekharan NV & Wickramasinghe PMTB) **52**: 493-500 (2024)

**SEM**

Quantifying the relationship between uniaxial compressive strength and slake durability index in gneiss rocks: an experimental approach (Kanagasundaram G, Dassanayake ABN, Jayawardena CL & Chaminda SP) **52**: 243-255 (2024)

**Shift cipher**

Symmetric encryption using snake graphs and supermagic covering (Ranasinghe R, Bandara RMVV & Athapaththu AMSLK) **52**: 435-440 (2024)

**Shot analysis**

Skeletal point analysis to determine the accuracy of forehand smash shots played by badminton players † (Krishnaram N, Ahamed J, Sathyamoorthy N, Sandaruwan KD & Athapaththu AMKB) **52**: 125-142 (2024)

**Skeleton point cloud**

Athlete body power and strength estimation using skeleton point cloud (Rangala H, Samaraweera S, Sandaruwan KD, Weerasinghe TA & Ranasinghe DC) **52**: 481-492 (2024)

**Skeleton points**

Evaluation of Taekwondo Poomsae movements using skeleton points † (Fernando M, Sandaruwan KD & Athapaththu AMKB) **52**: 143-156 (2024)

**Slake durability index**

Quantifying the relationship between uniaxial compressive strength and slake durability index in gneiss rocks: an experimental approach (Kanagasundaram G, Dassanayake ABN, Jayawardena CL & Chaminda SP) **52**: 243-255 (2024)

**Snake vertex labeling**

Symmetric encryption using snake graphs and supermagic covering (Ranasinghe R, Bandara RMVV & Athapaththu AMSLK) **52**: 435-440 (2024)

**Sol-gel method**

Effective removal of Pb(II) ions using Fe<sub>3</sub>O<sub>4</sub>/MgO adsorbent: A comprehensive study (Gurunanthanan V, Wijayarathne KB, Dassanayake BS, Mantilaka PG & Perera CS) **52**: 385-400 (2024)

**Sparrow search algorithm**

Predicting water content in engine oil using SPA-ISSA-BP methods (Chen Bin, Quan YuXuan, Liu Ge, Li JianZhong, Nie GaoXing, Zhang YongChang, Shan ChenZe, Chen JunSen, Chen Rui, Chen Xi and Zhang MengWei) **52**: 359-370 (2024)

**speaker recognition**

Construction of an effective telephone bandwidth specifically for speaker recognition (Thiruvaran T) **52**: 283-298 (2024)

**speaker specific information**

Construction of an effective telephone bandwidth specifically for speaker recognition (Thiruvaran T) **52**: 283-298 (2024)

**speech intelligibility**

Construction of an effective telephone bandwidth specifically for speaker recognition (Thiruvaran T) **52**: 283-298 (2024)

**Squat jump**

Athlete body power and strength estimation using skeleton point cloud (Rangala H, Samaraweera S, Sandaruwan KD, Weerasinghe TA & Ranasinghe DC) **52**: 481-492 (2024)

**Sri Lanka**

Impact of climate on tea yield: an empirical investigation from Sri Lanka (Jayasinghe-Mudalige UK, Wijeratne M, Kuruppu V, Jayathilake C, Wijesuriya W, Somarathna K, Karunaratne S, Jayawardana S, Gunathilaka D & Balasooriya D) **52**: 183-190 (2024)

**Sri Lanka market**

Determination of noise level and acoustic analysis of toys for children in Sri Lanka market (Kalansuriya CM, Weerasingha RM, Jayaratne DC & Darshana KKN) **52**: 191-197 (2024)

**Sri Lanka**

Prevalence and abundance of plant-parasitic nematodes associated with corn (*Zea mays* L.) in Anuradhapura, Sri Lanka (Thiruchelvan N, Casonato S, Mikunthan G, Condron LM, Moukarze R & Kularathna M) **52**: 299-309 (2024)

**Sri Lanka**

Variation in plant morphology and leaf essential oil composition of a representative *Cinnamomum verum* collection from Sri Lanka† (Prathibhani MR, Azad R, Ranaweera S, Jayasekara L, Ranawaka RAAK, Senanayake G, Abeynayake S & Geekiyanage S) **52**: 3-16 (2024)

**Structural mechanics**

Simplification of large-scale solid element model for seismic structural response analysis of buildings (Rathnasiri SC, Jayasinghe JASC & Dammika AJ) **52**: 469-480 (2024)

**structural networks**

Structural brain network topology in migraine vs. healthy subjects: A graph theory study (Amarasinghe ADI, Wijewickrama DIH, De Fonseka IS, Lawanya MAD, Fernando WNS, Wishwanthi DAD, Senanayake G, Pushpakumara S & Ediri Arachchi WM) **52**: 321-330 (2024)

**Supercapacitor**

An electrical double-layer supercapacitor based on a biomass- activated charcoal electrode and ionic liquid with excellent charge-discharge cycle stability (Kumara GRA, Medagedara ADT, Gadiarachchi HW, Karunaratne DGBC, Tennakone K, Rajapakse RMG & Bandara TMWJ) **52**: 331-341 (2024)

**Supermagic Covering**

Symmetric encryption using snake graphs and supermagic covering (Ranasinghe R, Bandara RMVV & Athapaththu AMSLK) **52**: 435-440 (2024)

**Superparamagnetic behaviour**

Effective removal of Pb(II) ions using Fe<sub>3</sub>O<sub>4</sub>/MgO adsorbent: A comprehensive study (Gurunathanan V, Wijayarathne KB, Dassanayake BS, Mantilaka PG & Perera CS) **52**: 385-400 (2024)

**Sustainable insulation materials**

Optimizing the alkaline concentration for coir fibre treatment and estimation of lifetime (Chamath LG, Srimal LKT, Sewvandi GA, Gallage R & Epaarachchi J) **52**: 515-525 (2024)

**Taekwondo**

Evaluation of Taekwondo Poomsae movements using skeleton points † (Fernando M, Sandaruwan KD & Athapaththu AMKB) **52**: 143-156 (2024)

**Tea cultivation**

Impact of climate on tea yield: an empirical investigation from Sri Lanka (Jayasinghe-Mudalige UK, Wijeratne M, Kuruppu V, Jayathilake C, Wijesuriya W, Somarathna K, Karunaratne S, Jayawardana S, Gunathilaka D & Balasooriya D) **52**: 183-190 (2024)

**Temperature**

Impact of climate on tea yield: an empirical investigation from Sri Lanka (Jayasinghe-Mudalige UK, Wijeratne M, Kuruppu V, Jayathilake C, Wijesuriya W, Somarathna K, Karunaratne S, Jayawardana S, Gunathilaka D & Balasooriya D) **52**: 183-190 (2024)

**Thermal loads**

Thermal performance of glass facade under fire loading: a numerical approach (Perera RGSS, Ruwanmali JHA, Thevega T, Jayasinghe JASC, Bandara CS & Dammika AJ) **52**: 229-241 (2024)

**Toys for children**

Determination of noise level and acoustic analysis of toys for children in Sri Lanka market (Kalansuriya CM, Weerasingha RM, Jayaratne DC & Darshana KKN) **52**: 191-197 (2024)

**Toys noise**

Determination of noise level and acoustic analysis of toys for children in Sri Lanka market (Kalansuriya CM, Weerasingha RM, Jayaratne DC & Darshana KKN) **52**: 191-197 (2024)

**Traditional rice**

Path coefficient analysis using traditional and improved rice genotypes for trait effect on grain yield (Shyamalee HAPA & Ranawake AL) **52**: 931-102 (2024)

**Triethylammonium thiocyanate**

An electrical double-layer supercapacitor based on a biomass- activated charcoal electrode and ionic liquid with excellent charge-discharge cycle stability (Kumara GRA, Medagedara ADT, Gadiarachchi HW, Karunaratne DGBC, Tennakone K, Rajapakse RMG & Bandara TMWJ) **52**: 331-341 (2024)

**Two-parameter Maxwell distribution**

Maximum likelihood estimation for the two-parameter Maxwell distribution (Kasap P & Faouri AO) **52:** 441-458 (2024)

**UCS**

Quantifying the relationship between uniaxial compressive strength and slake durability index in gneiss rocks: an experimental approach (Kanagasundaram G, Dassanayake ABN, Jayawardena CL & Chaminda SP) **52:** 243-255 (2024)

**Underwater images**

Unveiling the depths of underwater image enhancement with spatial blended CNN: Diving into clarity (Priyadharshi RA, Arivazhagan S & Ramajeyam K) **52:** 527-540 (2024)

**Vehicle routing**

Meta-heuristic method to schedule vehicle routing with moving shipments at the cross-docking facility (Gnanapragasam SR & Daundasekera WB) **52:** 169-181 (2024)

**Video classification**

Evaluation of Taekwondo Poomsae movements using skeleton points † (Fernando M, Sandaruwan KD & Athapaththu AMKB) **52:** 143-156 (2024)

**Viperidae**

Russell's viper (*Daboia russelii*) in the Jaffna peninsula, Sri Lanka bears signatures of incipient genetic divergence from the South Indian population (Abeyaweera ND, Sivaruban A, Murugananthan A & Amarasinghe KP) **52:** 199-214 (2024)

**Viperinae**

Russell's viper (*Daboia russelii*) in the Jaffna peninsula, Sri Lanka bears signatures of incipient genetic divergence from the South Indian population (Abeyaweera ND, Sivaruban **52:** 215-227 (2024)

**Water content**

Predicting water content in engine oil using SPA-ISSA-BP methods (Chen Bin, Quan YuXuan, Liu Ge, Li JianZhong, Nie GaoXing, Zhang YongChang, Shan ChenZe, Chen JunSen, Chen Rui, Chen Xi and Zhang MengWei) **52:** 359-370 (2024)

**WD repeat domain 36**

Prevalence and in silico analysis of p.D658G variant of WDR36 gene in patients affected with primary open angle glaucoma from Punjab Pakistan (Khazeema Yousaf, Zernish Shabbir, Rasheeda Bashir, Syed Mohsin Raza, Saiqa Ilyas and Rukhama Haq) **52:** 35-44 (2024)

**Wheel graph**

Symmetric encryption using snake graphs and supermagic covering (Ranasinghe R, Bandara RMVV & Athapaththu AMSLK) **52:** 435-440 (2024)

**Zea mays (maize)**

Prevalence and abundance of plant-parasitic nematodes associated with corn (*Zea mays* L.) in Anuradhapura, Sri Lanka (Thiruchelvan N, Casonato S, Mikunthan G, Condrón LM, Moukarze R & Kularathna M) **52:** 299-309 (2024)





# JOURNAL OF THE NATIONAL SCIENCE FOUNDATION OF SRI LANKA

## GUIDANCE TO CONTRIBUTORS

### GENERAL INFORMATION

#### Scope

The Journal of the National Science Foundation of Sri Lanka publishes the results of research in all aspects of Science and Technology. It is open for publication of Research Articles, Reviews, Research Communications and Correspondence.

#### IT related and other non-empirical articles

The JNSF is a journal primarily devoted to natural sciences. It also considers for publication significant and novel contributions from formal sciences. Authors of emerging sub-disciplines of Computing and related areas such as Machine Learning, Artificial Intelligence and Data Sciences are requested to carefully adhere to the following guidelines when submitting manuscripts for this journal.

- Clear formulation of outcome-oriented **Research Objective/s** for targeted knowledge (sub)domain/s or (sub)discipline/s.
- Selection and comprehensive summarization of **appropriate Research Method/s** adopted to achieve the stated Research Objective/s.
- Reporting a sound (**Empirical**) **Evaluation** of the research finding/s thereby arguing reliability, validity, and generalizability of research claim/s.

#### Categories of manuscripts

**Research Articles:** Research Articles are papers that present complete descriptions of original research. Research Articles should include an Abstract, Keywords, Introduction, Methodology, Results and Discussion, Conclusion and Recommendations where relevant. References should be prepared according to the "Guidelines for the preparation of manuscripts". Maximum length of the article should be limited to 30 pages with a word count less than 10,000 including references, figures and tables. Any articles above this limit will be returned. Please refer author guidelines for further details (<https://jnsfsl.sljol.info/about/submissions#author-guidelines>)

**Reviews:** Reviews are critical presentations on selected topics of Science or Technology. They should be well focused and organized and avoid general "textbook" style. As reviews are intended to be critical presentations on selected topics, the author (or the principal author in a multi-author review) need to have had substantial leadership in research supported by a publication track record in the areas covered by the review. A person/s wishing to submit a Review Article should obtain prior approval from the Editorial Board by submitting a concise summary of the intended article, along with a list of the author's publications in the related area ([jnsf@nsf.gov.lk](mailto:jnsf@nsf.gov.lk)). Maximum length of the article should be limited to 40 pages with a word count of 12,000 including references, figures and tables. Any articles beyond this limit will be returned.

**Research Communications:** Research Communications are intended to communicate important new findings in a specific area of limited scope that are worthy of rapid dissemination among the scientific community. Authors are required to provide a statement justifying the suitability of the submission for a Research Communication. The article should include an Abstract, Keywords, Introduction, Methodology, Results & Discussion, Conclusion and References. Maximum length of the article should be limited to 10 pages with a word count of 2,500 including references, figures and tables. Any articles beyond this limit will be returned.

**Correspondence:** Correspondence will be accepted regarding one or more articles in the preceding four issues of the Journal, as well as Letters to the Editor. Articles covering important scientific events or any other news of interest to scientists, reviews of books of scientific nature, articles presenting views on issues related to science and scientific activity will also be considered. Publication will be made at the discretion of the Editor-in-Chief. Maximum length of the article should be limited to 05 pages with a word count of 1,500 including references, figures and tables. Any articles beyond this limit will be returned.

### SUBMISSION OF MANUSCRIPT

Authors submitting articles to the JNSF should first create an account in the Sri Lanka Journals Online System (<https://jnsfsl.sljol.info/>). All manuscripts should be in MS Word format and must be submitted to the journal's online platform at <https://jnsfsl.sljol.info/submit/start/>. Submissions *via* emails are not encouraged. Please make sure that **no** author information is mentioned in the article submitted. Complete names and details of affiliations of all authors must be fed into the system during the online submission process. Authors are required to provide their personal, validated ORCID ID (by obtaining an ORCID ID from <https://orcid.org/>) when submitting the manuscript. No change to the authors or order of authors will be accepted after the submission. All those who have made significant contributions should be listed as co-authors. The corresponding author should ensure that all contributing co-authors are included in the author list and have approved the final version of the paper and have agreed to its submission for publication.

All submissions should be in English. If the manuscript conforms to the guidelines specified, the date received will be the date that the manuscript was submitted to the online system.

Submissions are accepted for processing on the understanding that they will be reviewed and that they have not been submitted for publication elsewhere (including publication as a full paper or extended abstract as a part of Conference Proceedings).

#### Articles deposited in pre-print repositories

Authors should agree to remove the manuscript from the pre-print repositories if the article is accepted for publication in the JNSF.

### **Suggesting potential reviewers by authors**

The authors are requested to suggest three names of referees when submitting their manuscript, in the Cover Letter space provided at the bottom of the page in the first stage of online submission. Referees should not be from the institution where the work was carried out and should not have been co-authors in previous publications. The address, institutional affiliation and e-mail of the suggested referees should be provided. Please note that the JNSF is not bound to select all or any of the suggested referees for sending the manuscript for reviewing

### **Authorship**

All authors designated as authors should be eligible for authorship. Those who have made a substantial contribution to the concept or design of the work; or acquisition, analysis or interpretation of data are recognized as Authors.

The corresponding author should be prompt and ensure adherence to timelines when responding to requests, queries and recommendation of reviewers conveyed by or on behalf of the Editor-in Chief and Editorial Board.

### **Supplementary materials**

Any experimental data necessary to evaluate the claims made in the paper but not included in the paper should be provided as supplementary materials. Supplementary materials will be sent to the reviewers and published online with the manuscript if accepted. The supplementary materials should conform to Journal guidelines and should be uploaded as separate files. Authors should number Supplementary Tables and Figures as, for example, 'Supplementary Table S1'. Refer to each piece of supplementary material at the appropriate point(s) in the main article. Supplementary Materials may include description of the materials and methods, controls, or tabulated data presented in Tables or Figures, and programming codes.

### **Peer review**

The manuscripts submitted to the JNSF will initially be screened by the Editorial Board and, if suitable, will be referred to at least two subject experts in the relevant field. The peer-review process of the JNSF is double-blind.

When revision of a manuscript has been requested, the revised manuscript should be submitted on or before the stated deadline. The authors' response to the comments of referees should be tabulated with the comment and response. The decision of the Editorial Board shall be final.

Accepted papers are subject to editing. The date of acceptance will be the date the Editorial Board accept the paper for publication.

### **Article processing fee**

Article processing fee of US\$ 250 will be levied for each manuscript in two stages, except when the corresponding author is affiliated with a Sri Lankan institution,

- An initial processing fee of US\$ 20 will be levied for each manuscript at the peer-review stage.
- The remaining US\$ 230 will be charged for accepted articles at the time of publication.

Payments can be made online via NSF Payment Portal (<http://pg.nsf.gov.lk/>)

### **Authors' declaration**

The authors are required to accept the conditions indicated in the online author declaration statement.

### **Copyright**

Articles in JNSF are published under the Creative Commons License CC-BY-ND. This license permits use, distribution and reproduction of articles for commercial and non-commercial purposes, provided that the original work is properly cited and is not changed in anyway. The copyright of the article is with the National Science Foundation of Sri Lanka. Therefore, authors are requested to check with institution's copyright and publication policy before submitting an article to the JNSF. Authors secure the right to reproduce any material that has already been published or copyrighted elsewhere. When an article is accepted for publication, the authors are required to submit the Transfer of Copyright document signed by all the authors.

### **Post-publication corrections**

The Editorial Board reserves the right to take action on publishing an erratum or corrigendum. If serious errors are identified in a published article, the Journal may consider a retraction or publishing a correction.

## **STRUCTURE OF MANUSCRIPT**

### **Manuscript**

The manuscript should be free of errors and prepared in single column, using double-spaced text of Times New Roman 12 font leaving 1 inch margins. Pages should be numbered consecutively.

#### **a. Style**

The paper should be written clearly and concisely. The style of writing should conform to scholarly writing. Slang, jargon, unauthorized abbreviations, abbreviated phrases should not be used. In general, the impersonal form should be used. Poor usage of language will result in rejection of the manuscript during initial screening.

#### **b. Layout**

Manuscripts other than review articles should be generally organized as follows: Title, Abstract, Keywords, Introduction, Methodology, Results and Discussion, Conclusions and Recommendations (where relevant), Acknowledgements and References. Pages should be arranged in the following order:

**First page** should include the title of the manuscript. **Author information should not be mentioned anywhere in the manuscripts.** Any statement (including acknowledgment) which can reveal author identity should be removed. If a major part of the research has been published as an abstract in conference proceedings, it should be mentioned with citation in the space provided for "Comments for Editor". Authors must also indicate the **general and specific research area** of the manuscript in the title page.

**Title:** Should accurately and concisely reflect the contents of the article.

**Running title:** Should be a shortened title (limited to a maximum of 50 characters) that could be printed at the top of every other page of the Journal article.

**Abstract:** Should be between 200 - 250 for research articles and 200 - 300 for reviews. It should not contain any references and should be able to stand on its own. It should outline objectives and methodology together with important results and conclusions.

**Keywords:** Include a maximum of six keywords, which may include the names of organisms (common or scientific), methods or other important words or phrases specific to the study.

**Introduction:** This should state the reasons for performing the work with a brief review of related research studies in the context of the work described in the paper. Objectives of the study should be clearly stated.

**Materials and Methods:** This section should give the details of how you conducted your study. New methods may be described in detail with an indication of their limitations. Established methods can be mentioned with appropriate references. Sufficient details should be included to allow direct repetition of the work by others. Where human subjects are involved, they should be referred to by numbers or fictitious names. A paper reporting the results of investigations on human subjects or on animals must include a statement to the effect that the relevant national or other administrative and ethical guidelines have been adhered to, and a copy of the ethical clearance certificate should be submitted. Methods of statistical analyses used should be mentioned where relevant.

#### **Results and Discussion**

Results: the results should be concisely and logically presented. Repetition of the same results in figures, tables or text should be avoided. Discussion: data essential for the conclusions emerging from the study should be discussed. Long, rambling discussions should be avoided. The discussion should deal with the interpretation of results. It should logically relate new findings to earlier ones. Unqualified statements and conclusions not completely supported by data should be avoided.

Molecular sequence data, such as gene or rDNA sequences, genome sequences, metagenomic sequences etc. must be deposited in a public molecular sequence repository, such as GenBank, that is part of the International Nucleotide Sequence Database Collaboration (INSDC). The accession numbers obtained must be cited in the text, Table or on Figures of phylogenetic trees of the manuscript.

**Conclusion:** The conclusion should be brief, highlight the outcomes of the study and should be aligned with the objectives of the study. It should not contain references.

**Competing Interest statement:** The authors should include a statement on conflict of interest disclosing any financial or other substantive conflicts of interest that may influence the results or interpretation of the research in the space provided in the online article submission form. All sources of financial support for the project should also be disclosed.

**Acknowledgement:** Should be brief and made for specific scientific, financial and technical assistance only. If a significant part of the research was performed in an institution other than the authors' affiliations should be acknowledged. All those who have made substantial contribution to the research but do not qualify to be authors should be acknowledged.

#### **References :**

The JNSF uses APA ( 7<sup>th</sup> Edition) reference style

All research work of other authors, when used or referred to or cited, should be correctly acknowledged in the text and in the References.

All the references in the text should be in the list and vice versa

Citing references in the text:

- References to the literature must be indicated in the text and tables as per the Author-Year System, by the author's last name and year, in parenthesis (i.e. Able, 1997) or (Able & Thompson, 1998).
- Citation to work by more than two authors should be abbreviated with the use of et al. (i.e. Able *et al.*, 1997).
- Multiple publications by the same first author in the same year should be coded by letters, (i.e. Thompson, 1991a, 1991b, 1992, 1993).
- Multiple citations of different authors should be made in chronological order and separated by a semicolon, (i.e. Zimmerman *et al.*, 1986; Able *et al.*, 1997).

Citing references in the List of references:

- The list of References should be arranged in alphabetical order based on the last name of the first author.
- In APA 7th ed., **up to 20 authors** should be included in a reference list entry. Write out the last name and first initial(s) for each contributor.

#### **Example for 2–20 authors:**

Wright, A., Komal, G., Siddharth, D., Boyd, G., Cayson, N., Beverley, K., Travers, K., Begum, A., Redmond, M., Mills, M., Cherry, D., Finley, B., Fox, M., Ferry, F., Almond, B., Howell, E., Gould, T., Berger, B., Bostock, T., & Fountain, A. (2020). Styling royalty. London Bridge Press.

- For references with more than 20 authors, after listing the 19th author replace any additional author names with an ellipsis ( ... ) followed by the final listed author's last name and first initial(s).

#### **Example for 21+ authors:**

Kalnay, E., Kanamitsu, M., Kistler, R., Collins, W., Deaven, D., Gandin, L., Iredell, M., Saha, S., White, G., Woolen, J., Zhu, Y., Chelliah, M., Ebisuzaki, W., Higgins, W., Janowiak, J., Mo, K.C., Ropelewski, C., Wang, J., Leetmaa, A., ... Joseph, D. (1996). The NCEP/NCAR 40-year reanalysis project. *Bulletin of the American Meteorological Society*, 77(3), 437-471. <http://doi.org/fg6rf9>

- All the initials of the author must be given after the last name and the year of publication should follow in parentheses.
- This should be followed by the full title of the referred publication.
- When journal articles are listed, the journal name should be given in full and in italics and followed by the volume number, issue number in parentheses and then the inclusive pages.
- Where there are several publications by the same author(s) and published in the same year they should be differentiated by adding a lower-case letter after the year.

#### **Example**

Clarke, P. N., & Fawcett, J. (2014a). Life as a mentor. *Nursing Science Quarterly*, 27(3), 213-215. <https://doi.org/10.1177/0894318414534492>

Clarke, P. N., & Fawcett, J. (2014b). Life as a nurse researcher. *Nursing Science Quarterly*, 27(1), 37-41. <https://doi.org/10.1177/0894318413509708>

- Digital object identifiers (DOIs) should be included for all references where available.

Details about this reference style can be obtained from below links

- <https://apastyle.apa.org/style-grammar-guidelines/references>
- <https://apastyle.apa.org/style-grammar-guidelines/references/examples>
- <https://libguides.jcu.edu.au/apa>

**Abbreviations and Symbols:** Unless common, these should be defined when first used, and not included in the abstract. The SI System of units should be used wherever possible. If measurements were made in units other than SI, the data should be reported in the same units followed by SI units in brackets, e.g. 5290 ft (1610 m).

**Formulae and Equations:** Equations should be typewritten and quadruple spaced. They should be started on the left margin and the number placed in parentheses to the right of the equation.

**Nomenclature:** Scientific names of plants and animals should be printed in italics. In the first citation, genus, species and authority must be given. e.g. *Borassus flabellifer* Linn. In latter citations, the generic name may be abbreviated, for example, *B. flabellifer* L.

**Tables and figures:** Tables and Figures should be clear and intelligible and kept to a minimum, and should not repeat data available elsewhere in the paper. Any reproduction of illustrations, tabulations, pictures etc. in the manuscript should be acknowledged.

**Tables:** Tables should be numbered consecutively with Arabic numerals and placed at the appropriate position in the manuscript. If a Table must be continued, a second sheet should be used and all the headings repeated. The number of columns or rows in each Table should be minimized. Each Table should have a title, which makes its general meaning clear, without reference to the text. All Table columns should have explanatory headings. Units of measurement, if any, should be indicated in parentheses in the heading of each column. Vertical lines should not be used and horizontal lines should be used only in the heading and at the bottom of the table. Footnotes to Tables should be placed directly below the Table and should be indicated by superscript lower case italic letters (<sup>a</sup>, <sup>b</sup>, <sup>c</sup>, etc.).

**Figures:** All illustrations are considered as figures, and each graph, drawing or photograph should be numbered consecutively with Arabic numerals and placed at the appropriate position in the manuscript. Any lettering to appear on the illustrations should be of a suitable size for reproduction and uniform lettering should be used in all the Figures of the manuscript. Scanned figures or photographs should be of high quality (**300 dpi**), to fit the proportions of the printed page (12 × 17 cm). Each figure should carry a legend so that the general meaning of the figure can be understood without reference to the text. Where magnifications are used, they should be stated.

#### Units of measurement

Length: km, m, mm, μm, nm

Area: ha, km<sup>2</sup>, m<sup>2</sup>

Capacity: kL, L, mL, μL

Volume: km<sup>3</sup>, m<sup>3</sup>, cm<sup>3</sup>

Mass: t, kg, g, mg, μg

Time: year(s), month(s), wk(s),

d(s), h, min, s

Concentration: M, mM, N, %,

g/L, mg/L, ppm

Temperature: °C, K

Gravity: x g

Molecular weight: mol wt

Others: Radio-isotopes: 32P

Radiation dose: Bq

Oxidation-reduction potential: rH

Hydrogen ion concentration: pH



**JOURNAL OF THE  
NATIONAL SCIENCE FOUNDATION  
OF SRI LANKA**

Volume 52 Number 4 December 2024

---

**C O N T E N T S**

---

**EDITORIAL**

- 417 **Big molecules that do not go away**  
*Ajit Abeysekera*

---

**RESEARCH ARTICLES**

- 419 **Decadal trends in antimicrobial susceptibility of *Escherichia coli* and *Salmonella* spp. in chicken from small-scale farm shops in Kandy district, Sri Lanka**  
*DS Thilakarathne, BYI Gamage, KSA Kottawatta, KGR Abayawansa, WSN Gunawardana and RS Kalupahana*
- 435 **Symmetric encryption using snake graphs and supermagic covering**  
*PGRS Ranasinghe, RMVV Bandara and AMSLK Athapaththu*
- 441 **Maximum likelihood estimation for the two-parameter Maxwell distribution**  
*P Kasap and AO Faouri*
- 459 **Estimating plant dominance using field-measured structural parameters and remotely sensed data; A case study from Rekawa mangrove forest, southern coast of Sri Lanka**  
*SMTM Samarakoon, SK Madarasinghe, NDS D Thilakarathne, AMNN Bandularathne, HD Wijayathilaka, and KAS Kodikara*
- 469 **Simplification of large-scale solid element model for seismic structural response analysis of buildings**  
*HMSC Rathnasiri, JASC Jayasinghe and AJ Dammika*
- 481 **Athlete body power and strength estimation using skeleton point cloud**  
*H Rangala, S Samaraweera, KD Sandaruwan, TA Weerasinghe and DC Ranasinghe*
- 493 **Establishment and evaluation of real-time PCR based SELEX platform for the identification of protein binding aptamers: A pilot study in Sri Lanka**  
*AI Abeykoon, KMN Kumarasinghe, NV Chandrasekharan and PMTB Wickramasinghe*
- 501 **Enhanced privacy-preserving federated convivial learning for internet of medical things (IoMT) through blockchain-enabled trust Q-learning**  
*Sudharson K, G Babu, R Santhiya and CS Anita*
- 515 **Optimizing the alkaline concentration for coir fibre treatment and estimation of lifetime**  
*LG Chamath, LKT Srimal, GA Sewvandi, R Gallage and J Epaarachchi*
- 527 **Unveiling the depths of underwater image enhancement with spatial blended CNN: Diving into clarity**  
*RAhila Priyadharshi, S Arivazhagan and K Ramajeyam*

I **List of Referees**

V **Author Index**

XI **Subject Index**

**Guidelines for Contributors**